

**LARGE SCALE SIMULATION STUDIES OF LITHIATED Li-Mn-O
NANOARCHITECTURES.**

RESEARCH THESIS

Submitted in fulfilment of the requirements for the degree of

DOCTOR of PHILOSOPHY

in

Physics

By

Beauty Shibiri

To

Faculty of Science and Agriculture

Department of Physics

(School of Physical and Mineral Sciences)

University of Limpopo, South Africa

Supervisor: Prof. P. E Ngoepe

Co-supervisor: Prof R. S Ledwaba

October 2021

Declaration

I declare that the thesis hereby submitted to the University of Limpopo for the degree of Doctor of Philosophy has not been previously submitted by me for a degree at this or any other university; that it is my work both in design and execution, and that all materials contained herein have been duly acknowledged.

Ms B. Shibiri

Signature:

A handwritten signature in black ink, appearing to read 'B. Shibiri', is written over a horizontal line.

Student Number: [REDACTED]

Date 29/10/2021

Dedication

This thesis is dedicated to:

My queen, my wonderful mother Mokgadi Josephine Shibiri

My father, Mafenele Jack Shibiri

My grandmother, Mmamolatelolo Mokwape Selowa

My late grandmother, Molewana Selowa Ramatladi.

My beautiful sisters, Jeaneth and Precious Shibiri

My brothers, Ruel Mahasha and the late Oscar Shibiri

My lovely nieces, Prosperity, Thembekile, Risima, Kwetsima and Langavi, and

My precious beautiful gift from God, my daughter Letago Ditheto Maake.

Thank you all for your constant prayers and support, I am truly grateful.

Acknowledgements

Foremost, I would like to express my gratitude to Prof P.E. Ngoepe, my supervisor for taking interest in this project, sharing insightful science experience towards the success of this project and for believing in me. The time you compromised just to attend to this project, is highly appreciated. I would also like to thank my co-supervisor Dr R.S Ledwaba for being patient in mentoring me and sharing insightful science experiences on this project. You inspire me to study further because of your achievements. I will forever be grateful for the times when you had to abandon your work and focus on mine. The times you had to play both the roles of being a supervisor and a sister. Thank you for being supportive when I was at my lowest and for always assuring me that everything will be okay at the end, and if not, that is probably not the end yet. To Kenneth Kgwatane, thank you for always being there when I needed help with executing complex calculations and always making sure that my workstation is user friendly. The time you invested in my work to see it to success is highly appreciated. To my family, thank you for the love, support and prayers. Had it not been for your belief in me, I wouldn't have made it thus far. I am also thankful to the NRF for financial support to help me realise my dreams. To MMC (Material Modelling Centre), I am grateful for the opportunity to study for my PhD and to all the members, I am thankful for your positive inputs towards making this project a success. Above all I would like to thank the Almighty God Jehovah, had it not been for Him, I would not have been where I am today. [Matthews 5:15-16]

Abstract

The vast majority of typical cathode materials for lithium ion batteries suffers from severe specific capacity due to structural changes that occur during the process of cycling, which may lead to fractures within the battery material. Nanostructured materials can act as lattice hosts to accommodate lithium during the charging and discharging process of lithium ion batteries. Nanoporous materials specifically have been studied and found to have large surface areas and volume density, which allows them to flex within their pores during cycling. However, not much has been done to apprehend their electrochemical and mechanical properties at nanoscale especially at intermediate lithium concentrations where the structures undergo phase transitions and how these changes or transitions affect cycling. For that reason, this study seeks to understand the implications that come with structural changes and how they affect the mechanical performance of the battery material; and eventually, come with a better structure that can withstand harsh battery conditions as severe capacity fade.

Computational simulation methods, using the amorphisation and recrystallisation technique employing the DL_POLY code, were used to generate and simulate the spinel LiMn_2O_4 nanoarchitectures. The conductive ion host capabilities of the Li-Mn-O composite nanoarchitectures (porous and bulk) with co-existing layered-spinel (Li_2MnO_3 , LiMnO_2 , LiMn_2O_4 and Mn_3O_4) materials are investigated to predict their structural, electrochemical and mechanical properties during the discharge process. These properties are very important since they provide information on microstructural features and possible volume variations that may occur during cycling. Furthermore, the amorphisation and recrystallisation technique can assist in investigating the effects of diffusion induced stress during the cycling process.

The discharge process was simulated by chemically lithiating the $\text{Li}_{1+x}\text{Mn}_2\text{O}_4$ nanoarchitectures and bulk at different lithium concentrations, where $0 \leq x \leq 1$. To be precise, the structures were lithiated to five different concentrations of $\text{Li}_{1.00}\text{Mn}_2\text{O}_4$, $\text{Li}_{1.25}\text{Mn}_2\text{O}_4$, $\text{Li}_{1.50}\text{Mn}_2\text{O}_4$, $\text{Li}_{1.75}\text{Mn}_2\text{O}_4$ and $\text{Li}_{2.00}\text{Mn}_2\text{O}_4$. The simulated structures are nanoporous 75 Å, nanoporous 69 Å, nanoporous 67 Å and the bulk (63 Å). The structures were amorphised and recrystallised at 1700 K, then characterised by interrogating their total radial distribution functions (RDFs) and their X-ray diffraction patterns (XRDs). Furthermore, the structural integrity of the materials was investigated through microstructural and structural changes in terms of volume variation, defects and grain evolution with increasing lithium concentration.

The total RDFs and structural snapshots for the Li-Mn-O composites show efficiently and spontaneously recrystallised structures that evolved into single and multiple grains. The multiple grained structures are observed mainly at the $\text{Li}_{1.75}\text{Mn}_2\text{O}_4$ concentration. However, few to no grain boundaries for nanoporous 69 Å recrystallised structures at NST and NVT are observed, respectively. Meanwhile, for the bulk recrystallised under the NST ensemble, the structure remains a single grain throughout the discharge process. The $\text{Li}_{1.75}\text{Mn}_2\text{O}_4$ is the concentration where the structures change symmetry from cubic to tetragonal phase. The harvested microstructures show a wealth of crystallographic defects that reduce with increasing lithium content. The increase in lithium concentration also influences the abundance of the spinel Mn_3O_4 , which reduces with lithiation. The microstructures also show the layered-spinel components co-existing within structures. The XRD validates the co-existence of layered-spinel structural composites by characterising the signature and fingerprint peaks of these materials when compared to the experimental. The XRDs for the simulated structures depict significant shifts, splits and broadening of peaks with lithiation.

The nanoporous, unlike the bulk structures, have channels (pores) that allow for better lithium atom transportation and diffusion. The lattice dimension of these nanoporous structures is relative to the pore size. This implies that a material with a larger lattice will have a bigger pore that can possibly accommodate more lithium atoms on its structure and cavity. Further investigations on the nanoporous structures reveal that pore sizes reduce with increasing lithium concentration under NVT ensemble recrystallisation, except for nanoporous 69 Å at $\text{Li}_{1.75}\text{Mn}_2\text{O}_4$, where the pore is observed to increase in size. Recrystallising the structures under the NST ensemble result in the pores increasing in size from $\text{Li}_{1.00}\text{Mn}_2\text{O}_4$ to $\text{Li}_{1.25}\text{Mn}_2\text{O}_4$, and thereafter reduce with increasing concentration where some pores completely close up at $\text{Li}_{1.75}\text{Mn}_2\text{O}_4$. However, full lithiating the structures to $\text{Li}_{2.00}\text{Mn}_2\text{O}_4$ under both ensembles results in the materials almost regaining their original pore sizes.

The structures were also exposed to temperature to investigate their lithium diffusivity and stability with lithiation. The diffusion coefficients of lithium in the structures with increasing concentration and temperature also show that pore size influences diffusivity. This is because nanoporous 75 Å shows the highest lithium diffusion compared to its counterparts followed by nanoporous 69 Å, then nanoporous 67 Å and lastly, the bulk, where the stability of the materials is maintained. The structures also undergo volume expansion during lithiation under the NST ensemble and they all maintain their structural integrity throughout. However, nanoporous 69 Å at $\text{Li}_{1.75}\text{Mn}_2\text{O}_4$ is observed to be resilient to expansion. Meanwhile, the bulk volume drops drastically from $\text{Li}_{1.75}\text{Mn}_2\text{O}_4$ to $\text{Li}_{2.00}\text{Mn}_2\text{O}_4$ concentration. The reason for the nanoporous structures to withstand lithiation without fail is attributed to their ability to flex within their pores and larger surface areas; meanwhile, for the bulk, the Mn_3O_4 walls could be collapsing.

The mechanical properties of the nanoporous materials investigated through stress-strain calculations, with the imposed uniaxial stress of 0.1 GPa, show RDFs which have broad and flat peaks with increasing radial distance r , implying the disorder in atom arrangement. Meanwhile, the XRDs show peaks merging to form one broad peak; while other peaks shift and split. The stress-strain plots reveal that nanoporous 69 Å especially at $\text{Li}_{1.75}\text{Mn}_2\text{O}_4$ has the highest yield strength when compared to its counterparts. This indicates that nanoporous 69 Å is more robust since it can evolve into one or few grains, resist expansion, fracture and also have efficient lithium diffusion at varied temperatures. This implies that nanoporous 69 Å material has the potential to curb the current battery setbacks such as volume expansion that causes cracks within the battery material during cycling causing battery degradation.

Table of Contents

CHAPTER 1	1
Introduction and general background	1
1.1 Literature review	4
1.1.1 Lithium ion cathodes and their setbacks.....	5
1.1.2 Enhancement of lithium ion battery through composites and nanoporous structures	7
1.1.3 Structural description	8
1.1.4 Lithiation/delithiation mechanism and effect of cycling	9
1.1.5 Structural deformations	10
1.2 Intentions of the study	12
1.3 Outline of the study	15
CHAPTER 2	16
Research methodology	16
2.1 Computational modelling.....	16
2.2 Molecular dynamics	18
2.2.1 Molecular dynamics ensembles	18
2.3 Molecular dynamics properties	19
2.3.1 Radial distribution function.....	19
2.3.2 X-ray diffraction patterns.....	20
2.3.3 Diffusion coefficients.....	20

2.4 Mechanical properties.....	21
2.5 Amorphisation and recrystallisation technique	24
2.6 Simulation code	25
2.7 The potential model.....	26
2.8 Crystallographic defects.....	28
2.8.1 Point defects	30
2.8.2 Planar /surface defects	31
2.8.3 Microstructures.....	31
CHAPTER 3	32
Effects of lithiation on the nanoporous and bulk electrode materials.....	32
3.1 Introduction.....	32
3.1.1 Generation and lithiation mechanism of the nanoporous and bulk materials	33
3.1.1 Amorphisation and recrystallisation of lithiated the Li-Mn-O materials.....	35
3.2 Microstructures and X-ray diffraction patterns for the nanoporous materials.....	43
3.2.1 Nanoporous 75 Å.....	43
3.2.2 Nanoporous 69 Å.....	51
3.2.3 Nanoporous 67 Å.....	58
3.2.4 Bulk (63 Å)	65
3.3 Structural characterisation of the nanoporous and bulk structures by X-ray diffraction patterns.....	72
3.3.1 XRDs for the nanoporous structures	72
3.3.2 XRDs for the bulk structure.....	78

3.4 Discussion.....	80
CHAPTER 4	82
Structural changes on the lithiated nanoporous and bulk electrode materials.....	82
4.1 Introduction.....	82
4.2 Method	83
4.3 Pore size effect and volume change on the nanoporous (75, 69, 67 Å) and bulk structures.....	84
4.4 Microstructural changes emanating from lithium intercalation.....	98
4.4.1 Nanoporous 75 Å.....	98
4.4.2 Nanoporous 69 Å.....	105
4.4.3 Nanoporous 67 Å.....	112
4.4.4 Bulk (63 Å)	119
4.5 Structural characterisation of the nanoporous and bulk structures by X-ray diffraction patterns.....	126
4.5.1 XRDs of nanoporous structures.....	126
4.5.2 XRDs for the bulk structure.....	134
4. 6 Discussion.....	137
CHAPTER 5	139
The effect of high temperature on $\text{Li}_{1+x}\text{Mn}_2\text{O}_4$ nanoporous and bulk materials	139
5.1 Introduction.....	139
5.2 Method	140

5.3 The lithium diffusion coefficients for the nanoporous and bulk at different lithium concentrations.....	140
5.4 The Li-Mn-O diffusion coefficients of the pristine nanoporous and bulk structures	144
5.5 Comparison of the lithium diffusion for nanoporous and bulk structures at similar concentrations.....	148
5.6 Discussion	152
CHAPTER 6	153
The mechanical properties of nanoporous structures	153
6.1 Introduction.....	153
6.2 Method	154
6.2.1 Generating the atomistic model structures	154
6.2.2 Simulating Uniaxial stress.....	154
6.3 Uniaxial stress for the nanoporous structures	155
6.4 Radial distribution functions and X-ray diffraction pattern analysis of the nanoporous structures under stress.....	164
6.4.1 Radial distribution functions response to stress.....	164
6.4.2 The X-ray diffraction pattern's response to stress	166
6.4 Discussion.....	173
CHAPTER 7	175
Conclusion and Recommendations.....	175
7.1 Conclusion.....	175

7.2 Recommendations	179
REFERENCES.....	181
SCIENTIFIC CONTRIBUTIONS.....	200
Papers at local conferences	200
Papers at international conferences.....	201
Awards.....	201
Publications	202

List of tables

Table 1.1: Structural properties of spinel LiMn_2O_4	9
Table 3.1: The intercalated lithium concentrations of spinel LiMn_2O_4 for nanoporous and bulk structures with lattice parameters of 75 Å, 69 Å, 67 Å and 63 Å, respectively.	33

List of figures

Chapter 1

Figure 1.1: The applications of Li-ion batteries in (a) electric vehicles replacing fuel, (b) smart grids as a network for digital communications technology to detect and react to local changes in electricity usage and (c) in electronics as a power source storage for cell phones, power banks, cameras and laptops.	4
Figure 1.2: The battery mechanism showing the cycling discharge (lithiation) and charge (delithiation) processes.	10

Chapter 2

Figure 2.1: The schematic illustration of the procedure to be followed when constructing the nanoarchitectures [34].	17
Figure 2.2: The stress-strain diagram illustrating the information on how much a material can withstand a force before permanent deformation [87].	24
Figure 2.3: Schematic illustration of defects in a crystal where, (a) is the vacancy, (b) interstitial impurity, (c) substitution impurity and (d) self-interstitial.	30

Chapter 3

Figure 3.1: Snapshots of the (a) conventional unit cell, (b) supercell, (c) nanosphere exposed to pressure to allow the formation of (d) nanoporous 75 Å, (e) nanoporous 69 Å, (f) nanoporous 67 Å and (g) bulk structures.	35
Figure 3.2: The lithiated nanoporous 75 Å structures of Li-Mn-O composites with different concentrations showing the tilted and front view of (a, b) $\text{Li}_{1.00}\text{Mn}_2\text{O}_4$, (c, d) $\text{Li}_{1.25}\text{Mn}_2\text{O}_4$, (e, f) $\text{Li}_{1.50}\text{Mn}_2\text{O}_4$, (g, h) multi grained $\text{Li}_{1.75}\text{Mn}_2\text{O}_4$ and (i, j) $\text{Li}_{2.00}\text{Mn}_2\text{O}_4$, respectively.....	38
Figure 3.3: The lithiated nanoporous 69 Å structures of Li-Mn-O composites with different concentrations showing the tilted and front view of (a, b) $\text{Li}_{1.00}\text{Mn}_2\text{O}_4$, (c, d) $\text{Li}_{1.25}\text{Mn}_2\text{O}_4$, (e, f) $\text{Li}_{1.50}\text{Mn}_2\text{O}_4$, (g, h) distorted $\text{Li}_{1.75}\text{Mn}_2\text{O}_4$ and (i, j) $\text{Li}_{2.00}\text{Mn}_2\text{O}_4$, respectively.....	39
Figure 3.4: The lithiated nanoporous 67 Å structures of Li-Mn-O composites with different concentrations showing the tilted and front view of (a, b) $\text{Li}_{1.00}\text{Mn}_2\text{O}_4$, (c, d) $\text{Li}_{1.25}\text{Mn}_2\text{O}_4$, (e, f) $\text{Li}_{1.50}\text{Mn}_2\text{O}_4$, (g, h) multi grained $\text{Li}_{1.75}\text{Mn}_2\text{O}_4$ and (i, j) $\text{Li}_{2.00}\text{Mn}_2\text{O}_4$, respectively.....	40
Figure 3.5: The lithiated bulk structures of Li-Mn-O composites with different lithium concentrations showing the tilted and front view of (a,b) $\text{Li}_{1.00}\text{Mn}_2\text{O}_4$, (c,d) $\text{Li}_{1.25}\text{Mn}_2\text{O}_4$, (e,f) $\text{Li}_{1.50}\text{Mn}_2\text{O}_4$, (g,h) $\text{Li}_{1.75}\text{Mn}_2\text{O}_4$ and (i,j) $\text{Li}_{2.00}\text{Mn}_2\text{O}_4$	41

Figure 3.6: The total RDFs of lithiated Li-Mn-O nanoporous and bulk structures with different lithium concentrations of $\text{Li}_{1+x}\text{Mn}_2\text{O}_4$, where $0 \leq x \leq 1$; depicting the amorphous and recrystallised structures of nanoporous 75 Å, 69 Å, 67 Å and the bulk..... 42

Figure 3.7: The simulated (i, a) nanoporous 75 Å structure at $\text{Li}_{1.00}\text{Mn}_2\text{O}_4$ concentration which has recrystallised into two grains magnified to illustrate the (b) Mn^{2+} atoms in the tetrahedral tunnels, where (c) is the perfect structural model of spinel Mn_3O_4 . The microstructure (ii, a) harvested from (i, a) depicting defective magnifications of (b) layered Li_2MnO_3 and (d) spinel LiMn_2O_4 components which are comparable to their structural model (c, e), respectively..... 46

Figure 3.8: The simulated (i, a) $\text{Li}_{1.25}\text{Mn}_2\text{O}_4$ nanoporous 75 Å structure depicting the magnified section of (b) spinel Mn_3O_4 structure compared with (c) its perfect structural model. The microstructure (ii, a) harvested from $\text{Li}_{1.25}\text{Mn}_2\text{O}_4$ nanoporous 75 Å show the magnified portions of the defective (b) layered Li_2MnO_3 component and (d) spinel LiMn_2O_4 which are comparable to their structural models (c, e). 47

Figure 3.9: The simulated (i, a) $\text{Li}_{1.50}\text{Mn}_2\text{O}_4$ nanoporous 75 Å structure illustrates (b) the Mn^{2+} atoms retained in tetrahedral tunnels, where (c) is the perfect structural model of spinel Mn_3O_4 . The microstructure slice (ii, a) cut from $\text{Li}_{1.50}\text{Mn}_2\text{O}_4$ nanoporous 75 Å structure shows the magnifications of (b) layered Li_2MnO_3 and (d) spinel LiMn_2O_4 components with defects compared with (c, e) their perfect structural models..... 48

Figure 3.10: The multi grained (i, a) nanoporous 75 Å structure at $\text{Li}_{1.75}\text{Mn}_2\text{O}_4$ concentration with distorted regions. The harvested microstructure (ii, a) from $\text{Li}_{1.75}\text{Mn}_2\text{O}_4$ nanoporous 75 Å structure depicting grain boundaries and the magnified section of (c) defective spinel LiMn_2O_4 component compared to (d) its perfect structural model..... 49

Figure 3.11: The distorted full lithiated (i, a) nanoporous 75 Å structure at $\text{Li}_{2.00}\text{Mn}_2\text{O}_4$ concentration depicting (b) Mn^{2+} atoms in the tetrahedral tunnels, where (c) is the perfect structural model of spinel Mn_3O_4 . The microstructure (ii, a) of $\text{Li}_{2.00}\text{Mn}_2\text{O}_4$ nanoporous 75

Å with a grain boundary, showing the magnifications of defected (b) spinel LiMn_2O_4 and (d) layered Li_2MnO_3 compared to their (c, e) perfect structural models. 50

Figure 3.12: Nanoporous 69 Å structure (i, a) at $\text{Li}_{1.00}\text{Mn}_2\text{O}_4$ concentration illustrating the (b) Mn^{2+} atoms retaining tetrahedral tunnels, with the (c) perfect structural model of spinel Mn_3O_4 . The microstructure (ii, a) show the defected magnification of (b) layered Li_2MnO_3 which is comparable to (c) its perfect structural model. 53

Figure 3.13: The $\text{Li}_{1.25}\text{Mn}_2\text{O}_4$ nanoporous 69 Å structure (i, a) depicting the magnified portion of (b) spinel Mn_3O_4 structure compared with (c) the perfect structural model. The microstructure slice (ii, a), harvested from the structure depicting the co-existence of (b) layered Li_2MnO_3 and (d) spinel LiMn_2O_4 components which are comparable to their (c, e) perfect structural models compared with the perfect structural models. 54

Figure 3.14: The nanoporous 69 Å structure (i, a) at $\text{Li}_{1.50}\text{Mn}_2\text{O}_4$ concentration depicting the magnified section of (b) spinel Mn_3O_4 structure, comparable with the (c) perfect structural model. The microstructure slice (ii, a) cut from $\text{Li}_{1.50}\text{Mn}_2\text{O}_4$ nanoporous 69 Å, illustrating the magnifications of (b) layered Li_2MnO_3 and (d) spinel LiMn_2O_4 components compared with (c, e) their perfect structural models. 55

Figure 3.15: The distorted nanoporous 69 Å structure (i, a) at $\text{Li}_{1.75}\text{Mn}_2\text{O}_4$ concentration showing the (b) Mn^{2+} atoms in the tetrahedral tunnels, where (c) Mn_3O_4 is the perfect structural model. The microstructure (ii, a) of $\text{Li}_{1.75}\text{Mn}_2\text{O}_4$ nanoporous 69 Å depicting the magnified sections of the defected (b) spinel LiMn_2O_4 and (d) layered Li_2MnO_3 components compared with (c, e) their perfect structural models, respectively. 56

Figure 3.16: The full lithiated nanoporous 69 Å structure (i, a) at $\text{Li}_{2.00}\text{Mn}_2\text{O}_4$ concentration illustrating the (b) Mn^{2+} atoms in the tetrahedral tunnels, compared to the (c) perfect structural model of spinel Mn_3O_4 . The harvested microstructure slice (ii, a) of the $\text{Li}_{2.00}\text{Mn}_2\text{O}_4$ nanoporous 69 Å structure, depicting the magnifications of (b) layered

Li₂MnO₃ and (d) spinel LiMn₂O₄ composites, compared with their (c, e) the perfect structural models. 57

Figure 3.17: The nanoporous 67 Å structure (i, a) at Li_{1.00}Mn₂O₄ depicting the magnified section of (b) spinel Mn₃O₄ structure compared with (c) its perfect model. The microstructure (ii, a) illustrates the magnifications of defected (b) layered Li₂MnO₃ and (d) spinel LiMn₂O₄ compared with their(c, e) perfect structural modes. 60

Figure 3.18: The Li_{1.25}Mn₂O₄ nanoporous 67 Å structure (i, a) illustrating the magnified section of (b) spinel Mn₃O₄ structure which is comparable to (c) its perfect structural model. The microstructure slice ((ii, a) harvested from Li_{1.25}Mn₂O₄ nanoporous 67 Å structure depicting the magnified sections of (b) layered Li₂MnO₃ and d) spinel LiMn₂O₄ components, compared with their (c, e) perfect structural models. 61

Figure 3.19: The nanoporous 67 Å structure (i, a) at Li_{1.50}Mn₂O₄ concentration illustrating the presence of (b) spinel Mn₃O₄ structure comparable to (c) its perfect structural model. The Microstructure (ii, a) cut from the Li_{1.50}Mn₂O₄ nanoporous 67 Å structure capturing the defected magnified portions of (b) spinel LiMn₂O₄ and (d) layered Li₂MnO₃ when compared to their (c, e) perfect structural models. 62

Figure 3.20: The distorted and multi grained nanoporous 67 Å structure (i, a) at Li_{1.75}Mn₂O₄ concentration. The microstructure (ii, a) harvested from the Li_{1.75}Mn₂O₄ nanoporous 67 Å, with multiple grain boundaries, depicting the magnified section of (b) spinel LiMn₂O₄ component comparable with (c) its perfect structural model. 63

Figure 3.21: The full lithiated nanoporous 67 Å structure (i, a) at Li_{2.00}Mn₂O₄ concentration illustrating (b) Mn²⁺ atoms retained in tetrahedral tunnels, compared to the perfect structural model of spinel Mn₃O₄. The microstructure of Li_{2.00}Mn₂O₄ nanoporous 67 Å (ii, a) illustrating the magnifications of (b) spinel LiMn₂O₄ and (d) layered Li₂MnO₃ comparable with (c, e) their perfect structural models. 64

Figure 3.22: The $\text{Li}_{1.00}\text{Mn}_2\text{O}_4$ bulk structure ((i) a) illustrating the presence of (b) Mn^{2+} retained in tetrahedral tunnels compared with (c) the perfect structural model of spinel Mn_3O_4 . The microstructure (ii, a) of the bulk cut from the $\text{Li}_{1.00}\text{Mn}_2\text{O}_4$ structure depicting the magnified portions of (b) layered Li_2MnO_3 and (d) of spinel LiMn_2O_4 compared to their (c, e) perfect structural models..... 67

Figure 3.23: The bulk structure (i, a) at $\text{Li}_{1.25}\text{Mn}_2\text{O}_4$ concentration depicting the magnified section of (b) spinel Mn_3O_4 structure comparable to its (c) perfect structural model. The microstructure (ii, a) harvested from the bulk $\text{Li}_{1.25}\text{Mn}_2\text{O}_4$ structure showing the defected magnified sections of (b) layered Li_2MnO_3 and (d) spinel LiMn_2O_4 compared to their (c, e) perfect structural models. 68

Figure 3.24: The $\text{Li}_{1.50}\text{Mn}_2\text{O}_4$ bulk structure (i, a) illustrating the magnified section of spinel Mn_3O_4 structure (b) compared with (c) the perfect structural model. The microstructure (ii, a) cut from $\text{Li}_{1.50}\text{Mn}_2\text{O}_4$ structure with magnified portions (b) the layered Li_2MnO_3 and (d) spinel LiMn_2O_4 components, which are comparable to (c, e) their perfect structural models. 69

Figure 3.25: The bulk structure (i, a), which has recrystallised into a multi grained material. The microstructure slice (ii, a) with grain boundaries from the $\text{Li}_{1.75}\text{Mn}_2\text{O}_4$ bulk depicting the magnified section of (b) layered Li_2MnO_3 component compared to (c) its perfect structural model..... 70

Figure 3.26: The full lithiated bulk structure (i, a) at $\text{Li}_{2.00}\text{Mn}_2\text{O}_4$ concentration magnified to illustrate that Mn^{2+} atoms are retaining the tetrahedral tunnels. The microstructure slice (ii, a) cut through the $\text{Li}_{2.00}\text{Mn}_2\text{O}_4$ bulk structure, illustrating the presence of (b) layered Li_2MnO_3 and (d) spinel LiMn_2O_4 compared with their (c, e) perfect structural models. ... 71

Figure 3.27: The XRDs for simulated (a) $\text{Li}_{1.00}\text{Mn}_2\text{O}_4$, (b) $\text{Li}_{1.25}\text{Mn}_2\text{O}_4$, (c) $\text{Li}_{1.50}\text{Mn}_2\text{O}_4$, (d) $\text{Li}_{1.75}\text{Mn}_2\text{O}_4$ and (e) $\text{Li}_{2.00}\text{-Mn}_2\text{O}_4$ nanoporous 75 Å structures; compared with the

experimental X-ray diffraction patterns for (f) spinel Mn_3O_4 [106], (g) layered $LiMnO_2$ [107], (h) layered Li_2MnO_3 [107] and (i) spinel $LiMn_2O_4$ [107]..... 75

Figure 3.28: The XRDs for simulated (a) $Li_{1.00}Mn_2O_4$, (b) $Li_{1.25}Mn_2O_4$, (c) $Li_{1.50}Mn_2O_4$, (d) $Li_{1.75}Mn_2O_4$ and (e) $Li_{2.00}Mn_2O_4$ nanoporous 69 Å structures; compared with the experimental for (f) spinel Mn_3O_4 [106], (g) layered $LiMnO_2$ [107], (h) layered Li_2MnO_3 [107] and (i) spinel $LiMn_2O_4$ [107]. 76

Figure 3.29: The XRDs for simulated (a) $Li_{1.00}Mn_2O_4$, (b) $Li_{1.25}Mn_2O_4$, (c) $Li_{1.50}Mn_2O_4$, (d) $Li_{1.75}Mn_2O_4$ and (e) $Li_{2.00}Mn_2O_4$ Li-Mn-O nanoporous 67 Å structures, compared with the experimental XRDs for (f) spinel Mn_3O_4 [106], (g) layered $LiMnO_2$ [107], (h) layered Li_2MnO_3 [107] and (i) spinel $LiMn_2O_4$ [107]. 77

Figure 3.30: The XRDs for simulated (a) $Li_{1.00}Mn_2O_4$ (b) $Li_{1.25}Mn_2O_4$, (c) $Li_{1.50}Mn_2O_4$, (d) $Li_{1.75}Mn_2O_4$ and (e) $Li_{2.00}Mn_2O_4$ bulk structures, compared with the experimental XRDs for (f) spinel Mn_3O_4 [106], (g) layered $LiMnO_2$ [107], (h) layered Li_2MnO_3 [107] and (i) spinel $LiMn_2O_4$ [107] structures. 79

Chapter 4

Figure 4.1: The structural changes on the lithiated NST nanoporous (75, 69 and 67 Å) and bulk materials with different lithium concentrations, $Li_{1+x}Mn_2O_4$, $0 \leq x \leq 1$, showing pore size effect as the lithium content is increased. 86

Figure 4.2: The total RDFs for the recrystallised lithiated Li-Mn-O nanoporous structures with different lithium concentrations; where (a) is the nanoporous 75 Å, (b) nanoporous 69 Å, (c) the nanoporous 67 Å and (d) the bulk. 87

Figure 4.3: The lithiated connolly surface structures for nanoporous 75 Å illustrating changes in the channels and volume with an increase in lithium concentration viewed in

“In-cell and Original” lattices, where (a) is the $\text{Li}_{1.00}\text{Mn}_2\text{O}_4$, (b) $\text{Li}_{1.25}\text{Mn}_2\text{O}_4$, (c) $\text{Li}_{1.50}\text{Mn}_2\text{O}_4$, (d) $\text{Li}_{1.75}\text{Mn}_2\text{O}_4$ and (e) the $\text{Li}_{2.00}\text{Mn}_2\text{O}_4$ concentrations. 90

Figure 4.4: The lithiated Li-Mn-O Connolly surface structures for nanoporous 69 Å illustrating the channel and volume occupied viewed in “In-cell and Original” lattices, where (a) is the $\text{Li}_{1.00}\text{Mn}_2\text{O}_4$, (b) $\text{Li}_{1.25}\text{Mn}_2\text{O}_4$, (c) $\text{Li}_{1.50}\text{Mn}_2\text{O}_4$, (d) $\text{Li}_{1.75}\text{Mn}_2\text{O}_4$ and (e) the $\text{Li}_{2.00}\text{Mn}_2\text{O}_4$ concentrations. 91

Figure 4.5: The lithiated Connolly surface structures for nanoporous 67 Å illustrating systems with volume and pore changes as lithium concentration is increased in them, viewed in “In-cell and Original” lattices, where (a) is the $\text{Li}_{1.00}\text{Mn}_2\text{O}_4$, (b) $\text{Li}_{1.25}\text{Mn}_2\text{O}_4$, (c) $\text{Li}_{1.50}\text{Mn}_2\text{O}_4$, (d) $\text{Li}_{1.75}\text{Mn}_2\text{O}_4$ and (e) the $\text{Li}_{2.00}\text{Mn}_2\text{O}_4$ concentrations. 92

Figure 4.6: Bulk (63 Å) structures illustrating the Connolly surfaces used to determine volume changes that occur with lithium intercalation viewed in “In-cell and Original” lattices, where (a) is the $\text{Li}_{1.00}\text{Mn}_2\text{O}_4$, (b) $\text{Li}_{1.25}\text{Mn}_2\text{O}_4$, (c) $\text{Li}_{1.50}\text{Mn}_2\text{O}_4$, (d) $\text{Li}_{1.75}\text{Mn}_2\text{O}_4$ and (e) the $\text{Li}_{2.00}\text{Mn}_2\text{O}_4$ concentrations. 93

Figure 4.7: The graphical representations for nanoporous (75, 69, and 67 Å) and bulk structures illustrating the changes in volume with increasing lithium concentration from $\text{Li}_{1.00}\text{Mn}_2\text{O}_4$ to $\text{Li}_{2.00}\text{Mn}_2\text{O}_4$, ($\text{Li}_{1+x}\text{Mn}_2\text{O}_4$, $0 \leq x \leq 1$). 96

Figure 4.8: Volume change plots for nanoporous (75, 69 and 67 Å) and bulk structures illustrating the changes in volume with increasing lithium concentration from $\text{Li}_{1.00}\text{Mn}_2\text{O}_4$ to $\text{Li}_{2.00}\text{Mn}_2\text{O}_4$, ($\text{Li}_{1+x}\text{Mn}_2\text{O}_4$, $0 \leq x \leq 1$). 97

Figure 4.9: The $\text{Li}_{1.00}\text{Mn}_2\text{O}_4$ polycrystalline nanoporous 75 Å structure (i, a) depicting the (b) magnified sections of Mn^{2+} atoms retraining the tetrahedral tunnels, compared with (c) the perfect Mn_3O_4 model. The microstructure (ii, a) at $\text{Li}_{1.00}\text{Mn}_2\text{O}_4$ illustrating the magnifications of (b) layered Li_2MnO_3 and (d) spinel LiMn_2O_4 components comparable to their perfect models (c, e), respectively. 100

Figure 4.10: The $\text{Li}_{1.25}\text{Mn}_2\text{O}_4$ nanoporous 75 Å structure (i, a) illustrating the magnified sections of the (b) spinel Mn_3O_4 and (c) its perfect model. The microstructure slice (ii, a) of $\text{Li}_{1.25}\text{Mn}_2\text{O}_4$ nanoporous 75 Å structure showing (b) the layered Li_2MnO_3 and (d) spinel LiMn_2O_4 components and their perfect models (c, e).....101

Figure 4.11: The nanoporous 75 Å structure (i, a) at $\text{Li}_{1.50}\text{Mn}_2\text{O}_4$ concentration demonstrating the (b) magnification of Mn^{2+} atoms retraining the tetrahedral tunnels, compared to (c) the perfect Mn_3O_4 model. The microstructure (ii, a) of $\text{Li}_{1.50}\text{Mn}_2\text{O}_4$ nanoporous 75 Å structure capturing (b) the layered Li_2MnO_3 and (d) spinel LiMn_2O_4 components compared to their perfect structural models (c, e), respectively.....102

Figure 4.12: The multi grained $\text{Li}_{1.75}\text{Mn}_2\text{O}_4$ nanoporous 75 Å (i, a) structure with grain boundaries depicting some distorted regions. The microstructure with grain boundaries (ii, a) illustrating the (b) spinel LiMn_2O_4 and (d) the layered Li_2MnO_3 components with their (c, e) perfect structural models.....103

Figure 4.13: The distorted $\text{Li}_{2.00}\text{Mn}_2\text{O}_4$ nanoporous 75 Å structure (i, a) depicting the (b) magnification of Mn^{2+} atoms retraining the tetrahedral tunnels compared to (c) the perfect Mn_3O_4 model. The microstructure (ii, a) of $\text{Li}_{2.00}\text{Mn}_2\text{O}_4$ nanoporous 75 Å structure illustrating (b) the layered Li_2MnO_3 and (d) spinel LiMn_2O_4 components compared to their (c, e) perfect structural models.....104

Figure 4.14: The $\text{Li}_{1.00}\text{Mn}_2\text{O}_4$ nanoporous 69 Å structure (i, a) illustrating the magnification of (b) spinel Mn_3O_4 comparable to (c) its perfect structural model. The microstructure (ii, a) of $\text{Li}_{1.00}\text{Mn}_2\text{O}_4$ nanoporous 69 Å structure capturing the defective (b) layered Li_2MnO_3 and (d) spinel LiMn_2O_4 components with their perfect models (c, e), respectively.....107

Figure 4.15: The nanoporous 69 Å structure (i, a) at $\text{Li}_{1.25}\text{Mn}_2\text{O}_4$ concentration depicting the (b) magnification of Mn^{2+} atoms retained in tetrahedral tunnels compared to (c) the perfect Mn_3O_4 model. The microstructure slice (ii, a) of $\text{Li}_{1.25}\text{Mn}_2\text{O}_4$ nanoporous 69 Å

structure capturing (b) the layered Li_2MnO_3 and (d) spinel LiMn_2O_4 components compared to (c, e) their perfect models.108

Figure 4.16: The nanoporous 69 Å structure at (i, a) $\text{Li}_{1.50}\text{Mn}_2\text{O}_4$ concentration demonstrating the (b) magnification of Mn^{2+} atoms retained in the tetrahedral tunnels, where (c) is the perfect Mn_3O_4 model. The $\text{Li}_{1.50}\text{Mn}_2\text{O}_4$ nanoporous 69 Å microstructure (ii, a) capturing (b) the layered Li_2MnO_3 and (d) spinel LiMn_2O_4 components with (c, e) their perfect structural models.109

Figure 4.17: The distorted $\text{Li}_{1.75}\text{Mn}_2\text{O}_4$ nanoporous 69 Å structure (i, a) depicting the (b) magnified section of Mn^{2+} atoms in the tetrahedral tunnels, where (c) is the perfect Mn_3O_4 model. The multi grained microstructure of $\text{Li}_{1.75}\text{Mn}_2\text{O}_4$ nanoporous 69 Å structure (ii, a) showing the defected (b) spinel LiMn_2O_4 component compared to (c) its perfect model.110

Figure 4.18: The $\text{Li}_{2.00}\text{Mn}_2\text{O}_4$ nanoporous 69 Å structure (i, a) illustrating the (b) magnifications of Mn^{2+} atoms in the tetrahedral tunnels, where the perfect Mn_3O_4 model is denoted by (c). The microstructure of (ii, a) $\text{Li}_{2.00}\text{Mn}_2\text{O}_4$ nanoporous 69 Å structure depicting the (b) spinel LiMn_2O_4 and (d) the layered Li_2MnO_3 components with (c, e) their perfect models.111

Figure 4.19: The $\text{Li}_{1.00}\text{Mn}_2\text{O}_4$ nanoporous 67 Å structure (i, a) with the magnification of (b) the Mn^{2+} atoms in the tetrahedral tunnels, where (c) is the perfect Mn_3O_4 model. The microstructure slice (ii, a) $\text{Li}_{1.00}\text{Mn}_2\text{O}_4$ of nanoporous 67 Å structure showing (b) the spinel LiMn_2O_4 and (d) the layered Li_2MnO_3 components compared to their perfect models (c, e), respectively.....114

Figure 4.20: The nanoporous 67 Å structure (i, a) at $\text{Li}_{1.25}\text{Mn}_2\text{O}_4$ concentration illustrating (b) the magnified segment of Mn^{2+} atoms in tetrahedral tunnels, (c) is the perfect Mn_3O_4 model. The harvested microstructure slice of $\text{Li}_{1.25}\text{Mn}_2\text{O}_4$ nanoporous 67 Å structure (ii, a)

illustrating (b) spinel LiMn_2O_4 and (d) layered Li_2MnO_3 components comparable to (c, e) their perfect models.....115

Figure 4.21: The nanoporous 67 Å structure of $\text{Li}_{1.50}\text{Mn}_2\text{O}_4$ (i, a) presenting (b) the magnification of spinel Mn_3O_4 and is comparable to (c) its perfect Mn_3O_4 model. The microstructure slice (ii, a) of $\text{Li}_{1.50}\text{Mn}_2\text{O}_4$ nanoporous 67 Å structure depicting (b) spinel LiMn_2O_4 and (d) the layered Li_2MnO_3 components with their (c, e) perfect structural models.116

Figure 4.22: The distorted and multi grained $\text{Li}_{1.75}\text{Mn}_2\text{O}_4$ nanoporous 67 Å structure (i, a) showing the magnifications (b) of Mn^{2+} atoms in the tetrahedral tunnels, where the perfect Mn_3O_4 model is denoted by (c). The microstructure of $\text{Li}_{1.75}\text{Mn}_2\text{O}_4$ nanoporous 67 Å structure with grain boundaries (ii, a) illustrating the (b) spinel LiMn_2O_4 and (d) layered Li_2MnO_3 components with (c, e) their perfect models.117

Figure 4.23: The $\text{Li}_{2.00}\text{Mn}_2\text{O}_4$ nanoporous 67 Å structure (i, a) portraying the (b) magnifications of Mn^{2+} atoms in the tetrahedral tunnels, where (c) is the perfect Mn_3O_4 model. The microstructure slice of (ii, a) $\text{Li}_{2.00}\text{Mn}_2\text{O}_4$ nanoporous 67 Å structure depicting (b) the layered Li_2MnO_3 and (d) spinel LiMn_2O_4 components compared to (c, e) their perfect structural models.118

Figure 4.24: The $\text{Li}_{1.00}\text{Mn}_2\text{O}_4$ bulk structure (i, a) depicting the magnified section of (b) spinel Mn_3O_4 and comparable to (c) its perfect structural model. The microstructure (ii, a) of $\text{Li}_{1.00}\text{Mn}_2\text{O}_4$ bulk structure capturing the (b) spinel LiMn_2O_4 and (d) layered Li_2MnO_3 components comparable to their perfect structural models (c, e), respectively.....121

Figure 4.25: The $\text{Li}_{1.25}\text{Mn}_2\text{O}_4$ bulk structure (i, a) illustrating the magnified section of (b) Mn^{2+} atoms retraining the tetrahedral tunnels compared to (c) the perfect Mn_3O_4 structural model. The microstructure (ii, a) of $\text{Li}_{1.25}\text{Mn}_2\text{O}_4$ bulk structure showing the (b) spinel LiMn_2O_4 and (d) the layered Li_2MnO_3 components, compared to (c, e) their perfect structural models122

Figure 4.27: The bulk structure (i, a) at $\text{Li}_{1.50}\text{Mn}_2\text{O}_4$ concentration demonstrating the (b) magnified section of Mn^{2+} atoms retraining the tetrahedral tunnels, compared to (c) the perfect Mn_3O_4 structural model. The microstructure (ii, a) of the $\text{Li}_{1.50}\text{Mn}_2\text{O}_4$ bulk structure illustrating the (b) spinel LiMn_2O_4 and (d) the layered Li_2MnO_3 components, which are comparable to (c, e) their perfect structural models, respectively.....123

Figure 4.28: The $\text{Li}_{1.75}\text{Mn}_2\text{O}_4$ bulk structure (i, a) depicting the magnification of (b) Mn^{2+} atoms retraining the tetrahedral tunnels, compared to (c) the perfect Mn_3O_4 structural model. The microstructure (ii, a) of $\text{Li}_{1.75}\text{Mn}_2\text{O}_4$ bulk structure capturing (b) the spinel LiMn_2O_4 component compared to (c) its perfect structural model.....124

Figure 4.29: The $\text{Li}_{2.00}\text{Mn}_2\text{O}_4$ bulk structure (i, a) illustrating (b) magnifications of Mn^{2+} atoms retraining the tetrahedral tunnels compared to (c) the perfect Mn_3O_4 structural model. The simulated microstructure of (ii, a) $\text{Li}_{2.00}\text{Mn}_2\text{O}_4$ bulk demonstrating the (b) layered Li_2MnO_3 and (d) spinel LiMn_2O_4 components, compared to their perfect structural models (c, e), respectively.....125

Figure 4.30: The lithiated XRDs for structures recrystallised under NST ensemble in their pristine form of $\text{Li}_{1.00}\text{Mn}_2\text{O}_4$ concentration for (a) nanoporous 75 Å, (b) nanoporous 69 Å and (c) nanoporous 67 Å structures compared to experimental XRDs for (d) spinel Mn_3O_4 [106], (e) spinel $\text{Li}_2\text{Mn}_2\text{O}_4$ [115], (f) layered LiMnO_2 [107], (g) layered Li_2MnO_3 [107] and (h) spinel LiMn_2O_4 [107].....130

Figure 4.31: The X-ray diffraction patterns (XRDs) for the $\text{Li}_{1+x}\text{Mn}_2\text{O}_4$, $0 \leq x \leq 1$ simulated nanoporous 75 Å structures where (a) is the $\text{Li}_{1.00}\text{Mn}_2\text{O}_4$, (b) $\text{Li}_{1.25}\text{Mn}_2\text{O}_4$, (c) $\text{Li}_{1.50}\text{Mn}_2\text{O}_4$, (d) $\text{Li}_{1.75}\text{Mn}_2\text{O}_4$ and (e) $\text{Li}_{2.00}\text{Mn}_2\text{O}_4$ concentration.131

Figure 4.32: The Li-Mn-O X-ray diffraction patterns at different lithium concentrations of $\text{Li}_{1+x}\text{Mn}_2\text{O}_4$ where $0 \leq x \leq 1$ for simulated (a) $\text{Li}_{1.00}\text{Mn}_2\text{O}_4$, (b) $\text{Li}_{1.25}\text{Mn}_2\text{O}_4$, (c) $\text{Li}_{1.50}\text{Mn}_2\text{O}_4$, (d) $\text{Li}_{1.75}\text{Mn}_2\text{O}_4$ and (e) $\text{Li}_{2.00}\text{Mn}_2\text{O}_4$ Li-Mn-O nanoporous 69 Å structures.....132

Figure 4.33: The X-ray diffraction patterns for $\text{Li}_{1+x}\text{Mn}_2\text{O}_4$, $0 \leq x \leq 1$ nanoporous 67 Å structures for (a) $\text{Li}_{1.00}\text{Mn}_2\text{O}_4$, (b) $\text{Li}_{1.25}\text{Mn}_2\text{O}_4$, (c) $\text{Li}_{1.50}\text{Mn}_2\text{O}_4$, (d) $\text{Li}_{1.75}\text{Mn}_2\text{O}_4$ and (e) $\text{Li}_{2.00}\text{Mn}_2\text{O}_4$ concentrations.133

Figure 4.34: The NST X-ray diffraction patterns (XRDs) for the simulated pristine bulk structure at (a) $\text{Li}_{1.00}\text{Mn}_2\text{O}_4$ concentration, compared with the experimental XRDs for (b) spinel Mn_3O_4 [106], (c) spinel $\text{Li}_2\text{Mn}_2\text{O}_4$ [115], (d) layered LiMnO_2 [107], (e) layered Li_2MnO_3 [107] and (f) spinel LiMn_2O_4 [107].135

Figure 4.35: The NST X-ray diffraction patterns (XRDs) for simulated bulk structures depicting the (a) $\text{Li}_{1.00}\text{Mn}_2\text{O}_4$, (b) $\text{Li}_{1.25}\text{Mn}_2\text{O}_4$, (c) $\text{Li}_{1.50}\text{Mn}_2\text{O}_4$, (d) $\text{Li}_{1.75}\text{Mn}_2\text{O}_4$ and (e) $\text{Li}_{2.00}\text{Mn}_2\text{O}_4$ concentrations.136

Chapter 5

Figure 5.1: The diffusion coefficients plots for nanoporous 75 Å at different lithium concentrations of $\text{Li}_{1+x}\text{Mn}_2\text{O}_4$, where $0 \leq x \leq 1$ with increasing temperature (K).....142

Figure 5.2: Plots for the diffusion coefficients of lithium for nanoporous 69 Å structure with different concentrations of $\text{Li}_{1.00}\text{Mn}_2\text{O}_4$, $\text{Li}_{1.25}\text{Mn}_2\text{O}_4$, $\text{Li}_{1.50}\text{Mn}_2\text{O}_4$, $\text{Li}_{1.75}\text{Mn}_2\text{O}_4$ and $\text{Li}_{2.00}\text{Mn}_2\text{O}_4$ with increasing temperature.143

Figure 5.3: Different lithium concentrations, $\text{Li}_{1+x}\text{Mn}_2\text{O}_4$ ($0 \leq x \leq 1$) showing the diffusion coefficient plots for nanoporous 67 Å with increasing temperature (K).....143

Figure 5.4: Diffusion coefficients for bulk structures at $\text{Li}_{1.00}\text{Mn}_2\text{O}_4$, $\text{Li}_{1.25}\text{Mn}_2\text{O}_4$, $\text{Li}_{1.50}\text{Mn}_2\text{O}_4$, $\text{Li}_{1.75}\text{Mn}_2\text{O}_4$ and $\text{Li}_{2.00}\text{Mn}_2\text{O}_4$ concentrations with increasing temperature (K).144

Figure 5.5: The diffusion coefficients of the Li-Mn-O nanoporous 75 Å structure at $\text{Li}_{1.00}\text{Mn}_2\text{O}_4$ concentration with different temperatures.146

Figure 5.6: Nanoporous 69 Å structure at $\text{Li}_{1.00}\text{Mn}_2\text{O}_4$ concentration showing the diffusion coefficients of Li-Mn-O ions at different temperatures.	146
Figure 5.7: The diffusion coefficients of $\text{Li}_{1.00}\text{Mn}_2\text{O}_4$ nanoporous 67 Å structure illustrating the diffusivity of the Li-Mn-O ions at temperature increment.	147
Figure 5.8: The diffusion coefficients for Li-Mn-O bulk structure at $\text{Li}_{1.00}\text{Mn}_2\text{O}_4$ concentration with increasing temperature (K).	147
Figure 5.9: The lithium diffusion coefficients for the nanoporous (75, 69 and 67 Å) and bulk structures at $\text{Li}_{1.00}\text{Mn}_2\text{O}_4$ concentration with increasing temperature (K).	149
Figure 5.10: The diffusion coefficients of lithium for nanoporous and bulk structures at $\text{Li}_{1.25}\text{Mn}_2\text{O}_4$ concentration with increasing temperature (K).	150
Figure 5.11: Nanoporous and bulk structures depicting the lithium diffusion coefficients at $\text{Li}_{1.50}\text{Mn}_2\text{O}_4$ concentration with increasing temperature (K).	150
Figure 5.12: The diffusion coefficient plots for lithium of the nanoporous 75, 69, and 67 Å and bulk structures at $\text{Li}_{1.75}\text{Mn}_2\text{O}_4$ concentration with increasing temperature (K).	151
Figure 5.13: The plots of lithium diffusion coefficients for the nanoporous and bulk structures at $\text{Li}_{2.00}\text{Mn}_2\text{O}_4$ concentration with increasing temperature (K).	151

Chapter 6

Figure 6.1: The stress-strain plots for nanoporous 75, 69 and 67 Å structures at $\text{Li}_{1.00}\text{Mn}_2\text{O}_4$ concentration.	159
Figure 6.2: The stress-strain plots for nanoporous 75, 69 and 67 Å structures at $\text{Li}_{1.25}\text{Mn}_2\text{O}_4$ concentration.	160
Figure 6.3: The stress-strain plots for nanoporous 75, 69 and 67 Å structures at $\text{Li}_{1.50}\text{Mn}_2\text{O}_4$ concentration.	161

Figure 6.4: The stress-strain plots for nanoporous 75, 69 and 67 Å structures at $\text{Li}_{1.75}\text{Mn}_2\text{O}_4$ concentration.	162
Figure 6.5: The stress-strain plots for nanoporous 75, 69 and 67 Å structures at $\text{Li}_{1.75}\text{Mn}_2\text{O}_4$ concentration.	163
Figure 6.6: The total RDFs of the lithiated Li-Mn-O nanoporous structures under the stress of 0.1 GPa with different lithium concentrations for (a) nanoporous 75 Å, (b) nanoporous 69 Å and (c) nanoporous 67 Å.	165
Figure 6.7: The X-ray diffraction patterns (XRDs) for structures in their pristine form at $\text{Li}_{1.00}\text{Mn}_2\text{O}_4$ concentration under the stress of 0.1 GPa for (a) nanoporous 75 Å, (b) nanoporous 69 Å and (c) nanoporous 67 Å structures; compared to the experimental XRDs for (d) spinel Mn_3O_4 [106], (e) spinel $\text{Li}_2\text{Mn}_2\text{O}_4$ [115], (f) layered LiMnO_2 [107], (g) layered Li_2MnO_3 [107] and (h) spinel LiMn_2O_4 [107].	169
Figure 6.8: The X-ray diffraction patterns (XRDs) for nanoporous 75 Å structure under the stress of 0.1 GPa, at $\text{Li}_{1+x}\text{Mn}_2\text{O}_4$ where $0 \leq x \leq 1$, for the simulated (a) $\text{Li}_{1.00}\text{Mn}_2\text{O}_4$, (b) $\text{Li}_{1.25}\text{Mn}_2\text{O}_4$, (c) $\text{Li}_{1.50}\text{Mn}_2\text{O}_4$, (d) $\text{Li}_{1.75}\text{Mn}_2\text{O}_4$ and (e) $\text{Li}_{2.00}\text{Mn}_2\text{O}_4$ concentrations.	170
Figure 6.9: The X-ray diffraction patterns (XRDs) under the stress of 0.1 GPa for nanoporous 69 Å structure at $\text{Li}_{1+x}\text{Mn}_2\text{O}_4$ where $0 \leq x \leq 1$, for the simulated (a) $\text{Li}_{1.00}\text{Mn}_2\text{O}_4$, (b) $\text{Li}_{1.25}\text{Mn}_2\text{O}_4$, (c) $\text{Li}_{1.50}\text{Mn}_2\text{O}_4$, (d) $\text{Li}_{1.75}\text{Mn}_2\text{O}_4$ and (e) $\text{Li}_{2.00}\text{Mn}_2\text{O}_4$ concentrations.	171
Figure 6.10: The simulated nanoporous 67 Å structure at $\text{Li}_{1+x}\text{Mn}_2\text{O}_4$, where $0 \leq x \leq 1$ concentrations illustrating the X-ray diffraction patterns (XRDs) under the stress of 0.1 GPa for (a) $\text{Li}_{1.00}\text{Mn}_2\text{O}_4$, (b) $\text{Li}_{1.25}\text{Mn}_2\text{O}_4$, (c) $\text{Li}_{1.50}\text{Mn}_2\text{O}_4$, (d) $\text{Li}_{1.75}\text{Mn}_2\text{O}_4$ and (e) $\text{Li}_{2.00}\text{Mn}_2\text{O}_4$	172

CHAPTER 1

Introduction and general background

Lithium ion batteries play an important role and are dominant power sources for consumer electronics in modern society [1]. These batteries are used universally in portable electronic devices, electric vehicles and smart grids. Consumer preferences motivate developments of technologies that supports fast charging for these devices. Fast charging is needed and very necessary for these devices, however, the accelerated degradation of lithium ion batteries is one of the major setbacks [2]. The energy storage field focuses mainly on the development of ideal materials that can have high performance, economic benefits and environmental affinity [3]. However, some of these materials come with significant energy consumption costs [4, 5]. As such high-voltage lithium-rich and manganese-based cathode materials, which are emerging as cost-competitive players in low carbon electricity systems and vehicles, have attracted wide attention due to their high capacity (>250 mAh/g), which is significantly superior to the conventional cathode materials, such as layered LiCoO_2 , spinel LiMn_2O_4 , olivine LiFePO_4 and layered $\text{LiMn}_{1/3}\text{Ni}_{1/3}\text{Co}_{1/3}\text{O}_{2.2}$ [6, 7].

Lithium manganese-based metal oxides (LMOs) are considered to be one of the promising cathode materials, because they can be used on a large scale for hybrid-electric vehicles and electric vehicles applications [8]. Spinel LiMn_2O_4 in particular, is one of the materials which have been identified as a potential candidate for the supply of energy, conversion and storage because it is cheap, has good structural stability with improved safety conditions and environmental friendliness [9, 10]. This has made it become a lithium-ion battery research hotspot [3]. Furthermore, it has an excellent rate performance with 3D

Li⁺ diffusion channels [11]. On the other hand, Manganese is found abundantly in nature in the form of minerals as well as alkaline-manganese batteries [12]. However, spinel LiMn₂O₄, suffer from a severe loss in specific capacity and voltage fade [9, 13, 14]; especially, under high temperatures operations, hampering their commercial applications in lithium batteries [3, 11]. This causes limited cycle life due to the dissolution of manganese and structural distortion [3].

The discovery of spinel LiMn₂O₄ for battery applications came from the pursuit of finding a cost-effective oxide cathode material [11]. The first conversion of LiMn₂O₄ into a new form of manganese dioxide λ-MnO₂ by chemical delithiation in an aqueous acidic solution was reported by Hunter in 1981 [15]. Thackeray then reported on the electrochemical lithiation and delithiation of LiMn₂O₄ in 1983; shedding a light on the research for Li-Mn-O cathode materials, where thermal stability was addressed [16, 17]. Further research of complex phase diagrams and structures of manganese-based materials also established efforts to optimize the electrochemical properties during the charge and discharge processes and steered to the finding and improvement of high voltage spinel cathodes and high capacity layered lithium and manganese-rich cathodes [11, 18, 19].

Spinel LiMn₂O₄ has a smaller capacity and energy density compared to the layered LiNi_{1-x-y}Co_xMn_yO₂, LiNi_{1-x-y}Co_xAl_yO₂, Li-/Mn-rich cathodes and LiCoO₂, it is, however, cost-effective, environmentally friendly and non-hazardous. Furthermore, it has a more robust crystal structure with fast diffusion kinetics. Therefore, it is often blended with layered cathodes to optimise structural and thermal stability, reduce cost and improve rate performance [11, 20]. Layered-layered cathode materials, especially lithium excess layered transitional metals such as xLi₂MnO₃·(1-x)LiMO₂ (M = Mn, Ni, Co) have drawn much attention due to their ability to achieve a high capacity for lithium ion batteries [21]. However, this has been hampered by voltage fade which has recently been reduced by the addition of a spinel

component, but with a reduced capacity [7]. Other layered-layered cathode materials performance limitations include structural stability and low first-cycling stability which ultimately give rise to poor rate performance [22, 23].

The development of nanostructured materials has been underway and is concentrated on the advancements of synthesis, characterisation and optimisation of nanomaterials for building high-performance lithium ion batteries [24]. Nanomaterials are convenient materials to be used as energy storage materials due to their ability to accommodate strain in high-capacity electrodes and to provide better storage coupled with capacity retention with a minimum compromise to the battery life cycle [24]. Furthermore, they are capable of shortening the diffusion lengths or path for the lithium ion materials travelling to the core of the surface from the particle and transfer to the electrolyte allowing a higher electrode-electrolyte contact area [13, 24, 25]. Layered-spinel lithium manganese oxides have a spontaneously great reversible capacity of 302 mAh/g and superior rate capability [26, 27, 28]. In the layered spinel composite, the layered Li_2MnO_3 component is not only capable of contributing high capacity but is also capable of stabilizing the spinel after its electrochemical activation during the initial cycle [21].

Over the years, lithium ion batteries have shown constant improvements in portability (size and weight) and lifespan during cycling [29]. With the ever-changing market, lithium ion batteries require efficient, sustainable, continuous innovation and enhancement to meet the high demand for energy storage [1]. To overcome the current battery obstacles, the use of nanostructured materials for the development of fast charging electrodes is the best approach [30]. Figure 1.1 shows some of the applications of lithium ion batteries in our everyday lives as part of energy storage sources.

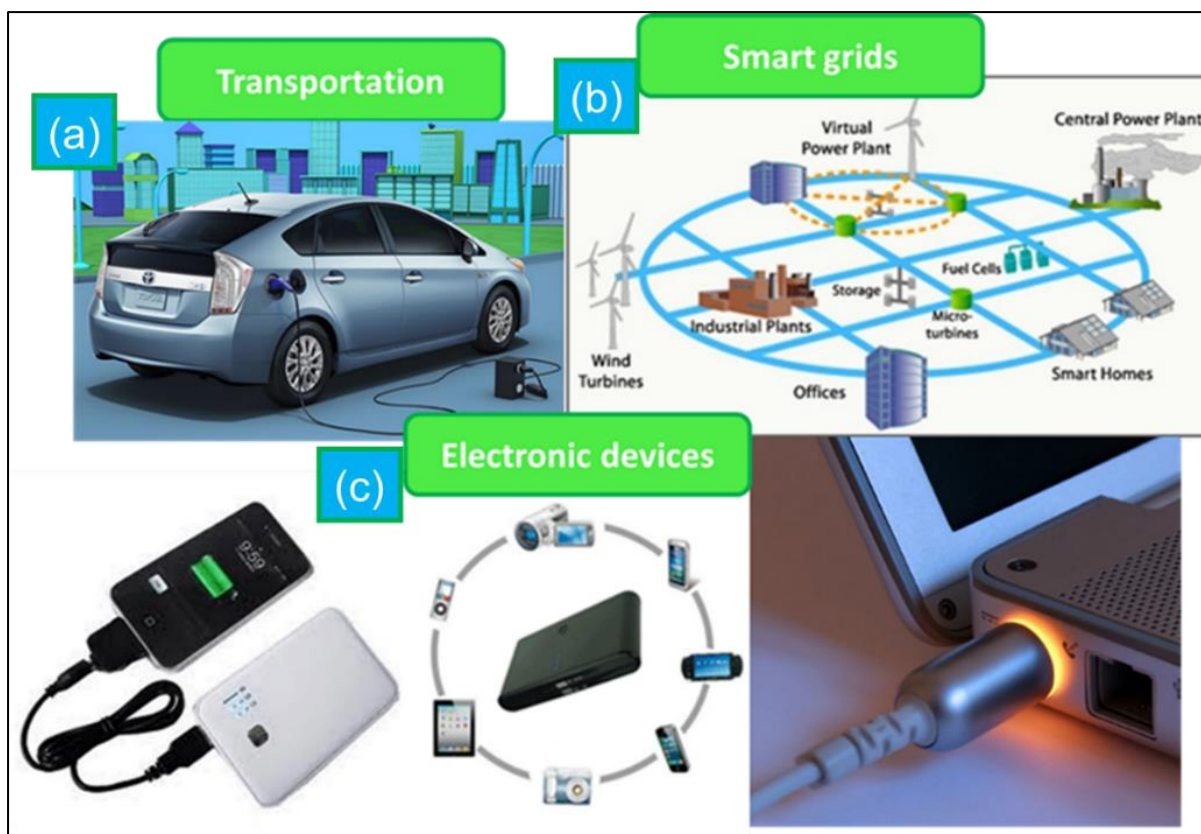


Figure 1. 1: The applications of Li-ion batteries in (a) electric vehicles replacing fuel, (b) smart grids as a network for digital communications technology to detect and react to local changes in electricity usage and (c) in electronics as a power source storage for cell phones, power banks, cameras and laptops.

1.1 Literature review

Many technologies particularly those focusing on the energy storage are burdened by the limited durability of present lithium ion cells. One of the limitations has been the achievement of high specific capacity, which can give reasonable driving distances of electric vehicles before recharge. Over the past years, spinel LiMn_2O_4 has become the most paramount material, received tremendous attention and became the centre of research especially for lithium ion batteries which are desired for their properties such as low cost and minimal safety hazards [9, 31]. However, spinel LiMn_2O_4 suffers from rapid high capacity fade especially at high temperatures [13, 31]. This is due to factors such as

lattice distortion caused by the Jahn-Teller effect, dissolution of manganese and oxygen defects [3]. The Jahn-Teller distortion causes deterioration of the LiMn_2O_4 life cycle, this happens when the manganese oxidation state is ≤ 3.5 which then generates stresses that may result in particle cracking and electric contact loss upon cycling [32]. Studies have concentrated on improving the specific capacity, where not much has been done to understand and manipulate the electrochemical potentials of the electrode materials to achieve or optimise the battery performance [4, 5]. To overcome this problem, porous cathodes are currently being utilized [6]. Computational modelling has played a vital role in studying lithium intercalated cathode materials for lithium-ion batteries, in particular, the amorphisation and recrystallisation techniques employing computer methods have been successfully used to synthesise various nanoarchitectures of metal oxides such as TiO_2 and MnO_2 [33, 34]. Lithium intercalation of these binary systems showed that they are capable of producing results similar to those observed experimentally in terms of microstructures and X-ray diffraction patterns.

1.1.1 Lithium ion cathodes and their setbacks

Presently, the more established cathode materials are layered LiCoO_2 , olivine structure of LiFePO_4 , $\text{LiNi}_{1-x-y}\text{Co}_x\text{Mn}_y\text{O}_2$ ($M=\text{Mn, Al}$) of the ternary layered structure and spinel LiMn_2O_4 [35].

Lithium cobalt oxide (LiCoO_2) and layered lithium cobalt oxide (Li_xCoO_2) introduced by Goodenough is the earliest and most commonly used cathode for lithium ion batteries [36]. Li_xCoO_2 has a charge density of 140 mAhg^{-1} (specific capacity), with low irreversible capacity loss and good cycling capacity. Cobalt resources are scarce, poisonous, have low thermal stability and the production of their cathodes is expensive [22, 31, 37].

Among the olivine group, there are phosphate compounds. Lithium iron phosphate (LiFePO_4) is one of the lithium cathodes which have also received a lot of attention due to its low cost, non-toxicity, good thermal and chemical stability [38]. However, LiFePO_4 suffers from a low electrochemical performance at room temperature due to low lithium diffusion and poor electronic conductivity [38]. Other olivine structures include LiMnPO_4 which gives ~ 0.4 V higher than LiFePO_4 leading to higher specific energy, however, this compound also suffers from low conductivity [36, 39].

Ternary layered materials such as $\text{LiNi}_x\text{MnyCo}_{1-x-y}\text{O}_2$ for cathode battery materials have also been considered for lithium ion batteries. This is because $\text{LiNi}_x\text{MnyCo}_{1-x-y}\text{O}_2$ not only hold all the advantages of LiCoO_2 but have less cobalt, better thermal stability and higher capacity. However, the issue of Li/Ni disorder severely restricts their electrochemical properties [40].

Lithium manganese oxides (LMO/ LiMn_2O_4) are of great interest due to their stability and theoretical capacity of 140 mAhg^{-1} , with the actual capacity of 120 mAhg^{-1} [35]. Furthermore, LMO's and their derivatives such as $\text{LiNi}_{0.5}\text{Mn}_{1.5}\text{O}_4$ are desired for their cost-effectiveness, high environmental affinity and the natural abundance of Mn, thus they have great development aspects [35, 41]. Moreover, LMO is of high advantage considering its high Li intercalation voltage range of 3.0 – 4.3 V [42]. Unfortunately, the cycling stability of LMO and its high rate discharge performance are not optimal enough, especially at elevated temperatures and the attenuation of discharge specific capacity also limits its large scale application [35]. The Jahn-Teller effect, which causes a change in symmetry of the LMO structure from cubic to tetragonal and the dissolution Mn are the major shortcomings [43, 44]. The dissolution of Mn into the electrolyte causes the inhomogeneous distribution, generation of new structural phases and related micro-strains during the cycling process in the structure [45].

1.1.2 Enhancement of lithium ion battery through composites and nanoporous structures

Using composite materials for lithium ion batteries is one of the means to enhance battery performance [21, 46]. As such alternatively layered composite materials such $x\text{Li}_2\text{MnO}_3 \cdot (1-x)\text{LiMO}_2$ (M=Mn, Ni, Co) are being studied. The layered-layered cathode materials, especially lithium excess layered transitional metals such as $x\text{Li}_2\text{MnO}_3 \cdot (1-x)\text{LiMO}_2$ (M=Mn, Ni, Co) are cathode materials that have received extensive scrutiny due to their ability to achieve high capacity for lithium ion batteries [21].

An approach to incorporate a spinel component into a layered (L) or layered-layered (LL) materials to form complex, structurally integrated layered-spinel (LS) or layered layered-spinel (LLS) electrodes has demonstrated substantial promise, especially when targeting a spinel content of 5-10 mol % [7, 22, 47]. The reason behind this approach is that 25 % of the transition metal cations in the lithiated spinel component are located in the lithium rich layers and therefore, increase the binding energy of the close-packed oxygen array [22, 48]. Indeed, it has been shown that the incorporation of a spinel component, in a low concentration, can improve cycling stability and rate capability and reduce first-cycle irreversible capacity losses of layered electrode systems [22, 49]. This was also confirmed by studies done by Long, *et al.* [7] and Deng, *et al.* [27], which have predicted that $x\text{Li}_2\text{MnO}_3 \cdot (1-x)\text{LiMO}_2$ cathodes are capable of delivering >250 mAh/g when charged to high potentials (>4.4 Vs. Li). This phenomenon was achieved by controlling the spinel content in the layered-layered spinel electrode materials and regulating the electrochemical voltage window of the lithium cells, thus yielding a high capacity with minimum voltage fade.

The success of the use of composite structures embraces considerable promise for further improvements in the compositional design and performance of high manganese content cathode material with multi-functional character. This is because such composite structures are capable of producing a favourable outcome for the development and high exploitation of high capacity electrodes with good cycling efficiency [50].

Nanoporous structured electrode materials have been widely investigated and gained great success in Li-ion batteries and Li-air batteries. When these are compared with normal electrodes, they usually show improved electrochemical performance which is mainly originated from and attributed to the three-dimensional bicontinuous architectures which offer high surface areas readily accessible by carrier charges and electrolytes. Furthermore, porous structures at the nanoscale shorten the lithium ion diffusion length between the electrolyte and the electrode. Moreover, the residual space in the electrode composite is capable of accommodating large volume expansion during discharging–charging processes [51, 52, 53]. Therefore, using composite nanoporous materials for lithium ion battery cathodes might curb the current battery hazards and optimise their performance.

1.1.3 Structural description

Spinel LiMn_2O_4 comprises of a cubic structure with the space group of $Fd-3m$ and lattice constant/parameter of $a = 8.239 \text{ \AA}$ [54]. This is the symmetry in which the lithium and manganese ions occupy the (8a) tetrahedral and (16d) octahedral sites respectively, with a close-packed array of oxygen ions in the 32e sites [55]. The edge-sharing octahedral MnO_6 is very stable and holds a series of intersecting tunnels as a result of face-sharing tetrahedral sites and the vacant octahedral (16c) sites [11, 56, 57]. These tunnels form a bonded network which allows for three-dimensional (3D) diffusion of lithium to take place [13]. The cathodes of lithium ion rechargeable batteries store lithium ions through

electrochemical intercalation and must contain appropriate lattice sites or spaces to store and release working ions reversibly [58]. Table 1.1 shows the constant lattice parameters of spinel LiMn_2O_4 obtained experimentally with a cubic structure and the space group of Fd-3m.

Table 1.1: Structural properties of spinel LiMn_2O_4 .

LiMn_2O_4	Exp [54].
Lattice parameters	$a = b = c = 8.239 \text{ \AA}$
Space group	Fd-3m
Crystal system	Cubic structure

1.1.4 Lithiation/delithiation mechanism and effect of cycling

The lithiation and delithiation processes or rather the discharge and charge processes of a battery material uses lithium ions as the intercalation component. Lithiation (discharge) is when the Li^+ atoms are inserted into the electrode (cathode), meanwhile, delithiation (charge) atoms are removed from the electrode (anode). Materials can be lithiated experimentally and computationally by chemical or electrochemical lithiation. In chemical lithiation, the structure is intercalated with lithium while it is still in its amorphous state, while for electrochemical lithiation, the material is lithiated while recrystallised.

The potential of the host material (electrode), changing of the valence states, and the availability of space to accommodate the lithium ions and the reversibility of the intercalation reactions, are the factors that determine the storage capacity of the battery [58]. The functionality of lithium ion batteries occurs when the lithium ions are transported between the two electrodes (anode and cathode) through the electrolyte. Upon discharging, the lithium ions migrate to the anode from the cathode through the electrolyte

and vice versa for the charging process. The insertion and extraction reaction of lithium from one electrode to another can cause the electrodes to deform. This can result in stresses that cause fractures and cracks [59, 60].

The movement of lithium from the tetrahedral-octahedral sites takes place when lithiating spinel LiMn_2O_4 to create average $\text{Li}_{1+x}\text{Mn}_2\text{O}_4$ ($0 < x < 1$), which is a two-phase reaction of spinel to ordered tetragonal rock salt $\text{Li}_2\text{Mn}_2\text{O}_4$, and provides a flat voltage plateau of 3 V versus Li^+/Li , this phenomenon is associated with the Jahn-Teller distortion. Lithiation of spinel LiMn_2O_4 is charge compensated for $\text{Mn}^{4+}/\text{Mn}^{3+}$ by redox couple, where $\text{Li}_{1+x}\text{Mn}_2\text{O}_4$ has Mn^{3+} and Mn^{4+} on the average with $x > 0$. Mn^{3+} is a Jahn-Teller ion, while Mn^{4+} is not; this implies that excessive Mn^{3+} initiates cooperative Jahn-Teller distortion in the lattice and disrupts the cubic symmetry to tetragonal. This degrades the material upon electrochemical cycling [11, 44].

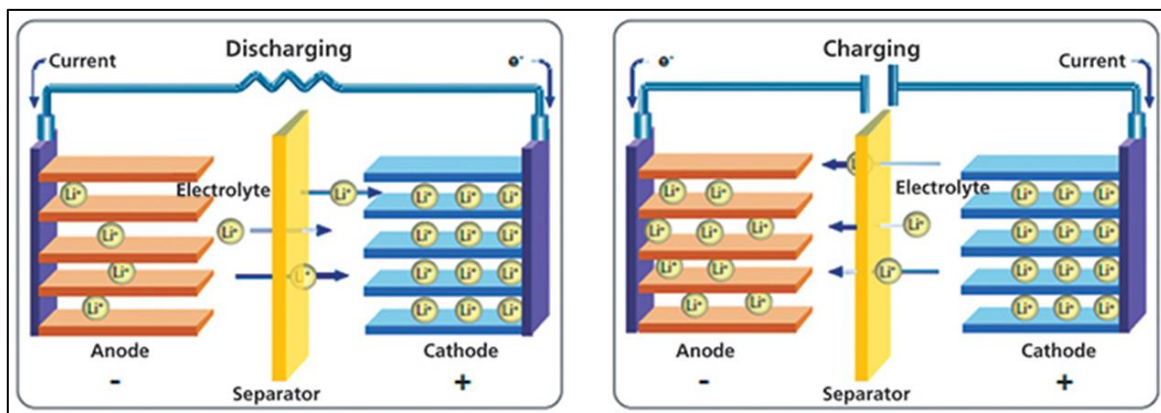


Figure 1.2: The battery mechanism showing the cycling discharge (lithiation) and charge (delithiation) processes.

1.1.5 Structural deformations

Structural deformation of a material entails the change in its size or shape when force is applied to it. Significant dimensional and volume changes are associated with variations in lattice parameters and transformations of crystalline/amorphous phases that occur during

electrochemical cycling and cause structural deformations. The lithium ion battery material such as LiMn_2O_4 can store and accommodate a lot of lithium ions but have large structural change and volume expansion which can cause mechanical failure due to structural deformations such as stress [30]. Furthermore, the lithiation induced deformations and the strategies adopted for addressing the stress-related issues raises various concerns that still need to be addressed to overcome the stress related problems. These issues are some of the major bottlenecks towards the development of new high-capacity electrode materials for Li-ion batteries. The stresses can cause fragmentation, disintegration, fracturing, and loss in contact between current collectors and the active electrode materials, which can also expose fresh surfaces to the electrolyte [61]. Mechanical characteristics of lithium ion batteries are of paramount importance when designing electrodes with maximised energy density and lifespan [62, 63]. Mechanical ageing is believed to be of the reasons for early and unexpected cell death. This is due to inherent volume variations during the operation of lithium ion batteries [64].

Lisa K. Willenberg et al. currently reported on volume changes on lithium ion batteries to demonstrate their impact on battery ageing [62]. An irreversible effect over the lifetime of the battery was observed which results in the death of the battery [62]. However, porous materials have been reported to have larger surface areas because of their pores and they are capable of enhancing the mechanical stability and electrochemical performance of lithium ion batteries [52].

1.2 Intentions of the study

Sustainable, efficient and cost-effective energy conversion and storage technologies are very important for the development and enhancement of newer applications for lithium ion batteries. Previous studies have revealed that the major setback in lithium ion batteries is the loss in specific capacity, which emanates from inherent material properties such as the low diffusion of lithium ions in the cathodes [52, 65]. Researchers have investigated ways to prevail from this problem by studying the morphological design and microstructures of the cathode, which can ensure to improve the insertion and extraction of the lithium ion with a reduction in diffusion pathway [52, 65, 66].

Computational modelling methods, employing both quantum mechanical and empirical approaches have played a crucial role in expediting lithium ion battery developments. In particular, the amorphisation and recrystallisation techniques have been successfully used to synthesize various nanoarchitectures of metal oxides such as TiO_2 [33, 67] and MnO_2 [68]. Lithium intercalation of these binary systems showed that they can act as good electrodes considering their ability to store and transport lithium atoms during the charging/discharging process [33, 34]. Furthermore, computational methods have accelerated material design efforts through rapid and comprehensive prediction of materials stability and properties [69]. Computational material science has made major strides in becoming a predictive discipline, impacting fundamental science as well as the development programs of industrial materials [70]. This approach brings together elements from diverse fields of study such as physics, mathematics and chemistry, and has the potential to handle multiscale and multi-disciplinary simulations in realistic situations [71]. Computer simulations also known as computer experiments adds a new dimension to scientific investigation and has been established as an investigative research tool that is as important as the traditional approaches of experiment and theory. Computer

simulations are much less impaired by many degrees of freedom, lack of symmetries, or non-linearity of equations than analytical approaches. This implies that computer simulations can establish their greatest value for those systems where the gap between theoretical prediction and laboratory measurements is large [71]. Therefore, the proposed study aim to predict the electrochemical and mechanical behaviour of the 3D LiMn_2O_4 bulk and nanoporous structures with their polymorphs (Mn_3O_4 , Li_2MnO_3 and LiMnO_2) at their atomistic level using simulation methods to find a suitable cathode material that can limit battery degradation. The LiMn_2O_4 nanoarchitectures investigated in this research study have been successfully generated by R.S Ledwaba [72] by employing the amorphisation and recrystallisation technique which have been reported to be cost-effective [73].

For the first time, the current study seeks to carry out the simulated synthesised of the bulk and nanoporous materials at varied lithium concentrations of $\text{Li}_{1+x}\text{Mn}_2\text{O}_4$, where $0 \leq x \leq 1$. Three nanoporous structures with varying lattice dimensions, namely; nanoporous 75 Å, nanoporous 69 Å and nanoporous 67 Å will be investigated together with their bulk at 63 Å. The structures will be investigated in their pristine concentration of $\text{Li}_{1.00}\text{Mn}_2\text{O}_4$, then lithiated to $\text{Li}_{1.25}\text{Mn}_2\text{O}_4$, $\text{Li}_{1.50}\text{Mn}_2\text{O}_4$, $\text{Li}_{1.75}\text{Mn}_2\text{O}_4$ and $\text{Li}_{2.00}\text{Mn}_2\text{O}_4$. The bulk and nanoporous structures will be studied at their atomistic level by the specialised amorphisation recrystallisation method, involving a large number of atoms, from 26 000 to approximately 30 000 atoms [74]. The simulation of the discharge process for the materials will be achieved by inserting lithium atoms into the bulk and nanoporous structures using a lithiation software programme while monitoring the effect of lithium increment on the spinel $\text{Li}_{1+x}\text{Mn}_2\text{O}_4$. The volume changes on the structures will be investigated by recrystallising the materials under the NST ensemble where N = constant number of atoms, S = constant stress and T = constant temperature. This ensemble allows the volume to change with lithiation during recrystallisation. The volume changes in the

electrodes lead to battery degradation. This is because volume changes can cause cracks within the battery material. The mechanical properties in this study will be scrutinised by applying the uniaxial stress of 0.1 GPa in the y-direction. The materials will be analysed through stress-strain plots to evaluate mainly their yield strengths as this determines their robustness and resilience to fracture.

The execution of the study will be carried out using the following procedure; firstly, the unit cell of LiMn_2O_4 will be built into a supercell, then amorphised into a sphere, which will be subjected to pressure to produce three dimensional (3D) nanoporous and (3D) bulk structures. The structures will then be recrystallised and thereafter be equilibrated to 0 K. Since the amorphisation and recrystallisation technique complements experiments as it permits and allows for spontaneous grain evolution, aiding the formation of defects and other structural properties that materialise during the nucleation and crystallisation process [72]; then the exploration of the internal structure through microstructures will be possible, assisting in the identification of formation for structural components that may emanate. Furthermore, from the simulated structures, RDFs, XRDs, volume changes, pore changes, lithium diffusion at varied temperatures and their yield strengths will be investigated.

The phenomenon of lithiation and delithiation has not been thoroughly investigated in ternary electrodes at the nanoscale [75]. Therefore, this study intends to investigate the electrochemical and mechanical properties of Li-Mn-O bulk and nanoporous structures at nanoscale during the discharge process, in the hope of finding a potential cathode material that can impede current battery issues. The findings of this study will shed light on the development of spinel layered electrodes with optimal operational capacity and hopefully, make strides in contributing to fast charge lithium ion batteries, with high energy density for energy storage while maintaining structural integrity during cycling.

1.3 Outline of the study

Chapter 1 outlines the significance of this work. The general background and literature review of lithium ion batteries, the structural descriptions, drawbacks, current developments on Li-Mn-O nanoarchitectures and the intentions of this study are outlined. Chapter 2 outlines the computational methods, codes and techniques used in this study. Chapter 3, focuses on the simulations of the generated nanoporous $\text{Li}_{1+x}\text{Mn}_2\text{O}_4$ ($0 \leq x \leq 1$) structures and discussion of the results obtained on the lithiated nanoporous and bulk structures in terms of the radial distribution functions, X-ray diffraction patterns and microstructures. Chapter 4, focuses on the recrystallisation of the structures under the NST ensemble to investigate structural changes, mainly volume changes. Chapter 5, outlines the effects of temperature in terms of diffusion coefficients for Li-Mn-O with increasing lithium concentration and temperature. Chapter 6, focuses on the mechanical properties of the nanoporous structures with increasing lithium concentration. Finally, Chapter 7 concludes the findings of the bulk and porous nanoarchitectures and recommends what could be done in future to better understand and improve the Li-Mn-O composite cathode materials for lithium ion batteries.

CHAPTER 2

Research methodology

In this chapter, computational methods used throughout this study will be discussed and defined. To be precise, the simulation code and potential models used to grow, amorphise, recrystallise and cool the nanostructures will be discussed in detail. Computational techniques or methods have been used to examine or investigate the structural properties of the Li-Mn-O structures at their atomistic level. Computer simulations methods help complement experimental methods because they are capable of predicting results beyond experiments [73].

2.1 Computational modelling

Computational modelling techniques have made it possible to study materials using computer simulations. This makes it possible to perform calculations such as the Energy Minimisation (EM) and Molecular Dynamics (MD). Computational methods and techniques have bridged the gap between material science and industries by assisting in the design and manufacturing of products, especially with complex materials and have improved their applications. These methods go as far as giving a better data acquisition approach than experiments. In addition, they complement experimental data, whereby they are able to mimic real structural models and predict structural behaviour of materials in terms of bonding in solids, model surfaces and interfaces, atomic transport and defects on structures, etc. [76].

Figure 2.1 shows a schematic diagram illustrating the procedure which was followed to construct the nanoarchitectures. A periodic array of nanoparticles is constructed in which they are introduced into the simulation of size $a_1 \times a_2$ (top left). The cell sizes are then

reduced (top middle). The close propinquity between the nanoparticles along a_1 causes the nanoparticles, under molecular dynamics (M.D), to start to agglomerate (top right), facilitating the evolution of a one-dimensional nanorod. If the sizes of the simulation cells are reduced (bottom left), the nanoparticles can agglomerate in two directions facilitating the formation of a nanosheet (bottom right). If the nanoparticles agglomerate in all three directions, then a porous nanoarchitecture is formed [34]. This method was successfully used on the generation of ceria nanoparticles, nanotubes and mesoporous architectures; where it showed the capability of producing hierarchical structural complexity including the crystal structure, microstructures and nanoarchitectures, similar to those observed experimentally [77].

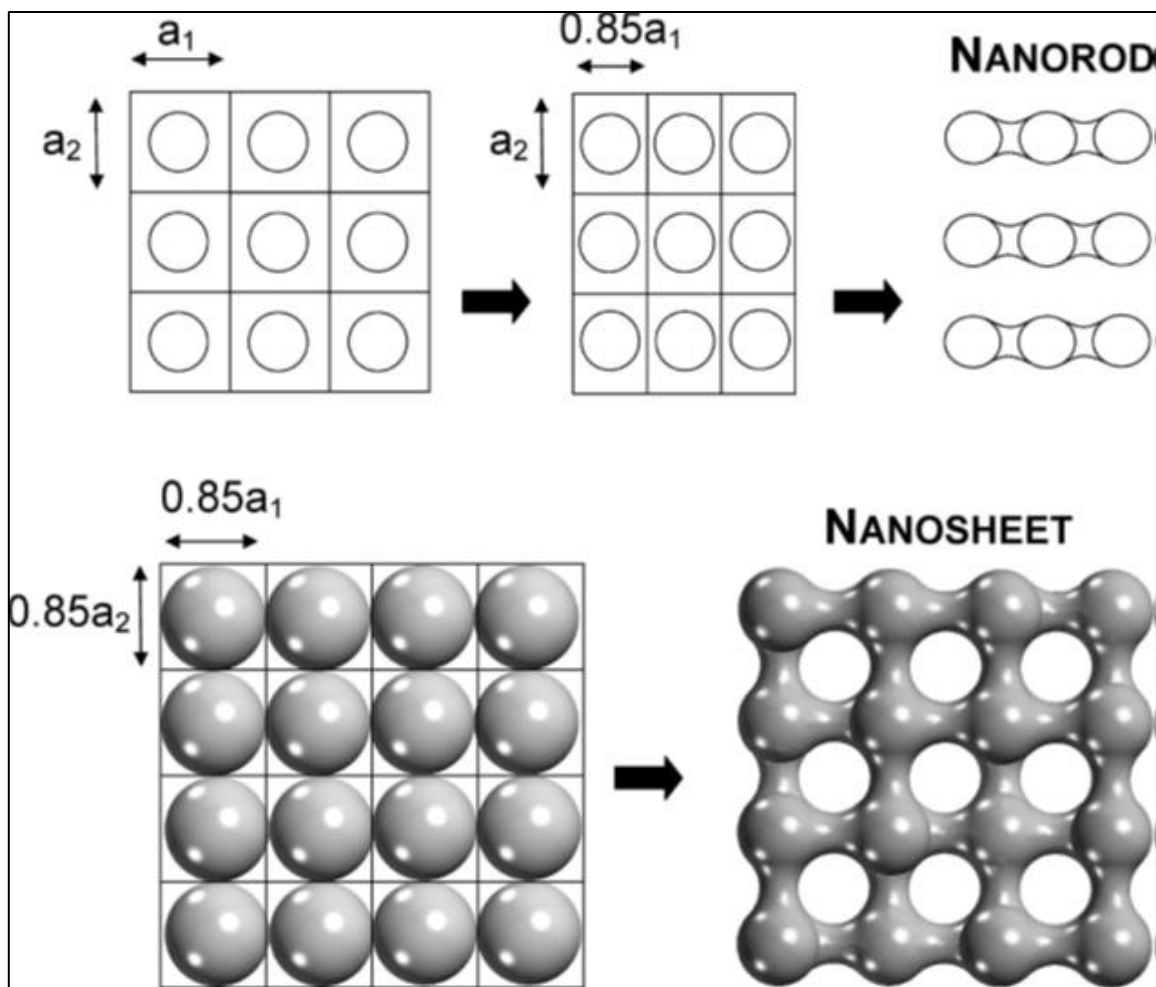


Figure 2.1. The schematic illustration of the procedure to be followed when constructing the nanoarchitectures [34].

2.2 Molecular dynamics

Molecular dynamics is a computational simulation method that is used to study the movements of atoms and molecules. It serves as a tool to facilitate the understanding of material properties such as structural, kinetic, dynamic and equilibrium properties at specific thermodynamic conditions of temperatures and pressures [78]. These atoms can interact at a fixed period, thus giving a dynamic evolution of the system followed by integrating their equations of motion. MD simulations are capable of giving very similar data to experiments. The forces between the particles and potential energy are defined by molecular mechanics force fields. Furthermore, MD follow the laws of classical mechanics, particularly Newton's 2nd law of motion, where:

$$F = ma \quad (2.1)$$

where a is the acceleration, F the force and m the mass. From the above equation, velocity and the position can be determined by integration and variation after chosen time steps derived from their algorithms such as the Verlet algorithm [79], given by:

$$r(t + \delta t) = r(t) + v(t)\delta t + \frac{1}{2}\alpha(t)\delta t^2 \quad (2.2)$$

where $r(t)$ is the ensemble of position, $v(t)$ is the velocity, $\alpha(t)$ is the acceleration with respect to time t .

2.2.1 Molecular dynamics ensembles

Statistical mechanics simulations have different ensembles, each serving a specific purpose to the calculations desired to be performed. Ensembles allow us to perform or control thermodynamic quantities such as pressure, temperature or the number of particles in a given system. Three principal ensembles can be used in molecular dynamics calculations, these include the microcanonical ensemble (NVE), canonical ensemble (NVT)

and isothermal-isobaric ensemble (NPT). These are the concepts of physics within statistical physics [80]. The microcanonical ensemble (NVE) is used in systems where the total number of atoms (N), volume (V) and energy are kept constant throughout the MD simulation. Furthermore, in a microcanonical molecular dynamic trajectory, the potential energy may be observed to change to kinetic energy where the total energy of the system is conserved. In the canonical ensemble, the number of particles (N), the volume (V) and temperature are kept constant throughout the simulation. Last but not least, we have the isothermal-isobaric ensemble, where the number of particles (N), pressure (P) and temperature (T) is kept constant. NPT simulations are performed initially to bulk structures to remove any lattice strains on the cell. When considering surfaces, constant volume ensembles NVT and NVE are used [81, 82].

2.3 Molecular dynamics properties

Molecular dynamics simulations allow for calculations over a wide variety of thermodynamic properties and give predictions that are comparable to experiments, thus giving validation to the results.

2.3.1 Radial distribution function

Radial distribution functions (RDF) define the variation of atomic density as a function of distance from a reference atom representing the liquid and solid phases of a structure. RDFs are used for describing the time-averaged, local coordination around a specific atom and are capable of indicating the materials internal structure. The function $g(r)$ represents the probability of finding an atom at a distance r from the reference atom. It can also be used to estimate the coordination number $n_{ij}(r)$ for specific atomic sites in the structure. The coordination number of the reference atom indicates the number of the nearest

neighbours to the reference atom which is used in structural analysis. This number is associated with the bond length [83]. The coordination number $n_{ij}(r)$ is given by:

$$n_{ij}(r) = 4\pi\rho \int_{r_{min}}^{r_{max}} r^2 g(r)dr \quad (2.3)$$

where ρ is the number density and is given as $p \frac{N}{V}$ where N is the number of atoms in a system of volume and $g(r)$ is the radial distribution function in a system of particles.

2.3.2 X-ray diffraction patterns

X-ray diffraction (XRD) pattern can be defined as the scattering of X-rays by atoms of a crystal that is capable of producing an interference effect so that the resulting diffraction pattern provides information on the structure of the identity of a crystalline structure. Its primary use is for phase identification of a crystalline material and can provide information on unit cell dimensions. The analysed material is finely ground, homogenized, and the average bulk composition is determined. X-ray powder diffraction is most widely used for the identification of unknown crystalline materials, for example, minerals and inorganic compounds. Determination of unknown solids is very important and critical to studies in material science [84, 85].

2.3.3 Diffusion coefficients

The diffusion coefficient is defined as the proportionality constant between molar flux due to molecular diffusion and the gradient concentration of the species. Diffusion is the overall or net movement of molecules from an area of higher concentration to an area of lower concentration until an equilibrium state is reached. Molecular diffusion is the thermal motion of particles at temperatures above absolute zero. The diffusion coefficient in this type of molecular dynamics simulation is calculated as the slope of the graph of

mean square displacement as a function of time [72]. Molecular diffusion in solids at different temperatures is described by Fick's law, where the Diffusion coefficient D is given by:

$$D = D_0 e^{-E_A/RT}, \quad (2.4)$$

where D_0 is the maximum diffusion coefficient at infinite temperature, E_A is the activation energy for diffusion in dimensions of the energy in (amount of substance)⁻¹, T is the temperature in units measured in kelvins, degrees or Rankine and R is the gas constant in the dimensions of the energy in (amount of substance)⁻¹. A diffusion process that obeys Fick's laws is called normal or Fickian diffusion; if the law is not obeyed then, it is called anomalous diffusion or non-Fickian diffusion.

2.4 Mechanical properties

Mechanical properties of a material are the measure of how a material is resilient to stress when strain is applied to it. Mechanical properties determine the behaviour of a material when subjected to mechanical stresses, the properties include elastic modulus, ductility, hardness, and various measures of strength [86].

Mechanical stress

The stress of a material entails its strength and can be defined as the force experienced by the object/material which causes a change in that object. The strength of a material determines its ability to withstand breaking or failing when force is applied to it. There are two types of mechanical stress, shear stress and axial stress [87].

Axial stress

Axial stress is the measure of internal resistance exhibited by a body when an external force is applied to it and it is denoted by sigma σ . Mathematically it is equal to the internal resisting force acting on the body per unit area and can be expressed as:

$$\sigma = \frac{R}{A}, \quad (2.5)$$

where σ is the stress, R is the resistive force and A is the cross-sectional area given in Pascal.

Shear stress

The shear stress can be defined as the stress acting on a body when two equal and opposite forces are applied to it and tends to cause adjacent portions of the material to slide against each other. The shear stress is defined as:

$$\tau = \frac{F}{A} \quad (2.6)$$

Where τ is the stress, F is the applied force and A is the cross-sectional area over which deflection occurs, given by the Pascal unit (N/m², Pa).

Strain

The strain is the measure of the deformation of the material. Strain inside a material may arise due to stress applied by external forces and is denoted by ϵ . Any strain of a solid material generates internal elastic stress.

Elastic and plastic behaviour

All materials deform when subjected to an external force up to a certain point where they can, if the force is removed, regain their original shape; this is called the elastic behaviour/region. The load at which the material remains elastic is called the elastic limit.

The strain produced within the elastic limit is directly proportional to the load or stress and that is where Hooke's Law applies. i.e. stress \propto Strain = E (elastic/ Young's modulus).

Given by:

$$\sigma_e = E_e \quad (2.7)$$

σ is the strain and E is the modulus elasticity and measures the inherent stiffness of a material

Mechanical stress and strain relationship

Stress and strain are the most important concepts for the comprehension of the mechanics of solids. The stress-strain curves reveal many properties of a material such as mechanical properties, which include the Young's/elastic modulus that measures the tensile stiffness of a material, the yield strength which is the point that indicates the limit of the elastic region and the beginning of a plastic region. Below the yield point, a material will deform elastically, this implies that it is capable of returning to its original shape when the applied stress is removed from it. When the external force applied or load exceeds the elastic limit, the deformation is permanent and called the plastic region; at this region, Hooke's Law is no longer valid. The yield point marks the beginning of plastic deformation [86]. The end of the plastic region results in the fracture point of the material where the structure collapses [87]. Figure 2. 2 illustrates the stress-strain relationship plot, explaining the above phenomena.

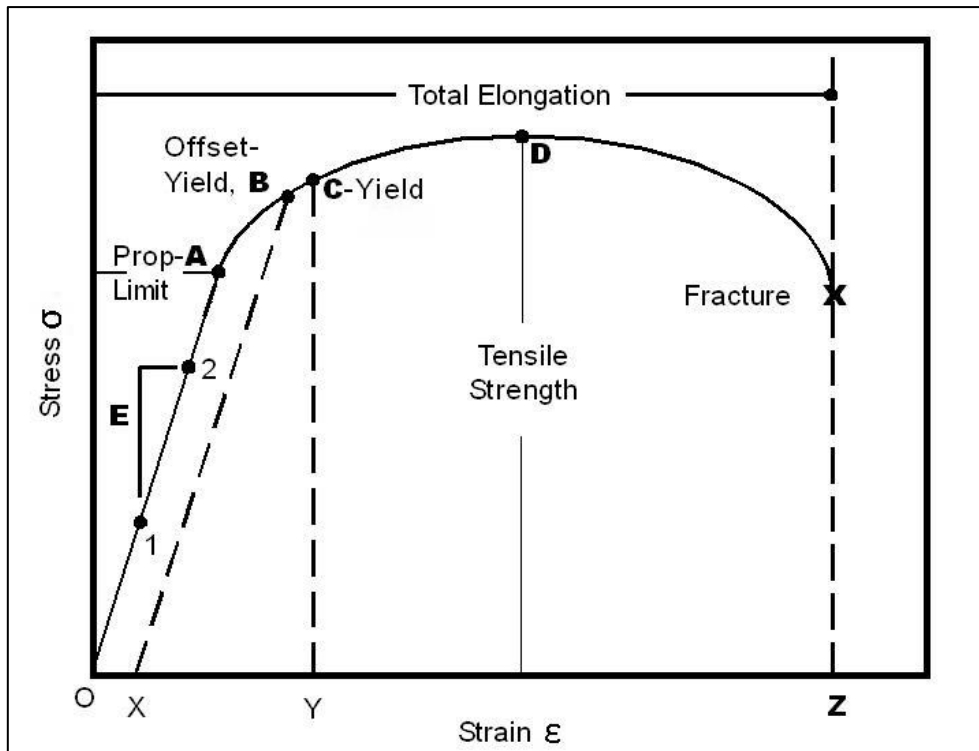


Figure 2. 2: The stress-strain diagram illustrating the information on how much a material can withstand a force before permanent deformation [87].

2.5 Amorphisation and recrystallisation technique

Amorphisation and recrystallization technique has been successfully used for atomistic simulations for complex structures. The technique or procedure starts by generating the amorphous configuration for the material, which is allowed to nucleate and recrystallize [73]. The amorphisation and recrystallisation methods are capable of allowing the material to move in low-energy configurations within the available timescale in the simulation; this is limited in dynamic simulations in crystalline solids, due to barrier heights for ionic mobility. The basic approach is to control the transformation to an amorphous state using an initial strain on the nanoparticle structure, where the subsequent application of temperature to the nanoparticle structure results in the amorphisation of the nanoparticle [73, 88].

As the material recrystallises it will evolve and microstructural features (point defects, dislocations, grain boundaries, morphology and so forth) will materialize [73]. This technique complements data synthesized experimentally because of the above-mentioned qualities (microstructural features) [68]. It is important to heed that the properties of a material are influenced by its microstructure [89]. The amorphisation and recrystallisation technique is therefore an appropriate method to explore complex structures [73, 90]. This is because it does not need one to generate an atomistic structure that includes all microstructural features before simulating with dynamics or statistic methods [73, 91]. Moreover, the formation of composites in the structure contributes to the improvement of electrode material [92].

2.6 Simulation code

The DL_POLY code is used over a wide variety of molecular systems of simple liquids, ionic liquids and solids, small polar and non-polar molecular systems, simple metals and alloys, ionic polymers and glasses solutions [93]. In this study, the DL_POLY code is employed to simulate the composite Li-Mn-O nanoarchitectures. The input files (CONTROL, FIELD and CONFIG) were used to carry out all calculations and are compulsory in each directory to be able to execute the DL_POLY script. The CONTROL file specifies the control variables or conditions for the execution of DL_POLY calculation, while the FIELD file specifies the force field information defining the molecular forces which contain the topology of the system, of which the sequence must match the crystallographic description of the system in the CONFIG file. Finally, the CONFIG file defines the positions of the atoms, periodic boundary conditions and atomic labels, velocities, coordinates, forces in the system and specifies the simulation file [94].

2.7 The potential model

The potential model defines the distinction in the energy of molecules or solids in terms of atomic coordinates. The validity of the calculations depends on the quality and accuracy of the potential model. The fundamental purpose of this method is to calculate the total interaction energy. This technique uses simple parameterization analytical functions to define the interactions between the species in the system, hence allowing the interaction energy to be calculated [91, 95].

Born model of ionic solids

The atomistic simulation techniques which are proposed in this study are based on the Born model of ionic solids. This technique studies the energy and its derivatives, defined as the simulation of all interactions between the atoms in the system which give rise to the total interaction and the total net force acting on each atom as a result of the force from other atoms [96]. This technique uses analytic functions to define interactions of one or more ions or species in a crystal. The atoms of a system are represented by point charges that interact through long range electrostatics forces and short range electrostatic forces. The interaction energy between and the atoms is given by:

$$U_{ij} = \frac{1}{4\pi\epsilon} \frac{q_i q_j}{r_{ij}} + \Phi(r_{ij}) \quad (2.8)$$

where U_{ij} is the long range Coulombic interaction, ϵ is the permittivity of the vacuum, q_i and q_j are the ionic charges and r_{ij} is the interatomic distance between the ionic charges and $\Phi(r_{ij})$ defines the short range interactions between ions, where the repulsion between electron charge clouds is and the Van Der Waals attraction forces are encountered.

Long and short range interactions

When two atoms interact from infinity to their lattice sites positions within the crystal the interaction energy of a system is released. The interaction energy corresponds to the potential energy of the long range electrostatic interaction forces and is given by;

$$\varphi = \sum_{i,j,l} \frac{q_i q_j}{4\pi\epsilon_0 (r_{ij+l})} \quad (2.9)$$

where q_i and q_j are the charges on the ions i and j , l is the set of lattice vectors representing the periodicity of the crystal lattice and r_{ij} is the displacement of ions from i to j .

The short range repulsive and attractive interactions are defined by simple parameterized models. It is very important that the model accurately defines the lattice properties so that quantitative results are obtained. Two adjacent charges can overlap if they are brought close to each other, thus causing repulsive interactions. These repulsive interactions can also be encountered even if the distance between the atoms is relatively small and the charges are opposite. This is described by Pauli's exclusion rule which states that no two fermions can occupy the same quantum state.

When there are two identical atoms, the Van de Waals force varies proportionally to r^{-6} . This is a quantum mechanical effect and r^{-6} can be derived from classical electrostatics. Therefore, the short range repulsive energy is given by;

$$\Phi_{s-r} = \sum_{ij} \Phi_{ij} + \sum_{ijk} \Phi_{ijk} + \sum_{ijkl} \Phi_{ijkl} + \dots \quad (2.10)$$

where ij represents all the pair interactions and ijk all the three-body interactions.

Buckingham potential

The Buckingham potential explains the exchange of repulsion, which is from the Pauli Exclusion Principle. It explains the repulsion by a realistic exponential function of a distance r . It is used to model two body non-bonded interactions in ionic solids. The Buckingham potential is finite even at smaller distances, this poses a threat of an unphysical Bucking catastrophe at short range when used in simulations of charged systems.

The Bucking potential is given by:

$$\Phi_{ij} = A_{ij} \cdot \exp\left(\frac{r_{ij}}{\rho_{ij}}\right) - \frac{C_{ij}}{r_{ij}^6} \quad (2.11)$$

where the first term is the Born-Mayer potential and the attraction in which the Bucking potential is added. A_{ij} and C_{ij} are the ion size and hardness parameters respectively.

The attraction term is often not considered because it does not contribute much to the short-range potential for the cation-anion, or the interaction is incorporated into ρ and A parameters [97].

2.8 Crystallographic defects

A perfect crystal with every atom of the same species in its correct or original position does not exist. Hence, there always exists a crystalline defect. Defects or imperfections can be defined as any deviation from the perfect crystal atomic arrangement in a crystal; or lattice irregularity having one or more of its dimensions on the order of an atomic dimension. Although defects may be thought of as bad things, they influence the electrochemical and mechanical properties of solids. In other words, defects are usually responsible for the existence of useful properties in materials, such as atomic/ionic diffusion, colour, and luminescence and so forth. Defects are crucial as they influence the behaviour of

materials, and almost all technology involving materials depends on the existence of some kind of defect [98].

There are two types of defects, intrinsic defect and extrinsic defect. The intrinsic defect forms when an atom is missing from a position that must be occupied or filled, leaving a vacancy behind (vacancy) or the atom occupies an interstitial site where no atom would appear (interstitially). Interstitial sites are commonly small in crystalline solids or have an unfavourable bonding configuration. However, vacancies are found to be in a large concentration in all crystal materials. Ordered compounds can generally have more intrinsic defects. An intrinsic defect destroys the charge balance of the material, which must be reinstated in some way. Extrinsic defects define the presence of foreign atoms in the lattice crystal. These are called solutes if they are intentionally added to the material and impurities if they are not. If the foreign atom occupies the lattice site, it is called the substitutional solute or impurity. If it fills an interstitial site, then it is called an interstitial solute. Since interstitial solutes are quite small, the type of solute is determined by its size. Small atoms are commonly found at interstitial sites, whereas larger atoms are commonly substitutional [99].

Crystalline defects can be classified into four major groups, namely; zero-dimensional, one dimensional, two dimensional and three dimensional. The zero-dimensional group classifies the point defects group, occurring at a single lattice point in a crystal. One dimensional classifies the linear defects, also known as dislocations, occurring along a row of atoms. Two-dimensional defects classify the planar/surface defects occurring over a two-dimensional surface in a crystal. And finally, the three-dimensional defects classifies defects occurring over a three-dimensional crystal such as voids and inclusions [98].

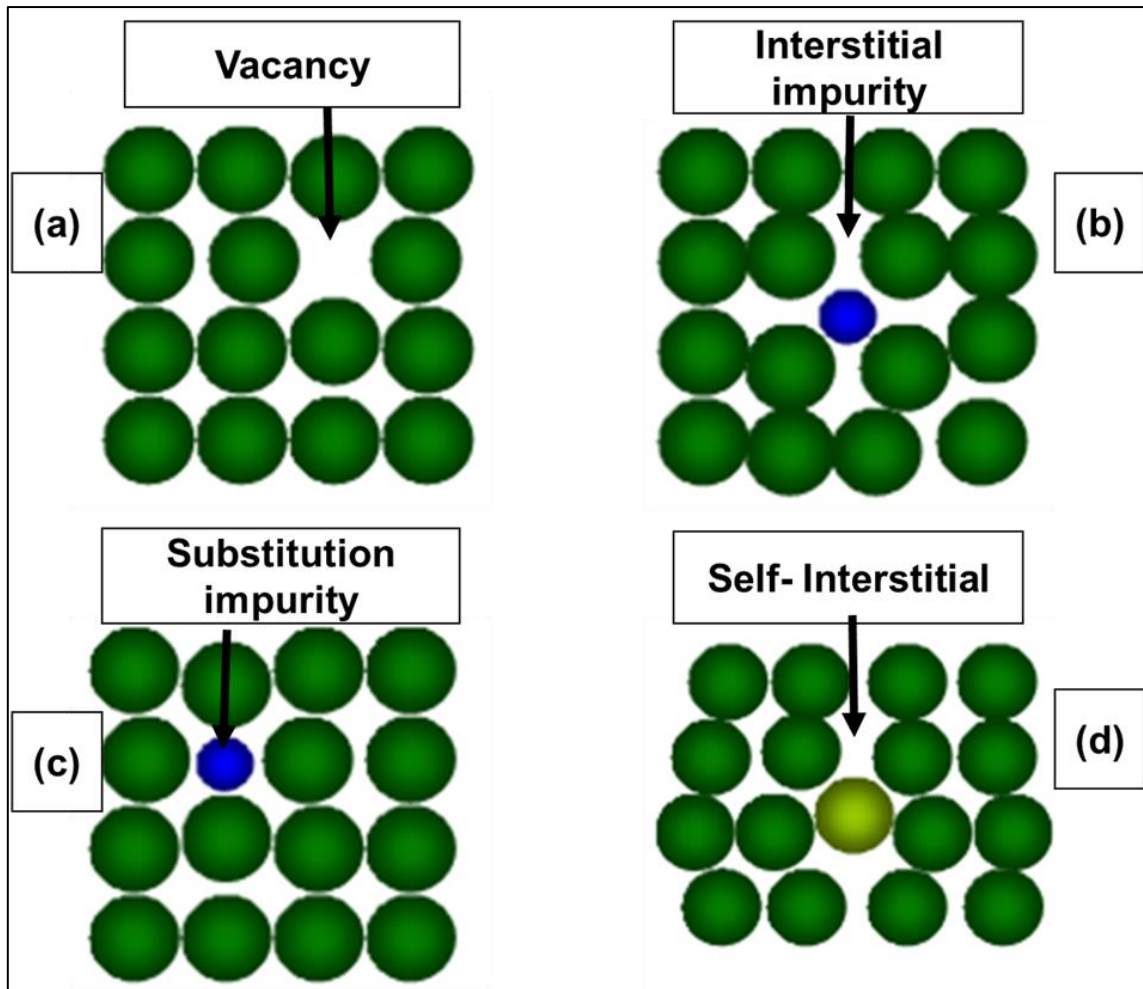


Figure 2.3: Schematic illustration of defects in a crystal where, (a) is the vacancy, (b) interstitial impurity, (c) substitution impurity and (d) self-interstitial.

2.8.1 Point defects

Point defects can be defined as when an atom is missing or is in an irregular place in the lattice structure and occur only at or around a single lattice point [98]. The ordinary point imperfections in a crystal are chemical impurities, vacant lattice sites and extra atoms not in their regular or original positions [100]. Point defects disturb the crystal pattern at a lattice site and these include Schottky and Frenkel defects. Schottky defect is a type of vacancy in which an atom migrates from its original site through successive steps and settles at the crystal surface (a pair of anions and cations vacancies). The Frenkel defect

is a pair of cation vacancy and a cation interstitial, or instead of pair cation, the vacancy is for anion pair [98].

2.8.2 Planar /surface defects

Grain boundaries are classified under planar defects, which can be defined as the disruptions on the long range orientation of a crystal. The size of the grains within a material has an effect on the strength of the material. The boundary between grains acts as a barrier to stacking defect movement and the resulting slip due to adjacent grains that have different orientations. Smaller grains have shorter distances than atoms and can move along a particular slip plane, as a result, they improve the strength of a material [100, 99]. Grain boundaries are numerous atoms spaces apart and have a mismatch of the orientation of grains on the crystalline solid. Polycrystalline materials, despite the disordered orientation of atoms at the grain boundaries, still have strong cohesive forces within and across the boundary [98].

2.8.3 Microstructures

The chemical, electrochemical and physical properties of a material are greatly influenced by its microstructure, crystal structure and electronic structure. The electrochemical properties of the electrode are determined by the nature of the material, but their microstructures may differ due to synthesis methods and the conditions used. Microstructures govern or influence the properties of a material. Microstructures help to evaluate the structural compositions and properties of a material at the atomic level. Furthermore, how they are aligned within the material and how they coexist with other impurities (if any) in the material. In addition, the host capabilities of the material can be understood by proper analysis of the composition features of the material [58, 91].

CHAPTER 3

Effects of lithiation on the nanoporous and bulk electrode materials

3.1 Introduction

Nanoporous materials consist of a regular framework that supports the porous structure at nanoscale and has voids (channels). The voids show a translational repetition in 3-D space. For a material to be characterized as “porous”, the pore sizes should be around 1000 nanometres and less. Nanoporous materials have pores that are capable of permitting substances to pass through their membranes (allow for diffusion) [101]. Meanwhile, bulk materials consist of a large number of closely packed atoms, where clusters remain as tiny particles. The major interest in these materials is the fact that their structural and functional properties differ significantly from those of coarse-grained analogues, and since nano-dimensional microstructural features can be harvested from materials, then bulk structures can be classified as nanostructured bulk materials [102].

The performance of the battery cathode is depended on the electrode morphology, inherent electrochemical properties and most importantly its microstructures [30]. In this chapter, we present the Li-Mn-O 75 Å, 69 Å, 67 Å nanoporous and bulk structures with different lithium concentrations within the range of $0 \leq x \leq 1$, ($\text{Li}_{1+x}\text{Mn}_2\text{O}_4$). To be precise, the structures will be investigated in the $\text{Li}_{1.00}\text{Mn}_2\text{O}_4$, $\text{Li}_{1.25}\text{Mn}_2\text{O}_4$, $\text{Li}_{1.50}\text{Mn}_2\text{O}_4$, $\text{Li}_{1.75}\text{Mn}_2\text{O}_4$ and $\text{Li}_{2.00}\text{Mn}_2\text{O}_4$ concentrations.

The amorphised and recrystallized Li-Mn-O materials are investigated by analysing their radial distribution functions (RDFs) and structural evolution. As such, structures that have

a defined pattern indicate recrystallised materials and those that do not indicate amorphous materials. The effect of lithiation on the pore sizes and the structural integrity of the materials during the discharge process are investigated by interrogating X-ray diffraction patterns (XRDs) and microstructures with increasing lithium concentration.

Table 3.1: The intercalated lithium concentrations of spinel LiMn_2O_4 for nanoporous and bulk structures with lattice parameters of 75 Å, 69 Å, 67 Å and 63 Å, respectively.

Spinel system	The total number of lithium atoms introduced to/ in the system (inserted).	Lithium concentration percentage (%)	The total number of atoms in the spinel nanoporous and bulk systems
$\text{Li}_{1.00}\text{Mn}_2\text{O}_4$	3806	50	26446
$\text{Li}_{1.25}\text{Mn}_2\text{O}_4$	4758	63	27594
$\text{Li}_{1.50}\text{Mn}_2\text{O}_4$	5709	75	28545
$\text{Li}_{1.75}\text{Mn}_2\text{O}_4$	6661	88	29497
$\text{Li}_{2.00}\text{Mn}_2\text{O}_4$	7612	100	30448

Table 3.1 shows the five different lithium concentrations of the $\text{Li}_{1+x}\text{Mn}_2\text{O}_4$ spinel where, $0 \leq x \leq 1$, with the total number of inserted lithium species in each structure, their lithium content percentage and the overall number of Li-Mn-O atoms in each system or structure.

3.1.1 Generation and lithiation mechanism of the nanoporous and bulk materials

Molecular dynamics simulation methods (amorphisation and recrystallisation technique) using the DL_POLY computer code was employed to carry out the Li-Mn-O nanoporous and bulk calculations. The amorphous spherical structures (NVE ensemble) used in this study

were synthesized by Ledwaba [72] for a PhD study. The METADISE code was used for energy minimization (optimization) and generation of the spherical spinel composite structures with five different concentrations from 26446 atoms (mono-lithiation) to 30448 atoms (full lithiation), expending the three mandatory DL_POLY (CONFIG, FIELD and CONTROL) input files required for molecular dynamics simulations [72]. The pressure of 100 GPa was applied using the NPT ensemble to allow the amorphous spherical nanoarchitectures to form nanoporous structures, then the bulk with prolonged recrystallisation. The NPT ensemble enables the vector directions of the cell to change. Thus further exposure of pressure on the materials allows the molten nanoparticles to fill the cell and form the bulk structures. The snapshots in figure 3.1 illustrate the structures of the above-mentioned procedure. The nanoarchitectures, with prolonged molecular dynamics simulations under the NVT ensemble, were allowed to recrystallise in the following conditions; the temperature of 1700K for 150 ps, 0 Gpa, the cutoff of 10 Å and Ewald precision of 2 to calculate the electrostatic forces [103]. The cooling process of the recrystallised porous and bulk nanoarchitectures was done systemically by reducing the temperature until 0 K at 300 ps to allow the nanoparticles to be at their lowest energy. The nanoarchitectures were lithiated using a chemical process that allows the nanostructures to be lithiated in their amorphous state before recrystallisation using a lithiation programme. The lithiation program on this study was written and created by Kgatwane [104] in his MSc studies and was successfully used for lithiation of Li-Mn-O nanoarchitectures by R.S. Ledwaba [72].

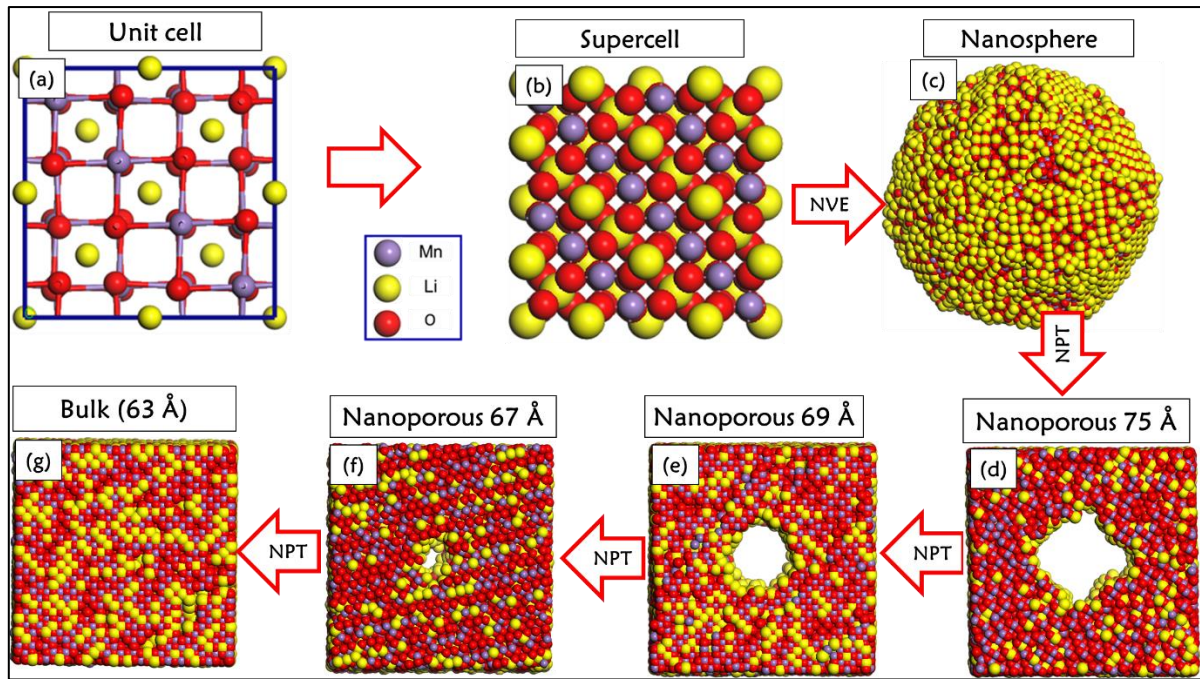


Figure 3. 1: Snapshots of the (a) conventional unit cell, (b) supercell, (c) nanosphere exposed to pressure to allow the formation of (d) nanoporous 75 Å, (e) nanoporous 69 Å, (f) nanoporous 67 Å and (g) bulk structures.

3.1.1 Amorphisation and recrystallisation of lithiated the Li-Mn-O materials

Figure 3.2 to 3.5 depicts the tilted and front view snapshots for the lithiated Li-Mn-O nanoporous structural composites of different lattice sizes that is 75, 69 and 67 Å, together with their bulk of 63 Å, respectively, with varying lithium concentration of $\text{Li}_{1+x}\text{Mn}_2\text{O}_4$, $0 \leq x \leq 1$.

Nanoporous 75 Å structures depicted in figure 3.2 demonstrate materials that have been recrystallised into single grains for $\text{Li}_{1.00}\text{Mn}_2\text{O}_4$, $\text{Li}_{1.25}\text{Mn}_2\text{O}_4$, $\text{Li}_{1.50}\text{Mn}_2\text{O}_4$ and $\text{Li}_{2.00}\text{Mn}_2\text{O}_4$. Meanwhile, for the $\text{Li}_{1.75}\text{Mn}_2\text{O}_4$ concentration, the structure has evolved into multiple grains (tilted view). Furthermore, on the recrystallised structures, the pore increases in size from the $\text{Li}_{1.00}\text{Mn}_2\text{O}_4$ to $\text{Li}_{1.25}\text{Mn}_2\text{O}_4$ concentration. Then with lithium increment to

$\text{Li}_{1.50}\text{Mn}_2\text{O}_4$ concentration, the pore shape becomes spherical and consequently reduce in size. Further increment of lithium to $\text{Li}_{1.75}\text{Mn}_2\text{O}_4$ concentration continue to reduce the pore size. However, upon full lithiation, which is at the $\text{Li}_{2.00}\text{Mn}_2\text{O}_4$ concentrations, the pore increase in size or almost regains its original size with surplus lithium atoms floating at the cavity. Nevertheless, the structural integrity is maintained throughout.

Figure 3.3 depicts the nanoporous 69 Å structure and its different lithium concentrations from pristine to full lithiation. The structures evolved into single crystals, however, the $\text{Li}_{1.75}\text{Mn}_2\text{O}_4$ concentration (front view) shows a structure that is partially distorted. The pore size increases from $\text{Li}_{1.00}\text{Mn}_2\text{O}_4$ to $\text{Li}_{1.25}\text{Mn}_2\text{O}_4$, then reduce at $\text{Li}_{1.50}\text{Mn}_2\text{O}_4$ concentration and become very small. Interestingly, at $\text{Li}_{1.75}\text{Mn}_2\text{O}_4$ the pore increases in size and is almost the same as that of $\text{Li}_{1.00}\text{Mn}_2\text{O}_4$. Upon full lithiation, the structure maintains the pore, however with a slight change in shape, where surplus lithium atoms are observed to be floating at the pore.

Recrystallised nanoporous 67 Å structures are illustrated in figure 3.4 and show structures that have involved into single crystals except for $\text{Li}_{1.75}\text{Mn}_2\text{O}_4$ which is multi grained (front view). On the other hand, the recrystallised structures show pore sizes that alter with increasing lithium concentration. The pore increase in size from $\text{Li}_{1.00}\text{Mn}_2\text{O}_4$ to $\text{Li}_{1.25}\text{Mn}_2\text{O}_4$, then reduce to $\text{Li}_{1.50}\text{Mn}_2\text{O}_4$ and eventually close up at $\text{Li}_{1.75}\text{Mn}_2\text{O}_4$ concentration. The pore re-opens and almost regains its original size upon full lithiation which is at the $\text{Li}_{2.00}\text{Mn}_2\text{O}_4$ concentration.

The snapshots for the lithiated Li-Mn-O bulk composites with increasing lithium concentration showing the tilted and front view of the recrystallised structures are illustrated in figure 3.5. All the structures evolve into single grains except for the one at $\text{Li}_{1.75}\text{Mn}_2\text{O}_4$ concentration.

The radial distribution functions define the probability of finding a particle at a distance r , away from the reference particle, relative to that of an ideal gas. Figure 3.6 depicts the total radial distribution function graph snapshots for the lithiated amorphous and recrystallised Li-Mn-O nanoporous and bulk structures at different lithium concentrations ($\text{Li}_{1+x}\text{Mn}_2\text{O}_4$, $0 \leq x \leq 1$). The amorphous snapshots show structures that have broader and flatter peaks as a result of scattered atoms that are displaced at different positions within the materials. In contrast to this, the total RDFs for the recrystallised structures depict sharp peaks, implying that the structures are well defined. Furthermore, a lower $g(r)$ (the probability of finding an atom at distance r) is observed at $\text{Li}_{2.00}\text{Mn}_2\text{O}_4$ concentration for all the structures when compared to the other four concentrations. For both the recrystallised and amorphous RDFs the peaks reduce in height (gr) with increasing radial distance (r), and the first peak for all the structures is observed at 2 Å.

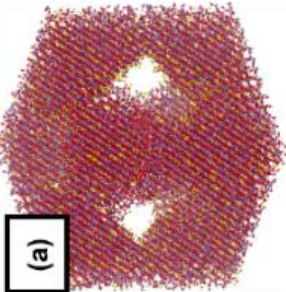
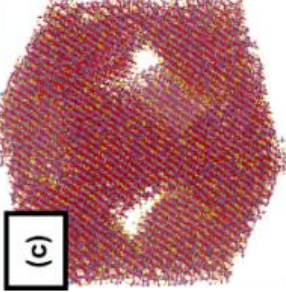
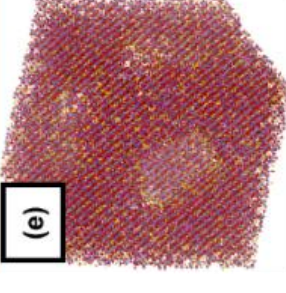
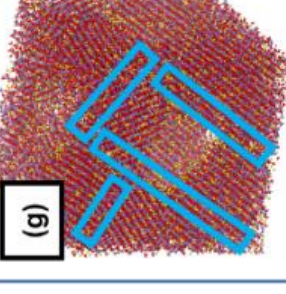
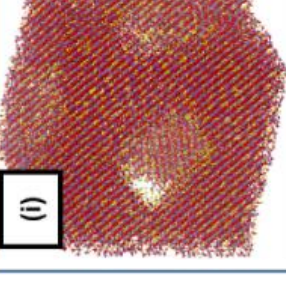
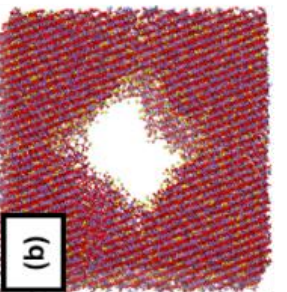
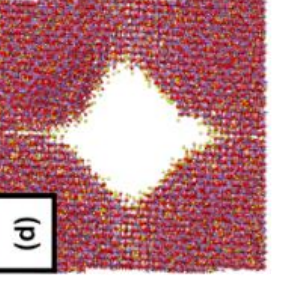
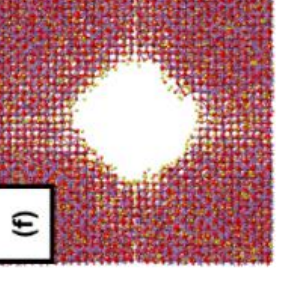
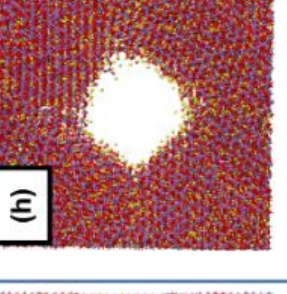
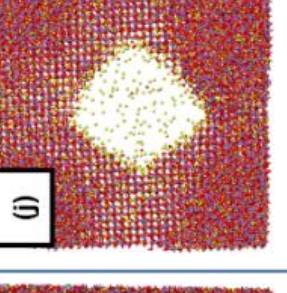
Cell size (75 Å)		Li Concentration				
		$\text{Li}_{1.00}\text{Mn}_2\text{O}_4$	$\text{Li}_{1.25}\text{Mn}_2\text{O}_4$	$\text{Li}_{1.50}\text{Mn}_2\text{O}_4$	$\text{Li}_{1.75}\text{Mn}_2\text{O}_4$	$\text{Li}_{2.00}\text{Mn}_2\text{O}_4$
Tilted view	 (a)	 (c)	 (e)	 (g)	 (i)	
Front view	 (b)	 (d)	 (f)	 (h)	 (j)	

Figure 3. 2: The lithiated nanoporous 75 Å structures of Li-Mn-O composites with different concentrations showing the tilted and front view of (a, b) $\text{Li}_{1.00}\text{Mn}_2\text{O}_4$ (c, d) $\text{Li}_{1.25}\text{Mn}_2\text{O}_4$ (e, f) $\text{Li}_{1.50}\text{Mn}_2\text{O}_4$ (g, h) multi grained $\text{Li}_{1.75}\text{Mn}_2\text{O}_4$ and (i, j) $\text{Li}_{2.00}\text{Mn}_2\text{O}_4$ respectively.

Li Concentration		$\text{Li}_{1.00}\text{Mn}_2\text{O}_4$	$\text{Li}_{1.25}\text{Mn}_2\text{O}_4$	$\text{Li}_{1.50}\text{Mn}_2\text{O}_4$	$\text{Li}_{1.75}\text{Mn}_2\text{O}_4$	$\text{Li}_{2.00}\text{Mn}_2\text{O}_4$
Cell size (69 Å)						
Tilted view	(a)	(c)	(e)	(g)	(i)	
Front view	(b)	(d)	(f)	(h)	(j)	

Figure 3. 3: The lithiated nanoporous 69 Å structures of Li-Mn-O composites with different concentrations showing the tilted and front view of (a, b) $\text{Li}_{1.00}\text{Mn}_2\text{O}_4$ (c, d) $\text{Li}_{1.25}\text{Mn}_2\text{O}_4$ (e, f) $\text{Li}_{1.50}\text{Mn}_2\text{O}_4$ (g, h) distorted $\text{Li}_{1.75}\text{Mn}_2\text{O}_4$ and (i, j) $\text{Li}_{2.00}\text{Mn}_2\text{O}_4$ respectively

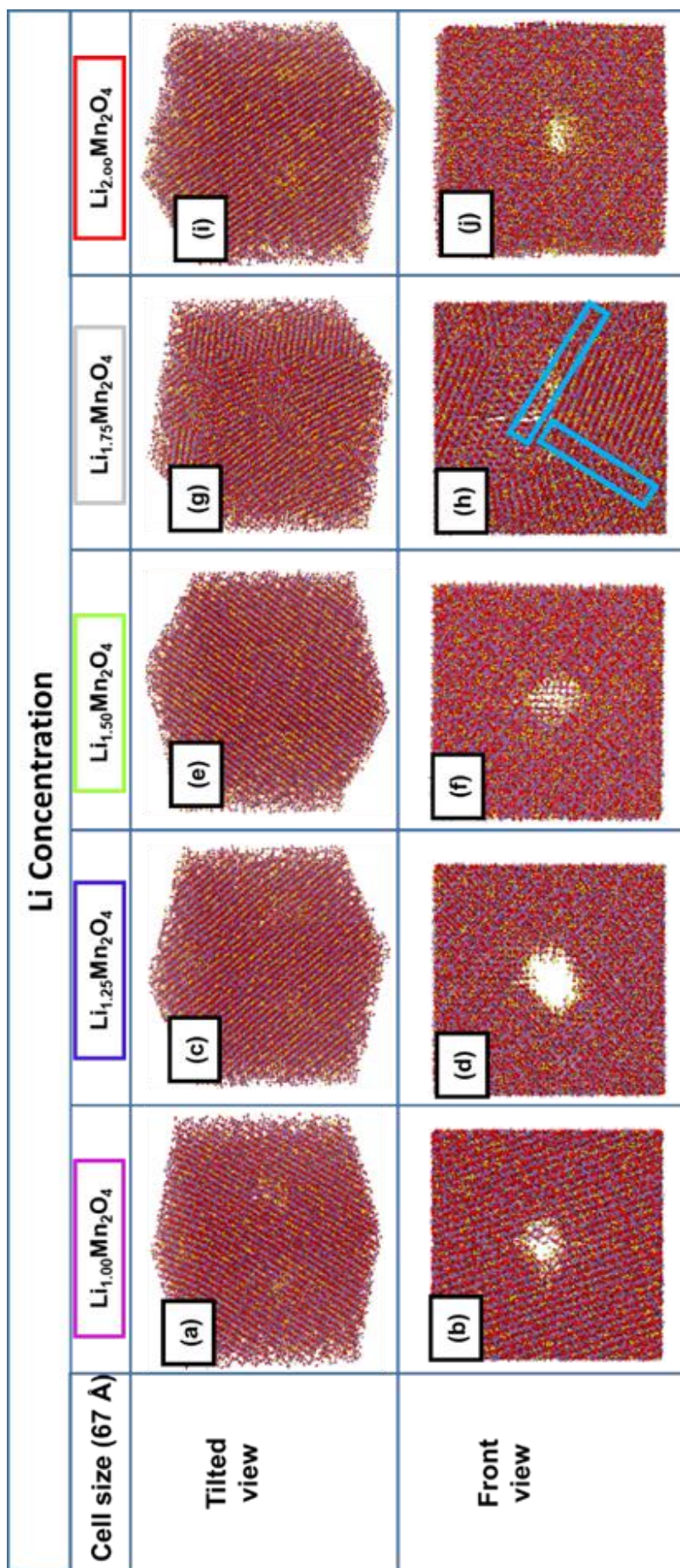


Figure 3. 4: The lithiated nanoporous 67 Å structures of Li-Mn-O composites with different concentrations showing the tilted and front view of (a, b) $\text{Li}_{1.00}\text{Mn}_2\text{O}_4$ (c, d) $\text{Li}_{1.25}\text{Mn}_2\text{O}_4$ (e, f) $\text{Li}_{1.50}\text{Mn}_2\text{O}_4$ (g, h) multi grained $\text{Li}_{1.75}\text{Mn}_2\text{O}_4$ and (i, j) $\text{Li}_{2.00}\text{Mn}_2\text{O}_4$ respectively.

		Li Concentration				
Bulk (63 Å)		$\text{Li}_{1.00}\text{Mn}_2\text{O}_4$	$\text{Li}_{1.25}\text{Mn}_2\text{O}_4$	$\text{Li}_{1.50}\text{Mn}_2\text{O}_4$	$\text{Li}_{1.75}\text{Mn}_2\text{O}_4$	$\text{Li}_{2.00}\text{Mn}_2\text{O}_4$
Tilted view	(a)	(c)	(e)	(g)	(i)	(j)
Front view	(b)	(d)	(f)	(h)	(i)	(j)

Figure 3. 5: The lithiated bulk structures of Li-Mn-O composites with different lithium concentrations showing the tilted and front view of (a,b) $\text{Li}_{1.00}\text{Mn}_2\text{O}_4$ (c,d) $\text{Li}_{1.25}\text{Mn}_2\text{O}_4$ (e,f) $\text{Li}_{1.50}\text{Mn}_2\text{O}_4$ (g,h) $\text{Li}_{1.75}\text{Mn}_2\text{O}_4$ and (i,j) $\text{Li}_{2.00}\text{Mn}_2\text{O}_4$.

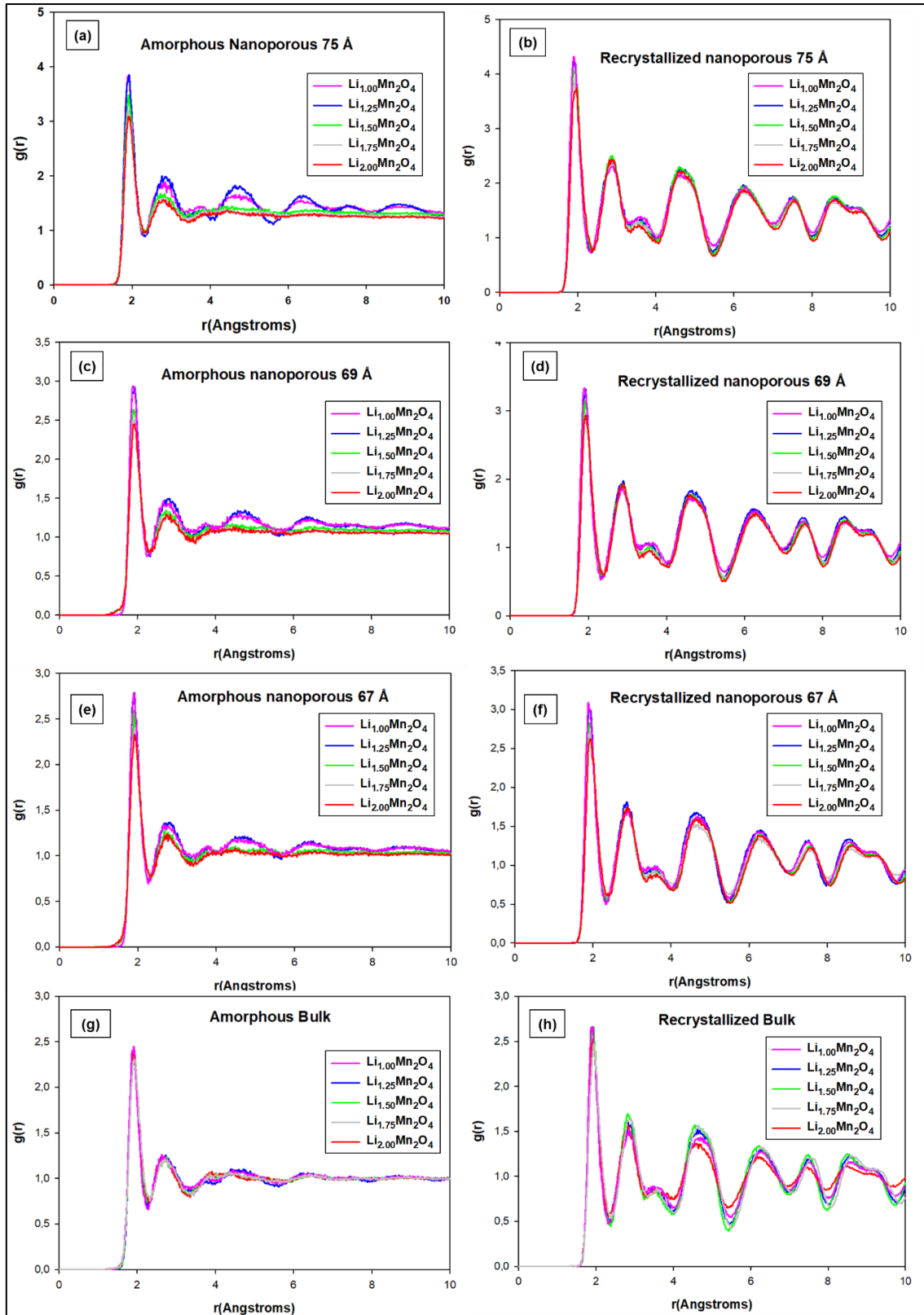


Figure 3. 6: The total RDFs of lithiated Li-Mn-O nanoporous and bulk structures with different lithium concentrations of $Li_{1+x}Mn_2O_4$, where $0 \leq x \leq 1$; depicting the amorphous and recrystallised structures of nanoporous 75 Å, 69 Å, 67 Å and the bulk.

3.2 Microstructures and X-ray diffraction patterns for the nanoporous materials

3.2.1 Nanoporous 75 Å

The simulated lithiated nanoporous 75 Å structures with different lithium concentrations with their microstructures are illustrated in figures 3.7 to 3.11.

The nanoporous 75 Å structure at $\text{Li}_{1.00}\text{Mn}_2\text{O}_4$ concentration is demonstrated in figure 3.7 (i, a) and depicts (b) the magnification of Mn^{2+} atoms retrained in tetrahedral tunnels with some tunnels unoccupied which can facilitate lithium transportation. In the same figure, the microstructure slice harvested from the $\text{Li}_{1.00}\text{Mn}_2\text{O}_4$ nanoporous 75 Å structure (ii, a) is illustrated and shows a grain boundary. The microstructure demonstrates the magnifications of the defective (b) layered Li_2MnO_3 and (d) spinel LiMn_2O_4 which are comparable to their (c, e) perfect structural models. The layered Li_2MnO_3 with distortions captures lithium vacancies and Mn atoms displaced from their original lattice positions (Frenkel defect). Meanwhile, the defective spinel LiMn_2O_4 captures both the lithium and Mn vacancies with Mn interstitials.

Figure 3.8 represents the (i, a) structure for nanoporous 75 Å at lithium concentration $\text{Li}_{1.25}\text{Mn}_2\text{O}_4$ with a distorted region. The magnification from the structure shows the formation of (b) spinel Mn_3O_4 that is comparable with (c) the perfect structural model. Spinel Mn_3O_4 captures Mn^{2+} atoms in the tetrahedral tunnels and unoccupied tunnels that can accommodate lithium ions during the discharge process. Figure 3.8 (ii) depicts the microstructure slice (a) cut from the $\text{Li}_{1.25}\text{Mn}_2\text{O}_4$ nanoporous 75 Å structure. The microstructure shows a defective magnified portion of (b) layered Li_2MnO_3 compared to (c) its perfect structural model with the presence of lithium vacancies and distortions. Furthermore, the microstructure also shows the defective magnification of (d) spinel

LiMn_2O_4 component when compared to its (e) perfect structural model. LiMn_2O_4 captures lithium vacancies and Mn interstitials which indicates the presence of Frenkel defects.

The structure for nanoporous 75 Å at concentration $\text{Li}_{1.50}\text{Mn}_2\text{O}_4$ is depicted in figure 3.9 (i, a). The presence of (b) Mn^{2+} atoms retaining tetrahedral tunnels is observed with some unoccupied tunnels and the spinel Mn_3O_4 perfect structural model is labelled (c) for comparison. Spinel Mn_3O_4 component is getting reduced when compared to the concentrations of nanoporous 75 Å at $\text{Li}_{1.00}\text{Mn}_2\text{O}_4$ and $\text{Li}_{1.25}\text{Mn}_2\text{O}_4$. Figure 3.9 (ii) depicts the microstructure slice (a) cut from the simulated $\text{Li}_{1.50}\text{Mn}_2\text{O}_4$ nanoporous 75 Å. The microstructure depicts the magnifications of defective (b) layered Li_2MnO_3 and (d) LiMn_2O_4 components, these are comparable to their perfect structural models (c, e), respectively. Layered Li_2MnO_3 magnification demonstrates lithium and Mn vacancies with some distortions. Meanwhile, on the magnification of spinel LiMn_2O_4 defects such as lithium vacancies, distortions and Mn interstitials are observed.

The recrystallised nanoporous 75 Å structure at $\text{Li}_{1.75}\text{Mn}_2\text{O}_4$ concentration is illustrated in figure 3.10 (i, a). The structure has recrystallised into multiple grains with distorted regions, as such the presence of spinel Mn_3O_4 cannot be easily identified at any rotation. The microstructure (ii, a) harvested from the $\text{Li}_{1.75}\text{Mn}_2\text{O}_4$ nanoporous 75 Å depicts some grain boundaries due to the material becoming polycrystalline with lithiation. Magnification of the microstructure captures the presence of (b) the defective spinel LiMn_2O_4 with Mn vacancies and distorted regions. The simulated LiMn_2O_4 is comparable to (d) its perfect structural model. The formation of the spinel LiMn_2O_4 component is favoured at this concentration.

The full lithiated nanoporous 75 Å structure at concentration $\text{Li}_{2.00}\text{Mn}_2\text{O}_4$ with a distorted region is demonstrated in figure 3.11 (i, a). The structure captures Mn^{2+} atoms on the

magnified portion (b) retaining tetrahedral tunnels with some unoccupied tunnels. The formation of spinel Mn_3O_4 is getting reduced with increasing lithium concentration when compared to $\text{Li}_{1.00}\text{Mn}_2\text{O}_4$, $\text{Li}_{1.25}\text{Mn}_2\text{O}_4$, $\text{Li}_{1.50}\text{Mn}_2\text{O}_4$, and $\text{Li}_{1.75}\text{Mn}_2\text{O}_4$. The spinel Mn_3O_4 perfect structural model is labelled (c) for comparison. The Mn_3O_4 component decreasing with increasing lithium content is also validated by the findings of Tang et al. [105]. In the same figure, the microstructure (ii, a) cut from the $\text{Li}_{2.00}\text{Mn}_2\text{O}_4$ nanoporous 75 Å structure shows the presence of (b) spinel LiMn_2O_4 and (d) layered Li_2MnO_3 with reduced defects compared to the other four concentrations and these are comparable to their perfect structural models (c, e), respectively. Both the magnifications of layered and spinel components show distortions within their array or patterns.

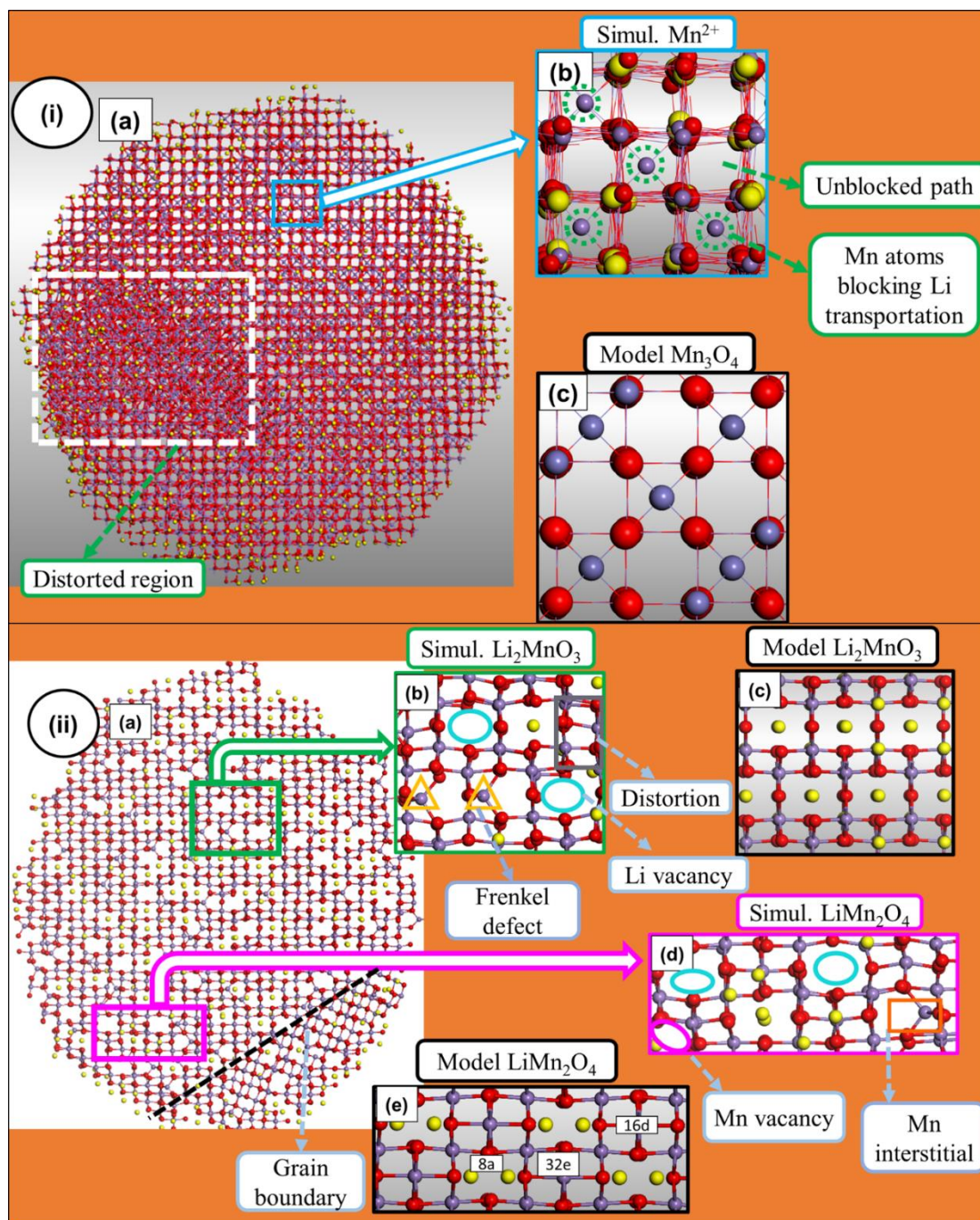


Figure 3. 7: The simulated (i, a) nanoporous 75 Å structure at $Li_{1.00}Mn_2O_4$ concentration which has recrystallised into two grains magnified to illustrate the (b) Mn^{2+} atoms in the tetrahedral tunnels, where (c) is the perfect structural model of spinel Mn_3O_4 . The microstructure (ii, a) harvested from (i, a) depicting defective magnifications of (b) layered Li_2MnO_3 and (d) spinel $LiMn_2O_4$ components which are comparable to their structural model (c, e), respectively.

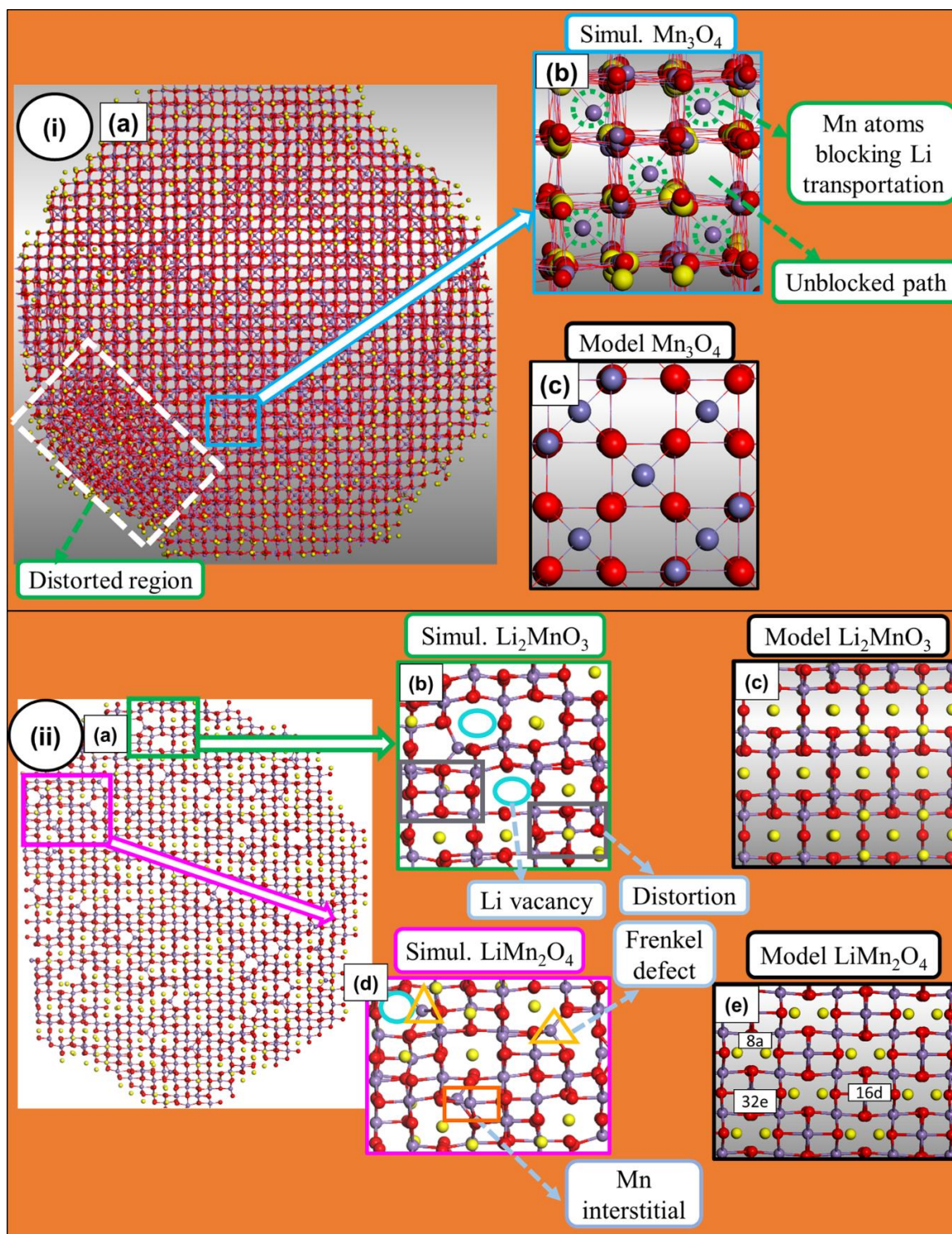


Figure 3. 8: The simulated (i, a) $\text{Li}_{1.25}\text{Mn}_2\text{O}_4$ nanoporous 75 Å structure depicting the magnified section of (b) spinel Mn_3O_4 structure compared with (c) its perfect structural model. The microstructure (ii, a) harvested from $\text{Li}_{1.25}\text{Mn}_2\text{O}_4$ nanoporous 75 Å show the magnified portions of the defective (b) layered Li_2MnO_3 component and (d) spinel LiMn_2O_4 which are comparable to their structural models (c, e).

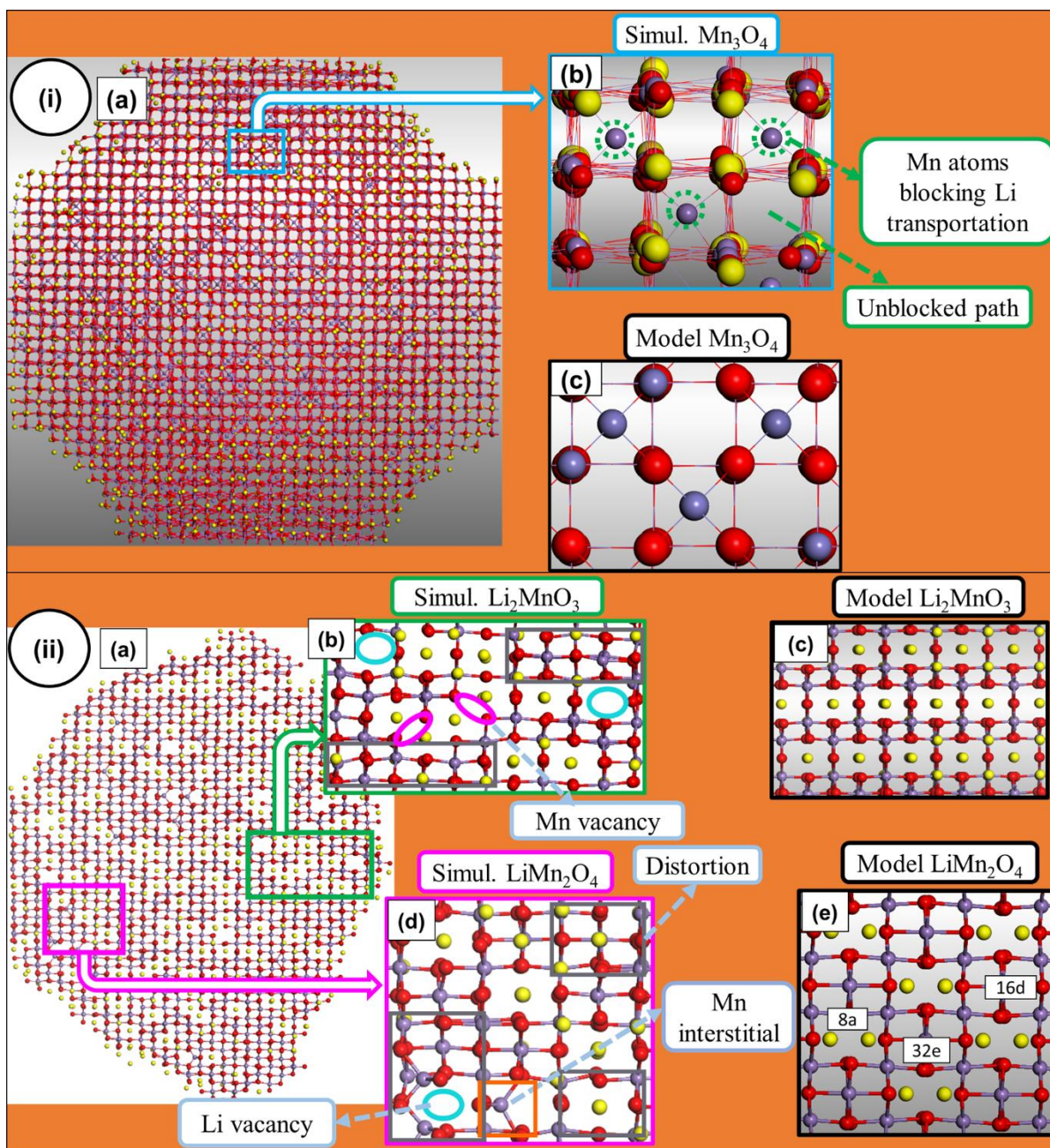


Figure 3. 9: The simulated (i, a) $\text{Li}_{1.5}\text{Mn}_2\text{O}_4$ nanoporous 75 Å structure illustrates (b) the Mn^{2+} atoms retained in tetrahedral tunnels, where (c) is the perfect structural model of spinel Mn_3O_4 . The microstructure slice (ii, a) cut from $\text{Li}_{1.5}\text{Mn}_2\text{O}_4$ nanoporous 75 Å structure shows the magnifications of (b) layered Li_2MnO_3 and (d) spinel LiMn_2O_4 components with defects compared with (c, e) their perfect structural models.

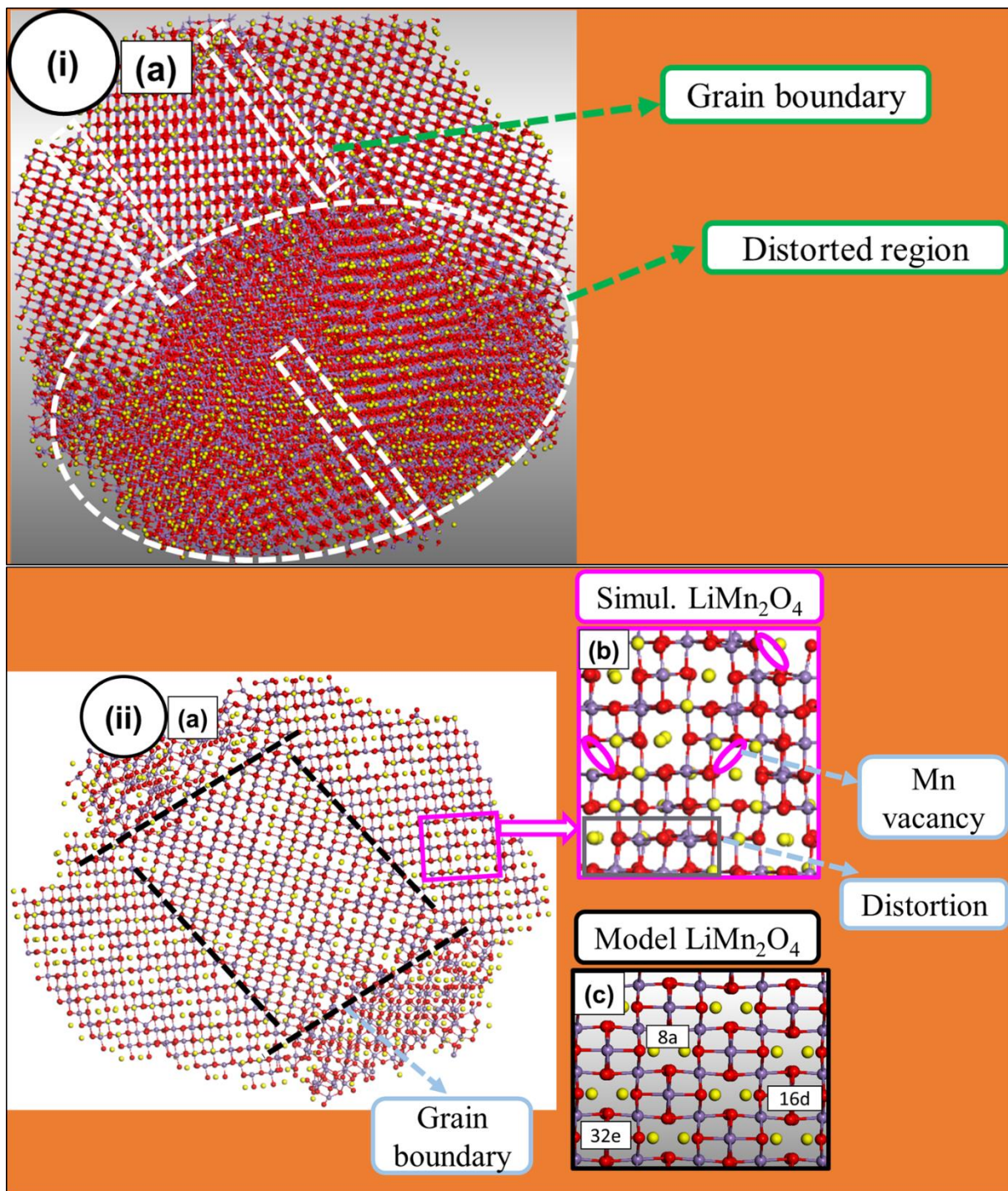


Figure 3. 10: The multi grained (i, a) nanoporous 75 Å structure at $\text{Li}_{1.75}\text{Mn}_2\text{O}_4$ concentration with distorted regions. The harvested microstructure (ii, a) from $\text{Li}_{1.75}\text{Mn}_2\text{O}_4$ nanoporous 75 Å structure depicting grain boundaries and the magnified section of (c) defective spinel LiMn_2O_4 component compared to (d) its perfect structural model.

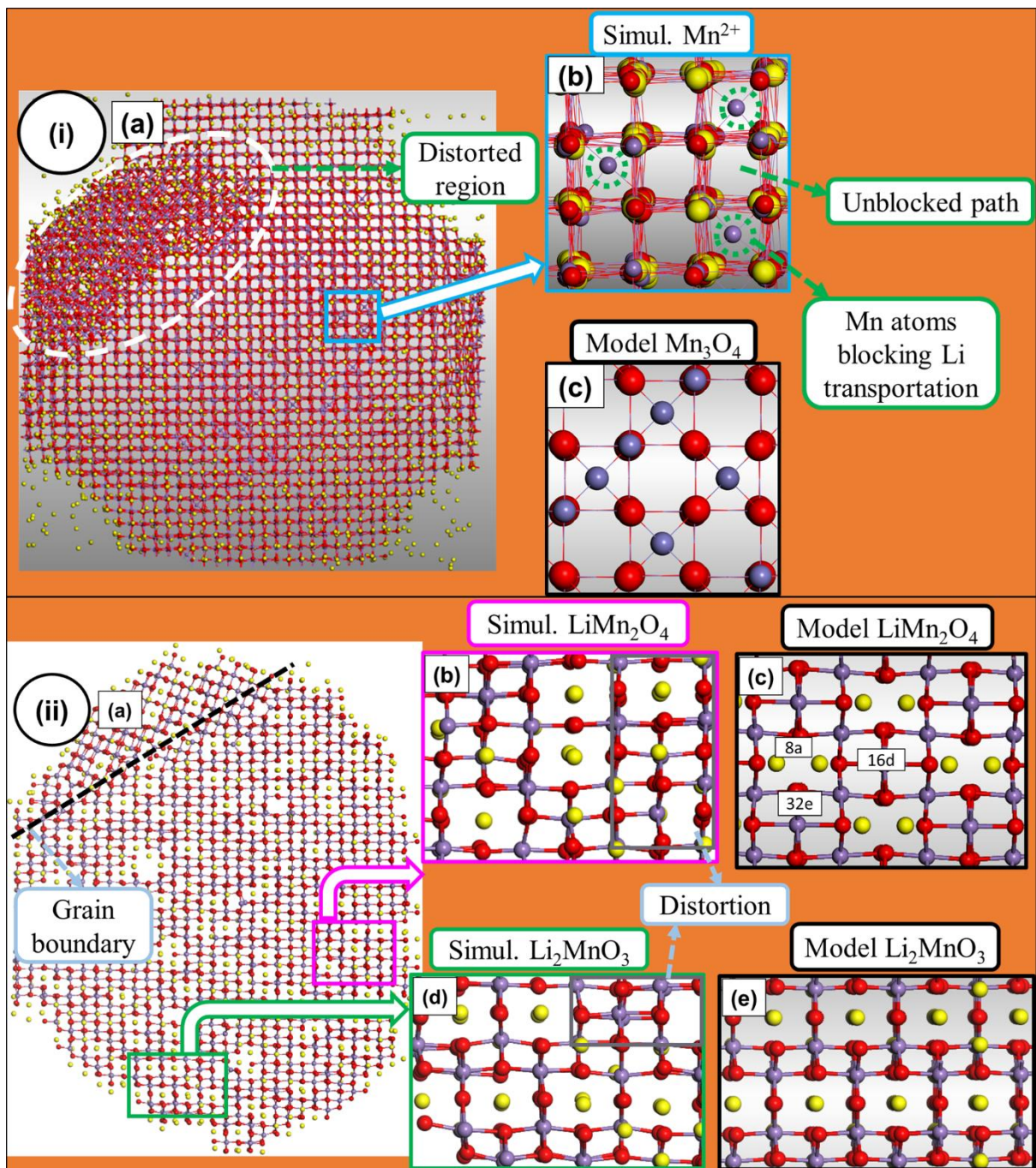


Figure 3. 11: The distorted full lithiated (i, a) nanorous 75 Å structure at $\text{Li}_{2.00}\text{Mn}_2\text{O}_4$ concentration depicting (b) Mn^{2+} atoms in the tetrahedral tunnels, where (c) is the perfect structural model of spinel Mn_3O_4 . The microstructure (ii, a) of $\text{Li}_{2.00}\text{Mn}_2\text{O}_4$ nanorous 75 Å with a grain boundary, showing the magnifications of defected (b) spinel LiMn_2O_4 and (d) layered Li_2MnO_3 compared to their (c, e) perfect structural models.

3.2.2 Nanoporous 69 Å

The simulated recrystallised nanoporous 69 Å structure at $\text{Li}_{1.00}\text{Mn}_2\text{O}_4$ concentration is illustrated in figure 3.12 (i, a). The magnification from the structure shows the presence of (b) Mn^{2+} atoms in the structure retaining tetrahedral tunnels with some unoccupied tunnels. The perfect structural model is denoted by (c). Furthermore, the (ii, a) microstructure of $\text{Li}_{1.00}\text{Mn}_2\text{O}_4$ nanoporous 69 Å structure depicts magnification of (b) layered Li_2MnO_3 component with the presence of lithium and Mn vacancies, distortions and Frenkel defects. The simulated Li_2MnO_3 is comparable to (c), its perfect structural model. The layered Li_2MnO_3 appears to be a dominant component on the microstructure since the presence of spinel LiMn_2O_4 pattern cannot easily be identified.

The $\text{Li}_{1.25}\text{Mn}_2\text{O}_4$ concentration of nanoporous 69 Å structure is demonstrated in figure 3.13 (i, a). The structure shows the presence of the (b) spinel Mn_3O_4 and is comparable to (c) its perfect structural model. The microstructure slice harvested from the structure is depicted in (ii, a) with the defected magnifications of (b) layered Li_2MnO_3 and (d) spinel LiMn_2O_4 component comparable to their perfect structural models (c, e), respectively. The layered Li_2MnO_3 magnification captures the presence of lithium and Mn vacancies, distortions and Mn interstitials; while the magnified portion of spinel LiMn_2O_4 depicts distortions, Mn interstitials and Frenkel defects.

Figure 3.14 (i, a) depicts the snapshots of the recrystallised nanoporous 69 Å structure at $\text{Li}_{1.50}\text{Mn}_2\text{O}_4$ concentration and its (ii, a) microstructure. From the structure (i, a), the presence of (b) spinel Mn_3O_4 is observed and is comparable to (c) its perfect structural model. The microstructure illustrates the defected magnification of (b) layered Li_2MnO_3 with Mn and lithium vacancies, Mn interstitials and distortions. The defected magnification of (d) spinel LiMn_2O_4 component shows the occurrence of distortions, Mn vacancies and

interstitials, which indicates the presence of Frenkel defects. The perfect structural models of (c, e) layered Li_2MnO_3 and spinel LiMn_2O_4 are comparable to the simulated.

The nanoporous 69 Å structure at $\text{Li}_{1.75}\text{Mn}_2\text{O}_4$ concentration with a distorted region is illustrated in figure 3.15 (i, a). The structure shows the magnification of (b) Mn^{2+} atoms retained in tetrahedral tunnels and unoccupied tunnels which can allow for lithium diffusion during cycling. The Mn_3O_4 spinel component is getting reduced with increasing lithium concentration. The microstructure slice (ii, a) cut from $\text{Li}_{1.75}\text{Mn}_2\text{O}_4$ nanoporous 69 Å structure shows the magnifications of (b) the spinel LiMn_2O_4 and (d) layered Li_2MnO_3 components which are comparable to their (c, e) perfect structural models. Observations made from the spinel LiMn_2O_4 reveal Mn vacancies and interstitials with distortions. While observations made on the layered show distortions with Mn vacancies.

The full lithiated nanoporous 69 Å structure at $\text{Li}_{2.00}\text{Mn}_2\text{O}_4$ is illustrated in figure 3.16 (i). From the structure, Mn^{2+} atoms (b) retained in tetrahedral tunnels are observed from the magnified portion. Lithium increment results in the reduction of spinel Mn_3O_4 with observations made from $\text{Li}_{1.00}\text{Mn}_2\text{O}_4$, $\text{Li}_{1.25}\text{Mn}_2\text{O}_4$, and $\text{Li}_{1.50}\text{Mn}_2\text{O}_4$ and $\text{Li}_{1.75}\text{Mn}_2\text{O}_4$ concentrations. In the same figure, the microstructure slice (ii, a) harvested from the $\text{Li}_{2.00}\text{Mn}_2\text{O}_4$ nanoporous 69 Å structure is depicted with defected magnifications of (b) layered and (d) spinel, which are comparable to (c, e) their perfect structural models. The layered Li_2MnO_3 shows Mn interstitials and distortions. Spinel LiMn_2O_4 magnification captures some distortions in the atom pattern. The structural defects appear to be reduced with increasing the lithium content.

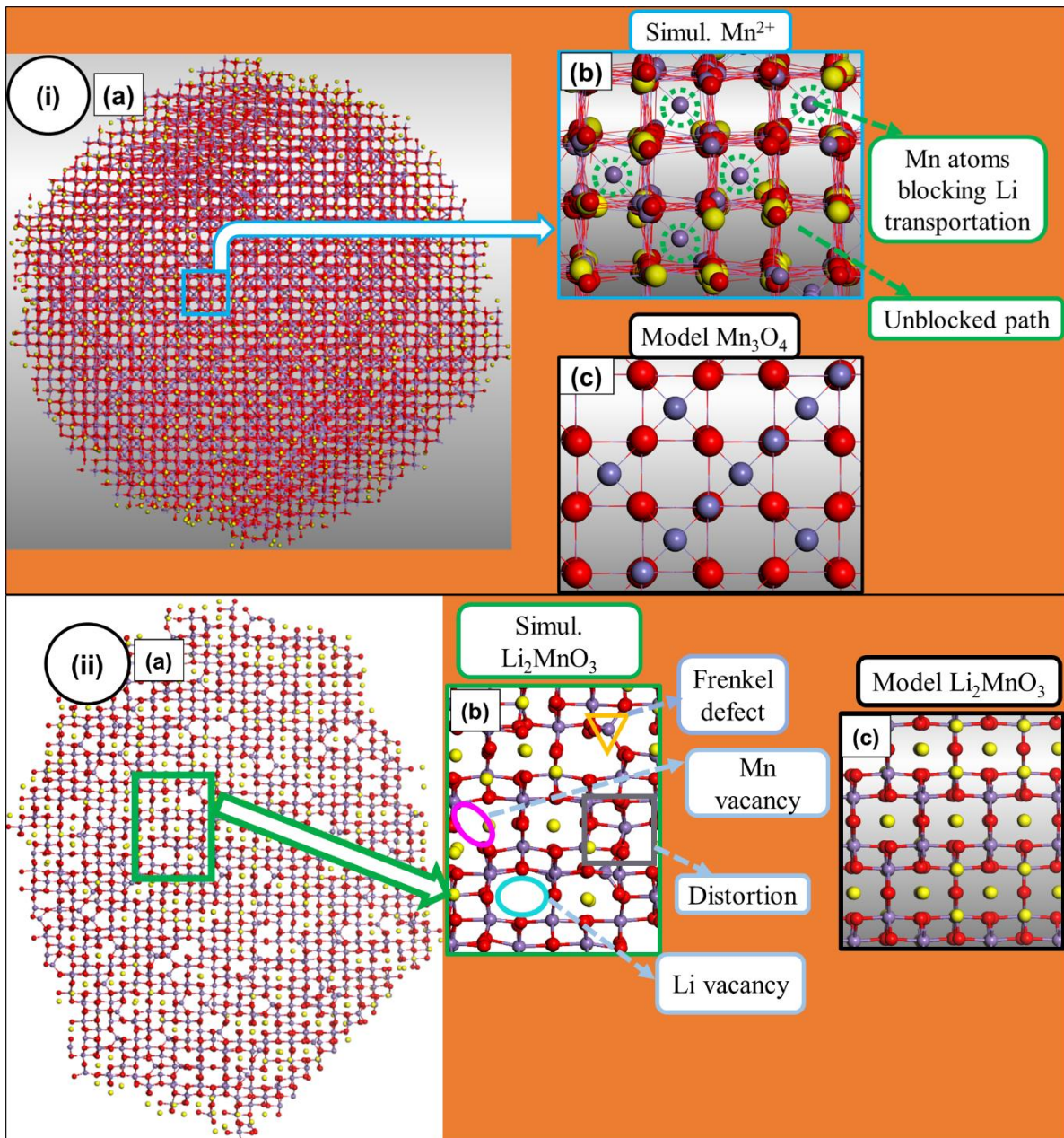


Figure 3. 12: Nanoporous 69 Å structure (i, a) at $\text{Li}_{1.00}\text{Mn}_2\text{O}_4$ concentration illustrating the (b) Mn^{2+} atoms retaining tetrahedral tunnels, with the (c) perfect structural model of spinel Mn_3O_4 . The microstructure (ii, a) show the defected magnification of (b) layered Li_2MnO_3 which is comparable to (c) its perfect structural model.

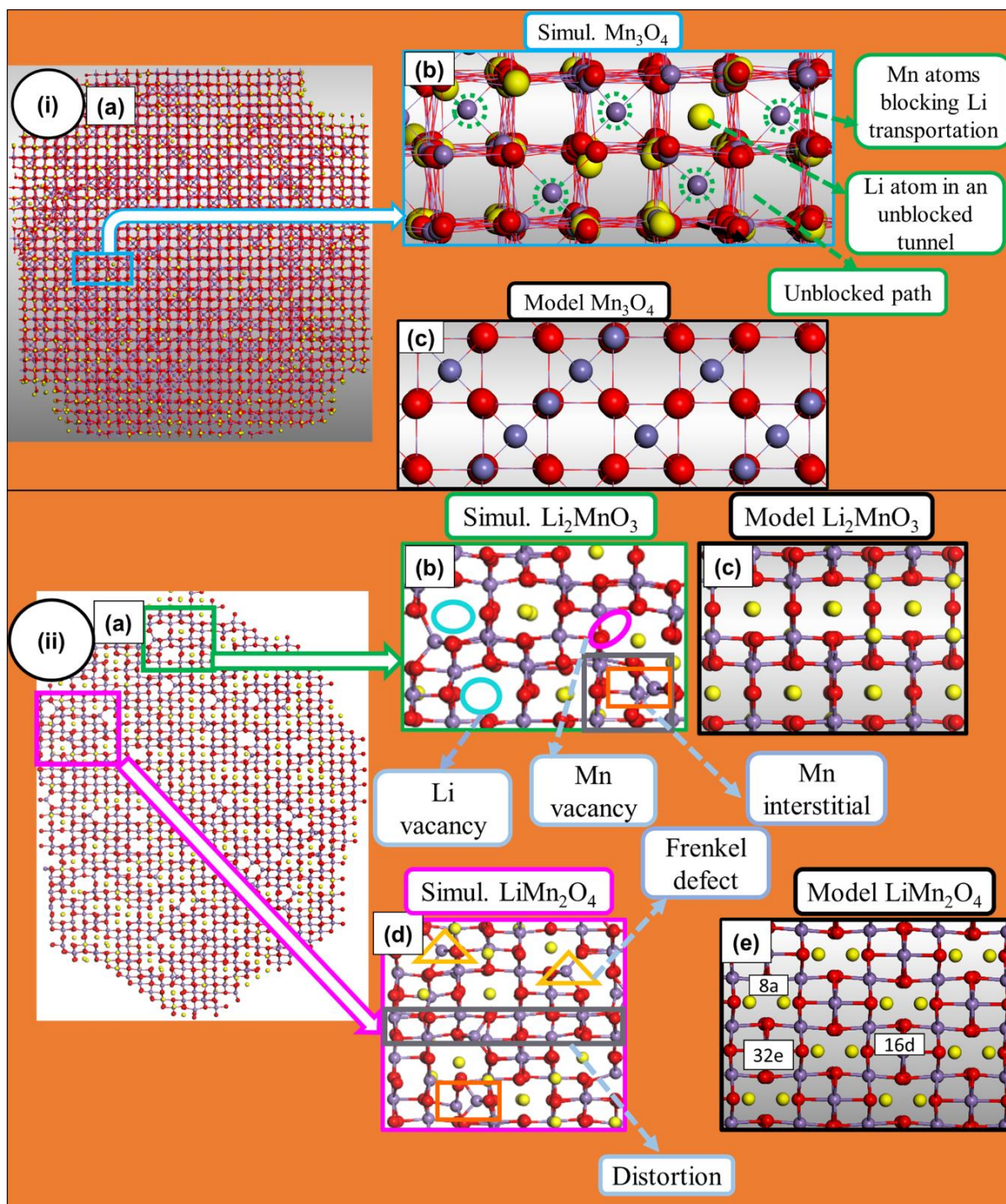


Figure 3. 13: The $\text{Li}_{1.25}\text{Mn}_2\text{O}_4$ nanoporous 69 Å structure (i, a) depicting the magnified portion of (b) spinel Mn_3O_4 structure compared with (c) the perfect structural model. The microstructure slice (ii, a), harvested from the structure depicting the co-existence of (b) layered Li_2MnO_3 and (d) spinel LiMn_2O_4 components which are comparable to their (c, e) perfect structural models compared with the perfect structural models.

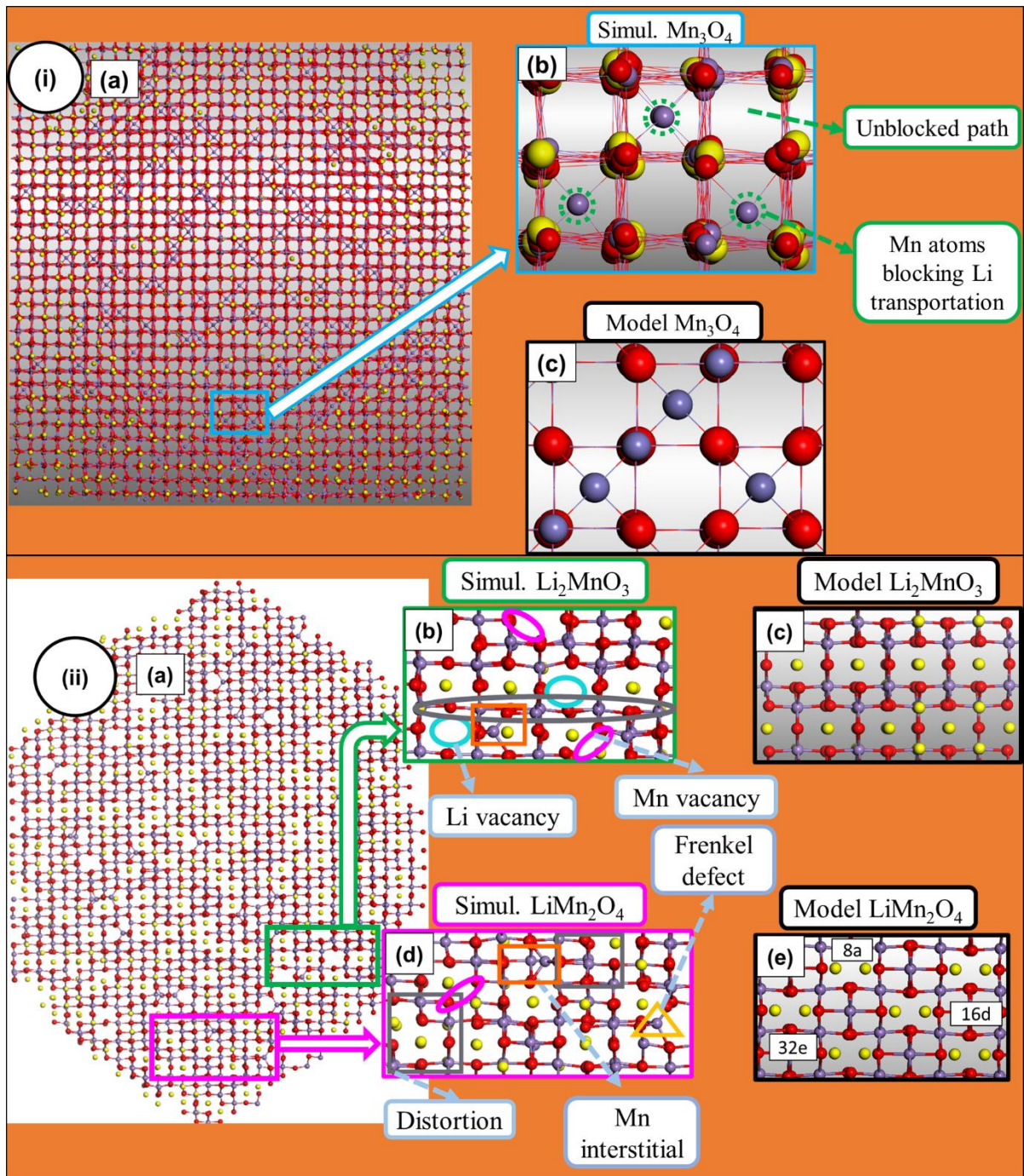


Figure 3. 14: The nanoporous 69 Å structure (i, a) at $Li_{1.50}Mn_2O_4$ concentration depicting the magnified section of (b) spinel Mn_3O_4 structure, comparable with the (c) perfect structural model. The microstructure slice (ii, a) cut from $Li_{1.50}Mn_2O_4$ nanoporous 69 Å, illustrating the magnifications of (b) layered Li_2MnO_3 and (d) spinel $LiMn_2O_4$ components compared with (c, e) their perfect structural models.

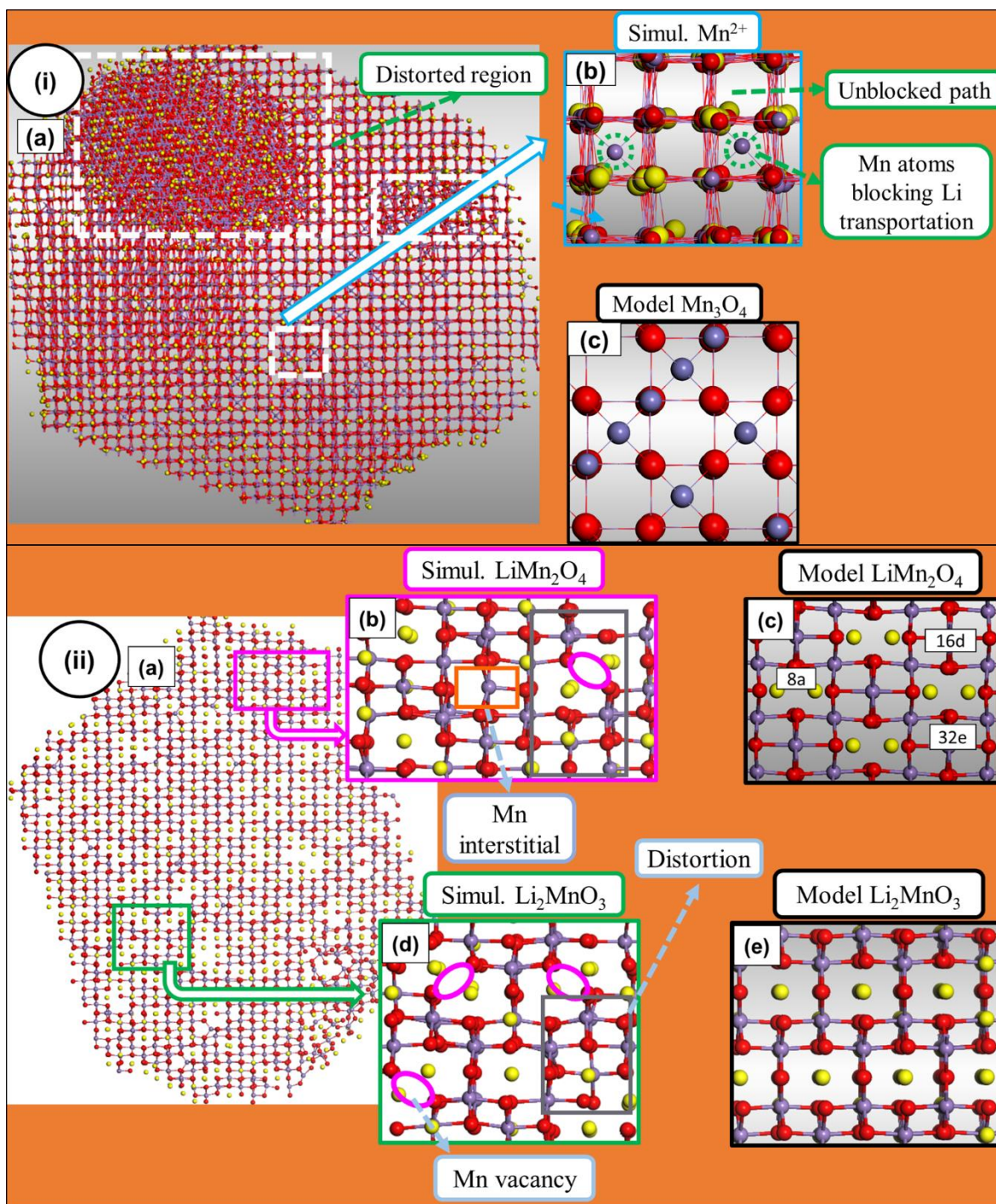


Figure 3. 15: The distorted nanoporous 69 Å structure (i, a) at $\text{Li}_{1.75}\text{Mn}_2\text{O}_4$ concentration showing the (b) Mn^{2+} atoms in the tetrahedral tunnels, where (c) Mn_3O_4 is the perfect structural model. The microstructure (ii, a) of $\text{Li}_{1.75}\text{Mn}_2\text{O}_4$ nanoporous 69 Å depicting the magnified sections of the defected (b) spinel LiMn_2O_4 and (d) layered Li_2MnO_3 components compared with (c, e) their perfect structural models, respectively.

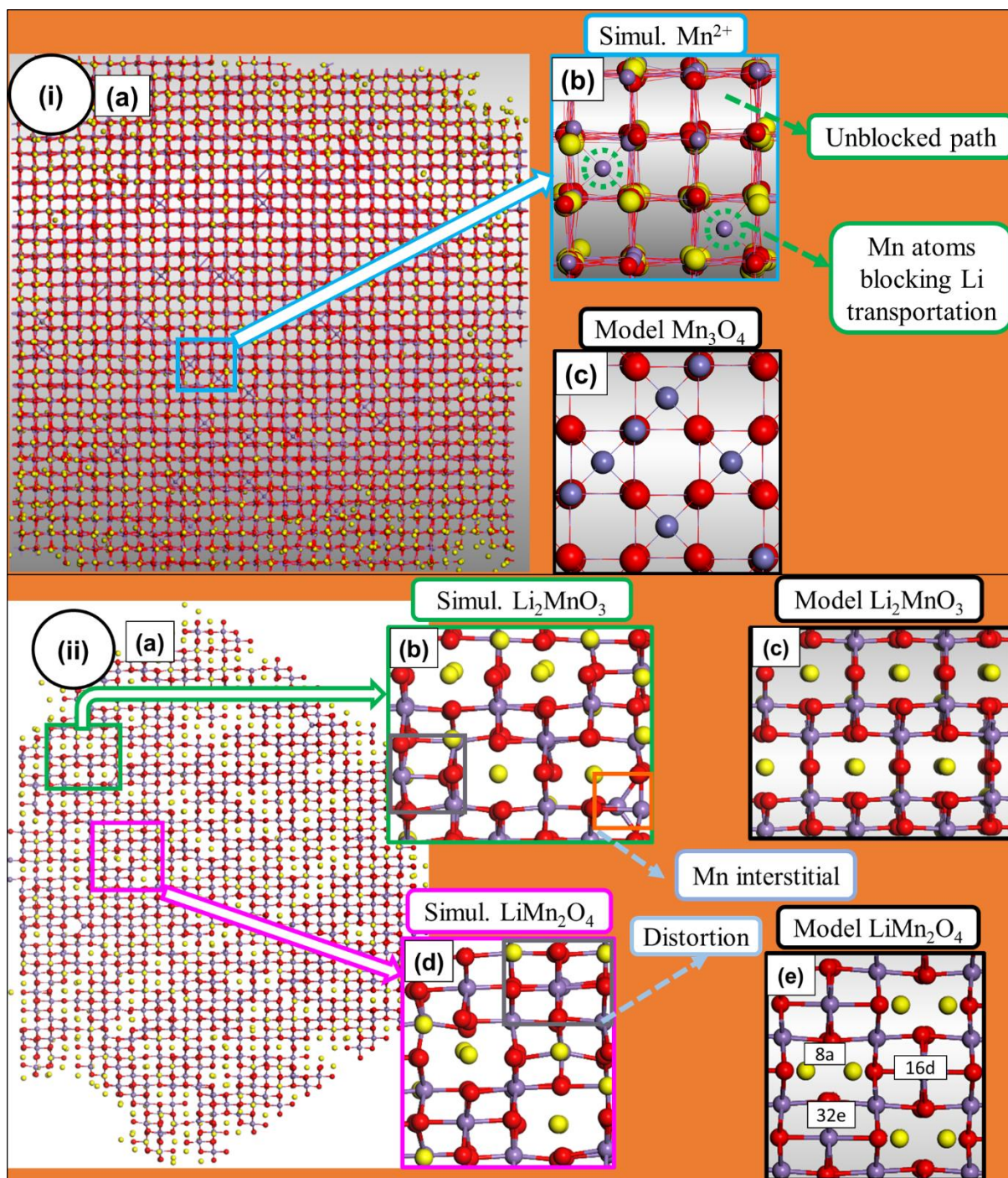


Figure 3. 16: The full lithiated nanoporous 69 Å structure (i, a) at $\text{Li}_{2.00}\text{Mn}_2\text{O}_4$ concentration illustrating the (b) Mn^{2+} atoms in the tetrahedral tunnels, compared to the (c) perfect structural model of spinel Mn_3O_4 . The harvested microstructure slice (ii, a) of the $\text{Li}_{2.00}\text{Mn}_2\text{O}_4$ nanoporous 69 Å structure, depicting the magnifications of (b) layered Li_2MnO_3 and (d) spinel LiMn_2O_4 composites, compared with their (c, e) the perfect structural models.

3.2.3 Nanoporous 67 Å

The recrystallised lithiated Li-Mn-O nanoporous 67 Å structures with their microstructures at different lithium concentrations are illustrated in figures 3.17 to 3.21.

The nanoporous 67 Å structure at $\text{Li}_{1.00}\text{Mn}_2\text{O}_4$ concentration is depicted in figure 3.17 (i, a). The formations of (b) spinel Mn_3O_4 within the simulated nanoporous 67 Å structure is observed and is comparable to (c) its perfect structural model. The microstructure slice (ii, a) harvested from nanoporous 67 Å structure demonstrates the magnifications of the defected (b) layered Li_2MnO_3 and (d) spinel LiMn_2O_4 composites which are comparable to (c, e) their perfect structural models. The layered Li_2MnO_3 captures lithium vacancies, distortions and Mn interstitials. Meanwhile, the spinel LiMn_2O_4 captures lithium and Mn vacancies with some Frenkel defects.

Figure 3.18 (i, a) illustrates nanoporous 67 Å structure at $\text{Li}_{1.25}\text{Mn}_2\text{O}_4$ concentration. From the structure, the formations of (b) spinel Mn_3O_4 are observed and are comparable to (c) the perfect structural model. The microstructure slice (ii, a) cut from $\text{Li}_{1.25}\text{Mn}_2\text{O}_4$ nanoporous 67 Å structure shows the magnifications of (b) layered Li_2MnO_3 and (d) spinel LiMn_2O_4 , which are comparable to the (c, e) perfect structural models. Observations made on the magnifications reveal defects such as lithium vacancies, distortions and Frenkel for the layered; meanwhile, for the spinel, lithium vacancies, Mn interstitials and Frenkel defects are observed.

The $\text{Li}_{1.50}\text{Mn}_2\text{O}_4$ nanoporous 67 Å structure (i, a) is illustrated in figure 3.19. The structure shows the presence of (b) spinel Mn_3O_4 component which is getting reduced when compared to the $\text{Li}_{1.00}\text{Mn}_2\text{O}_4$ and $\text{Li}_{1.25}\text{Mn}_2\text{O}_4$ concentrations. The magnified structure of Mn_3O_4 is comparable with (c) the perfect structural model. The microstructure (ii, a) slice cut from the nanoporous 67 Å structure illustrates the magnifications of (b) spinel LiMn_2O_4

and (d) layered Li_2MnO_3 components, which are comparable to their (c, e) perfect structural models, respectively. The prior capture the presence of Mn vacancies, while the latter reveals both the lithium and Mn vacancies with some distortions.

The nanoporous 67 Å structure at $\text{Li}_{1.75}\text{Mn}_2\text{O}_4$ concentration (i, a) is depicted in figure 3.20. The structure has recrystallised into a multi grained material denoted by grain boundaries and show some distorted regions as well. Due to the presence of distortions the spinel Mn_3O_4 component cannot be easily identified in the material. The microstructure slice (ii, a) from the $\text{Li}_{1.75}\text{Mn}_2\text{O}_4$ nanoporous 67 Å structure shows a grain boundary and the presence of a (b) defective spinel LiMn_2O_4 which reveal Mn vacancies with some distortions. The spinel is comparable to the (c) perfect structural model.

Figure 3.21 illustrates the full lithiated nanoporous 67 Å structure (i, a) at $\text{Li}_{2.00}\text{Mn}_2\text{O}_4$ concentration. The structure illustrates (b) Mn^{2+} atoms retained in the tetrahedral tunnels and some unoccupied tunnels that can allow for better lithium diffusion. The spinel Mn_3O_4 perfect structural model is denoted by (c) and gets reduced with increasing lithium concentration when compared to $\text{Li}_{1.00}\text{Mn}_2\text{O}_4$, $\text{Li}_{1.25}\text{Mn}_2\text{O}_4$, $\text{Li}_{1.50}\text{Mn}_2\text{O}_4$ and $\text{Li}_{1.75}\text{Mn}_2\text{O}_4$. The microstructure slice (i, a) cut from $\text{Li}_{2.00}\text{Mn}_2\text{O}_4$ nanoporous 67 Å structure depict the magnifications of (b) spinel LiMn_2O_4 and (d) layered Li_2MnO_3 which are comparable to (c, e) their perfect structural models. Spinel LiMn_2O_4 reveal the presence of Mn vacancies and some distortions. The layered Li_2MnO_3 magnification display Mn vacancies. The structural defects observed from the nanoporous 67 Å structures get reduced with increasing lithium concentration, as such they are very minimal at $\text{Li}_{2.00}\text{Mn}_2\text{O}_4$.

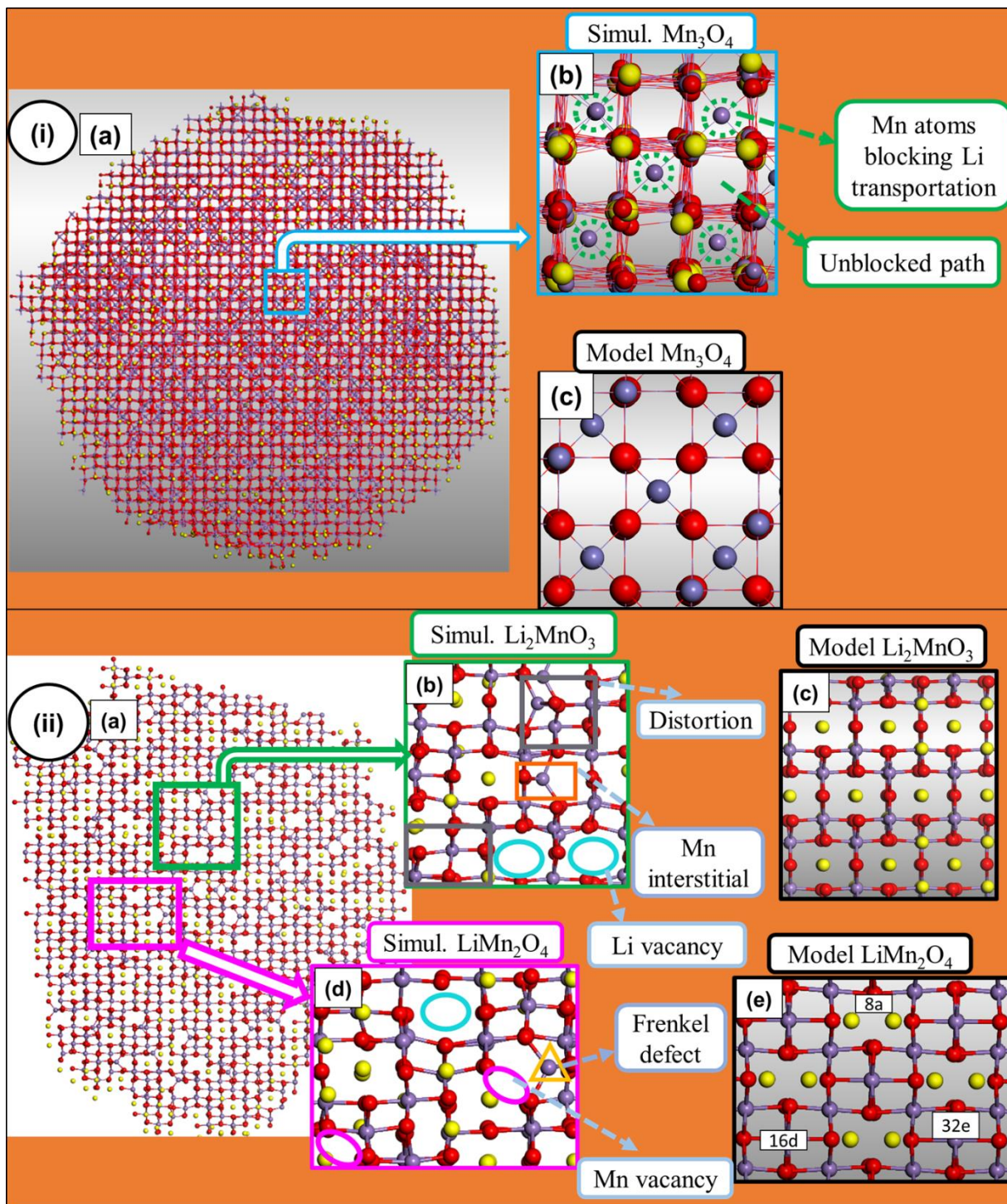


Figure 3. 17: The nanoporous 67 Å structure (i, a) at $\text{Li}_{1.00}\text{Mn}_2\text{O}_4$ depicting the magnified section of (b) spinel Mn_3O_4 structure compared with (c) its perfect model. The microstructure (ii, a) illustrates the magnifications of defected (b) layered Li_2MnO_3 and (d) spinel LiMn_2O_4 compared with their(c, e) perfect structural modes.

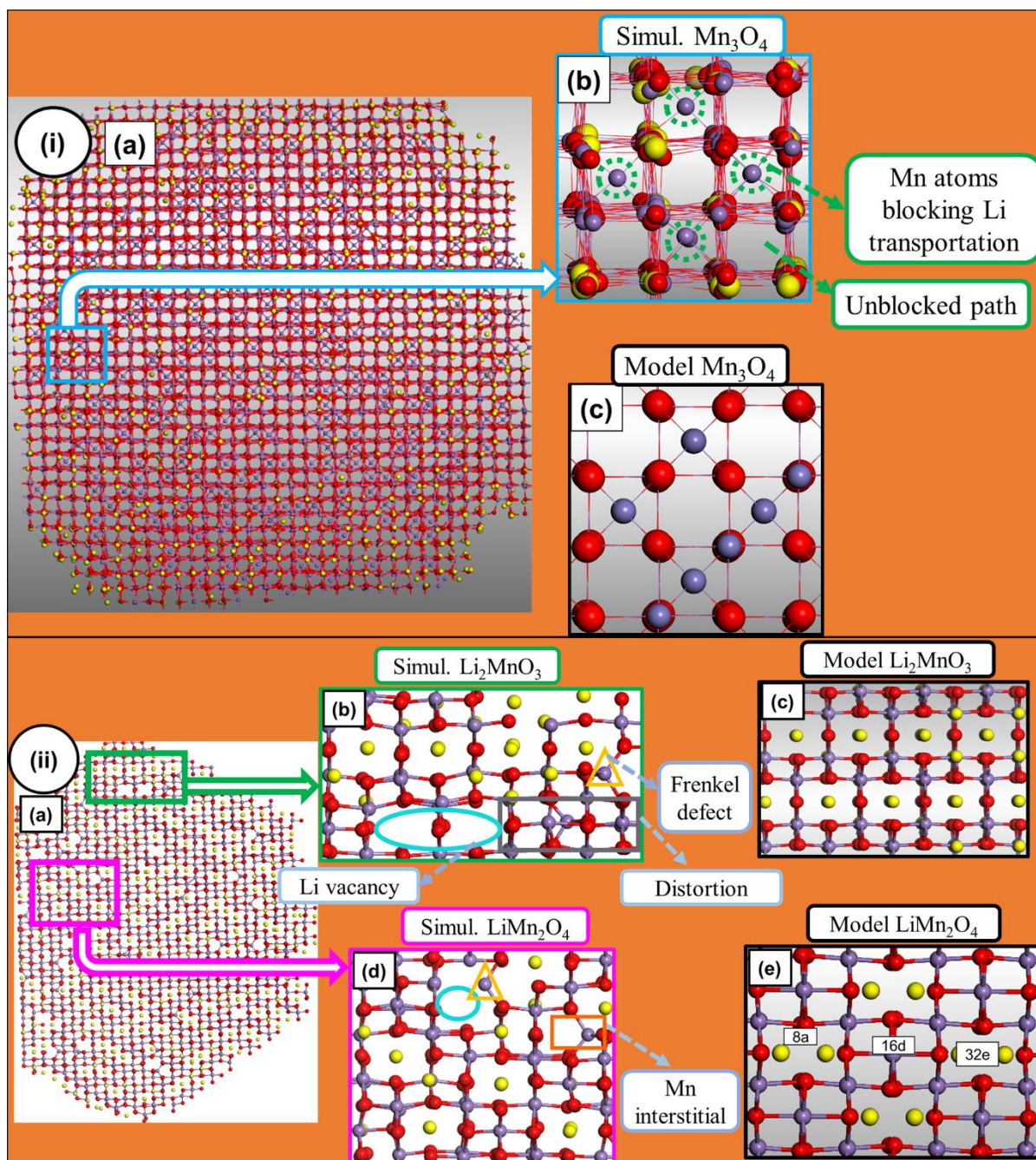


Figure 3. 18: The $\text{Li}_{1.25}\text{Mn}_2\text{O}_4$ nanoporous 67 \AA structure (i, a) illustrating the magnified section of (b) spinel Mn_3O_4 structure which is comparable to (c) its perfect structural model. The microstructure slice ((ii, a) harvested from $\text{Li}_{1.25}\text{Mn}_2\text{O}_4$ nanoporous 67 \AA structure depicting the magnified sections of (b) layered Li_2MnO_3 and d) spinel LiMn_2O_4 components, compared with their (c, e) perfect structural models.

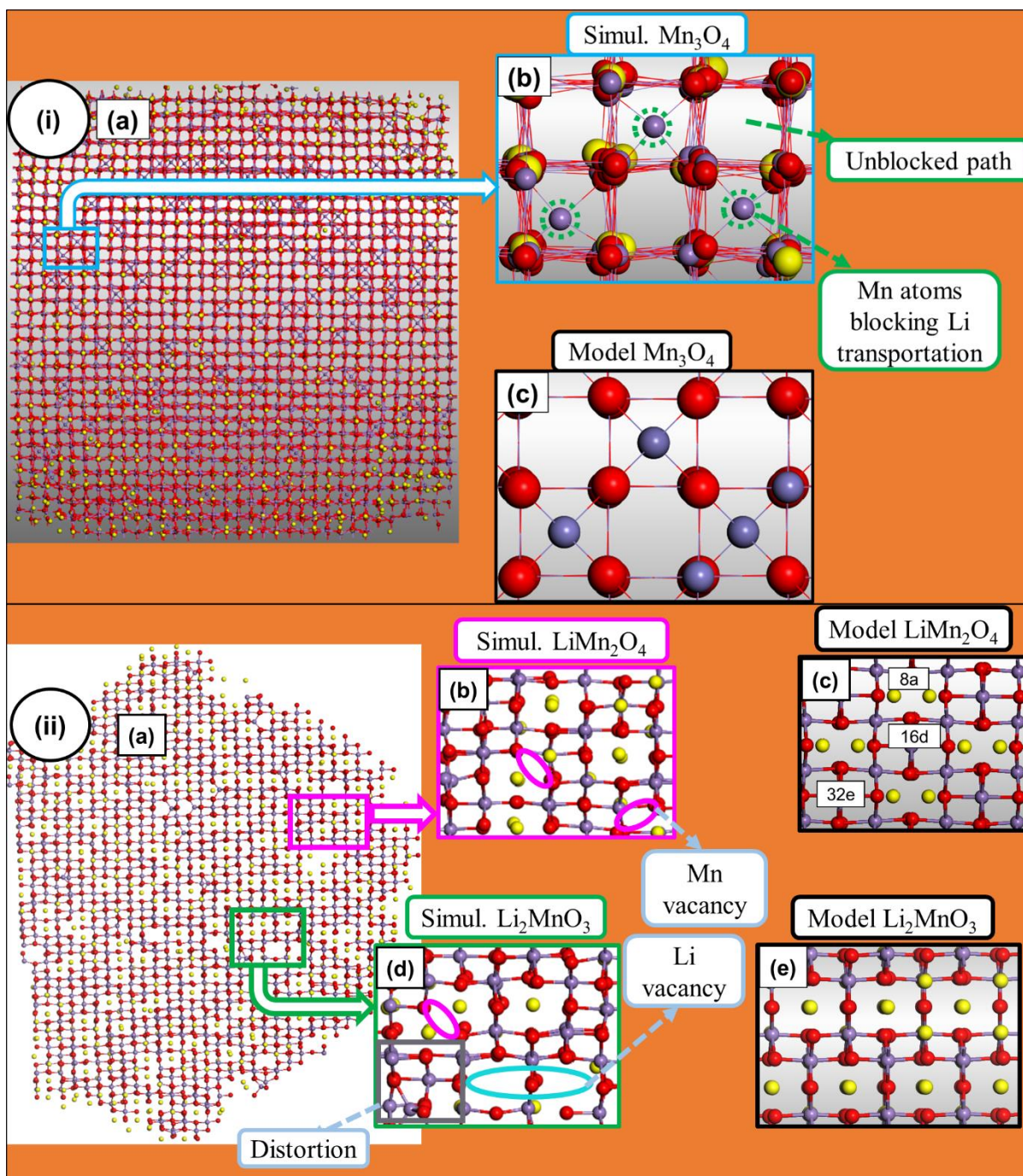


Figure 3. 19: The nanoporous 67 \AA structure (i, a) at $\text{Li}_{1.50}\text{Mn}_2\text{O}_4$ concentration illustrating the presence of (b) spinel Mn_3O_4 structure comparable to (c) its perfect structural model. The Microstructure (ii, a) cut from the $\text{Li}_{1.50}\text{Mn}_2\text{O}_4$ nanoporous 67 \AA structure capturing the defected magnified portions of (b) spinel LiMn_2O_4 and (d) layered Li_2MnO_3 when compared to their (c, e) perfect structural models.

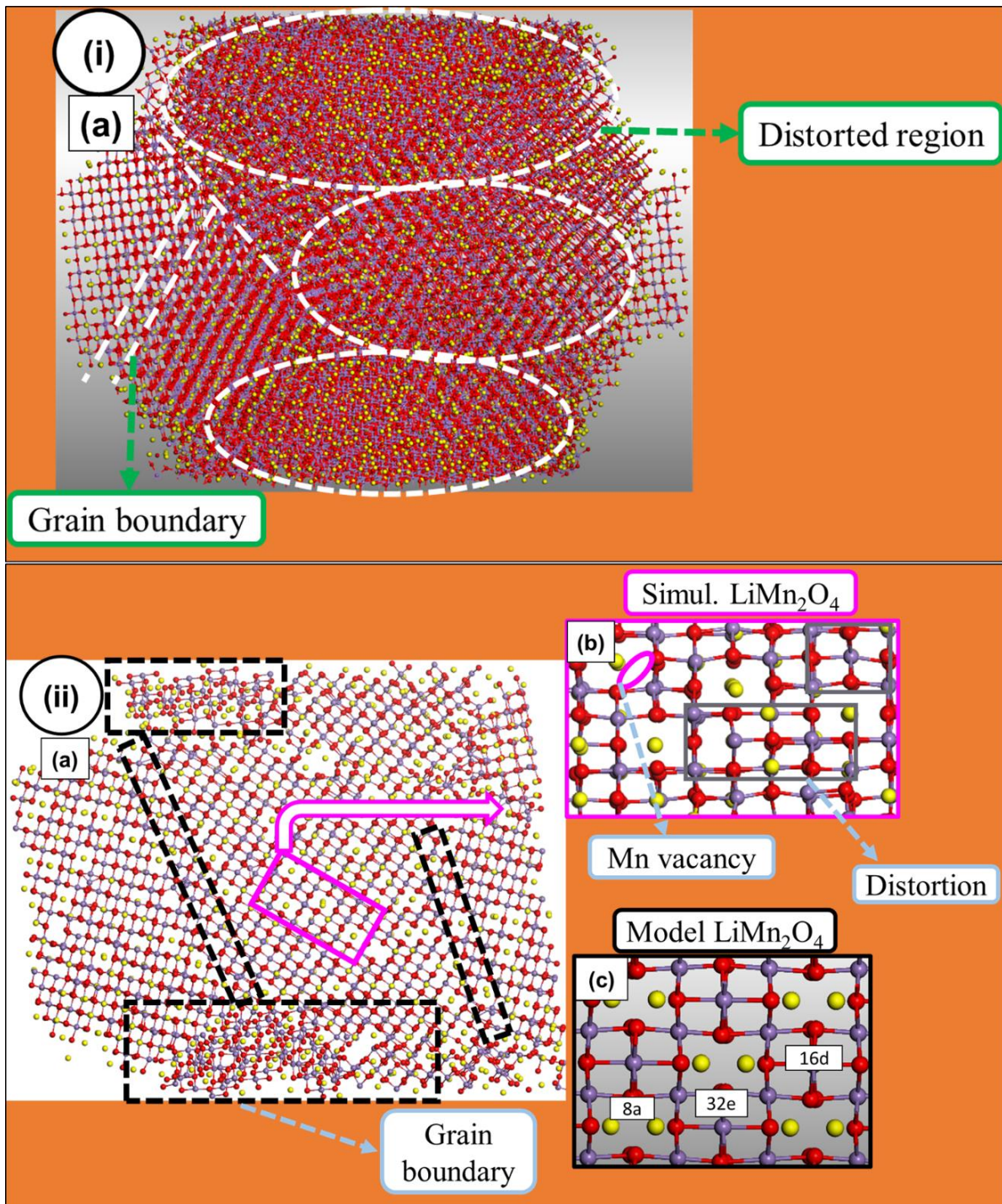


Figure 3. 20: The distorted and multi grained nanoporous 67 Å structure (i, a) at $\text{Li}_{1.75}\text{Mn}_2\text{O}_4$ concentration. The microstructure (ii, a) harvested from the $\text{Li}_{1.75}\text{Mn}_2\text{O}_4$ nanoporous 67 Å, with multiple grain boundaries, depicting the magnified section of (b) spinel LiMn_2O_4 component comparable with (c) its perfect structural model.

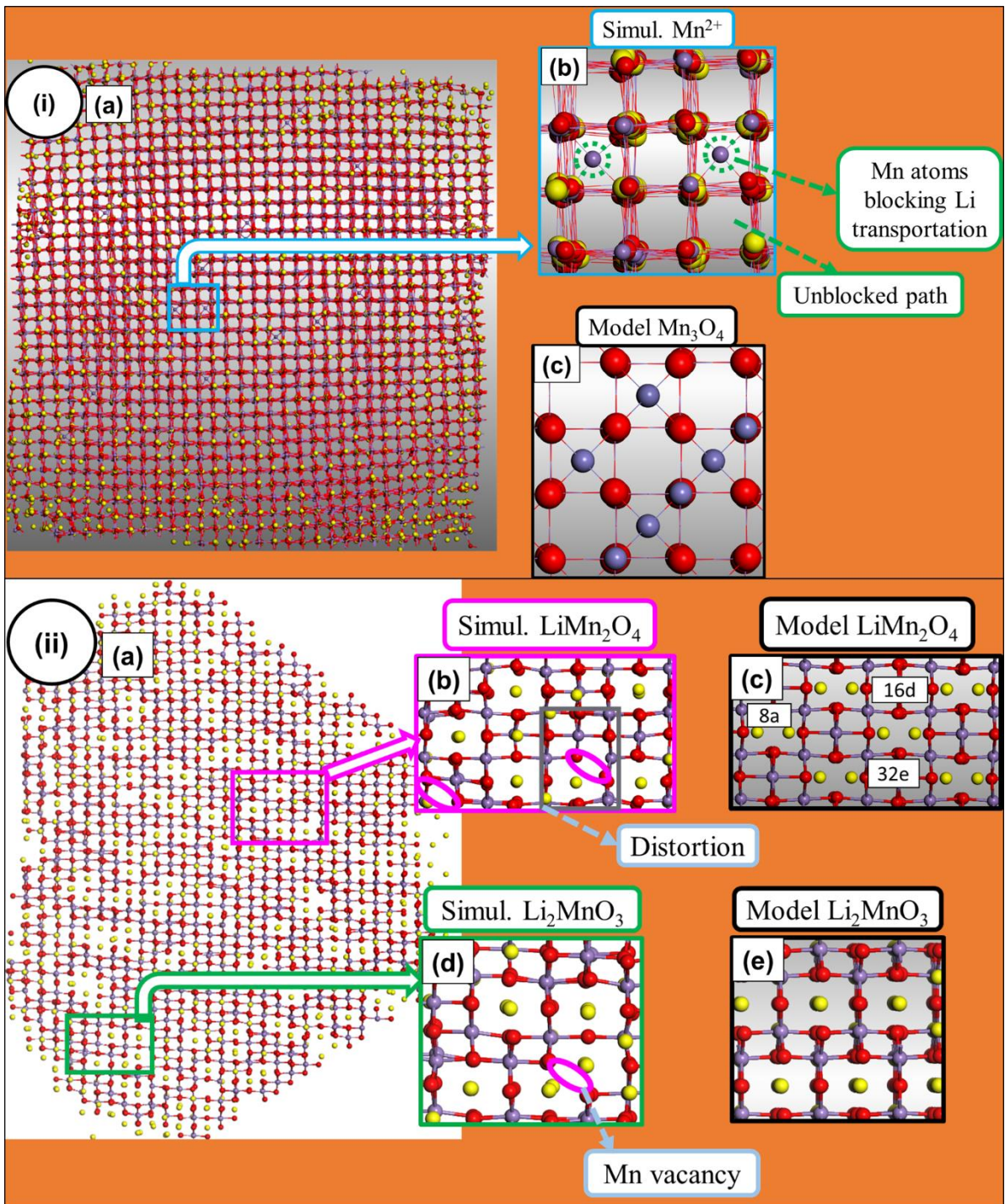


Figure 3. 21: The full lithiated nanoporous 67 Å structure (i, a) at $\text{Li}_{2.00}\text{Mn}_2\text{O}_4$ concentration illustrating (b) Mn^{2+} atoms retained in tetrahedral tunnels, compared to the perfect structural model of spinel Mn_3O_4 . The microstructure of $\text{Li}_{2.00}\text{Mn}_2\text{O}_4$ nanoporous 67 Å (ii, a) illustrating the magnifications of (b) spinel LiMn_2O_4 and (d) layered Li_2MnO_3 comparable with (c, e) their perfect structural models.

3.2.4 Bulk (63 Å)

Figure 3.22 to 3.26 illustrate the simulated recrystallised Li-Mn-O bulk structures and their microstructures with different lithium concentrations.

The bulk structure at $\text{Li}_{1.00}\text{Mn}_2\text{O}_4$ concentration (i, a) is depicted in figure 3.22 and is magnified to show the (b) Mn^{2+} atoms retained in tetrahedral tunnels, with some unoccupied tunnels that can accommodate surplus lithium during intercalation. The spinel Mn_3O_4 perfect structural model is denoted by (c). The harvested microstructure (ii, a) depicts the magnification of (b) the layered Li_2MnO_3 compared with its (c) perfect structural model. The layered Li_2MnO_3 reveal the presence of defects such as lithium vacancies and Mn interstitials. Another magnification from the microstructure captures the presence of (d) spinel LiMn_2O_4 component with distortions, compared to (e) its perfect structural model.

The $\text{Li}_{1.25}\text{Mn}_2\text{O}_4$ bulk structure is illustrated in figure 3.23 (i, a) and demonstrates the formation of (b) spinel Mn_3O_4 is comparable to (c) the perfect structural model. The presence of the spinel Mn_3O_4 component is getting reduced when compared to the $\text{Li}_{1.00}\text{Mn}_2\text{O}_4$ bulk structure. The microstructure slice (ii, a) cut from the $\text{Li}_{1.25}\text{Mn}_2\text{O}_4$ bulk depicts the magnifications of (b) of layered Li_2MnO_3 and (d) spinel LiMn_2O_4 components, compared to their (c, e) perfect structural models. The layered and spinel components indicate the Mn vacancies and distortions.

Figure 3.24 (i) depicts the bulk structure at $\text{Li}_{1.50}\text{Mn}_2\text{O}_4$ concentration, where the magnification of (b) spinel Mn_3O_4 component is observed and is comparable to the (c) perfect structural model. Further observations made on the structure indicate that the presence of the spinel Mn_3O_4 component is getting reduced when compared to the $\text{Li}_{1.00}\text{Mn}_2\text{O}_4$ and $\text{Li}_{1.25}\text{Mn}_2\text{O}_4$ concentrations. The layered-spinel components observed on

the microstructure (ii, a) depict their defective magnifications. The magnified section (b) of layered Li_2MnO_3 shows the Mn vacancies and distortions and is compared with (c) the perfect structural model. Further observations show the presence of (d) spinel LiMn_2O_4 component which is comparable to its (e) perfect structural model and reveal Mn vacancies, Mn interstitials and some distortion.

The bulk at $\text{Li}_{1.75}\text{Mn}_2\text{O}_4$ concentration is illustrated in figure 3.25 (i, a) and has crystallised into a multi grained structure, as a result, the formation of spinel Mn_3O_4 cannot be identified at any structural rotation view. A multi grained microstructure (ii, a) depicted from the figure show the magnification of (b) layered Li_2MnO_3 which is comparable to the (c) perfect structural model. The layered component capture Mn interstitial atoms and some distortions.

The $\text{Li}_{2.00}\text{Mn}_2\text{O}_4$ bulk structure is depicted in figure 3.26 (i, a). The structure illustrates the presence of (b) Mn^{2+} atoms retaining tetrahedral tunnels and some which are unoccupied, compared with (c) the spinel Mn_3O_4 perfect structural model. From the bulk $\text{Li}_{1.00}\text{Mn}_2\text{O}_4$ to $\text{Li}_{2.00}\text{Mn}_2\text{O}_4$ concentration, the formation of the spinel Mn_3O_4 component is gradually getting reduced. The $\text{Li}_{2.00}\text{Mn}_2\text{O}_4$ microstructure (a) depicts the magnifications of layered and spinel composites. The (b) layered Li_2MnO_3 reveal the presence of lithium vacancies and distortions when compared to its (c) perfect structural model. Furthermore, the (d) spinel LiMn_2O_4 component reveals the presence of Mn vacancies and distortions when compared to (e) the perfect structural model. Upon full lithiation, the grain boundaries disappear.

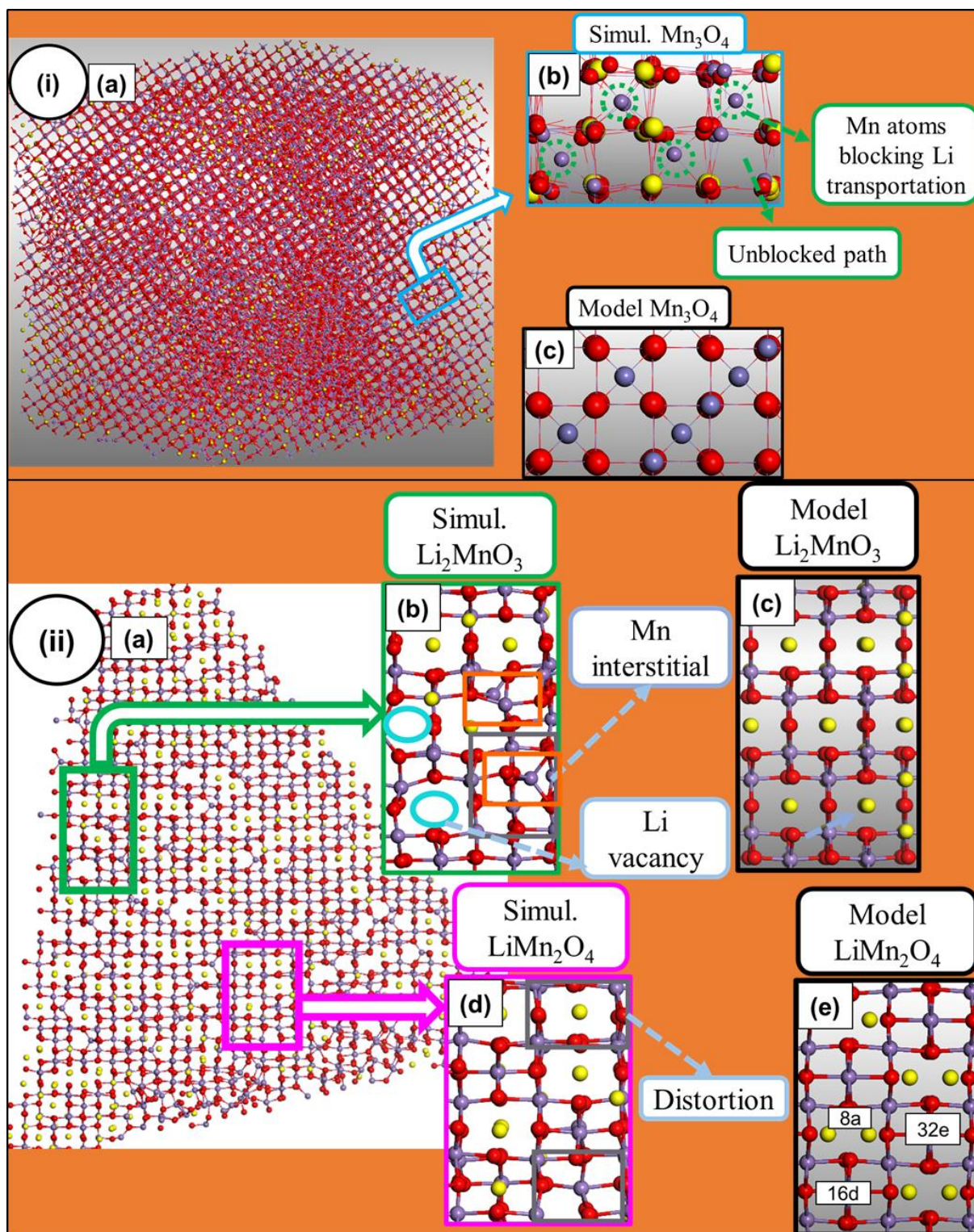


Figure 3. 22: The $\text{Li}_{1.00}\text{Mn}_2\text{O}_4$ bulk structure ((i) a) illustrating the presence of (b) Mn^{2+} retained in tetrahedral tunnels compared with (c) the perfect structural model of spinel Mn_3O_4 . The microstructure (ii, a) of the bulk cut from the $\text{Li}_{1.00}\text{Mn}_2\text{O}_4$ structure depicting the magnified portions of (b) layered Li_2MnO_3 and (d) of spinel LiMn_2O_4 compared to their (c, e) perfect structural models.

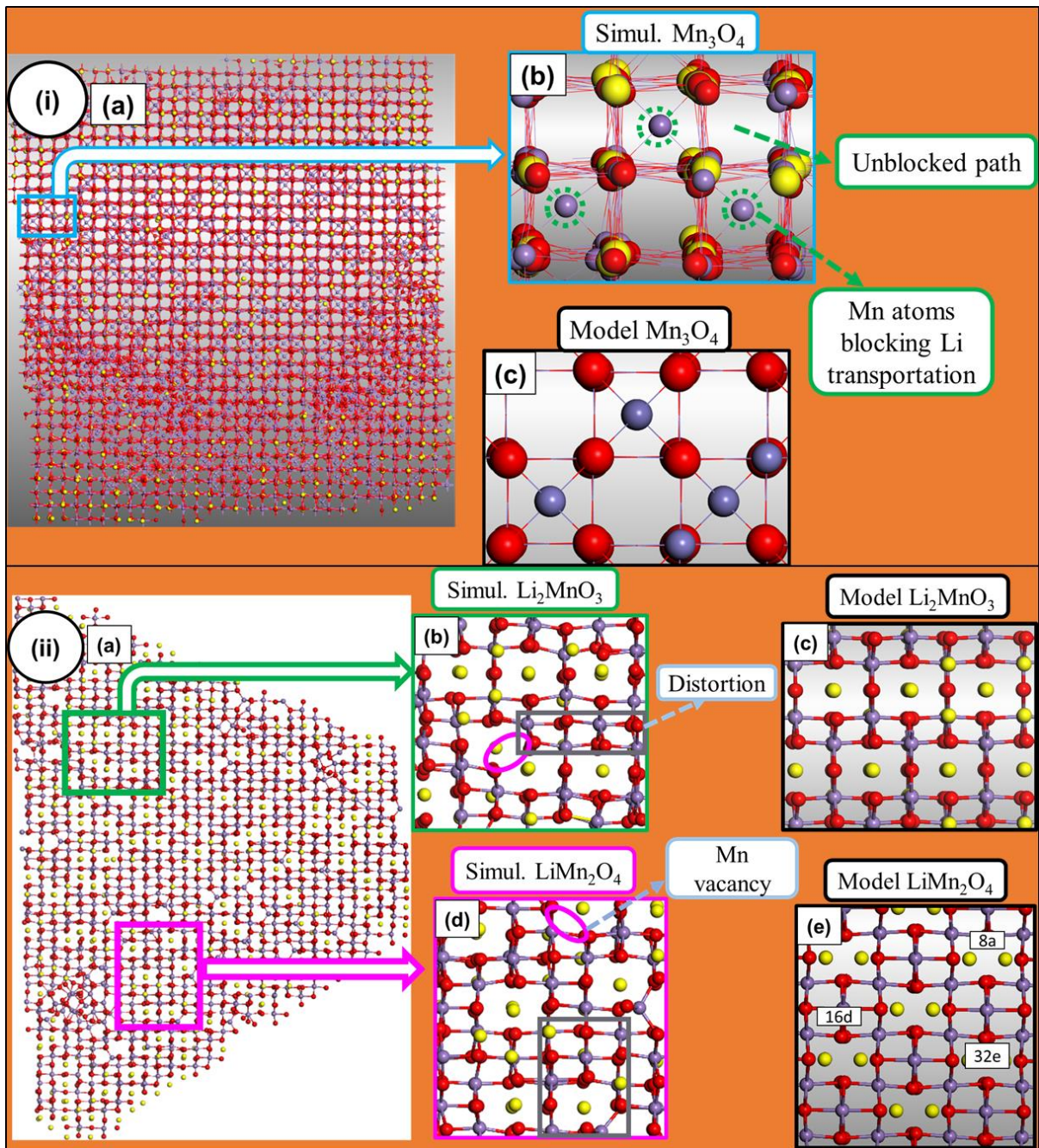


Figure 3. 23: The bulk structure (i, a) at $\text{Li}_{1.25}\text{Mn}_2\text{O}_4$ concentration depicting the magnified section of (b) spinel Mn_3O_4 structure comparable to its (c) perfect structural model. The microstructure (ii, a) harvested from the bulk $\text{Li}_{1.25}\text{Mn}_2\text{O}_4$ structure showing the defected magnified sections of (b) layered Li_2MnO_3 and (d) spinel LiMn_2O_4 compared to their (c, e) perfect structural models.

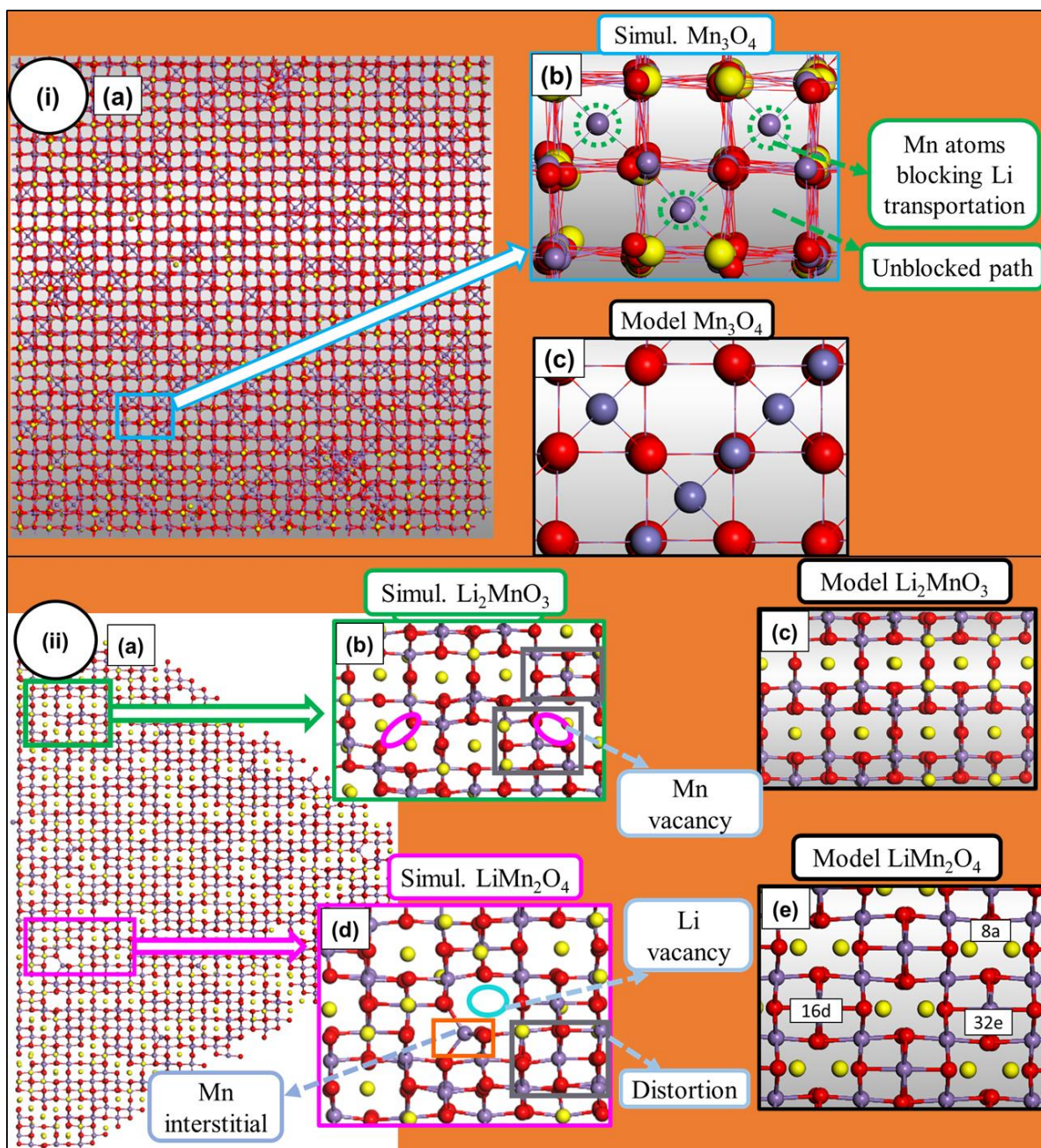


Figure 3. 24: The $\text{Li}_{1.50}\text{Mn}_2\text{O}_4$ bulk structure (i, a) illustrating the magnified section of spinel Mn_3O_4 structure (b) compared with (c) the perfect structural model. The microstructure (ii, a) cut from $\text{Li}_{1.50}\text{Mn}_2\text{O}_4$ structure with magnified portions (b) the layered Li_2MnO_3 and (d) spinel LiMn_2O_4 components, which are comparable to (c, e) their perfect structural models.

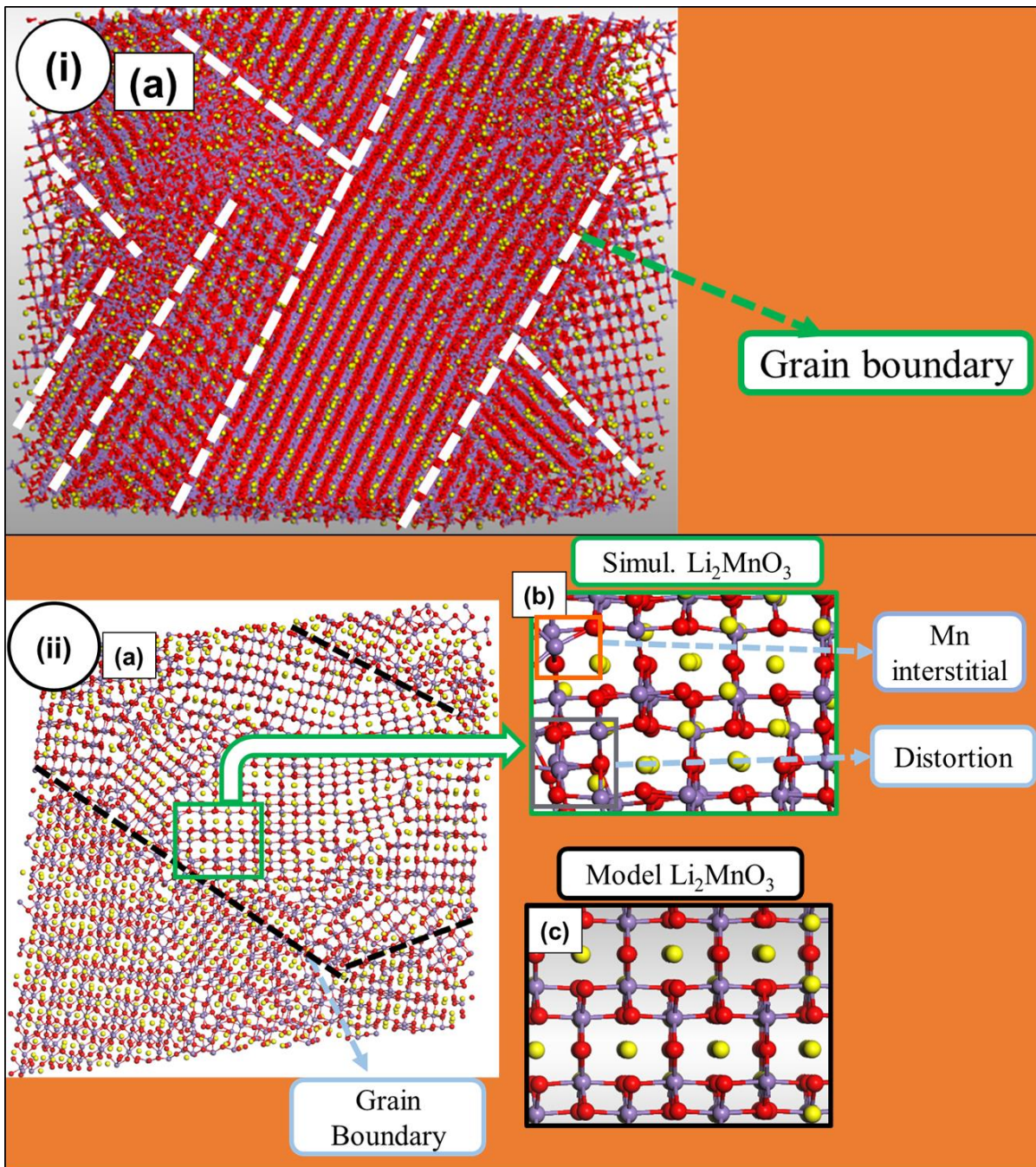


Figure 3. 25: The bulk structure (i, a), which has recrystallised into a multi grained material. The microstructure slice (ii, a) with grain boundaries from the $\text{Li}_{1.75}\text{Mn}_2\text{O}_4$ bulk depicting the magnified section of (b) layered Li_2MnO_3 component compared to (c) its perfect structural model.

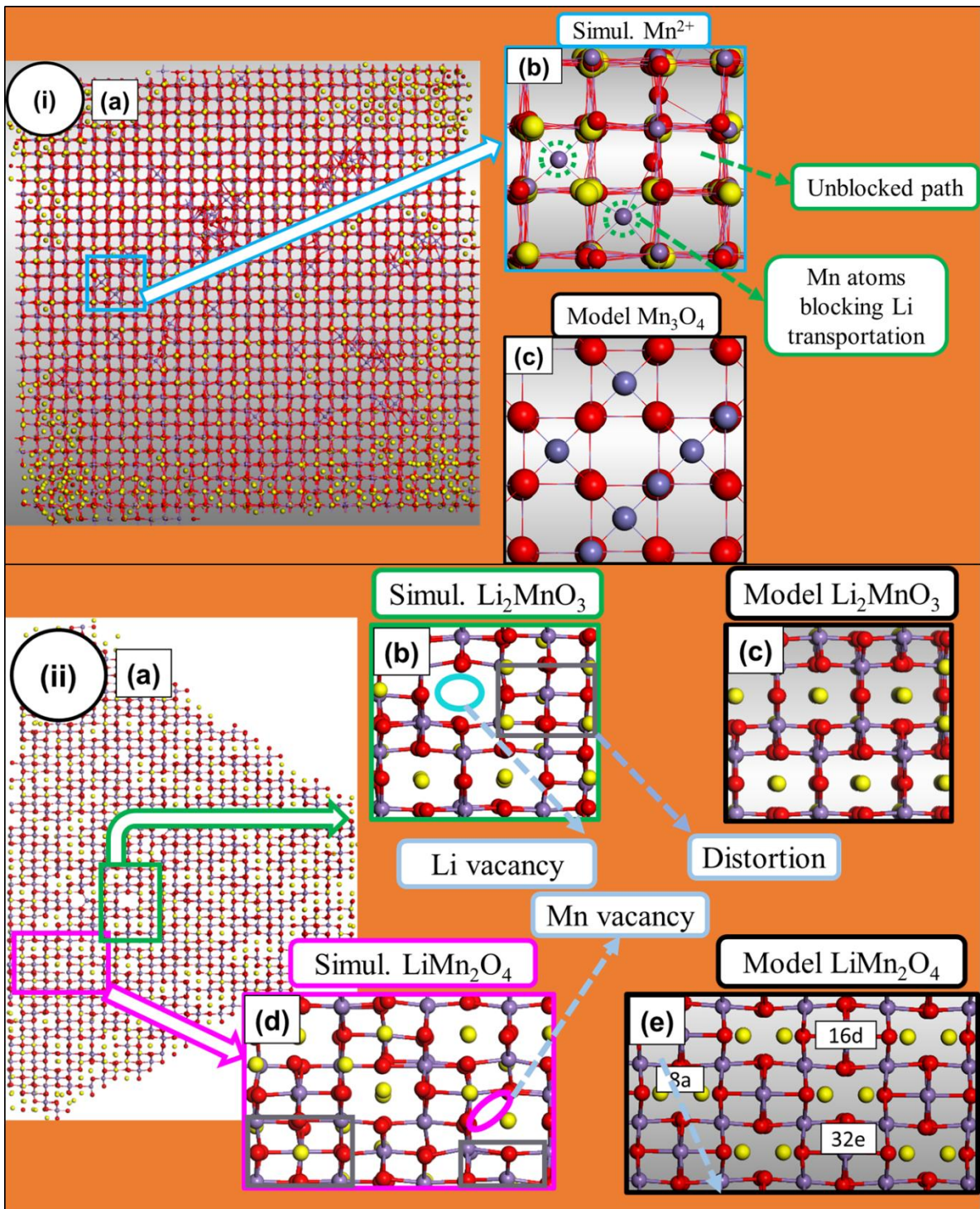


Figure 3. 26: The full lithiated bulk structure (i, a) at $\text{Li}_{2.00}\text{Mn}_2\text{O}_4$ concentration magnified to illustrate that Mn^{2+} atoms are retaining the tetrahedral tunnels. The microstructure slice (ii, a) cut through the $\text{Li}_{2.00}\text{Mn}_2\text{O}_4$ bulk structure, illustrating the presence of (b) layered Li_2MnO_3 and (d) spinel LiMn_2O_4 compared with their (c, e) perfect structural models.

3.3 Structural characterisation of the nanoporous and bulk structures by X-ray diffraction patterns

X-ray diffraction patterns are fingerprints to distinguish element compositions, existing and formation of new phases on a material. Herein, the X-ray diffractions patterns of nanoporous (75, 69 and 67 Å) and bulk structures are illustrated in figures 3.27 - 3.30, to characterise the structural components existing and formed within the materials during the amorphisation and recrystallisation process under the NVT ensemble.

3.3.1 XRDs for the nanoporous structures

The X-ray diffraction patterns for the simulated Li-Mn-O lithiated nanoporous 75 Å structure with different lithium concentrations ($\text{Li}_{1+x}\text{Mn}_2\text{O}_4$, $1 \leq x \leq 2$) are illustrated in figure 3.27. The simulated $\text{Li}_{1+x}\text{Mn}_2\text{O}_4$ X-ray diffraction patterns (a-e) are compared with the experimental, i.e. (f) spinel Mn_3O_4 [106], (g) layered Li_2MnO_3 co-existing with (h) layered LiMnO_2 [107] and (i) spinel LiMn_2O_4 [107]. The simulated XRDs depicts shoulder peaks at $\sim 2\theta = 18 - 23^\circ$ associated with spinel Mn_3O_4 , LiMn_2O_4 and layered Li_2MnO_3 which decrease gradually with lithium increment from $\text{Li}_{1.00}\text{Mn}_2\text{O}_4$ to $\text{Li}_{1.50}\text{Mn}_2\text{O}_4$ and re-emerge again at $\text{Li}_{1.75}\text{Mn}_2\text{O}_4$. The concentration at $\text{Li}_{1.75}\text{Mn}_2\text{O}_4$ is where the structure has recrystallised into a polycrystalline form. As the lithium content is increased to $\text{Li}_{2.00}\text{Mn}_2\text{O}_4$, the shoulder peaks in the range $\sim 2\theta = 18 - 23^\circ$ almost disappear. A similar trend is observed for $\sim 2\theta = 26 - 32^\circ$ peaks associated with spinel Mn_3O_4 on the simulated structures. A split of peaks at $\sim 2\theta = 36^\circ$ for $\text{Li}_{1.25}\text{Mn}_2\text{O}_4$, $\text{Li}_{1.50}\text{Mn}_2\text{O}_4$ and $\text{Li}_{2.00}\text{Mn}_2\text{O}_4$ accompanied by a shift to the right is observed. The shift favours the spinel LiMn_2O_4 component. Further splits and shifts at $\sim 2\theta = 44^\circ$ associated with spinel LiMn_2O_4 , Mn_3O_4 and layered Li_2MnO_3 components for $\text{Li}_{1.25}\text{Mn}_2\text{O}_4$, $\text{Li}_{1.50}\text{Mn}_2\text{O}_4$ and $\text{Li}_{2.00}\text{Mn}_2\text{O}_4$ structures are also observed. Likewise, at $\sim 2\theta = 64^\circ$, splits and shifts of peaks are still observed for

$\text{Li}_{1.25}\text{Mn}_2\text{O}_4$, $\text{Li}_{1.50}\text{Mn}_2\text{O}_4$ and $\text{Li}_{2.00}\text{Mn}_2\text{O}_4$ concentrations. The shifts are towards the right and favour the layered Li_2MnO_3 component. The $\text{Li}_{1.25}\text{Mn}_2\text{O}_4$, $\text{Li}_{1.50}\text{Mn}_2\text{O}_4$ and $\text{Li}_{2.00}\text{Mn}_2\text{O}_4$ concentrations have a similar trend and formation of peaks. The nanoporous 75 Å structure at $\text{Li}_{1.00}\text{Mn}_2\text{O}_4$ and $\text{Li}_{1.75}\text{Mn}_2\text{O}_4$ depicts broad peaks without any splitting but shifts. The shifts and splits observed in the X-ray diffraction patterns could be attributed to the mixing of Li and Mn layers, phase transitions or defects generated in the Li-Mn-O structures during cycling [108, 109, 110].

The X-ray diffraction patterns for the simulated lithiated Li-Mn-O nanoporous 69 Å structures (a-e) with different lithium concentrations of $\text{Li}_{1+x}\text{Mn}_2\text{O}_4$, $0 \leq x \leq 1$, compared with the experimental results of (f) spinel Mn_3O_4 [106], layered Li_2MnO_3 (g) co-existing with layered LiMnO_2 (h) [107] and spinel LiMn_2O_4 (i) [107] are illustrated in figure 3.28. The shoulder peak at $\sim 2\theta = 18 - 23^\circ$ associated with spinel Mn_3O_4 , LiMn_2O_4 and layered Li_2MnO_3 display peaks that progressively decrease with an increase in lithium concentration. A similar trend is observed for $\sim 2\theta = 26 - 32^\circ$, where the peak related to the spinel Mn_3O_4 is visible, however, decrease as the lithium concentration is increased. The peak appears to be flat upon full lithiation at $\text{Li}_{2.00}\text{Mn}_2\text{O}_4$ concentration. At $\sim 2\theta = 36^\circ$ there is a split of peaks observed for all the simulated structures associated with spinel Mn_3O_4 except for $\text{Li}_{1.00}\text{Mn}_2\text{O}_4$, accompanied by a shift to the right. The shift towards the right favours both the spinel LiMn_2O_4 and layered Li_2MnO_3 components. Further splits and shifts are observed at $\sim 2\theta = 44^\circ$ for all the simulated structures. The peak is associated with spinel LiMn_2O_4 , Mn_3O_4 and layered Li_2MnO_3 . Moreover, at $\sim 2\theta = 64^\circ$ splits and shifts of peaks for $\text{Li}_{1.25}\text{Mn}_2\text{O}_4$, $\text{Li}_{1.50}\text{Mn}_2\text{O}_4$ and $\text{Li}_{2.00}\text{Mn}_2\text{O}_4$ structures are observed, except for $\text{Li}_{1.00}\text{Mn}_2\text{O}_4$ and $\text{Li}_{1.75}\text{Mn}_2\text{O}_4$ concentrations. Interestingly, nanoporous 69 Å at $\text{Li}_{1.75}\text{Mn}_2\text{O}_4$ concentrations depicts narrow peaks in contrast to nanoporous 75 Å which displayed broad peaks. Shifts are observed at $\sim 2\theta = 64$ towards the right, favouring the layered

Li_2MnO_3 and spinel Mn_3O_4 components at $\sim 2\theta = 66^\circ$. The shifts and splits could be ascribed to the mixing of Li and Mn layers, phase transitions or defects generated in the Li-Mn-O systems during the lithiation process in the structure [108, 109, 110].

Figure 3.29 (a-e) depicts the X-ray diffraction patterns for the simulated Li-Mn-O lithiated nanoporous 67 Å structures with different lithium concentrations of $\text{Li}_{1+x}\text{Mn}_2\text{O}_4$ where, $0 \leq x \leq 1$ compared with the experimental results of spinel Mn_3O_4 (f) [106], layered Li_2MnO_3 (g) co-existing with layered LiMnO_2 (h) [107] and spinel LiMn_2O_4 (i) [107]. Shoulder peaks associated with spinel Mn_3O_4 , LiMn_2O_4 , layered Li_2MnO_3 and LiMnO_2 at $\sim 2\theta = 18 - 23^\circ$ decrease gradually as the lithium concentration increases from $\text{Li}_{1.00}\text{Mn}_2\text{O}_4$ to $\text{Li}_{1.50}\text{Mn}_2\text{O}_4$ and re-emerge at $\text{Li}_{1.75}\text{Mn}_2\text{O}_4$. The peak almost disappears again upon full lithiation at $\text{Li}_{2.00}\text{Mn}_2\text{O}_4$ concentration. Characteristics peaks for $\sim 2\theta = 26 - 32^\circ$, related to the spinel Mn_3O_4 is visible for all the structures except for $\text{Li}_{2.00}\text{Mn}_2\text{O}_4$. The peaks appear to be broad and intense for $\text{Li}_{1.00}\text{Mn}_2\text{O}_4$ and $\text{Li}_{1.75}\text{Mn}_2\text{O}_4$ concentrations. There is a split of peaks at $\sim 2\theta = 36^\circ$ for $\text{Li}_{1.25}\text{Mn}_2\text{O}_4$, $\text{Li}_{1.50}\text{Mn}_2\text{O}_4$ and $\text{Li}_{2.00}\text{Mn}_2\text{O}_4$ concentrations accompanied by a shift to the right. More splits and shifts are observed at $\sim 2\theta = 44^\circ$ and are associated with spinel Mn_3O_4 , LiMn_2O_4 and layered LiMn_2O_3 for $\text{Li}_{1.25}\text{Mn}_2\text{O}_4$, $\text{Li}_{1.50}\text{Mn}_2\text{O}_4$ and $\text{Li}_{2.00}\text{Mn}_2\text{O}_4$ components. The shift is observed to be towards the right and favour the spinel LiMn_2O_4 content. Furthermore, at $\sim 2\theta = 64^\circ$ peak splits and shifts for $\text{Li}_{1.25}\text{Mn}_2\text{O}_4$, $\text{Li}_{1.50}\text{Mn}_2\text{O}_4$ and $\text{Li}_{2.00}\text{Mn}_2\text{O}_4$ concentrations are still observed. These peaks are associated with spinel LiMn_2O_4 , Mn_3O_4 and layered LiMn_2O_3 . The shift is towards the right and favours the layered Li_2MnO_3 component. Nanoporous 67 Å at $\text{Li}_{1.75}\text{Mn}_2\text{O}_4$ concentration depicts broad, much intense and nosier peaks without any splitting but with slightly shifting. The shifts and splits observed on the XRD plots for the lithiated structures could be caused by the mixing of Li and Mn layers, phase transitions or defects generated in the Li-Mn-O systems during

lithium intercalation [108, 109, 110]. In addition, the $\text{Li}_{1.50}\text{Mn}_2\text{O}_4$ and $\text{Li}_{2.00}\text{Mn}_2\text{O}_4$ concentrations have a very similar form of peaks.

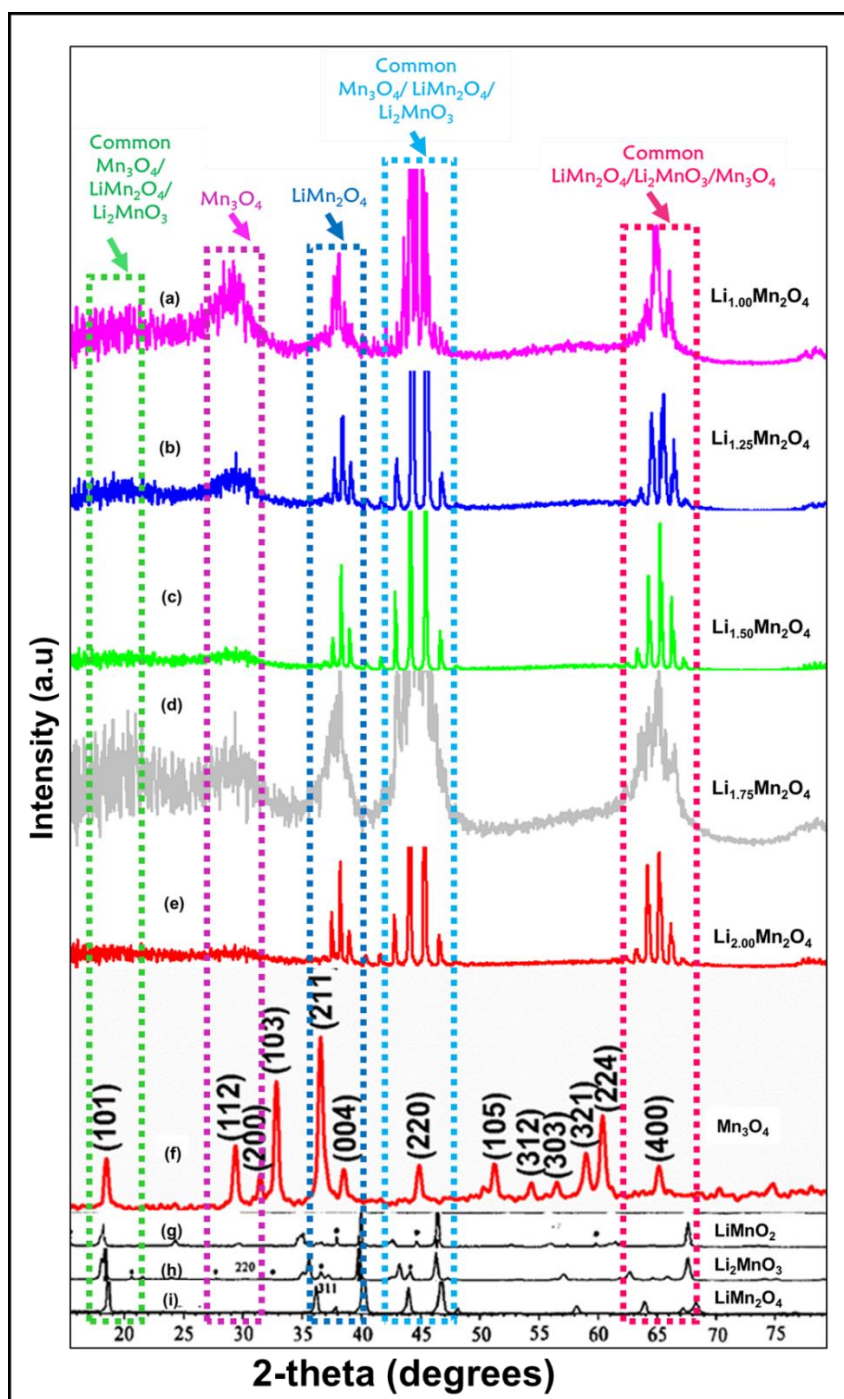


Figure 3. 27: The XRDs for simulated (a) $\text{Li}_{1.00}\text{Mn}_2\text{O}_4$, (b) $\text{Li}_{1.25}\text{Mn}_2\text{O}_4$, (c) $\text{Li}_{1.50}\text{Mn}_2\text{O}_4$, (d) $\text{Li}_{1.75}\text{Mn}_2\text{O}_4$ and (e) $\text{Li}_{2.00}\text{Mn}_2\text{O}_4$ nanoporous 75 Å structures; compared with the experimental X-ray diffraction patterns for (f) spinel Mn_3O_4 [106], (g) layered LiMnO_2 [107], (h) layered Li_2MnO_3 [107] and (i) spinel LiMn_2O_4 [107].

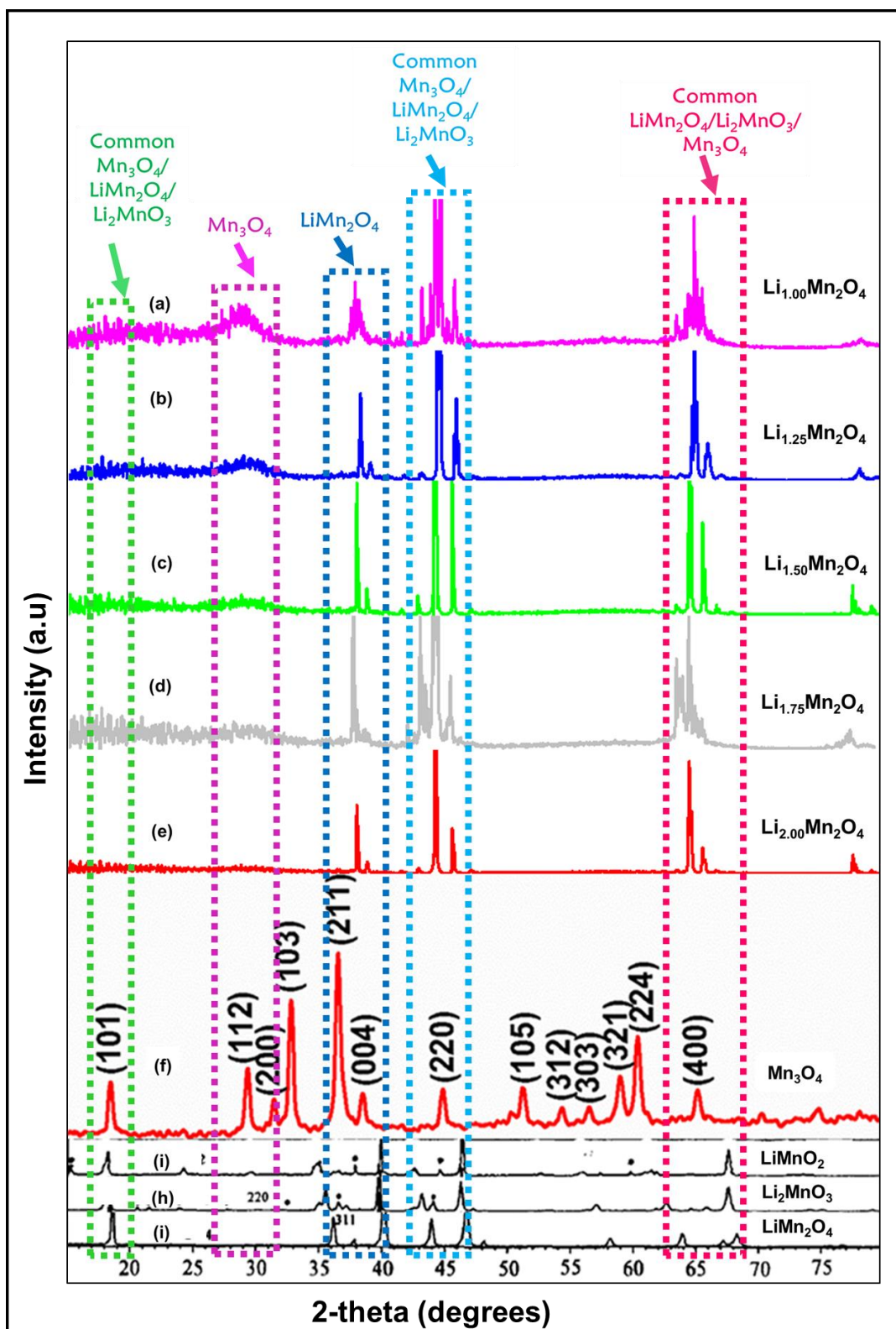


Figure 3. 28: The XRDs for simulated (a) $\text{Li}_{1.00}\text{Mn}_2\text{O}_4$, (b) $\text{Li}_{1.25}\text{Mn}_2\text{O}_4$, (c) $\text{Li}_{1.50}\text{Mn}_2\text{O}_4$, (d) $\text{Li}_{1.75}\text{Mn}_2\text{O}_4$ and (e) $\text{Li}_{2.00}\text{Mn}_2\text{O}_4$ nanoporous 69 Å structures; compared with the experimental for (f) spinel Mn_3O_4 [106], (g) layered LiMnO_2 [107], (h) layered Li_2MnO_3 [107] and (i) spinel LiMn_2O_4 [107].

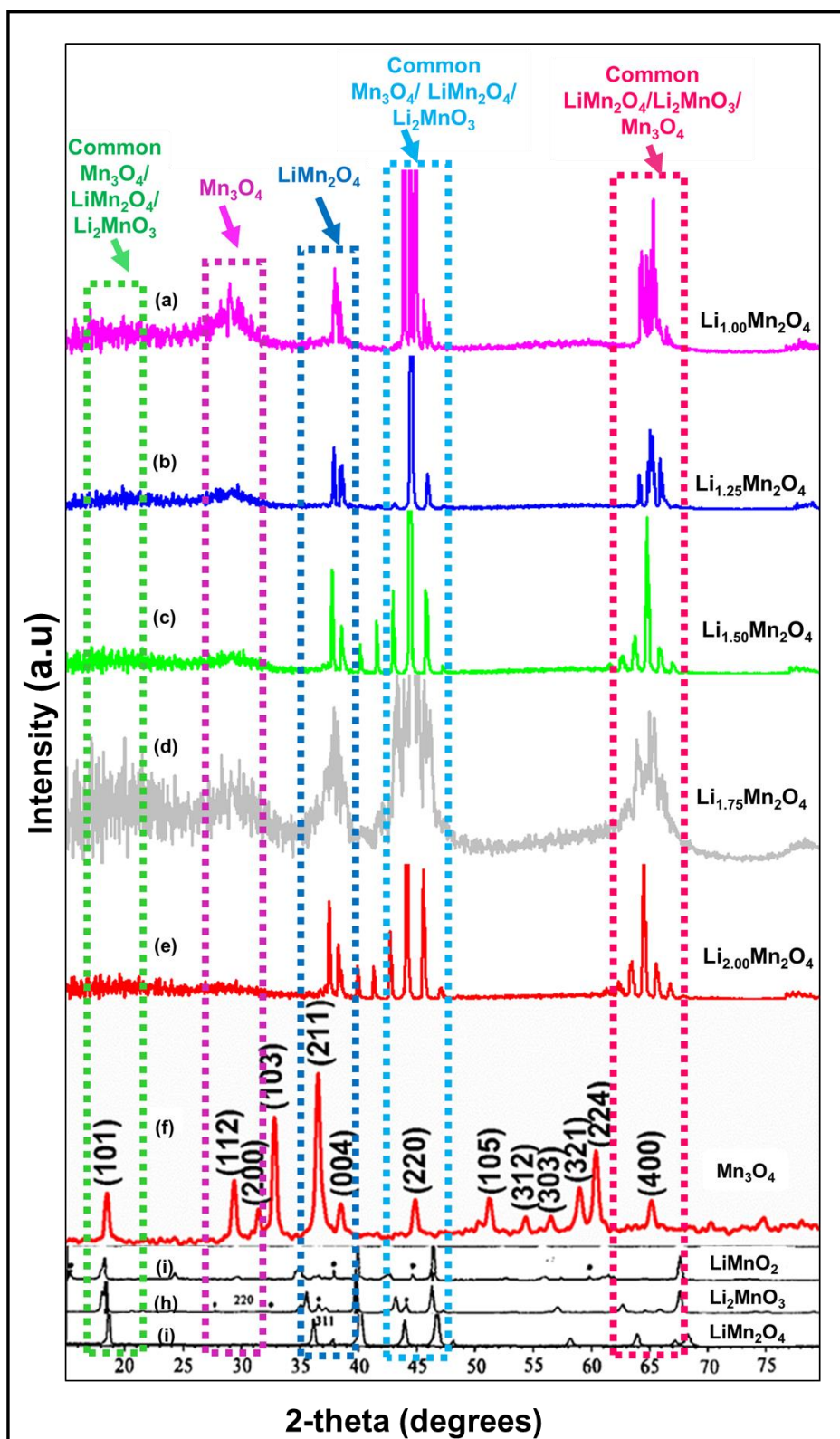


Figure 3. 29: The XRDs for simulated (a) $\text{Li}_{1.00}\text{Mn}_2\text{O}_4$, (b) $\text{Li}_{1.25}\text{Mn}_2\text{O}_4$, (c) $\text{Li}_{1.50}\text{Mn}_2\text{O}_4$, (d) $\text{Li}_{1.75}\text{Mn}_2\text{O}_4$ and (e) $\text{Li}_{2.00}\text{Mn}_2\text{O}_4$ Li-Mn-O nanoporous 67 Å structures, compared with the experimental XRDs for (f) spinel Mn_3O_4 [106], (g) layered LiMnO_2 [107], (h) layered Li_2MnO_3 [107] and (i) spinel LiMn_2O_4 [107].

3.3.2 XRDs for the bulk structure

The X-ray diffraction patterns for the simulated Li-Mn-O lithiated bulk structures (a-e) with different lithium concentration $\text{Li}_{1+x}\text{Mn}_2\text{O}_4$ where $0 \leq x \leq 1$, compared to the experimental results of (f) spinel Mn_3O_4 [106], (g) layered Li_2MnO_3 co-existing with (h) layered LiMnO_2 [107] and (i) spinel LiMn_2O_4 [107] are illustrated in Figure 3.30. The shoulder peaks at $2\theta \sim 18 - 23^\circ$ associated with Li_2MnO_3 , LiMn_2O_4 and Mn_3O_4 decrease gradually with increasing lithium content from $\text{Li}_{1.00}\text{Mn}_2\text{O}_4$ to $\text{Li}_{1.50}\text{Mn}_2\text{O}_4$ and re-emerge at $\text{Li}_{1.75}\text{Mn}_2\text{O}_4$. The structure at $\text{Li}_{1.75}\text{Mn}_2\text{O}_4$ concentration is the one that has recrystallised into a polycrystalline form, having grain boundaries. Increasing lithium concentration to $\text{Li}_{2.00}\text{Mn}_2\text{O}_4$, the peaks in the range $\sim 2\theta = 18 - 23^\circ$ almost disappear. A similar trend is observed for $\sim 2\theta = 26 - 32^\circ$, where the peak related to the spinel Mn_3O_4 becomes invisible. The peak at $\sim 2\theta = 36^\circ$ for $\text{Li}_{1.25}\text{Mn}_2\text{O}_4$ illustrates a split, accompanied by a shift to the right favouring the spinel LiMn_2O_4 component. Further, splits and shifts are observed for peaks at $\sim 2\theta = 44^\circ$ for $\text{Li}_{1.50}\text{Mn}_2\text{O}_4$ and $\text{Li}_{2.00}\text{Mn}_2\text{O}_4$ concentrations. Moreover, at $\sim 2\theta = 64^\circ$ peak splits and shifts are still observed for $\text{Li}_{1.25}\text{Mn}_2\text{O}_4$, $\text{Li}_{1.50}\text{Mn}_2\text{O}_4$ and $\text{Li}_{2.00}\text{Mn}_2\text{O}_4$ structures. The bulk $\text{Li}_{1.75}\text{Mn}_2\text{O}_4$ depicts broad peaks without any splitting but with shifts. The peak shift and split phenomenon could be attributed to the mixing of Li and Mn layers, phase transitions or defects generated in the Li-Mn-O systems during cycling [108, 109, 110].

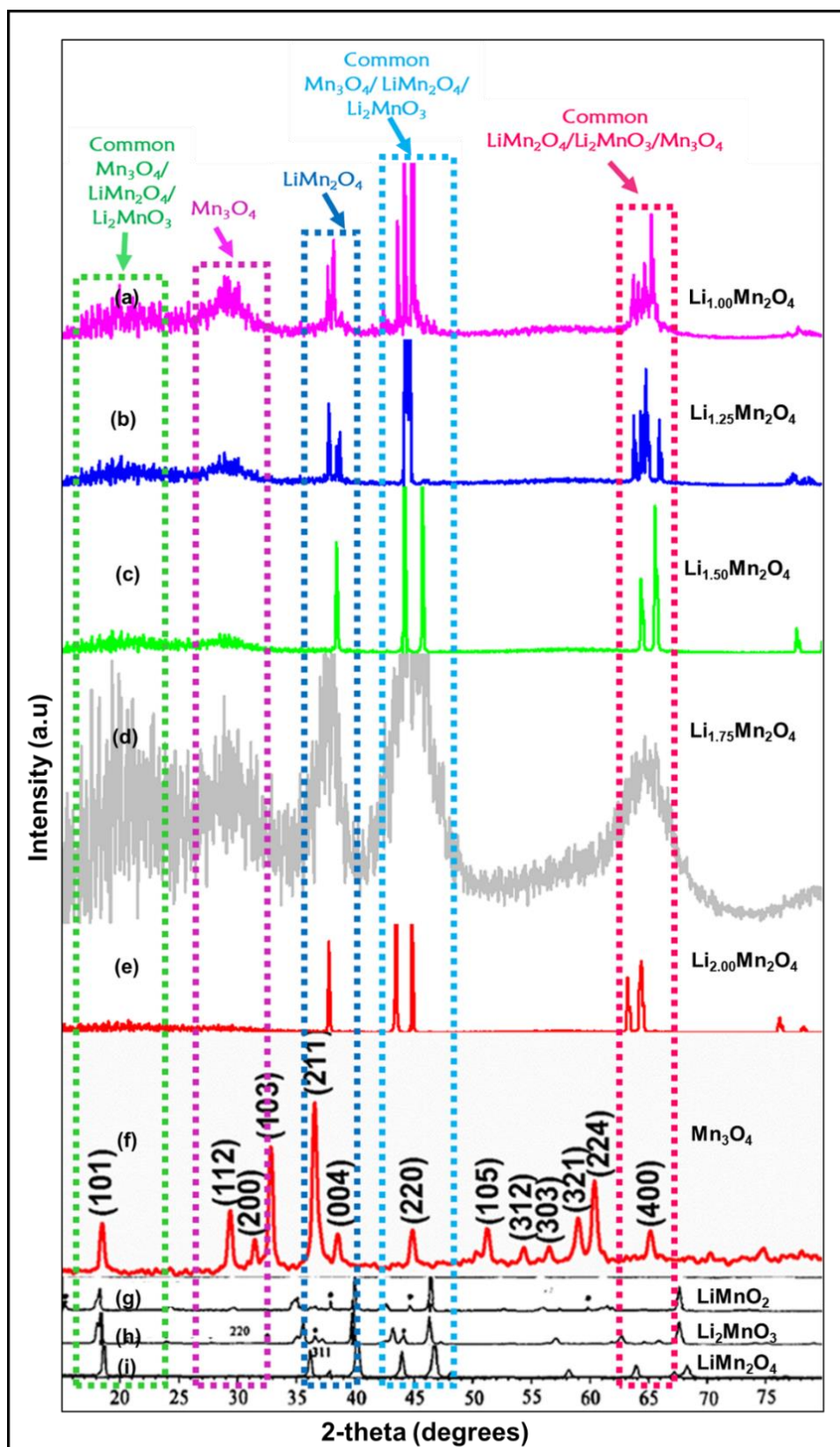


Figure 3. 30: The XRDs for simulated (a) $\text{Li}_{1.00}\text{Mn}_2\text{O}_4$ (b) $\text{Li}_{1.25}\text{Mn}_2\text{O}_4$, (c) $\text{Li}_{1.50}\text{Mn}_2\text{O}_4$, (d) $\text{Li}_{1.75}\text{Mn}_2\text{O}_4$ and (e) $\text{Li}_{2.00}\text{Mn}_2\text{O}_4$ bulk structures, compared with the experimental XRDs for (f) spinel Mn_3O_4 [106], (g) layered LiMnO_2 [107], (h) layered Li_2MnO_3 [107] and (i) spinel LiMn_2O_4 [107] structures.

3.4 Discussion

This chapter intended to investigate the host capabilities of the Li-Mn-O nanoporous and bulk structures during lithium intercalation under NVT ensemble, by interrogating their electrochemical properties. Lithiation of the nanoporous and bulk materials at different lithium concentrations $\text{Li}_{1+x}\text{Mn}_2\text{O}_4$, where $0 \leq x \leq 1$ was carried out using molecular dynamics simulation methods. The nanoporous and bulk nanoarchitectures have shown the effect of lithiation when the lithium concentration is increased on the structures, microstructures and X-ray diffraction patterns. The structures crystallised into single and multiple crystals with distortions especially at $\text{Li}_{1.75}\text{Mn}_2\text{O}_4$ concentration for all the structures; and also for concentrations at $\text{Li}_{1.00}\text{Mn}_2\text{O}_4$ and $\text{Li}_{2.00}\text{Mn}_2\text{O}_4$ for nanoporous 75 Å.

The pores for nanoporous materials increase in size from $\text{Li}_{1.00}\text{Mn}_2\text{O}_4$ to $\text{Li}_{1.25}\text{Mn}_2\text{O}_4$ and then reduce. However, at $\text{Li}_{1.75}\text{Mn}_2\text{O}_4$ concentration, the pore for nanoporous 75 Å reduce in size, while that of nanoporous 69 Å increase in size and that for nanoporous 67 Å close up. Upon full lithiation, at $\text{Li}_{2.00}\text{Mn}_2\text{O}_4$ concentration, all the structures almost regain their original size. Furthermore, at full lithiation lithium atoms float at the cavity of the nanoporous structures. No cavities are observed for the bulk structures.

The formation of spinel Mn_3O_4 and the retainment of the Mn^{2+} tetrahedral tunnels are observed on the structures. An increase in lithium concentration encourages the reduction of the Mn_3O_4 content in nanoporous and bulk structures. Moreover, the structural defects become minimal with increasing lithium concentration. The common defects captured on the microstructures are vacancies, grain boundaries, Mn interstitials, Frenkel and distortions. Some concentrations, especially at $\text{Li}_{1.75}\text{Mn}_2\text{O}_4$ for nanoporous 75 Å, 67 Å and the bulk favours the spinel LiMn_2O_4 component.

The X-ray diffraction pattern plots for simulated bulk and nanoporous Li-Mn-O structures are comparable with the experimental results. The simulated structures at different lithium concentrations depict shoulder peaks at $\sim 2\theta = 18 - 23^\circ$. This peak shows the same behaviour for all the simulated plots, where it gradually decreases from $\text{Li}_{1.00}\text{Mn}_2\text{O}_4$ to $\text{Li}_{1.50}\text{Mn}_2\text{O}_4$ and re-emerge at $\text{Li}_{1.75}\text{Mn}_2\text{O}_4$, then almost disappear again upon full lithiation. A similar trend is observed for the peak associated with Mn_3O_4 at $\sim 2\theta = 26 - 32^\circ$. Shifts and split peaks are observed at $\sim 2\theta = 36^\circ$, $\sim 2\theta = 44^\circ$ and $\sim 2\theta = 64^\circ$. At $\text{Li}_{1.75}\text{Mn}_2\text{O}_4$ concentration, peaks shift without splitting for all the structures. Furthermore, the peaks become broader for all structures except for nanoporous 69 Å. Nanoporous 75 and 67 Å show similar trends of peaks peak formation. The peak shifts observed are towards the right. The shifts and splits could be attributed to the mixing of Li and Mn layers, phase transitions or defects generated in the Li-Mn-O systems as the lithium content is increased or during the discharge process, as reported experimentally for NMCs [108, 109, 110].

CHAPTER 4

Structural changes on the lithiated nanoporous and bulk electrode materials

4.1 Introduction

The processes of lithiation and delithiation in the battery cathode can lead to severe mechanical fatigue because of the repeated expansion and compression of the host lattice during electrochemical cycling [44]. During cycling there is a volume change of about 7.7% related to volume expansion and contraction, which leads to the mismatch between Li⁺ rich and Li⁺ deficient domains in the electrode, causing mechanical degradation and fracture [44]. In addition, this results in a phase transition from cubic to a tetragonal phase accompanied by a 6.5% increase in the unit cell volume, which occurs due to surplus lithium intercalated into the spinel to reach a maximum Li₂Mn₂O₄ [13].

Nanoporous materials are widely utilised in lithium ion batteries because they offer good access between the electrolyte and electrode, through their short path length for lithium ion diffusion [53]. Furthermore, these materials are flexible, they can expand and contract during cycling and allow atoms to diffuse through them with ease. Moreover, they have high volumetric energy density [52, 53]. This suggests that they can provide a large surface area and pore volume for better interaction with the electrolyte and ionic diffusion, leading to enhanced electrochemical performance and mechanical stability [52, 111, 112]. The bulk structures comprise of particles that can be handled as individual items of material but are composed of nanocrystals and the dimensions of the material are in all directions [113]. As such their structural changes are of significance to comprehend so that clear conclusions on a suitable cathode material for lithium ion batteries can be made.

In this chapter, the three nanoporous materials and the bulk introduced in chapter 3 with the same number of atoms and lithium concentrations, $\text{Li}_{1+x}\text{Mn}_2\text{O}_4$ where $0 \leq x \leq 1$ are investigated for their structural changes during lithiation. The structures have been recrystallised under the NST ensemble, where N = constant number of atoms, S = constant stress and T = constant temperature. In the NST ensemble volume is not fixed, therefore it is allowed to vary flexibly with lithiation, and this allows effective investigation of volume changes in materials. The structural changes and pore size effect of lithium ion batteries materials need a thorough investigation to understand the structural evolution that comes with lithiation to improve battery performance. Therefore, this chapter focuses on investigating the potential changes that occur on these materials when the volume is allowed to vary during recrystallisation.

4.2 Method

Molecular dynamics methods employing the DL_POLY code was used to perform all the calculations to monitor the structural changes of the Li-Mn-O nanoporous (75, 69 and 67 Å) and bulk materials at different lithium concentrations, $\text{Li}_{1+x}\text{Mn}_2\text{O}_4$ ($0 \leq x \leq 1$). These are the amorphous structures generated under the NPT ensemble in chapter 3 which in this chapter have been recrystallised using the NST ensemble, where N = constant number of particles, S = constant stress and T = constant temperature to allow for volume changes in materials. Molecular dynamics simulations at 1700 K temperature for 150 ps and the pressure of 0 GPa were used to recrystallise the structures. The structures were then equilibrated to 0 K for 300 ps during the cooling process. The equilibrated structures were then exported to the Material Studio interface to visualise the pore changes, microstructural changes and to calculate volumetric changes using the Connolly surface tool [114]. Connolly surfaces encapsulate the whole surface of a structure and give the

volume of the entire system. Furthermore, the radial distribution functions and X-ray diffraction patterns were also used to characterise the structural components. The main reason to recrystallise with NST is to fully understand the structural changes that occur during the discharging process, especially because the battery undergo contractions and expansions with lithiation. Therefore, it is of great interest to discern these phenomenal changes that take place within the materials during cycling.

4.3 Pore size effect and volume change on the nanoporous (75, 69, 67 Å) and bulk structures

The simulated recrystallised nanoporous structures with cell size 75, 69, 67 Å and the bulk (63 Å) with varying lithium concentrations $\text{Li}_{1+x}\text{Mn}_2\text{O}_4$, $0 \leq x \leq 1$ are illustrated in figure 4.1. The structures have evolved into single and multiple crystals. The multi grained crystals are denoted by white dotted lines on the structures.

The nanoporous 75 Å structure at $\text{Li}_{1.00}\text{Mn}_2\text{O}_4$ depict a larger pore with an irregular shape. Increasing the lithium content to $\text{Li}_{1.25}\text{Mn}_2\text{O}_4$ results in the pore size reducing and becoming spherical. The pore size continues to reduce as more lithium is intercalated to $\text{Li}_{1.50}\text{Mn}_2\text{O}_4$ and $\text{Li}_{1.75}\text{Mn}_2\text{O}_4$ concentrations. The latter concentrations give a structure that has recrystallised into multiple grains. Upon full lithiation, the structure shows a similar pore size to that of $\text{Li}_{1.00}\text{Mn}_2\text{O}_4$, however, with a different shape and some excess lithium atoms at the pore.

In the same figure of 4.1, the impact of lithiation on nanoporous 69 Å structures is illustrated. The structure at $\text{Li}_{1.00}\text{Mn}_2\text{O}_4$ concentration depicts a pore that increases in size with lithium intercalation to $\text{Li}_{1.25}\text{Mn}_2\text{O}_4$ concentration. The pore size continues to reduce at $\text{Li}_{1.50}\text{Mn}_2\text{O}_4$ concentration, then eventually at $\text{Li}_{1.75}\text{Mn}_2\text{O}_4$ it completely closes up. This

is in contradiction to nanoporous 75 Å at the same concentration where the pore does not close up, rather increase in size from $\text{Li}_{1.50}\text{Mn}_2\text{O}_4$ to $\text{Li}_{1.75}\text{Mn}_2\text{O}_4$. Furthermore, at $\text{Li}_{1.75}\text{Mn}_2\text{O}_4$ concentration, no grain boundaries are observed. The full lithiated structure at $\text{Li}_{2.00}\text{Mn}_2\text{O}_4$ concentration shows a similar pore size to that at $\text{Li}_{1.00}\text{Mn}_2\text{O}_4$, however, with an irregular oval shape.

The nanoporous 67 Å structure at $\text{Li}_{1.00}\text{Mn}_2\text{O}_4$ concentration shows a small pore size compared to nanoporous 75 and 69 Å structures. Increment of lithium concentration to $\text{Li}_{1.25}\text{Mn}_2\text{O}_4$ increases the pore size. Further lithium increment to $\text{Li}_{1.50}\text{Mn}_2\text{O}_4$ result in a pore that slightly closes up, then completely close up at $\text{Li}_{1.75}\text{Mn}_2\text{O}_4$ concentration. Grain boundaries are observed at $\text{Li}_{1.75}\text{Mn}_2\text{O}_4$ concentration denoted by white dotted lines. Full lithiation of the structure to $\text{Li}_{2.00}\text{Mn}_2\text{O}_4$ results in similar pore size to that of the pristine concentration at $\text{Li}_{1.00}\text{Mn}_2\text{O}_4$. Lastly, the bulk structures show structures that have evolved into single crystals with increasing lithium concentration. The bulk structures do not have any pores in them.

Figure 4.2 depicts the total radial distribution function (RDFs) graphs for the lithiated recrystallised Li-Mn-O nanoporous and bulk composite materials of different cell dimensions and lithium concentrations. The total RDFs for the recrystallised structures depict sharp peaks, suggesting that the structures are well defined or have atoms in an ordered array or arrangement. As observed on the nanoporous and structures recrystallised in NVT, the $\text{Li}_{2.00}\text{Mn}_2\text{O}_4$ concentration has a lower $g(r)$ compared to the other four concentrations. Furthermore, the recrystallised RDFs peaks reduce in height ($g(r)$) with increasing radial distance (r).

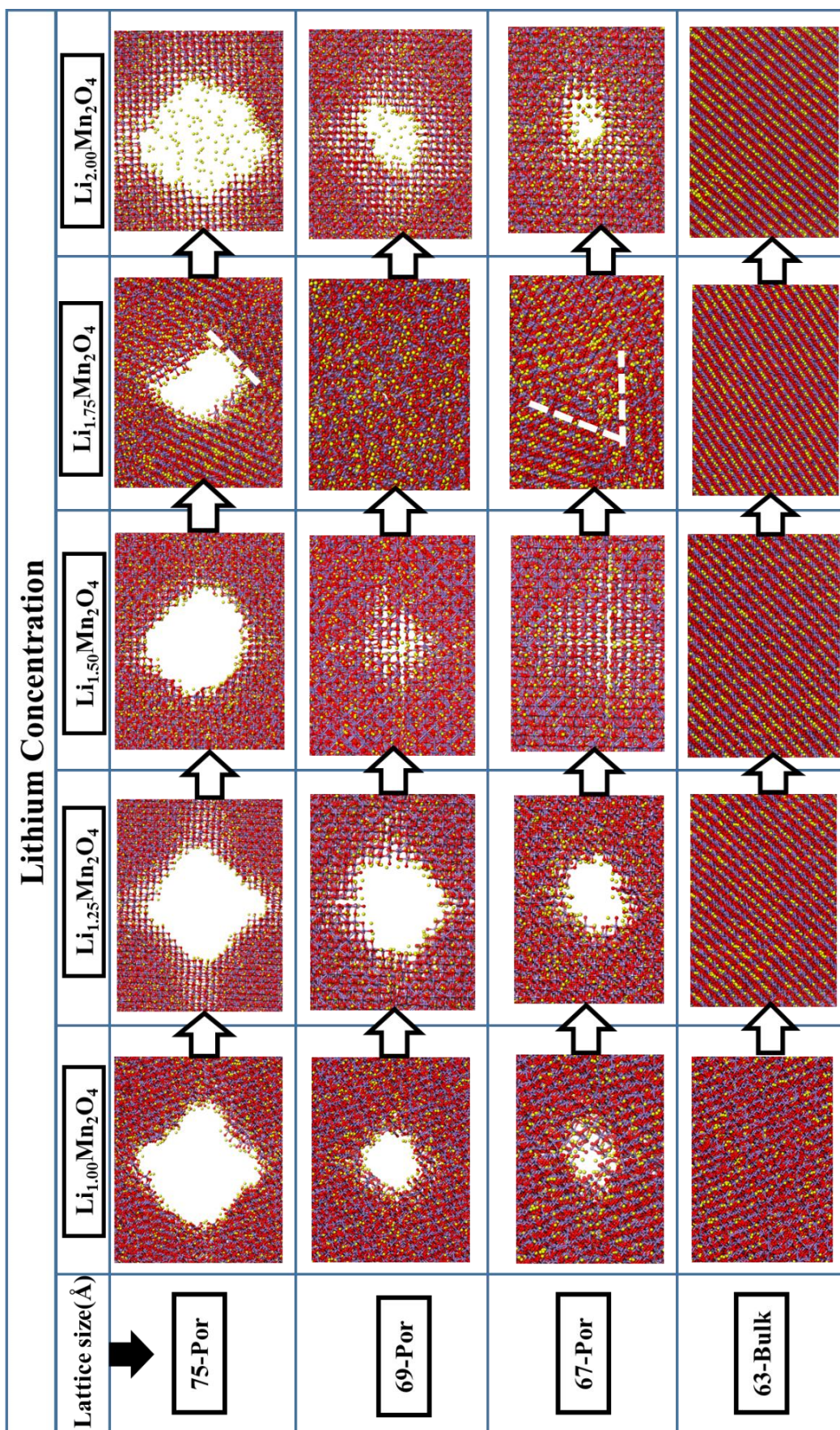


Figure 4. 1: The structural changes on the lithiated NST nanoporous (75, 69 and 67 Å) and bulk materials with different lithium concentrations, $\text{Li}_{1+x}\text{Mn}_2\text{O}_4$, $0 \leq x \leq 1$, showing pore size effect as the lithium content is increased.

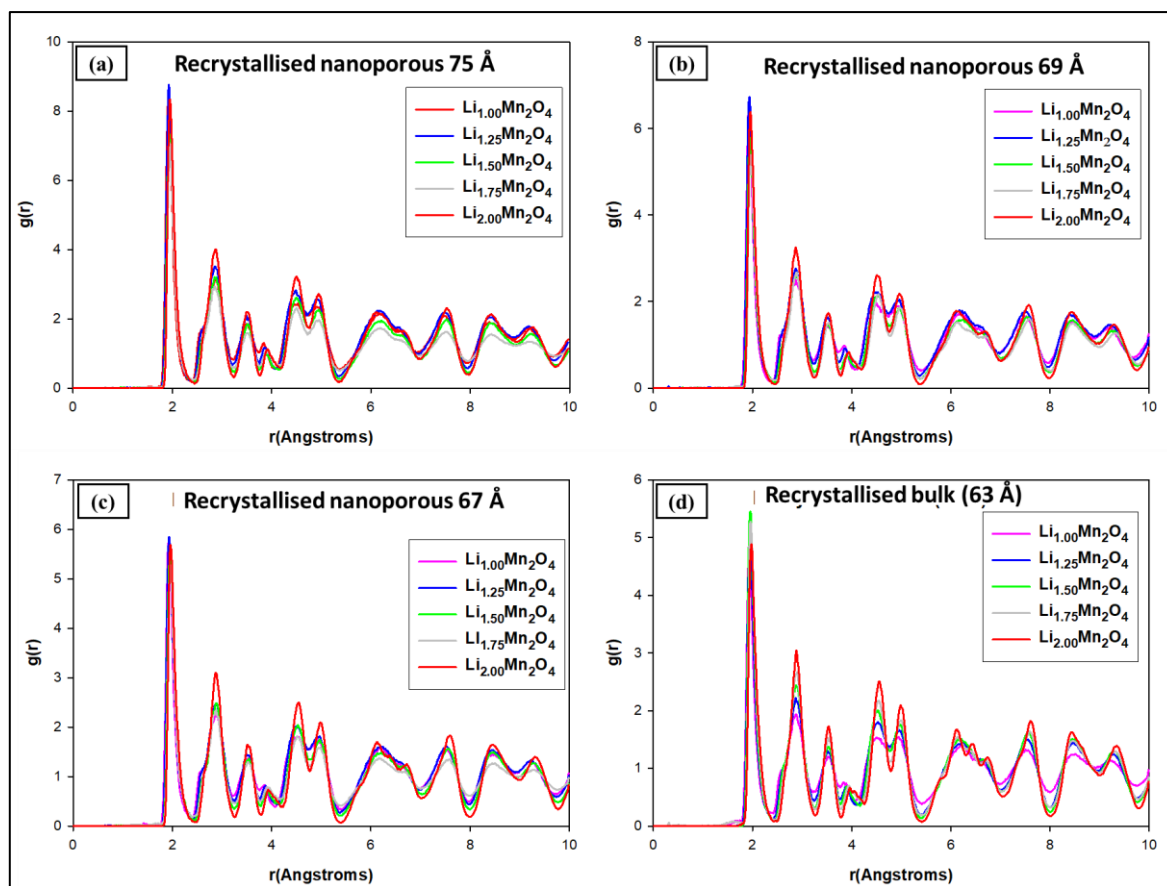


Figure 4. 2: The total RDFs for the recrystallised lithiated Li-Mn-O nanoporous structures with different lithium concentrations; where (a) is the nanoporous 75 Å, (b) nanoporous 69 Å, (c) the nanoporous 67 Å and (d) the bulk.

Connolly structures determine the overall volume of a system and how it has expanded or contracted when it is allowed to interact with other materials either by lithiation, coating, doping and etc. The connolly surfaces of the NST Li-Mn-O structures are illustrated in figures 4.3 to 4.6 for nanoporous 75 Å, nanoporous 69 Å, nanoporous 67 Å and the bulk at 63 Å, respectively. These structures have been viewed in the “in-cell and original” view under the Material studio interface. The structures viewed in “in cell” shows the outer surface of the channel vividly in grey and those viewed in “ original” shows the inner surface of the channel in blue. For simplicity; the blue-greyish section in the structures represents the voids/channels in the nanoporous materials, which are occupied during lithiation.

Figure 4.3 conforms with figure 4.1 of nanoporous 75 Å regarding the pore size changes, although different pore shapes are observed from $\text{Li}_{1.00}\text{Mn}_2\text{O}_4$ to $\text{Li}_{2.00}\text{Mn}_2\text{O}_4$ concentrations. Furthermore, a structure that has crystallised into multiple grains is also observed at $\text{Li}_{1.75}\text{Mn}_2\text{O}_4$. Upon full lithiation at $\text{Li}_{2.00}\text{Mn}_2\text{O}_4$ concentration, excess lithium atoms are floating within the cavity/channel and a pore size similar to the $\text{Li}_{1.00}\text{Mn}_2\text{O}_4$ is observed. Further observations on the structures, shows that the shaded blue areas reduce in size from $\text{Li}_{1.00}\text{Mn}_2\text{O}_4$ to $\text{Li}_{1.75}\text{Mn}_2\text{O}_4$, then slightly increase at $\text{Li}_{2.00}\text{Mn}_2\text{O}_4$, taking the pattern of the pore size increment and reduction explained in figure 4.1.

Observations made in figure 4.4 for nanoporous 69 Å regarding the pore size is also in accord with those in figure 4.1. When the lithium concentration is increased from $\text{Li}_{1.00}\text{Mn}_2\text{O}_4$ to $\text{Li}_{1.25}\text{Mn}_2\text{O}_4$ the pore size increases instead of reducing. Further lithiation to $\text{Li}_{1.50}\text{Mn}_2\text{O}_4$ results in a pore that reduces in size. Further increment in lithium concentration to $\text{Li}_{1.75}\text{Mn}_2\text{O}_4$, depicts a pore that closes up and a structure that has evolved into a single crystal. The full lithiated structure almost regains its original pore size. The blue shaded areas reduce with increasing concentration to $\text{Li}_{1.75}\text{Mn}_2\text{O}_4$, then increase at $\text{Li}_{2.00}\text{Mn}_2\text{O}_4$, also taking the pore size trend with lithium increment.

Nanoporous 67 Å conolly surfaces are presented in figure 4.5 and are almost in agreement with structural snapshots in figure 4.1. Lithiation from $\text{Li}_{1.00}\text{Mn}_2\text{O}_4$ to $\text{Li}_{1.25}\text{Mn}_2\text{O}_4$ resulted in the enlargement of the pore size. Increasing the lithium concentration to $\text{Li}_{1.50}\text{Mn}_2\text{O}_4$ causes the pore to partially close up. Meanwhile, increasing the lithium content to $\text{Li}_{1.75}\text{Mn}_2\text{O}_4$ resulted in the pore almost closing up completely. The latter concentration evolved into a multi grained structure. Lithiation to $\text{Li}_{2.00}\text{Mn}_2\text{O}_4$ resulted in a structure that has almost regained its original pore size, however without any grain boundaries. Further observations on the structure show the blue area increasing from $\text{Li}_{1.00}\text{Mn}_2\text{O}_4$ to $\text{Li}_{1.25}\text{Mn}_2\text{O}_4$ concentration, then reduce at $\text{Li}_{1.50}\text{Mn}_2\text{O}_4$ and $\text{Li}_{1.75}\text{Mn}_2\text{O}_4$.

At $\text{Li}_{2.00}\text{Mn}_2\text{O}_4$ concentration, the blue area increases again. This also follows the pore size change trend with increasing lithium content.

Figure 4.6 depicts the Connolly surface structures for the bulk. The $\text{Li}_{1.00}\text{Mn}_2\text{O}_4$ concentration depicts minor blue-greyish regions in the structures, however, as the lithium concentration increases to $\text{Li}_{1.25}\text{Mn}_2\text{O}_4$ the blue-greyish regions in the structure increase implying cell expansion. Further increase in lithium concentration results in volume expansion, denoted by more visibility of the grey-bluish regions. The expansion is further observed with lithium increment to $\text{Li}_{1.50}\text{Mn}_2\text{O}_4$ and $\text{Li}_{1.75}\text{Mn}_2\text{O}_4$ concentrations. Interestingly, for the NST simulated $\text{Li}_{1.75}\text{Mn}_2\text{O}_4$ structure, no grain boundaries are observed; whereas, in other structures for this concentration there are grain boundaries. Upon full lithiation, the structure almost regains its pristine form ($\text{Li}_{1.00}\text{Mn}_2\text{O}_4$), this can be confirmed by the drop in cell volume and minor blue-greyish regions at $\text{Li}_{2.00}\text{Mn}_2\text{O}_4$ concentration as depicted in figure 4.7. The blue areas are very minimal for $\text{Li}_{1.00}\text{Mn}_2\text{O}_4$, then increase for $\text{Li}_{1.25}\text{Mn}_2\text{O}_4$ and $\text{Li}_{1.50}\text{Mn}_2\text{O}_4$ concentrations. However, increasing the lithium concentration to $\text{Li}_{1.75}\text{Mn}_2\text{O}_4$ and $\text{Li}_{2.00}\text{Mn}_2\text{O}_4$ results in the reduction of the blue areas.

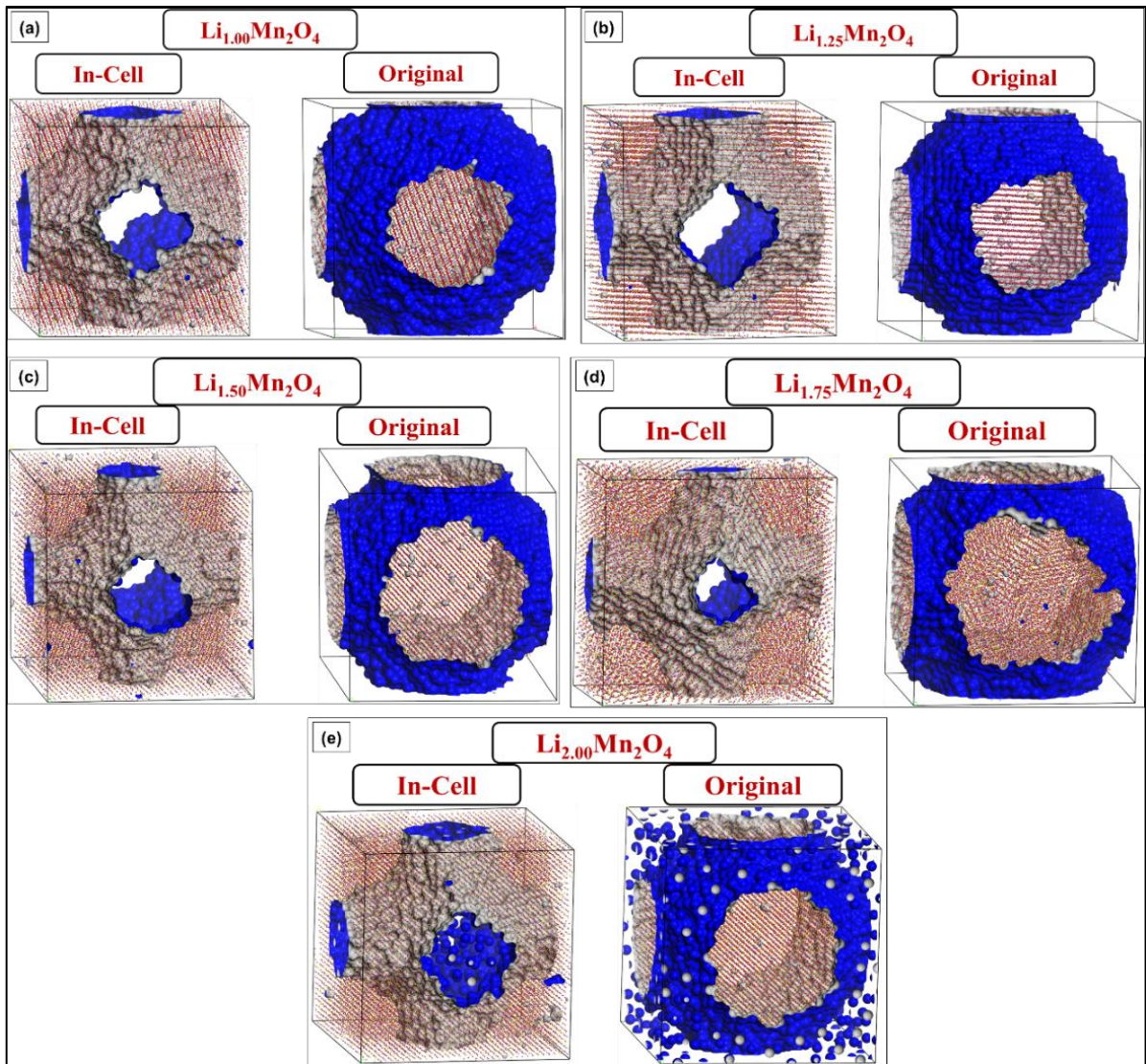


Figure 4. 3: The lithiated conolly surface structures for nanoporous 75 Å illustrating changes in the channels and volume with an increase in lithium concentration viewed in “In-cell and Original” lattices, where (a) is the $Li_{1.00}Mn_2O_4$, (b) $Li_{1.25}Mn_2O_4$, (c) $Li_{1.50}Mn_2O_4$, (d) $Li_{1.75}Mn_2O_4$ and (e) the $Li_{2.00}Mn_2O_4$ concentrations.

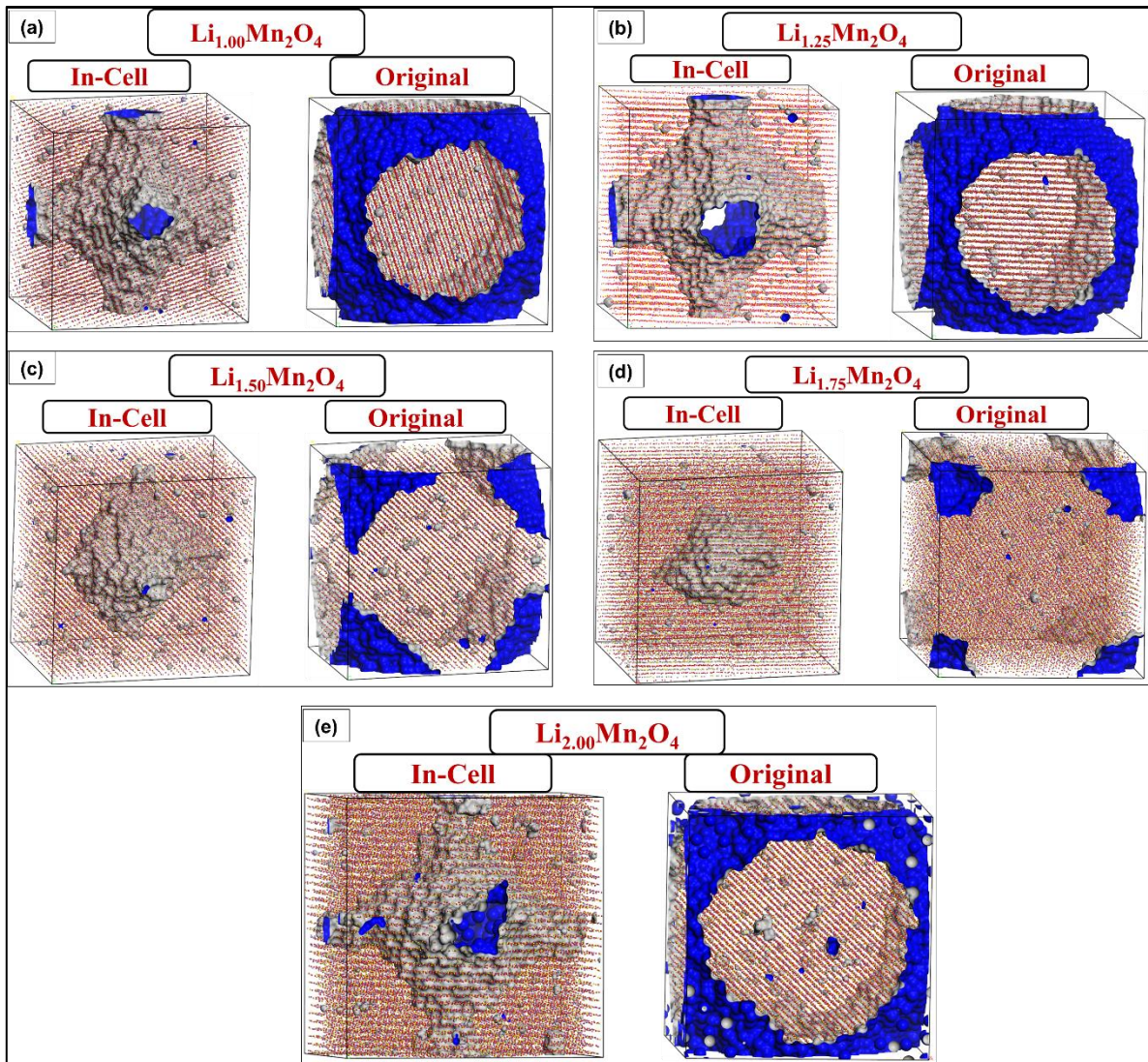


Figure 4. 4: The lithiated Li-Mn-O conolly surface structures for nanoporous 69 Å illustrating the channel and volume occupied viewed in “In-cell and Original” lattices, where (a) is the $Li_{1.00}Mn_2O_4$, (b) $Li_{1.25}Mn_2O_4$, (c) $Li_{1.50}Mn_2O_4$, (d) $Li_{1.75}Mn_2O_4$ and (e) the $Li_{2.00}Mn_2O_4$ concentrations.

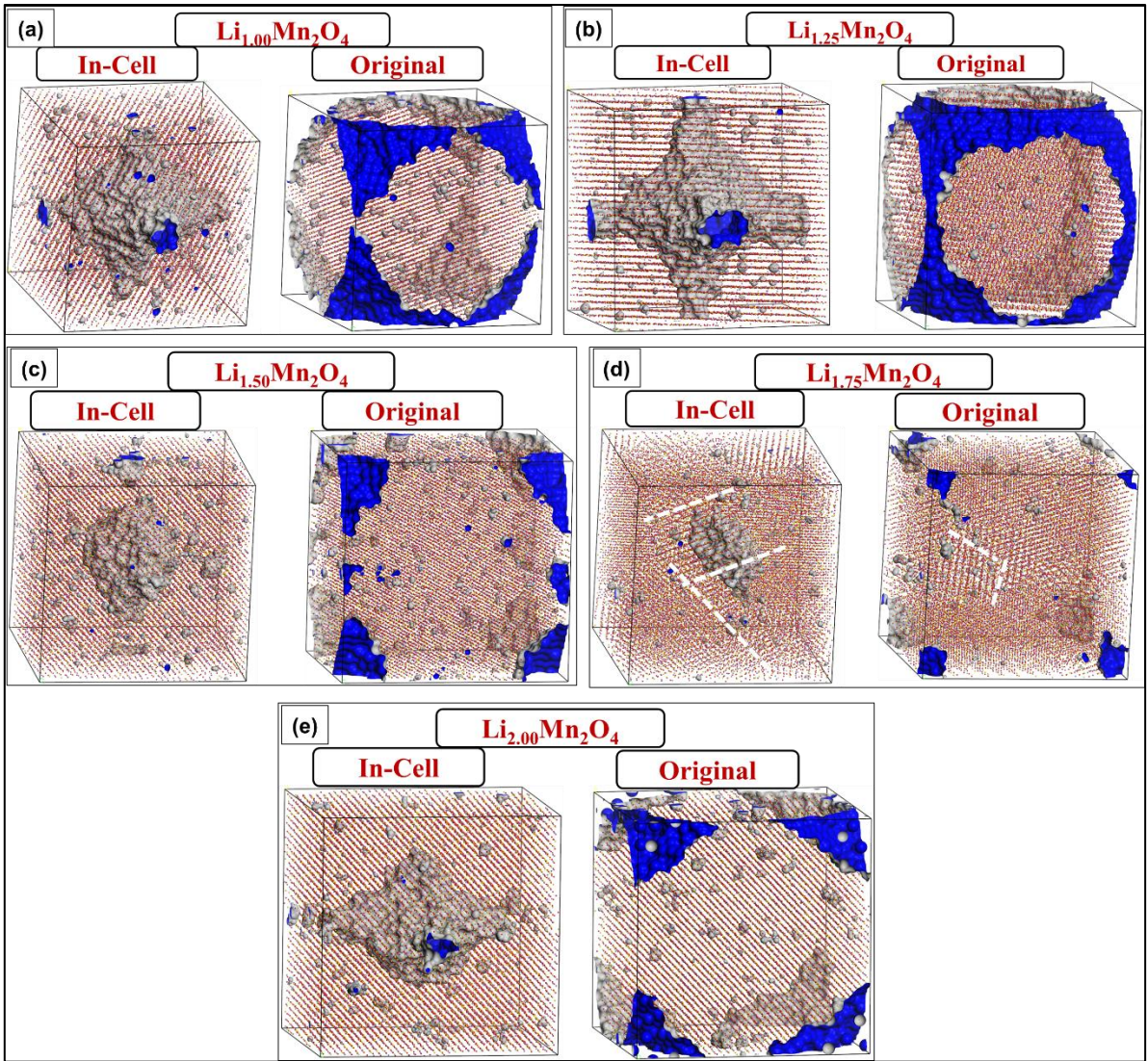


Figure 4. 5: The lithiated connolly surface structures for nanoporous 67 Å illustrating systems with volume and pore changes as lithium concentration is increased in them, viewed in “In-cell and Original” lattices, where (a) is the $Li_{1.00}Mn_2O_4$, (b) $Li_{1.25}Mn_2O_4$, (c) $Li_{1.50}Mn_2O_4$, (d) $Li_{1.75}Mn_2O_4$ and (e) the $Li_{2.00}Mn_2O_4$ concentrations.

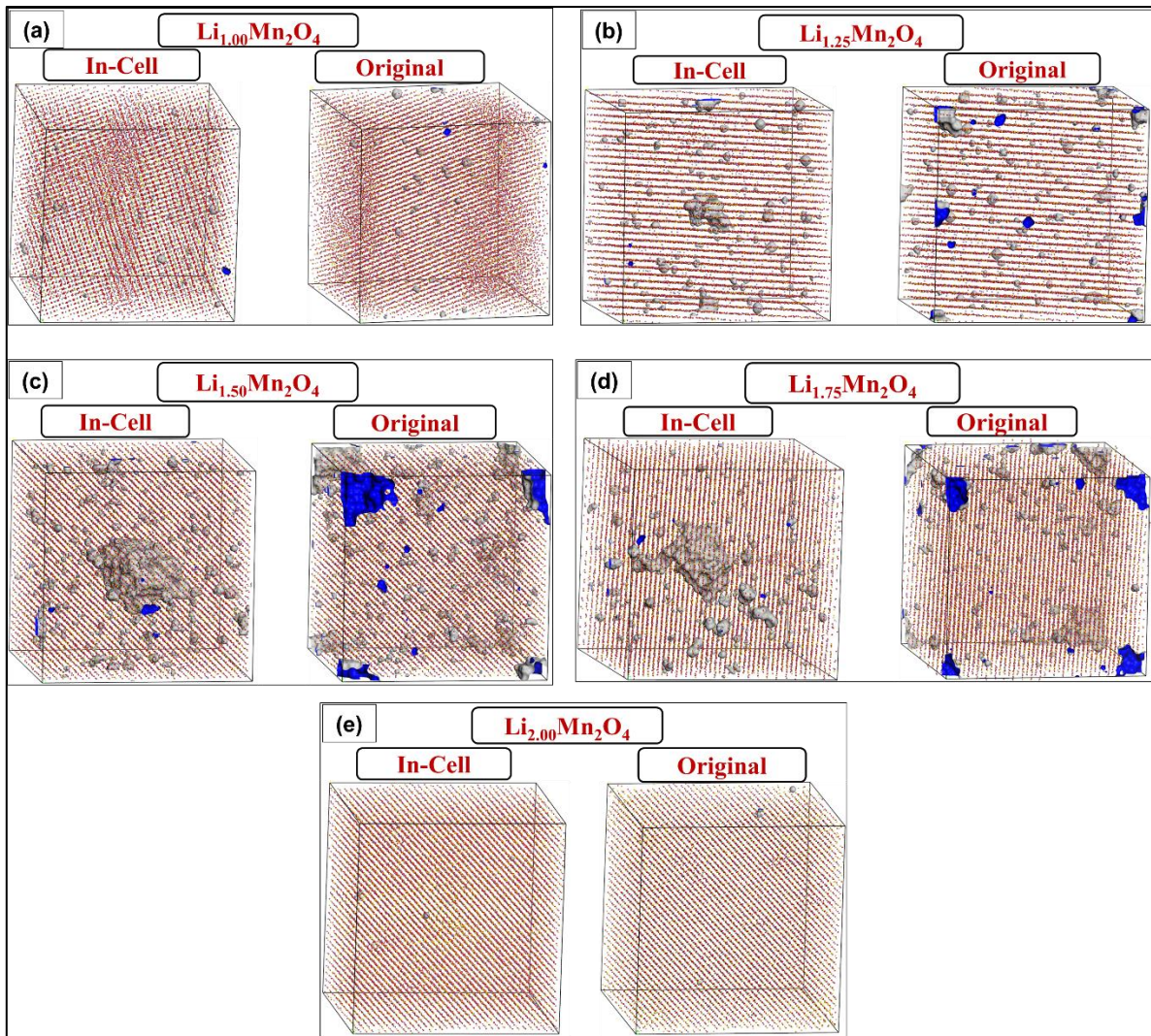


Figure 4. 6: Bulk (63 Å) structures illustrating the Connolly surfaces used to determine volume changes that occur with lithium intercalation viewed in “In-cell and Original” lattices, where (a) is the $\text{Li}_{1.00}\text{Mn}_2\text{O}_4$, (b) $\text{Li}_{1.25}\text{Mn}_2\text{O}_4$, (c) $\text{Li}_{1.50}\text{Mn}_2\text{O}_4$, (d) $\text{Li}_{1.75}\text{Mn}_2\text{O}_4$ and (e) the $\text{Li}_{2.00}\text{Mn}_2\text{O}_4$ concentrations.

The graphical representations for the volume changes of nanoporous and bulk structures are illustrated in figure 4.7. The nanoporous 75 Å depicts a volume expansion plot where the initial cell volume of $26.7 \times 10^4 \text{ \AA}^3$ at $\text{Li}_{1.00}\text{Mn}_2\text{O}_4$ experiences a drop in volume by $0.03 \times 10^4 \text{ \AA}^3$ to $26.67 \times 10^4 \text{ \AA}^3$ at the $\text{Li}_{1.25}\text{Mn}_2\text{O}_4$ concentration. Further lithium intercalation increase the volume to $26.97 \times 10^4 \text{ \AA}^3$ at $\text{Li}_{1.50}\text{Mn}_2\text{O}_4$ from $26.67 \times 10^4 \text{ \AA}^3$ ($\text{Li}_{1.25}\text{Mn}_2\text{O}_4$) by $\sim 0.3 \times 10^4 \text{ \AA}^3$. Increment of lithium concentration from $\text{Li}_{1.50}\text{Mn}_2\text{O}_4$ to $\text{Li}_{1.75}\text{Mn}_2\text{O}_4$ expands the cell volume to $27.54 \times 10^4 \text{ \AA}^3$ with an overall increase of $\sim 0.57 \times 10^4 \text{ \AA}^3$. Upon full lithiation, the cell volume expands by $\sim 0.88 \times 10^4 \text{ \AA}^3$ from $27.54 \times 10^4 \text{ \AA}^3$ to $28.42 \times 10^4 \text{ \AA}^3$ at $\text{Li}_{2.00}\text{Mn}_2\text{O}_4$ concentration.

The nanoporous 69 Å structures depict cell volume increment with an estimation of $\sim 0.03 \times 10^4 \text{ \AA}^3$ volumetric increase from $26.47 \times 10^4 \text{ \AA}^3$ at $\text{Li}_{1.00}\text{Mn}_2\text{O}_4$ to $26.5 \times 10^4 \text{ \AA}^3$ at $\text{Li}_{1.25}\text{Mn}_2\text{O}_4$ concentrations. Furthermore, an increase in cell volume of $\sim 0.54 \times 10^4 \text{ \AA}^3$ is observed from $26.5 \times 10^4 \text{ \AA}^3$ to $27.04 \times 10^4 \text{ \AA}^3$ between $\text{Li}_{1.25}\text{Mn}_2\text{O}_4$ and $\text{Li}_{1.50}\text{Mn}_2\text{O}_4$ concentrations, respectively. Moreover, $\text{Li}_{1.50}\text{Mn}_2\text{O}_4$ and $\text{Li}_{1.75}\text{Mn}_2\text{O}_4$ depict a cell volume increase of $\sim 0.03 \times 10^4 \text{ \AA}^3$ from $27.04 \times 10^4 \text{ \AA}^3$ to $27.07 \times 10^4 \text{ \AA}^3$. Finally, a higher volume increase of $\sim 1.31 \times 10^4 \text{ \AA}^3$ from $27.07 \times 10^4 \text{ \AA}^3$ to $28.38 \times 10^4 \text{ \AA}^3$ is observed from $\text{Li}_{1.75}\text{Mn}_2\text{O}_4$ to $\text{Li}_{2.00}\text{Mn}_2\text{O}_4$ concentrations.

On the other hand, nanoporous 67 Å, follows a similar trend of volume expansion to that of nanoporous 75 Å when lithium concentration is increased. A volume increase of $\sim 0.03 \times 10^4 \text{ \AA}^3$ is observed from $26.4 \times 10^4 \text{ \AA}^3$ to $26.43 \times 10^4 \text{ \AA}^3$ at $\text{Li}_{1.00}\text{Mn}_2\text{O}_4$ and $\text{Li}_{1.25}\text{Mn}_2\text{O}_4$ concentrations, followed by a volumetric increase of $\sim 0.72 \times 10^4 \text{ \AA}^3$ from $26.43 \times 10^4 \text{ \AA}^3$ to $27.15 \times 10^4 \text{ \AA}^3$ at $\text{Li}_{1.25}\text{Mn}_2\text{O}_4$ and $\text{Li}_{1.50}\text{Mn}_2\text{O}_4$ concentrations. Further expansion in cell volume is observed from $\text{Li}_{1.50}\text{Mn}_2\text{O}_4$ to $27.54 \times 10^4 \text{ \AA}^3$ for $\text{Li}_{1.75}\text{Mn}_2\text{O}_4$ by $\sim 0.37 \times 10^4 \text{ \AA}^3$. Finally, from $27.54 \times 10^4 \text{ \AA}^3$ at $\text{Li}_{1.75}\text{Mn}_2\text{O}_4$ concentration to $27.87 \times 10^4 \text{ \AA}^3$ at $\text{Li}_{2.00}\text{Mn}_2\text{O}_4$ concentration, where the cell has expanded by $\sim 0.35 \times 10^4 \text{ \AA}^3$.

The graphical representation for the volume changes on the bulk structure (63 Å) shows fluctuations in volume expansion during cycling to full lithiation. The initial cell volume of $25.58 \times 10^4 \text{ Å}^3$ at $\text{Li}_{1.00}\text{Mn}_2\text{O}_4$ increases to $26.13 \times 10^4 \text{ Å}^3$ at $\text{Li}_{1.25}\text{Mn}_2\text{O}_4$, then to $27.1 \times 10^4 \text{ Å}^3$ at $\text{Li}_{1.50}\text{Mn}_2\text{O}_4$ concentration. Further volume increment is observed until $27.32 \times 10^4 \text{ Å}^3$ at $\text{Li}_{1.75}\text{Mn}_2\text{O}_4$ concentration. A sudden drop to $26.33 \times 10^4 \text{ Å}^3$ is observed at $\text{Li}_{2.00}\text{Mn}_2\text{O}_4$ resulting in the cell volume reduction. This could imply that the structure is experiencing a change in symmetry and all the vacant sites are occupied through continuous lithiation and the Mn_3O_4 spinel walls are collapsing.

The volume change plots for the nanoporous and bulk structures are illustrated in figure 4.8. The observations made on the plots show that when the lithium concentration is increased from $\text{Li}_{1.00}\text{Mn}_2\text{O}_4$ to $\text{Li}_{1.25}\text{Mn}_2\text{O}_4$ there is a volume expansion for all the structures; however, the expansion is minimal for nanoporous structures ($\sim 0.11\%$ for all) and high for the bulk (2.71%). Increasing the concentration to $\text{Li}_{1.50}\text{Mn}_2\text{O}_4$ further results in volume expansion for all the structures. Similarly, volume expansion is still observed for $\text{Li}_{1.50}\text{Mn}_2\text{O}_4$ to $\text{Li}_{1.75}\text{Mn}_2\text{O}_4$ concentration. However, at the latter concentration, nanoporous 69 Å is more resilient to expansion. This is the concentration where nanoporous 69 Å depicts few grain boundaries compared to its nanoporous counterparts. Upon full lithiation ($\text{Li}_{2.00}\text{Mn}_2\text{O}_4$), all the nanoporous structures show a very high volume expansion especially nanoporous 67 and 75 Å. The ability of nanoporous structures to expand freely upon lithiation is due to their unique property of flexing within their pores owing to their large surface areas [52, 111, 112]. On the other hand, the bulk structure experiences an extensive volume drop at this concentration. In the case of the bulk structure, one of the factors contributing to the volume drop could be that the tunnels of the spinel Mn_2O_4 are collapsing with increasing lithium concentration [110].

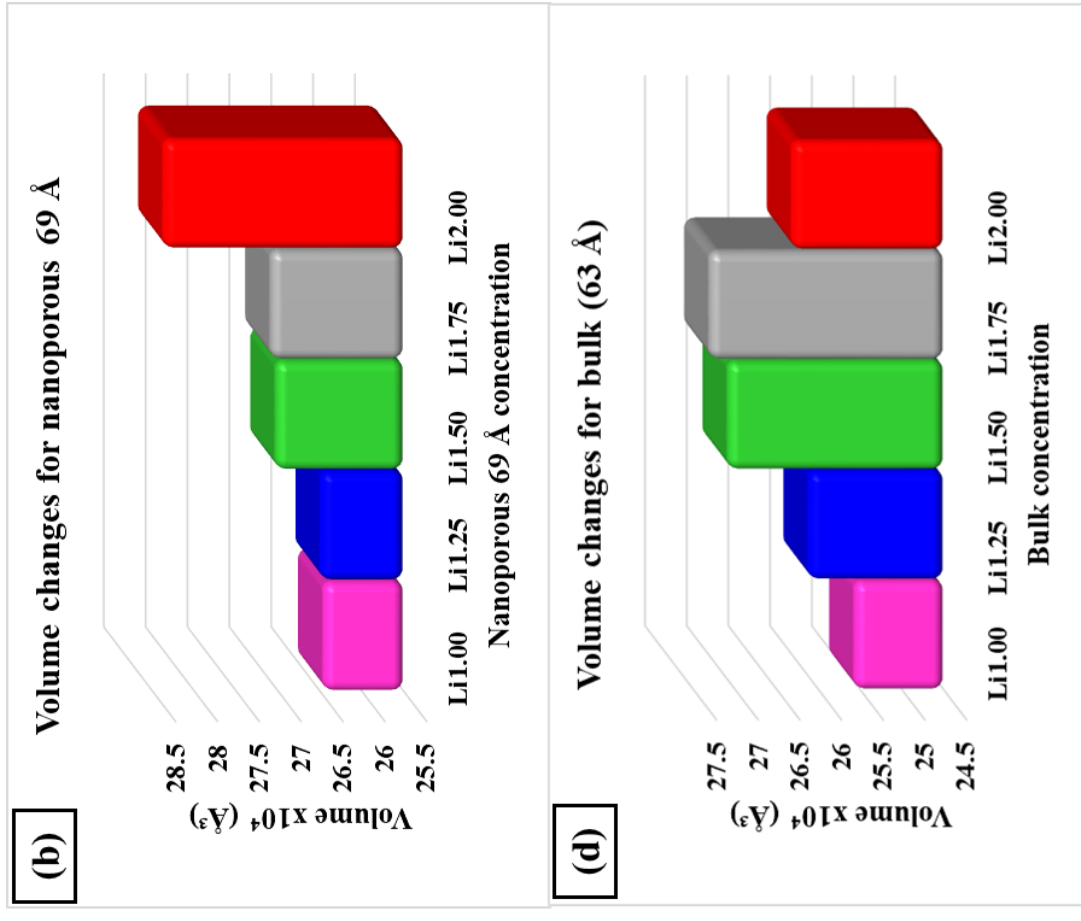
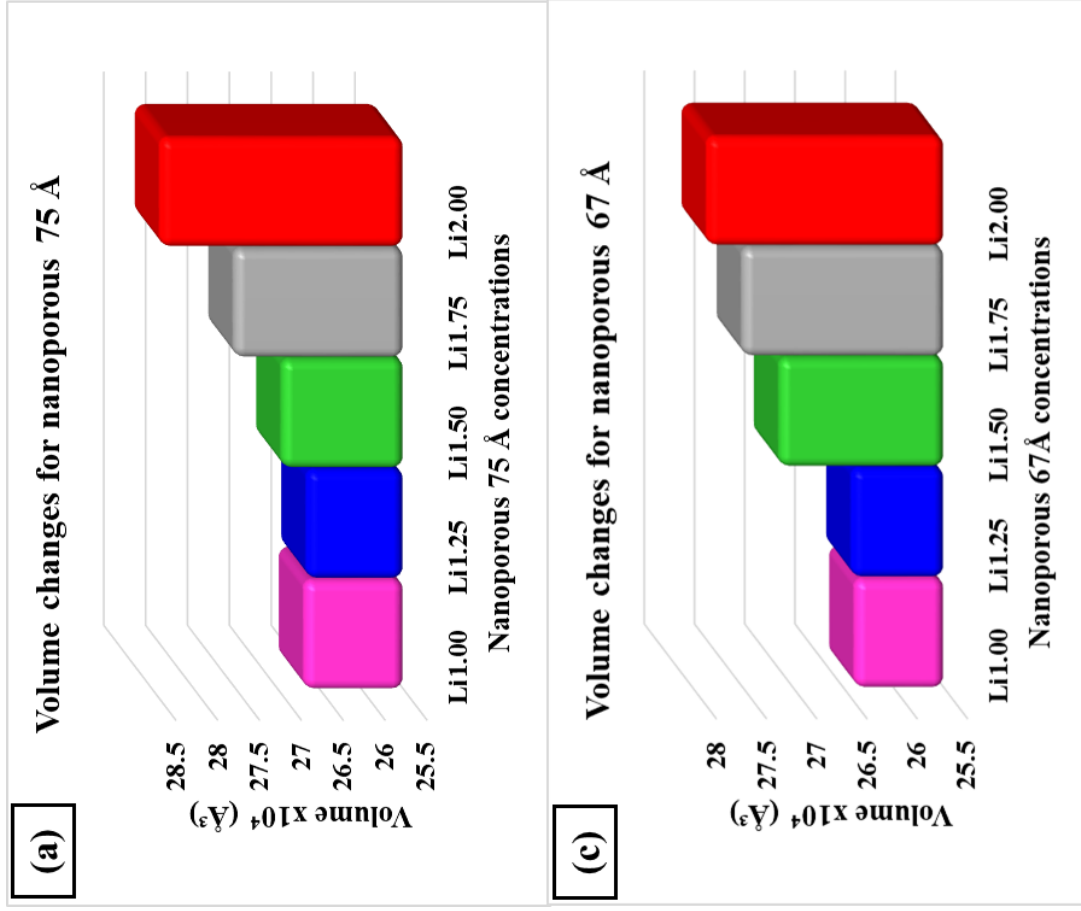


Figure 4. 7: The graphical representations for nanoporous (75, 69, and 67 Å) and bulk structures illustrating the changes in volume with increasing lithium concentration from $\text{Li}_{1.00}\text{MnO}_{2.4}$ to $\text{Li}_{2.00}\text{MnO}_{2.4}$ ($\text{Li}_{1+x}\text{MnO}_{2.4}$, $0 \leq x \leq 1$).

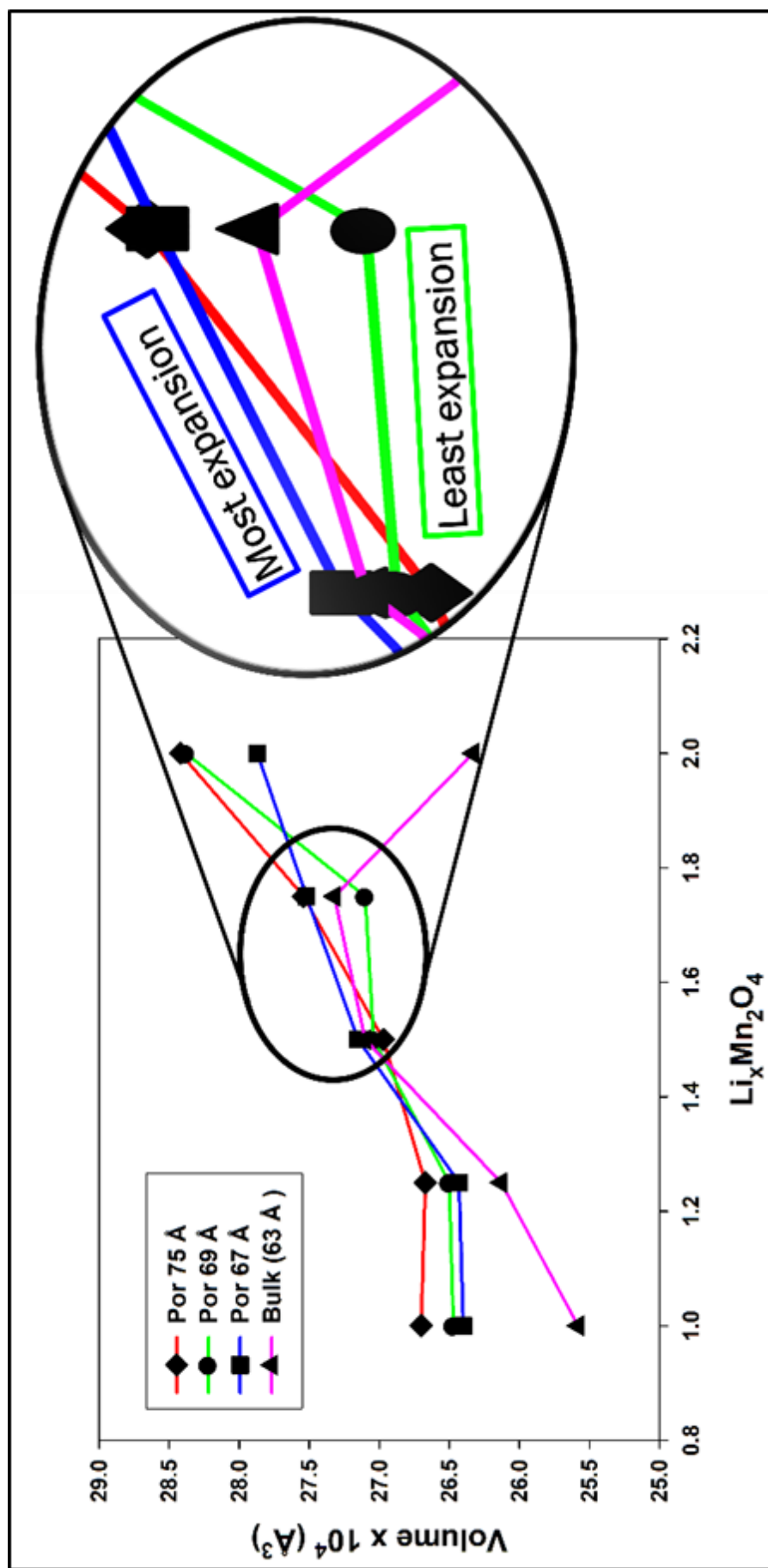


Figure 4. 8: Volume change plots for nanoporous (75, 69 and 67 Å) and bulk structures illustrating the changes in volume with increasing lithium concentration from $\text{Li}_{1.00}\text{Mn}_2\text{O}_4$ to $\text{Li}_{2.00}\text{Mn}_2\text{O}_4$, ($\text{Li}_{1+x}\text{Mn}_2\text{O}_4$, $0 \leq x \leq 1$).

4.4 Microstructural changes emanating from lithium intercalation

Microstructural features of materials help to understand the electrochemical complexities of that structure in terms of atom position, defects formation, and vacant lattice sites that can accommodate extra atoms and so forth. This aid in the understanding of the functionality of that material and help improve its properties for better application. The microstructures of lithiated Li-Mn-O nanoporous and bulk structures ($\text{Li}_{1+x}\text{Mn}_2\text{O}_4$, $0 \leq x \leq 1$) are illustrated in this section to scrutinize their defects and structural integrity after being recrystallised under the NST ensemble during the discharge process.

4.4.1 Nanoporous 75 Å

Figure 4.9 illustrates the nanoporous 75 Å structure (i, a) at $\text{Li}_{1.00}\text{Mn}_2\text{O}_4$ concentration, which shows a distorted region. The magnified sections (b, d) reveal the presence of Mn^{2+} atoms in tetrahedral tunnels and some blocked tunnels by the Mn atoms; the perfect Mn_3O_4 structural model is denoted by (c) on the illustration. The microstructure with grain boundaries in (ii, a) reveals the magnified portions of (b) layered Li_2MnO_3 and (d) spinel LiMn_2O_4 components compared to their perfect models (c, e) respectively; where point defects such as Li and Mn vacancies, Mn interstitials and distortions are observed.

Increment of lithium content to $\text{Li}_{1.25}\text{Mn}_2\text{O}_4$ depicts a structure of nanoporous 75 Å which has recrystallised into a single crystal, illustrated in figure 4.10. The spinel Mn_3O_4 (b) component is observed in the structure and is comparable to (c) its perfect structural model. The overall Mn_3O_4 content is minimal when compared to $\text{Li}_{1.00}\text{Mn}_2\text{O}_4$ concentration. The microstructural features observed in the slice depicted in figure 5.8 (ii, a) demonstrate structural defects such as Li and Mn vacancies, Mn interstitials and distortions on the layered Li_2MnO_3 and spinel LiMn_2O_4 components coexisting in the structure.

Further lithium increment to $\text{Li}_{1.50}\text{Mn}_2\text{O}_4$ on the nanoporous 75 Å structure (i, a) is illustrated in figure 4.11. The Mn^{2+} atoms (b) are depicted occupying the tetrahedral tunnels where some are unoccupied with Li atoms diffusing through them; the spinel Mn_3O_4 perfect model is denoted by (c). Further observations on the structure show that the Mn_3O_4 content is getting reduced with increasing lithium concentration. The slice of the microstructure cut through the nanoporous 75 Å structure is demonstrated in figure 4.11 (ii, a). The magnifications of the defective (b) layered Li_2MnO_3 and (d) spinel LiMn_2O_4 components depict Li vacancies, distortions intergrowths and Mn interstitials. The simulated layered and spinel structures are comparable to (c, e) their perfect structural models. The spinel component is very minimal and highly defective compared to the layered.

The nanoporous 75 Å structure at $\text{Li}_{1.75}\text{Mn}_2\text{O}_4$ concentration evolves into multiple grained crystals after recrystallisation. The previously observed Mn_3O_4 component is not easily identifiable (figure 4.12 (i, a)). The harvested microstructure (ii, a) from the $\text{Li}_{1.75}\text{Mn}_2\text{O}_4$ structure captures a wealth of grain boundaries and some Mn vacancies and distortions from the (b) spinel LiMn_2O_4 and (d) layered Li_2MnO_3 components. The former and the latter are comparable to (c, e) their perfect structural models.

The full lithiated nanoporous 75 Å structure at $\text{Li}_{2.00}\text{Mn}_2\text{O}_4$ concentration with a distorted region is depicted in figure 4.13 (i, a). The structure has few Mn^{2+} atoms (b) in the tetrahedral tunnels, which imply more lithium atoms occupying and diffusing through the channels/tunnel. The Mn_3O_4 model is denoted by (c). The nanoporous 75 Å $\text{Li}_{2.00}\text{Mn}_2\text{O}_4$ microstructure is illustrated in (ii, a) with magnifications of (b) the layered Li_2MnO_3 and (d) spinel LiMn_2O_4 components showing distortions that alter the array of the Li-Mn-O composites. Further observations on the microstructure reveal that the defects reduce with an increase in lithium content.

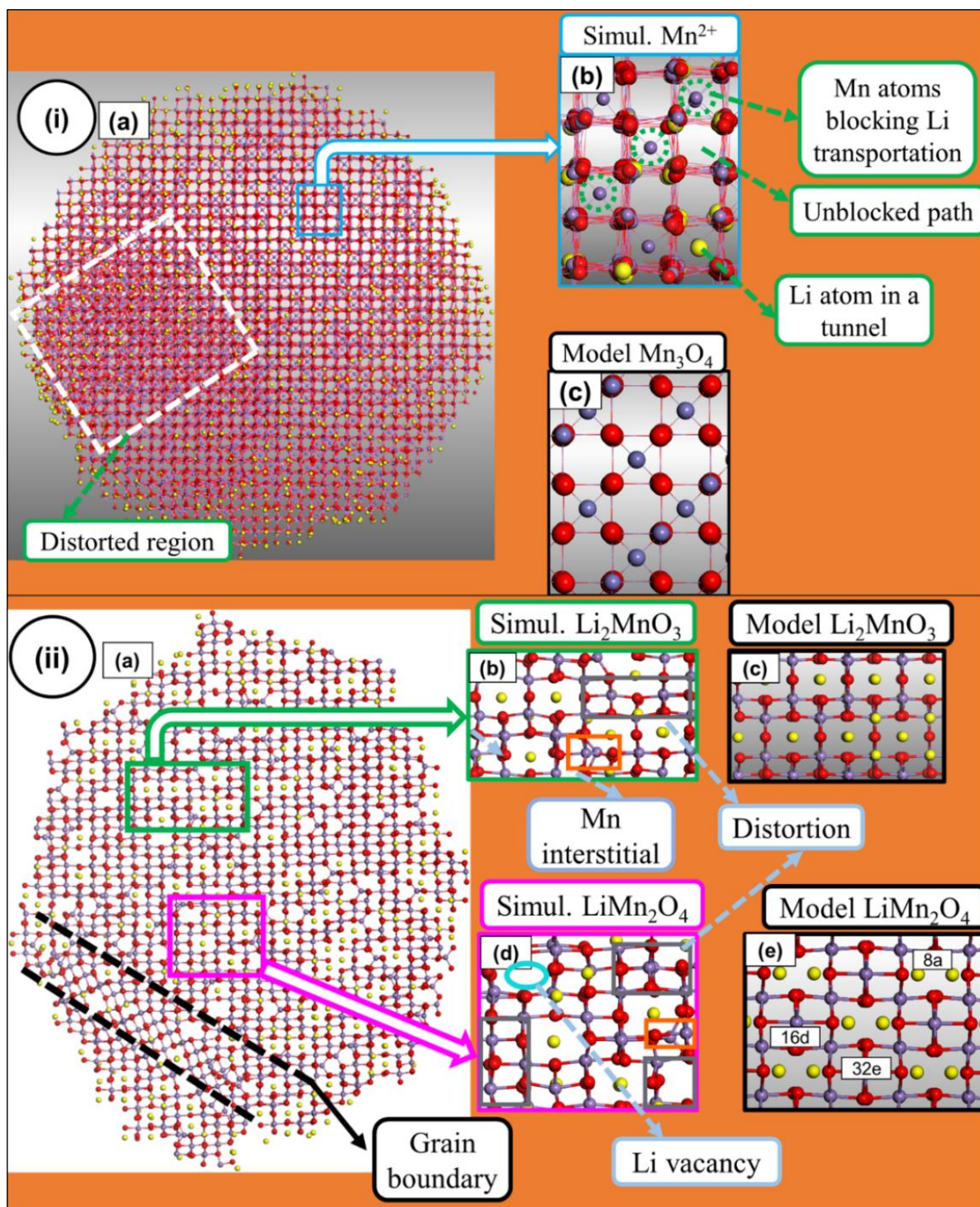


Figure 4. 9: The $\text{Li}_{1.00}\text{Mn}_2\text{O}_4$ polycrystalline nanoporous 75 Å structure (i, a) depicting the (b) magnified sections of Mn^{2+} atoms retraining the tetrahedral tunnels, compared with (c) the perfect Mn_3O_4 model. The microstructure (ii, a) at $\text{Li}_{1.00}\text{Mn}_2\text{O}_4$ illustrating the magnifications of (b) layered Li_2MnO_3 and (d) spinel LiMn_2O_4 components comparable to their perfect models (c, e), respectively.

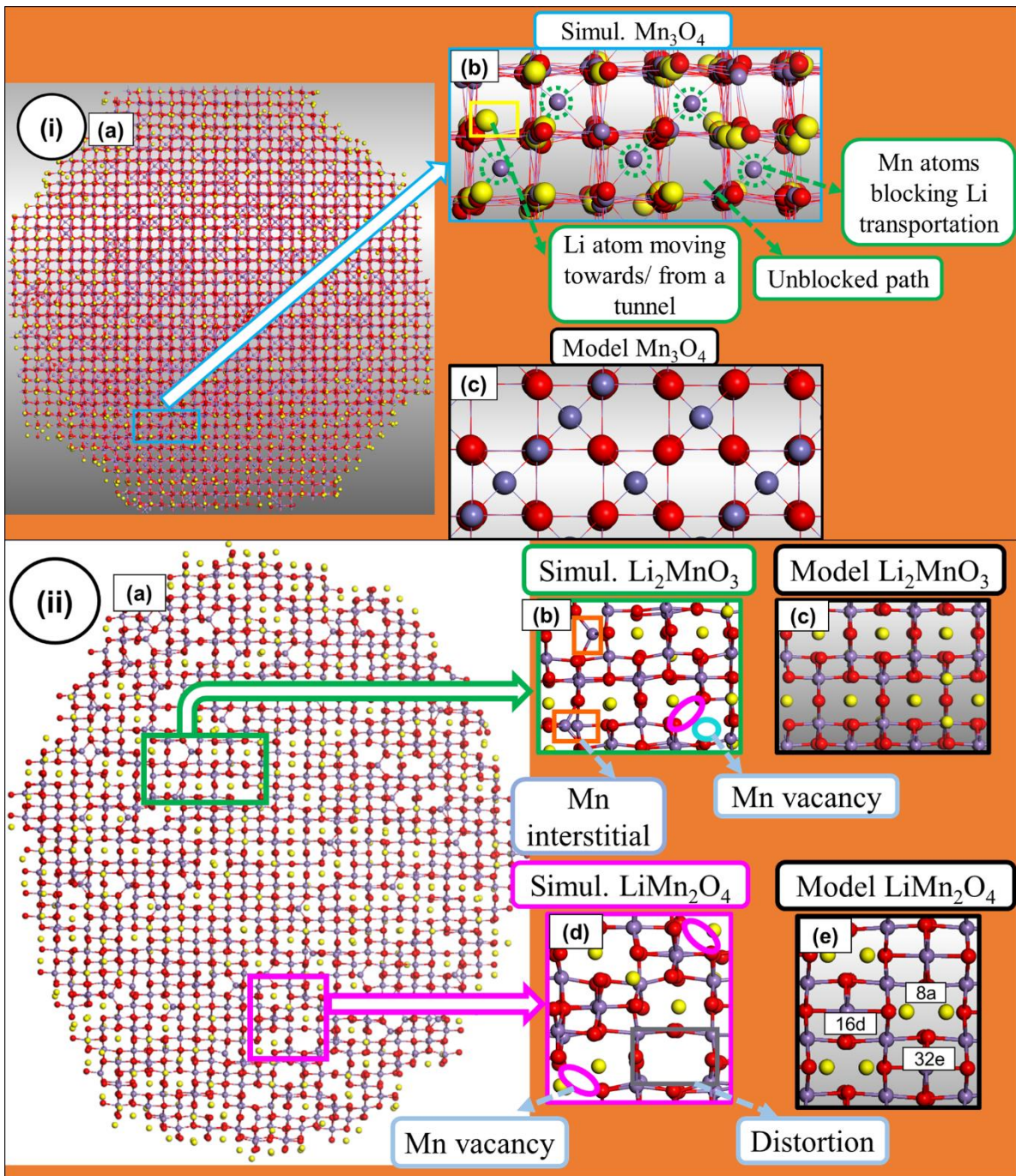


Figure 4. 10: The $\text{Li}_{1.25}\text{Mn}_2\text{O}_4$ nanoporous 75 \AA structure (i, a) illustrating the magnified sections of the (b) spinel Mn_3O_4 and (c) its perfect model. The microstructure slice (ii, a) of $\text{Li}_{1.25}\text{Mn}_2\text{O}_4$ nanoporous 75 \AA structure showing (b) the layered Li_2MnO_3 and (d) spinel LiMn_2O_4 components and their perfect models (c, e).

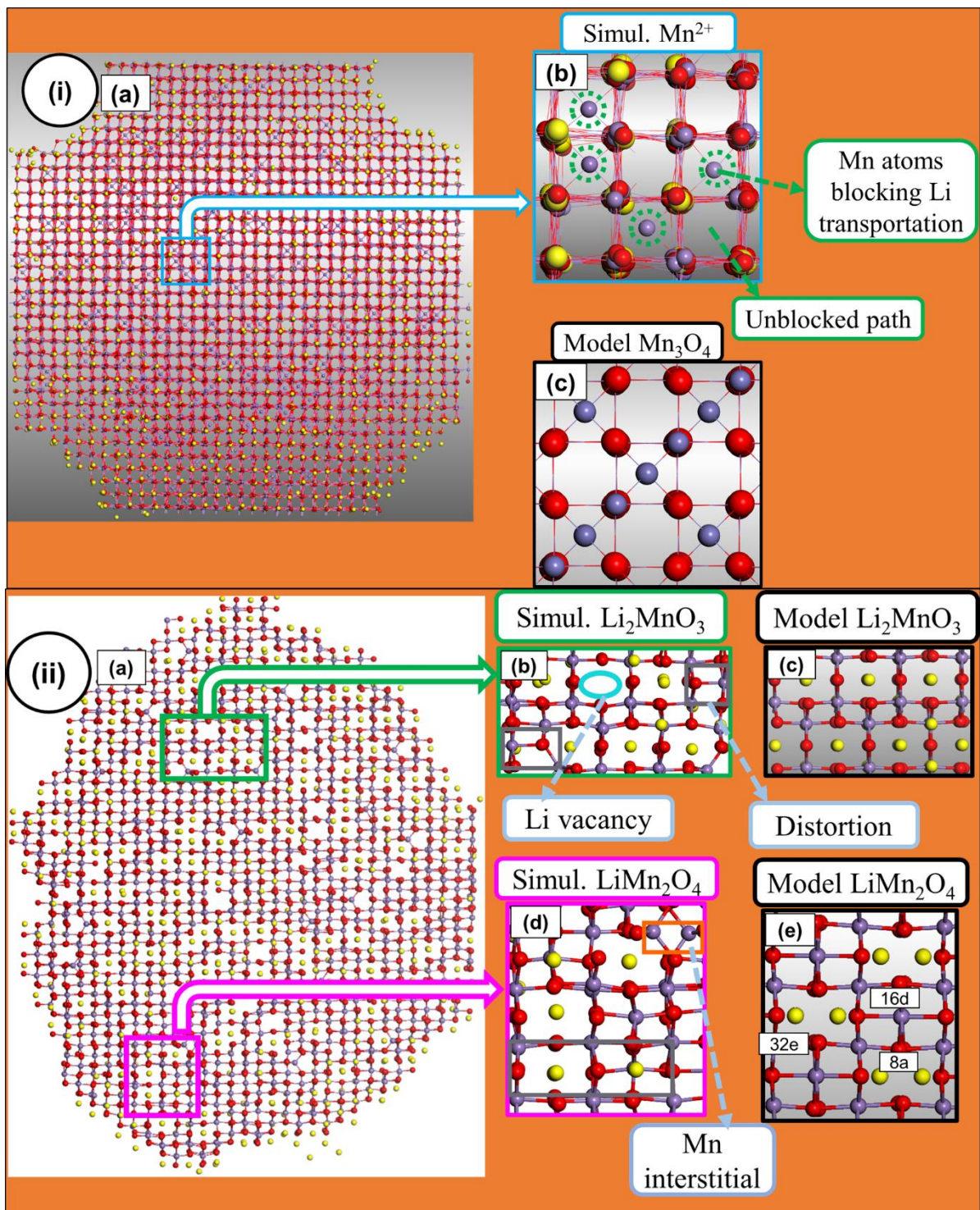


Figure 4. 11: The nanoporous 75 Å structure (i, a) at $\text{Li}_{1.50}\text{Mn}_2\text{O}_4$ concentration demonstrating the (b) magnification of Mn^{2+} atoms retraining the tetrahedral tunnels, compared to (c) the perfect Mn_3O_4 model. The microstructure (ii, a) of $\text{Li}_{1.50}\text{Mn}_2\text{O}_4$ nanoporous 75 Å structure capturing (b) the layered Li_2MnO_3 and (d) spinel LiMn_2O_4 components compared to their perfect structural models (c, e), respectively.

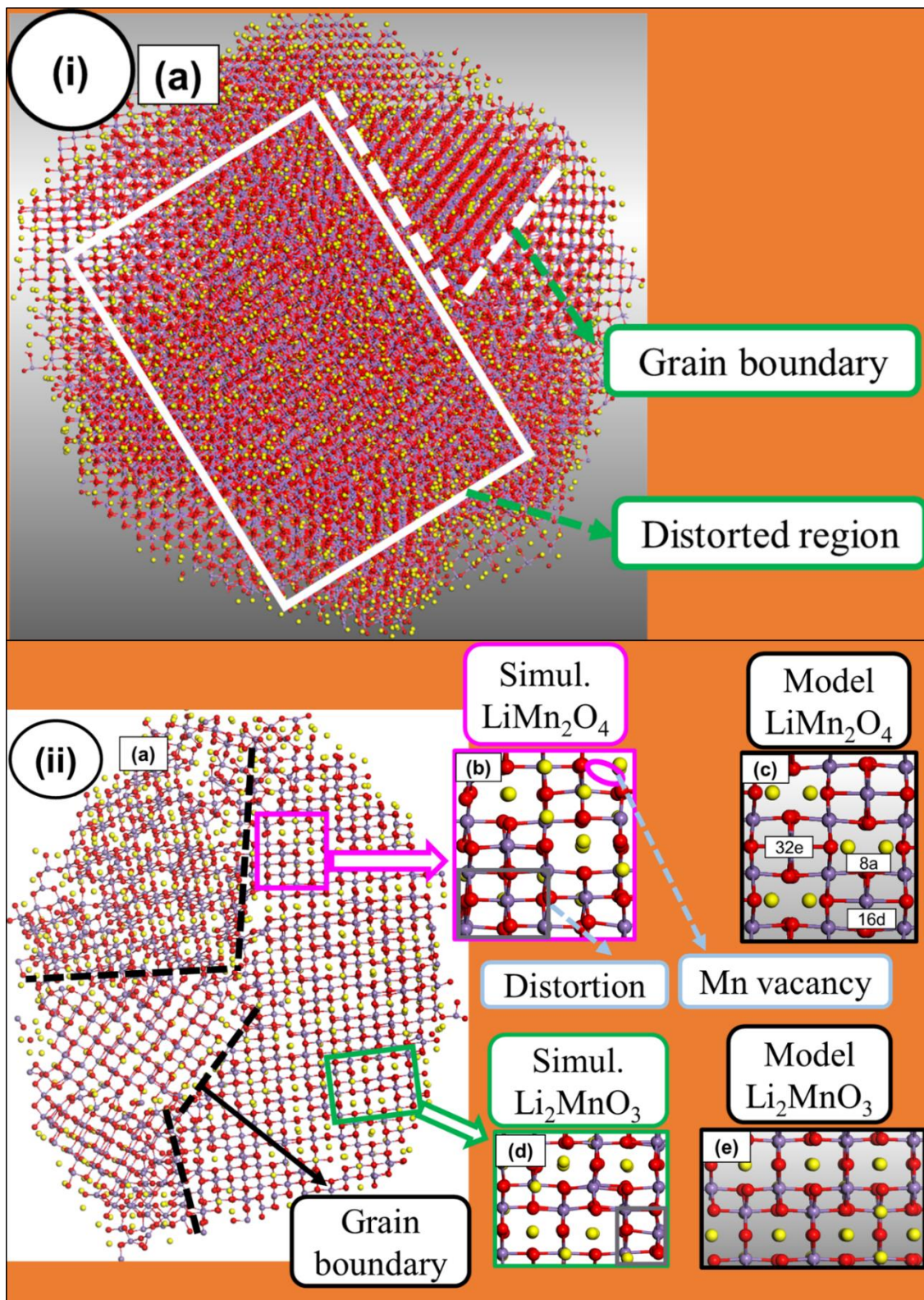


Figure 4. 12: The multi grained $\text{Li}_{1.75}\text{Mn}_2\text{O}_4$ nanoporous 75 Å (i, a) structure with grain boundaries depicting some distorted regions. The microstructure with grain boundaries (ii, a) illustrating the (b) spinel LiMn_2O_4 and (d) the layered Li_2MnO_3 components with their (c, e) perfect structural models.

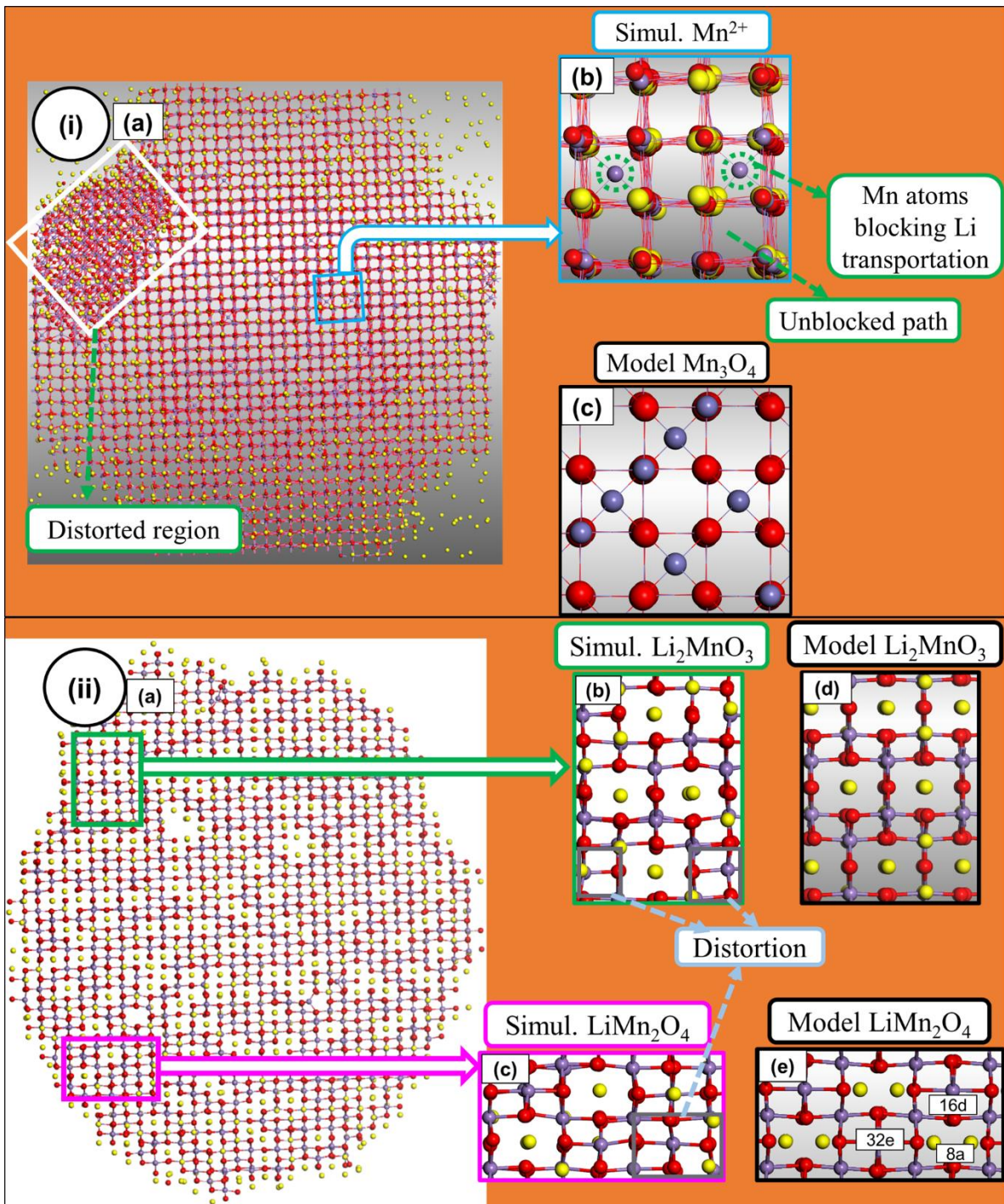


Figure 4.13: The distorted $\text{Li}_{2.00}\text{Mn}_2\text{O}_4$ nanoporous 75 \AA structure (i, a) depicting the (b) magnification of Mn^{2+} atoms retraining the tetrahedral tunnels compared to (c) the perfect Mn_3O_4 model. The microstructure (ii, a) of $\text{Li}_{2.00}\text{Mn}_2\text{O}_4$ nanoporous 75 \AA structure illustrating (b) the layered Li_2MnO_3 and (d) spinel LiMn_2O_4 components compared to their (c, e) perfect structural models.

4.4.2 Nanoporous 69 Å

The pristine ($\text{Li}_{1.00}\text{Mn}_2\text{O}_4$) simulated nanoporous 69 Å structure is depicted in figure 4.14 (i, a). The structure has evolved into a single crystal with numerous (b) Mn^{2+} atoms populating the tetrahedral tunnels. The spinel Mn_3O_4 perfect model is denoted by (c). The nanoporous 69 Å $\text{Li}_{1.00}\text{Mn}_2\text{O}_4$ microstructure (ii, a) shows the hetero-structural (b) layered Li_2MnO_3 and (d) spinel LiMn_2O_4 components with defects compared to their perfect models (c, e), respectively. The defects include Li vacancies, Mn self-interstitials and distortions for layered; and Mn interstitials for spinel.

Figure 4.15 depicts the snapshots of nanoporous 69 Å structure at $\text{Li}_{1.25}\text{Mn}_2\text{O}_4$ concentration. The illustrated diagram in (i, a) captures a single crystal populated by Mn^{2+} atoms (b) in the tetrahedral tunnels after recrystallisation. The Mn_3O_4 perfect model is denoted by (c). The microstructure (ii, a) slice from the nanoporous 69 Å structure illustrates the co-existence of (b) layered Li_2MnO_3 with (d) spinel LiMn_2O_4 component having defects common to those observed at $\text{Li}_{1.00}\text{Mn}_2\text{O}_4$ concentration.

Increment of lithium concentration to $\text{Li}_{1.50}\text{Mn}_2\text{O}_4$ on the nanoporous 69 Å structure is illustrated in figure 4.16 (i, a) and shows the magnifications of the (b) Mn^{2+} atoms in tetrahedral tunnels with (c) the perfect structural model of spinel Mn_3O_4 . The microstructure slice (ii, a) cut from the $\text{Li}_{1.50}\text{Mn}_2\text{O}_4$ nanoporous 69 Å shows the magnifications of (b) layered Li_2MnO_3 and (d) spinel LiMn_2O_4 components which are defected. The defects include Li/Mn vacancies and some distortions. The perfect models (c, e) are depicted alongside magnifications of layered and spinel for comparison purposes.

Further increment of lithium concentration to $\text{Li}_{1.75}\text{Mn}_2\text{O}_4$ results in the nanoporous 69 Å structure evolving into multiple grains with distorted regions, illustrated in figure 4.17 (i,

a). These multiple grains are characterised by grain boundaries. Furthermore, the structure demonstrates (b) the Mn^{2+} atoms retaining tetrahedral tunnels. The spinel Mn_3O_4 perfect structural model is denoted by (c). Further observations show the reduction in tetrahedral coordinated Mn^{2+} atoms. The microstructure (ii, a) of the $\text{Li}_{1.75}\text{Mn}_2\text{O}_4$ concentration for the nanoporous 69 Å structure depicts a grain boundary. Furthermore, the microstructure shows a high content of (b) spinel LiMn_2O_4 component with some defects, compared to (c) its perfect structural model. The defects observed include Mn interstitials and distortions and reduce with increasing lithium concentration.

The full lithiated nanoporous 69 Å structure at $\text{Li}_{2.00}\text{Mn}_2\text{O}_4$ concentration is illustrated in figure 4.18 (i, a) and recrystallises into a single crystal. The magnified section (b) depicts a few of the Mn^{2+} atoms in the tetrahedral tunnels and several vacant tunnels which can be occupied by lithium atoms during the discharge process. The tetrahedral coordinated Mn^{2+} atoms have reduced with lithiation from $\text{Li}_{1.00}\text{Mn}_2\text{O}_4$ to $\text{Li}_{2.00}\text{Mn}_2\text{O}_4$ concentration. The spinel Mn_3O_4 perfect model is denoted by (c). The microstructure of this concentration (ii, a) shows the magnified sections of (b) spinel LiMn_2O_4 and (d) layered Li_2MnO_3 components with reduced defects when compared to the pristine and the other intermediate concentrations; only distortions and Mn vacancies are observed on the magnifications.

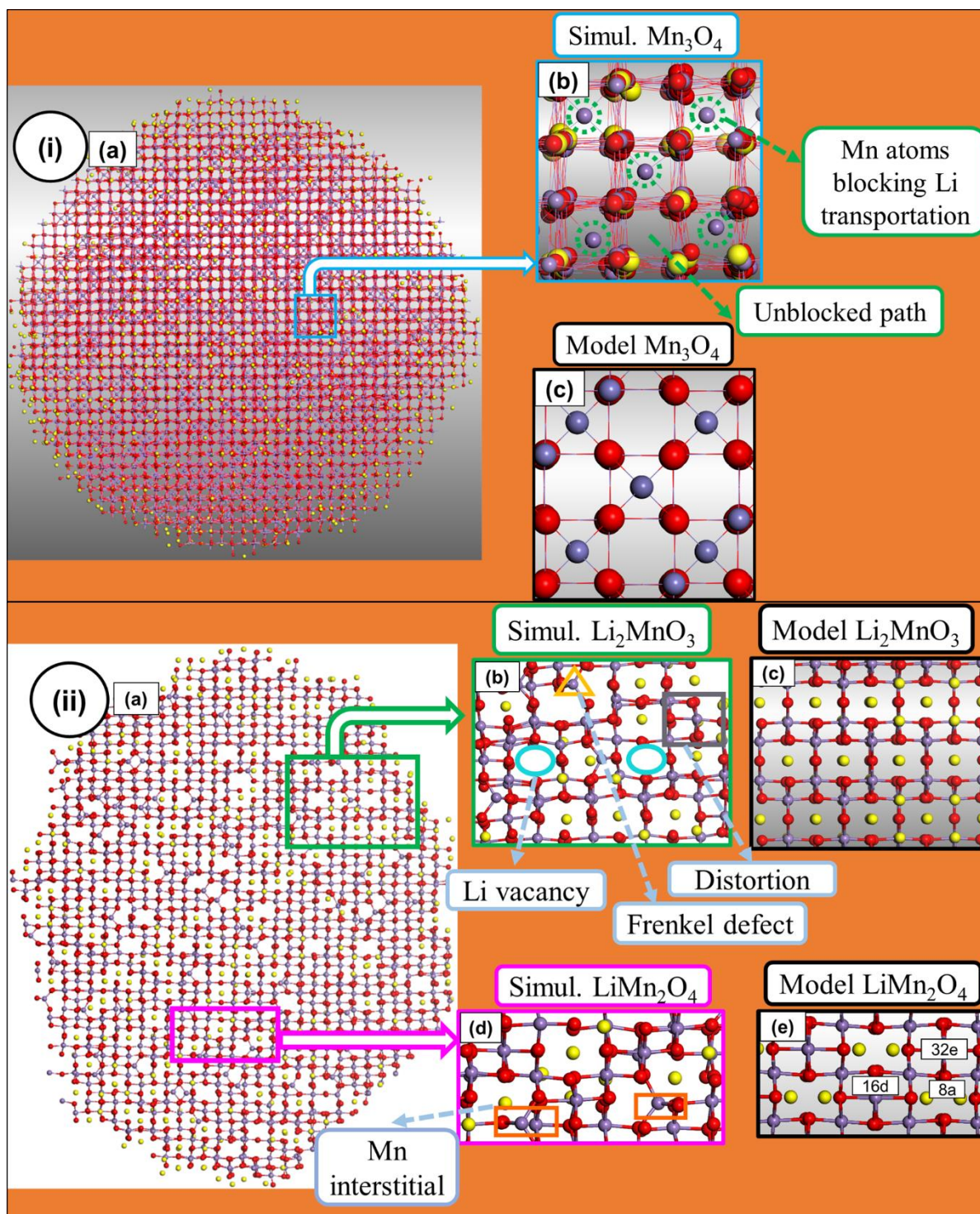


Figure 4. 14: The $\text{Li}_{1.00}\text{Mn}_2\text{O}_4$ nanoporous 69 Å structure (i, a) illustrating the magnification of (b) spinel Mn_3O_4 comparable to (c) its perfect structural model. The microstructure (ii, a) of $\text{Li}_{1.00}\text{Mn}_2\text{O}_4$ nanoporous 69 Å structure capturing the defective (b) layered Li_2MnO_3 and (d) spinel LiMn_2O_4 components with their perfect models (c, e), respectively.

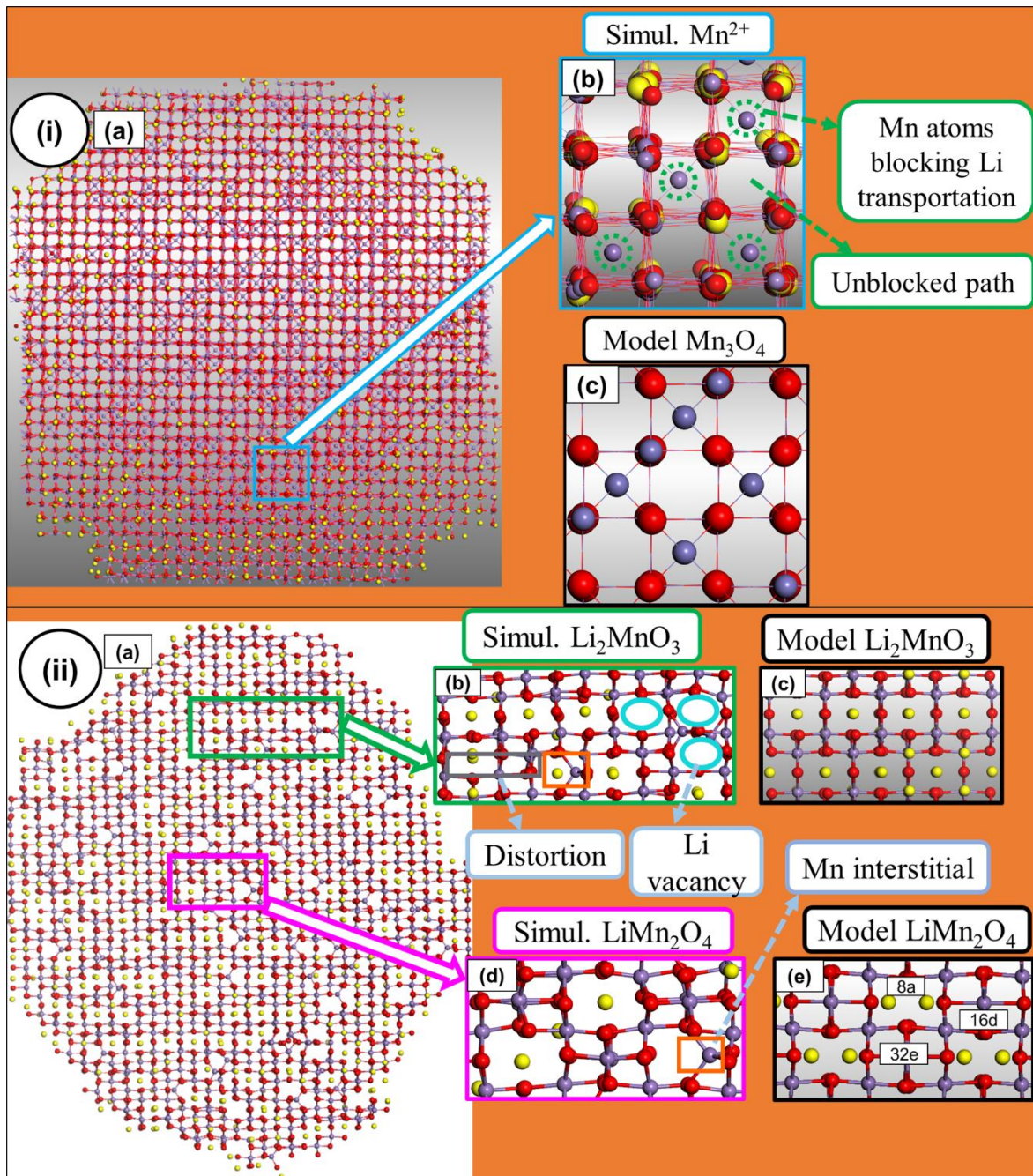


Figure 4. 15: The nanoporous 69 Å structure (i, a) at $Li_{1.25}Mn_2O_4$ concentration depicting the (b) magnification of Mn^{2+} atoms retained in tetrahedral tunnels compared to (c) the perfect Mn_3O_4 model. The microstructure slice (ii, a) of $Li_{1.25}Mn_2O_4$ nanoporous 69 Å structure capturing (b) the layered Li_2MnO_3 and (d) spinel $LiMn_2O_4$ components compared to (c, e) their perfect models.

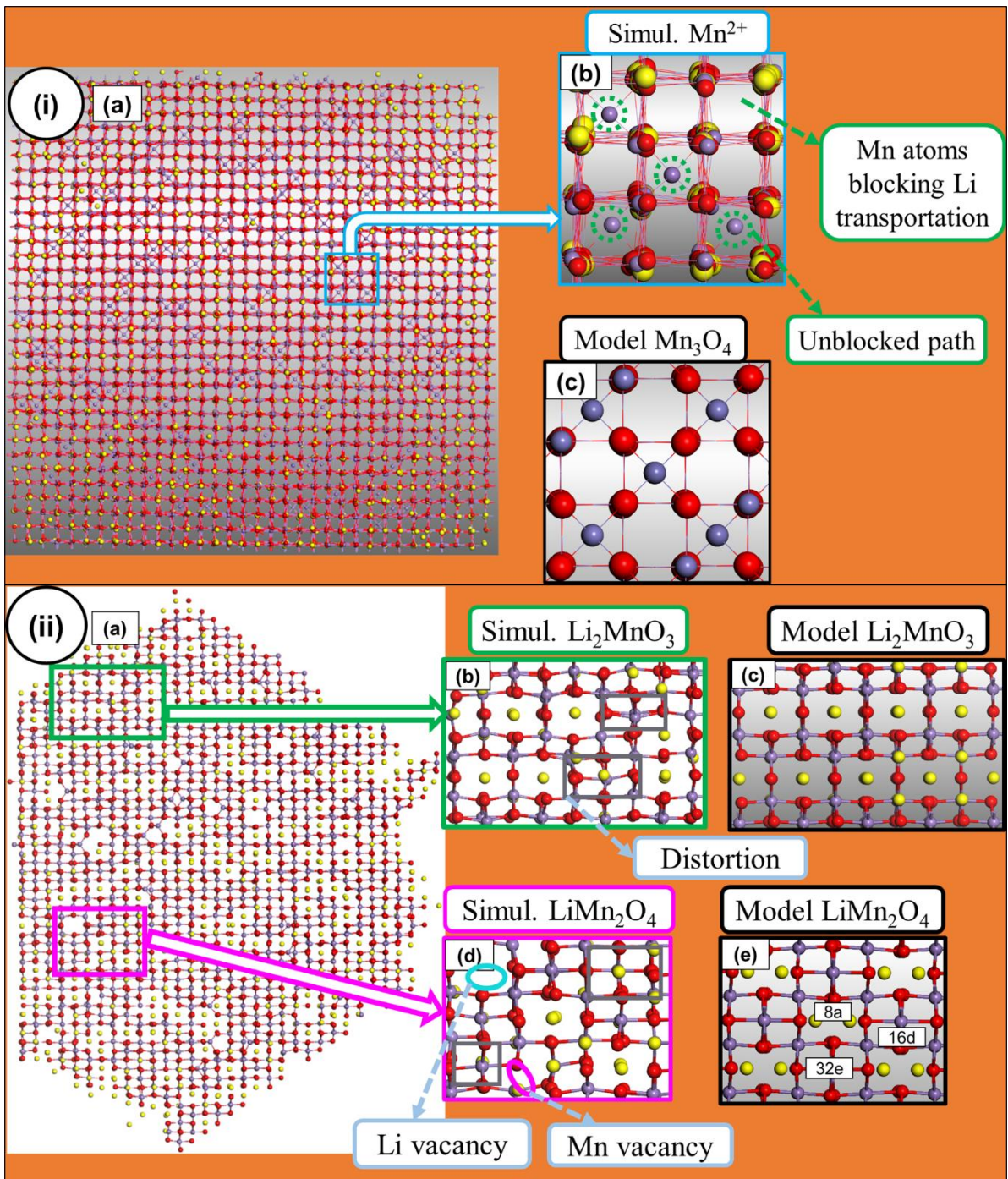


Figure 4. 16: The nanoporous 69 Å structure at (i, a) $Li_{1.50}Mn_2O_4$ concentration demonstrating the (b) magnification of Mn^{2+} atoms retained in the tetrahedral tunnels, where (c) is the perfect Mn_3O_4 model. The $Li_{1.50}Mn_2O_4$ nanoporous 69 Å microstructure (ii, a) capturing (b) the layered Li_2MnO_3 and (d) spinel $LiMn_2O_4$ components with (c, e) their perfect structural models.

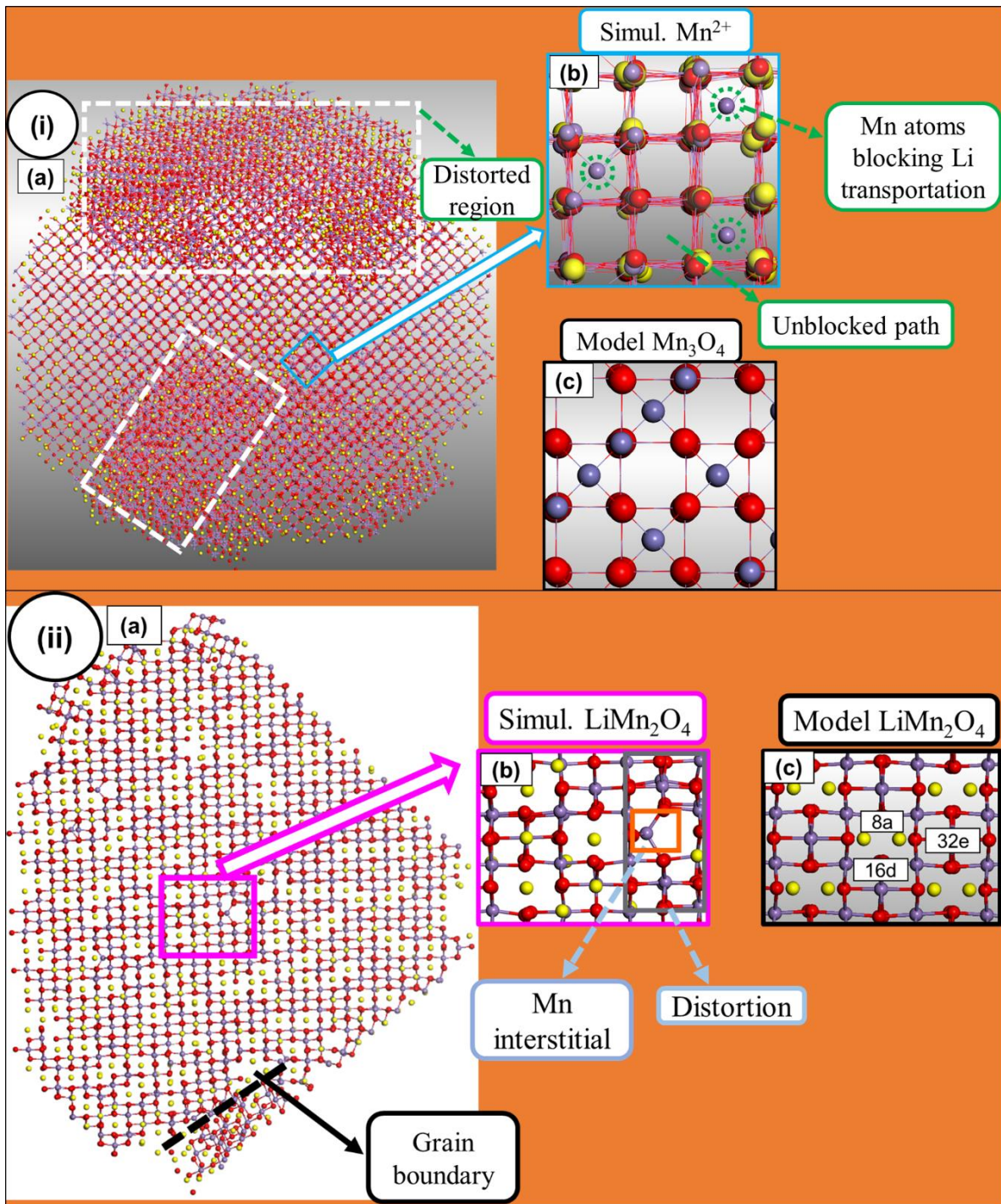


Figure 4. 17: The distorted $\text{Li}_{1.75}\text{Mn}_2\text{O}_4$ nanoporous 69 Å structure (i, a) depicting the (b) magnified section of Mn^{2+} atoms in the tetrahedral tunnels, where (c) is the perfect Mn_3O_4 model. The multi grained microstructure of $\text{Li}_{1.75}\text{Mn}_2\text{O}_4$ nanoporous 69 Å structure (ii, a) showing the defected (b) spinel LiMn_2O_4 component compared to (c) its perfect model.

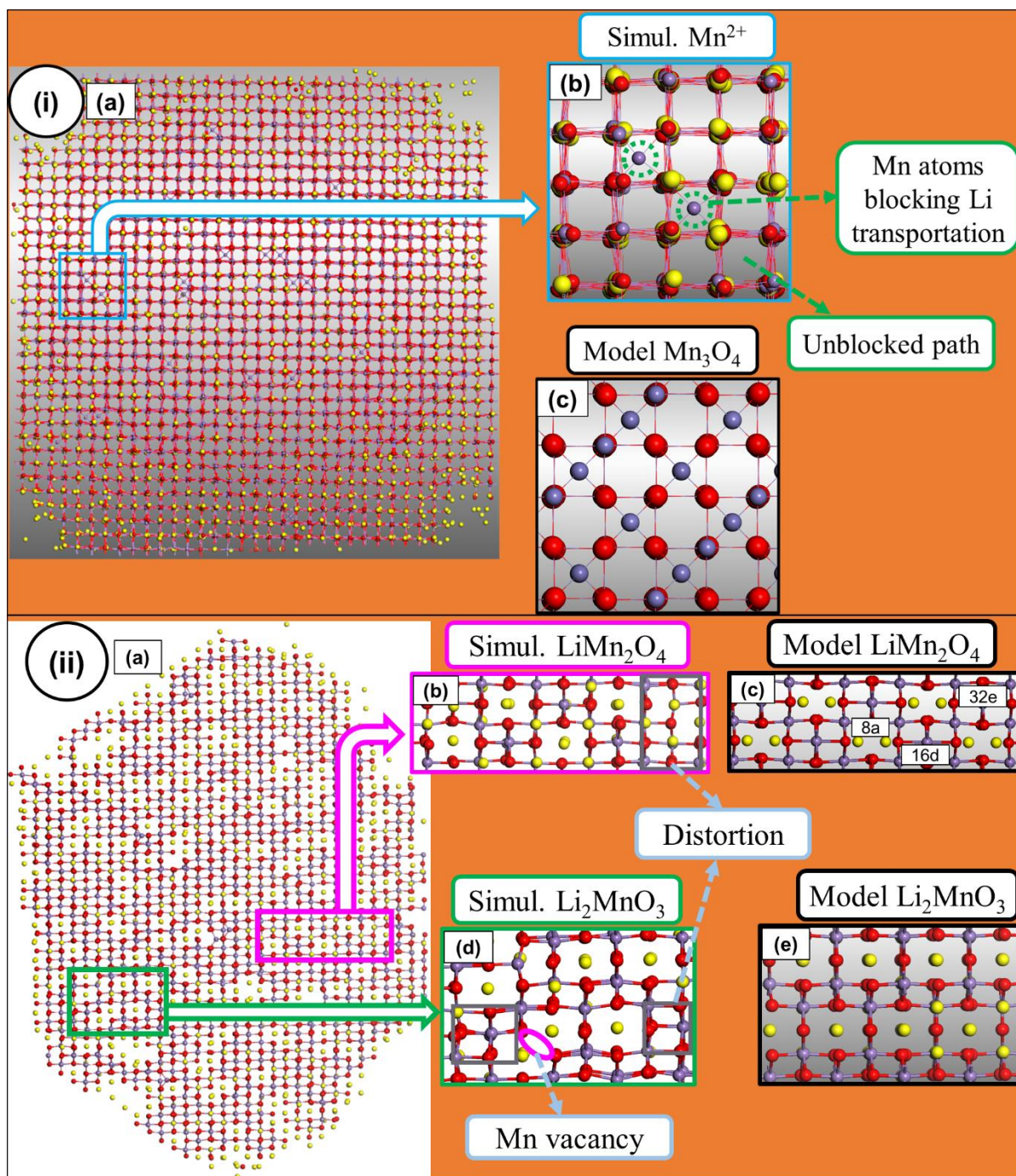


Figure 4. 18: The $\text{Li}_{2.00}\text{Mn}_2\text{O}_4$ nanoporous 69 Å structure (i, a) illustrating the (b) magnifications of Mn^{2+} atoms in the tetrahedral tunnels, where the perfect Mn_3O_4 model is denoted by (c). The microstructure of (ii, a) $\text{Li}_{2.00}\text{Mn}_2\text{O}_4$ nanoporous 69 Å structure depicting the (b) spinel LiMn_2O_4 and (d) the layered Li_2MnO_3 components with (c, e) their perfect models.

4.4.3 Nanoporous 67 Å

The nanoporous 67 Å structure at $\text{Li}_{1.00}\text{Mn}_2\text{O}_4$ is illustrated in figure 4.19 (i, a). The nanoporous 67 Å shows a structure that has recrystallised into a single crystal. The magnified section from the structure in (b) demonstrates the formation of the Mn_3O_4 component which compares well with (c) the Mn_3O_4 model. The microstructure (ii, a) of the $\text{Li}_{1.00}\text{Mn}_2\text{O}_4$ nanoporous 67 Å structure capture the magnified sections of (b) spinel LiMn_2O_4 and (d) Li_2MnO_3 layered components, compared to their (c, e) perfect models, respectively. The magnified spinel reveal the presence of Li and Mn vacancies, while the layered show Mn interstitials, which could suggest the presence of Frenkel defects.

Figure 4.20 (i, a) illustrates the snapshot of the $\text{Li}_{1.25}\text{Mn}_2\text{O}_4$ nanoporous 67 Å structure. The spinel Mn_3O_4 (b) component is observed and is comparable to its (c) perfect structural model. The microstructure slice (ii. a) harvested from the $\text{Li}_{1.25}\text{Mn}_2\text{O}_4$ nanoporous 67 Å structure captures the (b) spinel LiMn_2O_4 and (d) layered Li_2MnO_3 components with defects co-existing in the material and is comparable to their (c, e) perfect models. The observed defects include Li and Mn vacancies for spinel; whereas for the layered, distortions and Li vacancies are observed.

The increase in lithium concentration to $\text{Li}_{1.50}\text{Mn}_2\text{O}_4$ on the nanoporous 67 Å structure is illustrated in figure 4.21 (i, a). The magnification from the structure depicts the (b) spinel Mn_3O_4 component and is comparable to (c) its perfect structural model. The $\text{Li}_{1.50}\text{Mn}_2\text{O}_4$ microstructure only captures the presence of the (b) layered Li_2MnO_3 , which is compared to (c) its perfect model. However, this does not imply that spinel LiMn_2O_4 is not present in the structure, only that the portion or layer where the microstructure was harvested the layered Li_2MnO_3 content was abundant. Moreover, layered Li_2MnO_3 reveal Mn vacancies and distortions defects.

The structure illustrating the lithium increment to $\text{Li}_{1.75}\text{Mn}_2\text{O}_4$ concentration in the nanoporous 67 Å is depicted in figure 4.22 (i, a). The structure has evolved into multiple grains shown by grain boundaries and some distorted regions. Mn^{2+} atoms (b) are captured into the tetrahedral tunnels, compared to the (c) spinel Mn_3O_4 perfect model. The harvested microstructure (ii, a), depicts the magnification of only the (b) spinel LiMn_2O_4 component with distortions, which imply that it is the dominant component in that segment.

Upon full lithiation, in figure 4.23 (i, a), the $\text{Li}_{2.00}\text{Mn}_2\text{O}_4$ nanoporous 67 Å structure illustrates a structure that has recrystallised into a single crystal with only a few Mn^{2+} atoms (b) residing in the tetrahedral positions. This shows a great number of diffusion pathways (tunnels) for lithium, where (c) is the perfect Mn_3O_4 model. The microstructure (ii, a) slice harvested show the presence of defective (b) layered Li_2MnO_3 and (d) spinel LiMn_2O_4 polymorphs. These are comparable to their perfect models (c, e), respectively and have distortions.

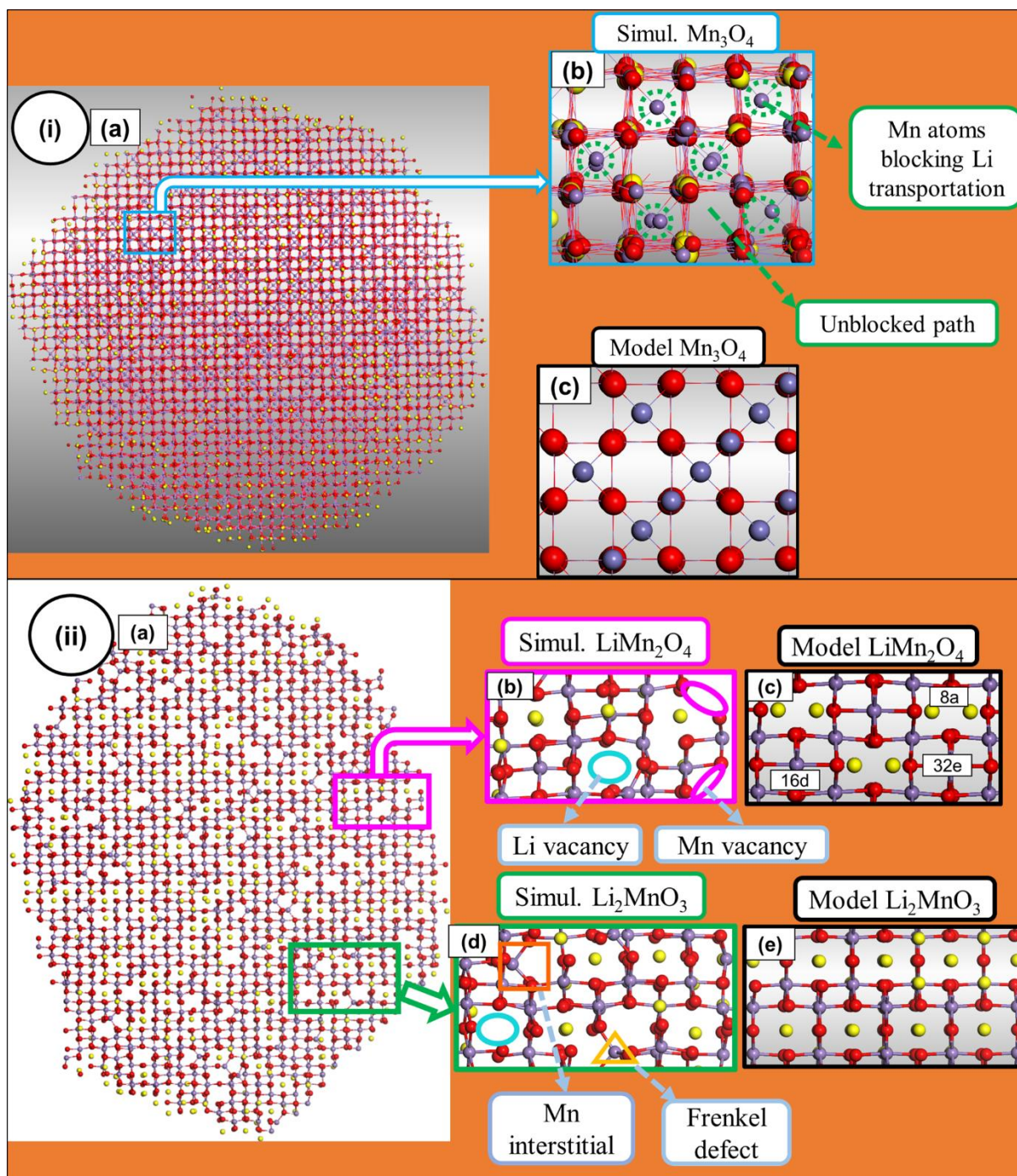


Figure 4. 19: The $\text{Li}_{1.00}\text{Mn}_2\text{O}_4$ nanoporous 67 Å structure (i, a) with the magnification of (b) the Mn^{2+} atoms in the tetrahedral tunnels, where (c) is the perfect Mn_3O_4 model. The microstructure slice (ii, a) $\text{Li}_{1.00}\text{Mn}_2\text{O}_4$ of nanoporous 67 Å structure showing (b) the spinel LiMn_2O_4 and (d) the layered Li_2MnO_3 components compared to their perfect models (c, e), respectively.

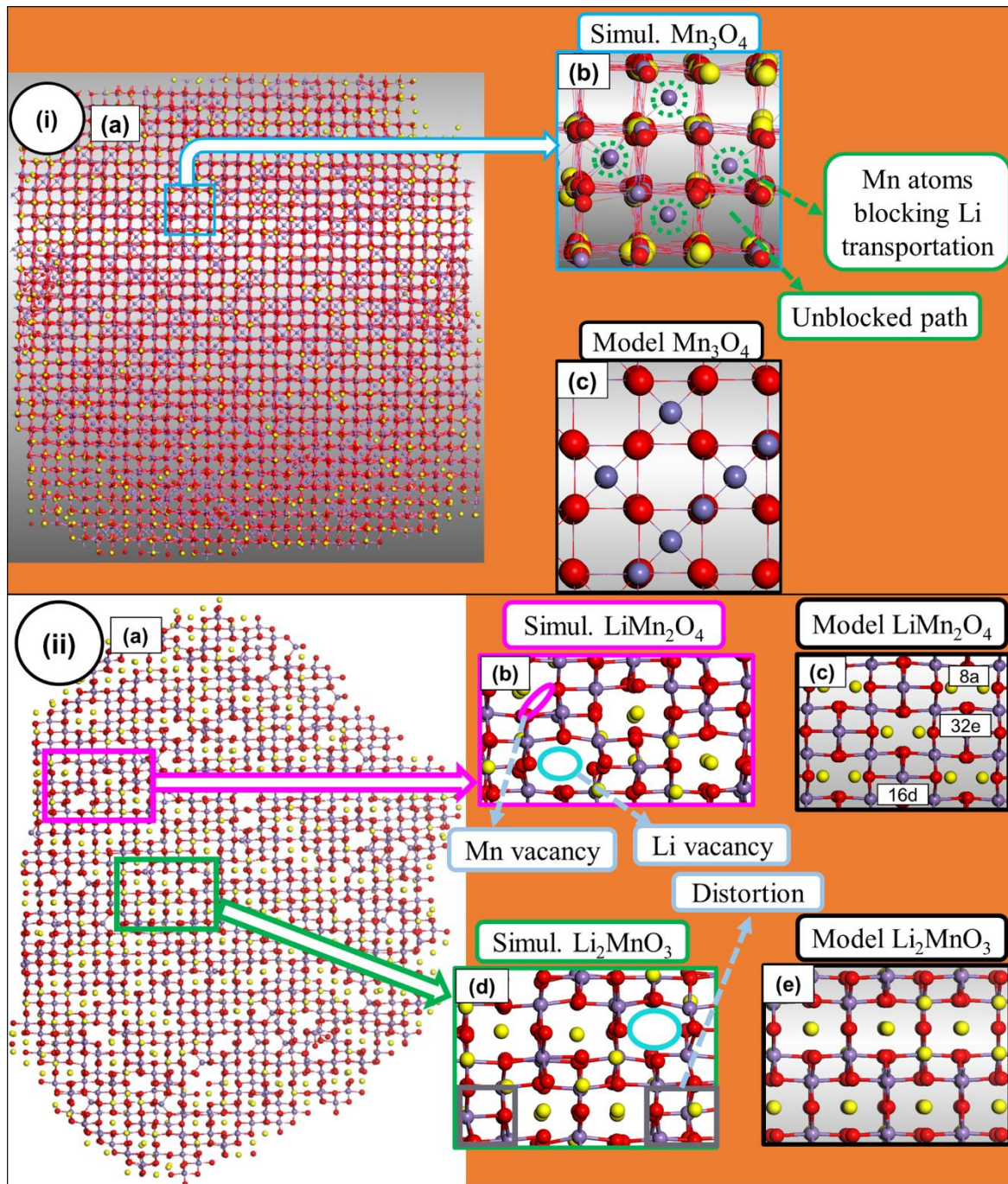


Figure 4. 20: The nanoporous 67 Å structure (i, a) at $Li_{1.25}Mn_2O_4$ concentration illustrating (b) the magnified segment of Mn^{2+} atoms in tetrahedral tunnels, (c) is the perfect Mn_3O_4 model. The harvested microstructure slice of $Li_{1.25}Mn_2O_4$ nanoporous 67 Å structure (ii, a) illustrating (b) spinel $LiMn_2O_4$ and (d) layered Li_2MnO_3 components comparable to (c, e) their perfect models.

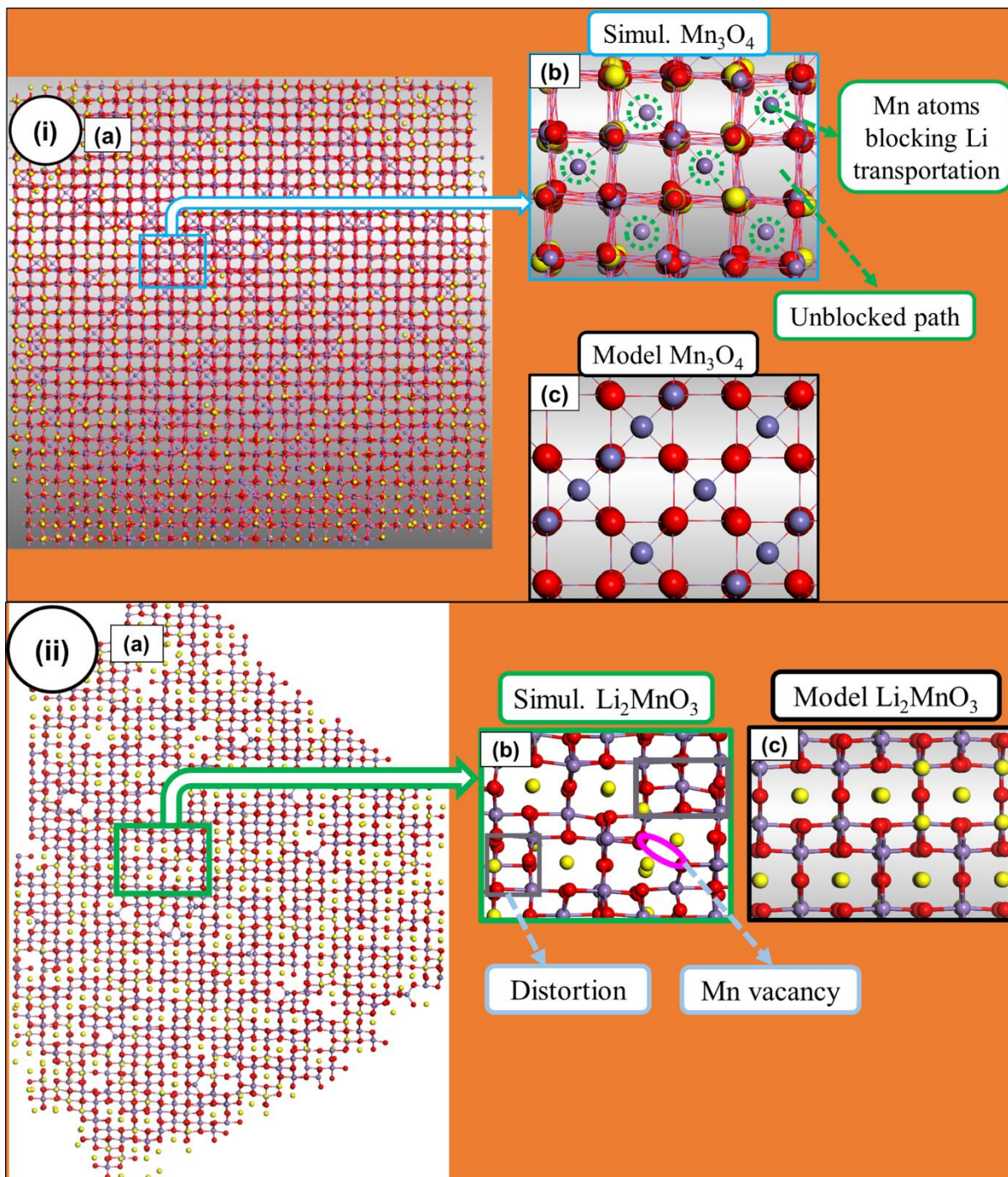


Figure 4. 21: The nanoporous 67 Å structure of $Li_{1.50}Mn_2O_4$ (i, a) presenting (b) the magnification of spinel Mn_3O_4 and is comparable to (c) its perfect Mn_3O_4 model. The microstructure slice (ii, a) of $Li_{1.50}Mn_2O_4$ nanoporous 67 Å structure depicting (b) spinel $LiMn_2O_4$ and (d) the layered Li_2MnO_3 components with their (c, e) perfect structural models.

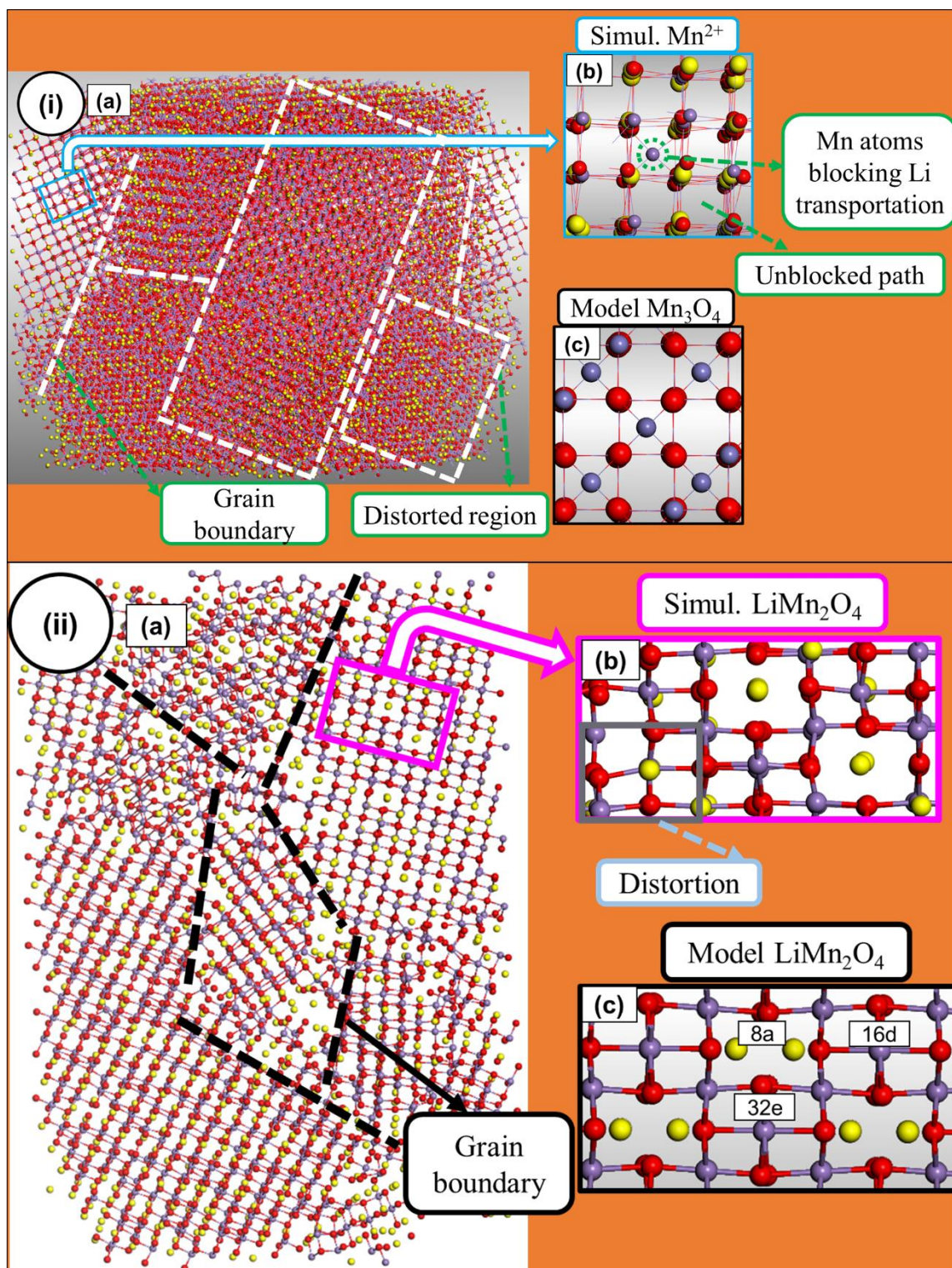


Figure 4. 22: The distorted and multi grained $\text{Li}_{1.75}\text{Mn}_2\text{O}_4$ nanoporous 67 Å structure (i, a) showing the magnifications (b) of Mn^{2+} atoms in the tetrahedral tunnels, where the perfect Mn_3O_4 model is denoted by (c). The microstructure of $\text{Li}_{1.75}\text{Mn}_2\text{O}_4$ nanoporous 67 Å structure with grain boundaries (ii, a) illustrating the (b) spinel LiMn_2O_4 and (d) layered Li_2MnO_3 components with (c, e) their perfect models.

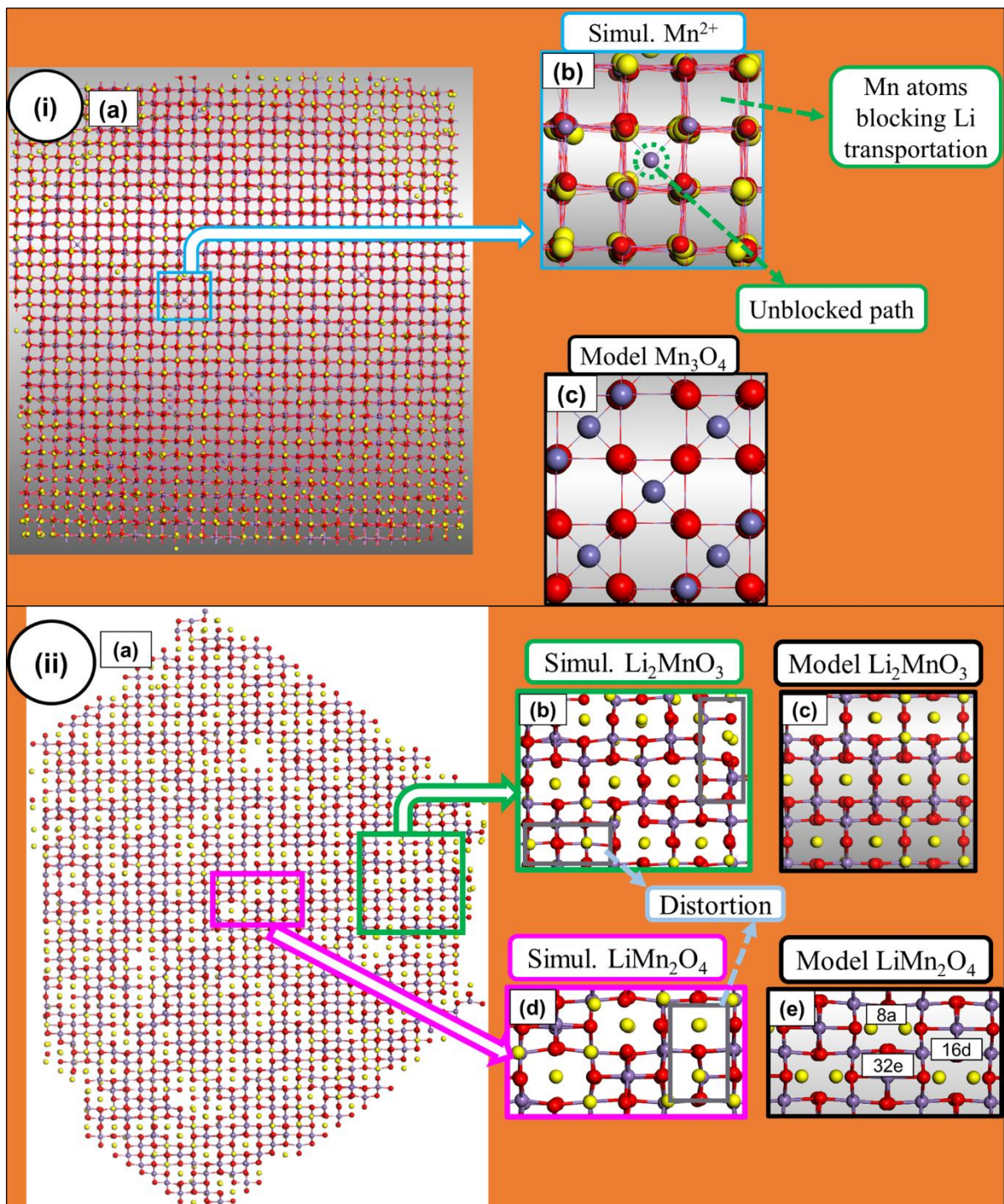


Figure 4. 23: The $\text{Li}_{2.00}\text{Mn}_2\text{O}_4$ nanoporous 67 Å structure (i, a) portraying the (b) magnifications of Mn^{2+} atoms in the tetrahedral tunnels, where (c) is the perfect Mn_3O_4 model. The microstructure slice of (ii, a) $\text{Li}_{2.00}\text{Mn}_2\text{O}_4$ nanoporous 67 Å structure depicting (b) the layered Li_2MnO_3 and (d) spinel LiMn_2O_4 components compared to (c, e) their perfect structural models.

4.4.4 Bulk (63 Å)

The pristine $\text{Li}_{1.00}\text{Mn}_2\text{O}_4$ bulk structure is illustrated in Figure 4.24 (i, a). The structure captures the (i, b) spinel Mn_3O_4 component and it is comparable to (c) its perfect structural model. The microstructure (ii, a) of the $\text{Li}_{1.00}\text{Mn}_2\text{O}_4$ bulk depicts two magnifications of (b) spinel LiMn_2O_4 and (d) layered Li_2MnO_3 which are comparable to their perfect structural models (c, e), respectively. The former component captures defects such as Mn interstitials and Mn vacancies, while the latter captures Li vacancies, Frenkel and distortions.

The $\text{Li}_{1.25}\text{Mn}_2\text{O}_4$ bulk structure is illustrated in figure 4.25 (i, a), and depicts the (b) Mn^{2+} atoms retaining the tetrahedral tunnels and (c) is the perfect Mn_3O_4 structural model. The microstructure (ii, a) harvested from bulk $\text{Li}_{1.25}\text{Mn}_2\text{O}_4$ shows the magnifications of (b) spinel LiMn_2O_4 and layered Li_2MnO_3 with defects and are comparable to their (c, e) perfect structural models. The captured defects on the materials are Li vacancies, Mn interstitials and distortions.

Increasing the lithium content to $\text{Li}_{1.50}\text{Mn}_2\text{O}_4$ (i, a) illustrates a bulk structure with (b) the spinel Mn_3O_4 component which is comparable to (c) its perfect structural model is illustrated in figure 4.26. The harvested microstructure (ii, b) from the $\text{Li}_{1.50}\text{Mn}_2\text{O}_4$ bulk depicts the magnifications of (b) the spinel LiMn_2O_4 and (d) layered Li_2MnO_3 components with defects such as Li/Mn vacancies and some distortions. These components are comparable with their perfect structural models (c, e), respectively.

Further lithium intercalation to $\text{Li}_{1.75}\text{Mn}_2\text{O}_4$ concentration (i, a) on the bulk captures a single crystalline structure depicted in figure 4.27. The magnifications of (b) Mn^{2+} atoms retaining the tetrahedral tunnels are observed and these are compared to (c) the perfect structural model of the spinel Mn_3O_4 . The spinel Mn_3O_4 content is getting reduced in the structure when compared to the lithium concentrations below $\text{Li}_{1.75}\text{Mn}_2\text{O}_4$. The harvested

microstructure (ii, a) under the same concentration favours the spinel LiMn_2O_4 component and is comparable to (c) its perfect structural model. The magnified spinel shows Li vacancies and distortions. A reduction in defects with increasing lithium concentration is observed.

The $\text{Li}_{2.00}\text{Mn}_2\text{O}_4$ bulk structure (i, a) in figure 4.28 shows the magnifications of (b) Mn^{2+} atoms retaining the tetrahedral tunnels. The Mn_3O_4 spinel content has been extremely reduced from the $\text{Li}_{1.00}\text{Mn}_2\text{O}_4$ to $\text{Li}_{2.00}\text{Mn}_2\text{O}_4$ concentration. The perfect structural model of Mn_3O_4 is denoted by (c) in the illustration. The harvested slice of the $\text{Li}_{2.00}\text{Mn}_2\text{O}_4$ bulk microstructure (ii, a) shows the coexistence of (b) spinel LiMn_2O_4 and (d) layered Li_2MnO_3 components. These capture a reduced content of defects; only the Mn vacancies and distortions are observed. The components of layered and spinel are comparable to their perfect structural models (c, e), respectively.

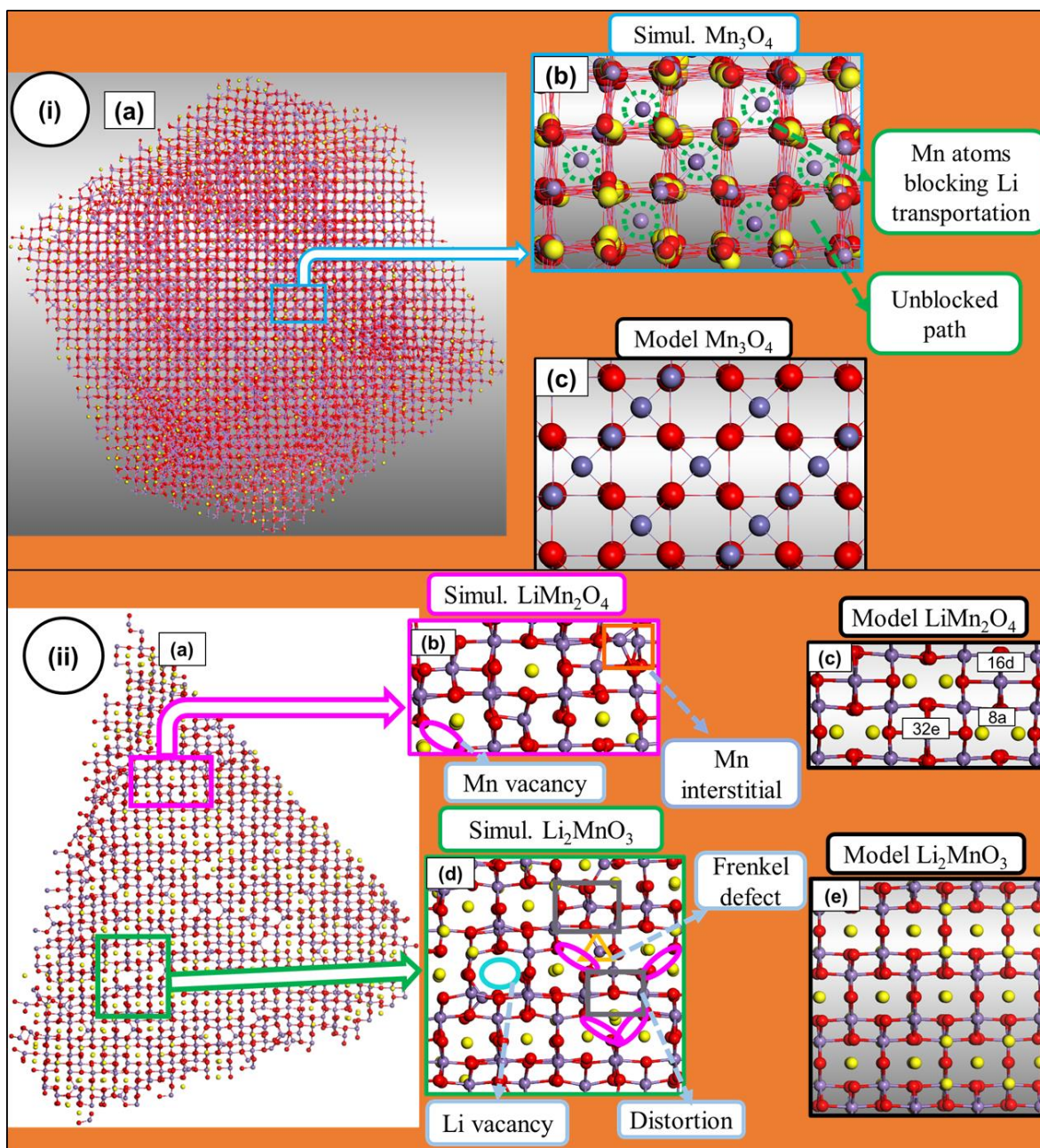


Figure 4. 24: The $\text{Li}_{1.00}\text{Mn}_2\text{O}_4$ bulk structure (i, a) depicting the magnified section of (b) spinel Mn_3O_4 and comparable to (c) its perfect structural model. The microstructure (ii, a) of $\text{Li}_{1.00}\text{Mn}_2\text{O}_4$ bulk structure capturing the (b) spinel LiMn_2O_4 and (d) layered Li_2MnO_3 components comparable to their perfect structural models (c, e), respectively.

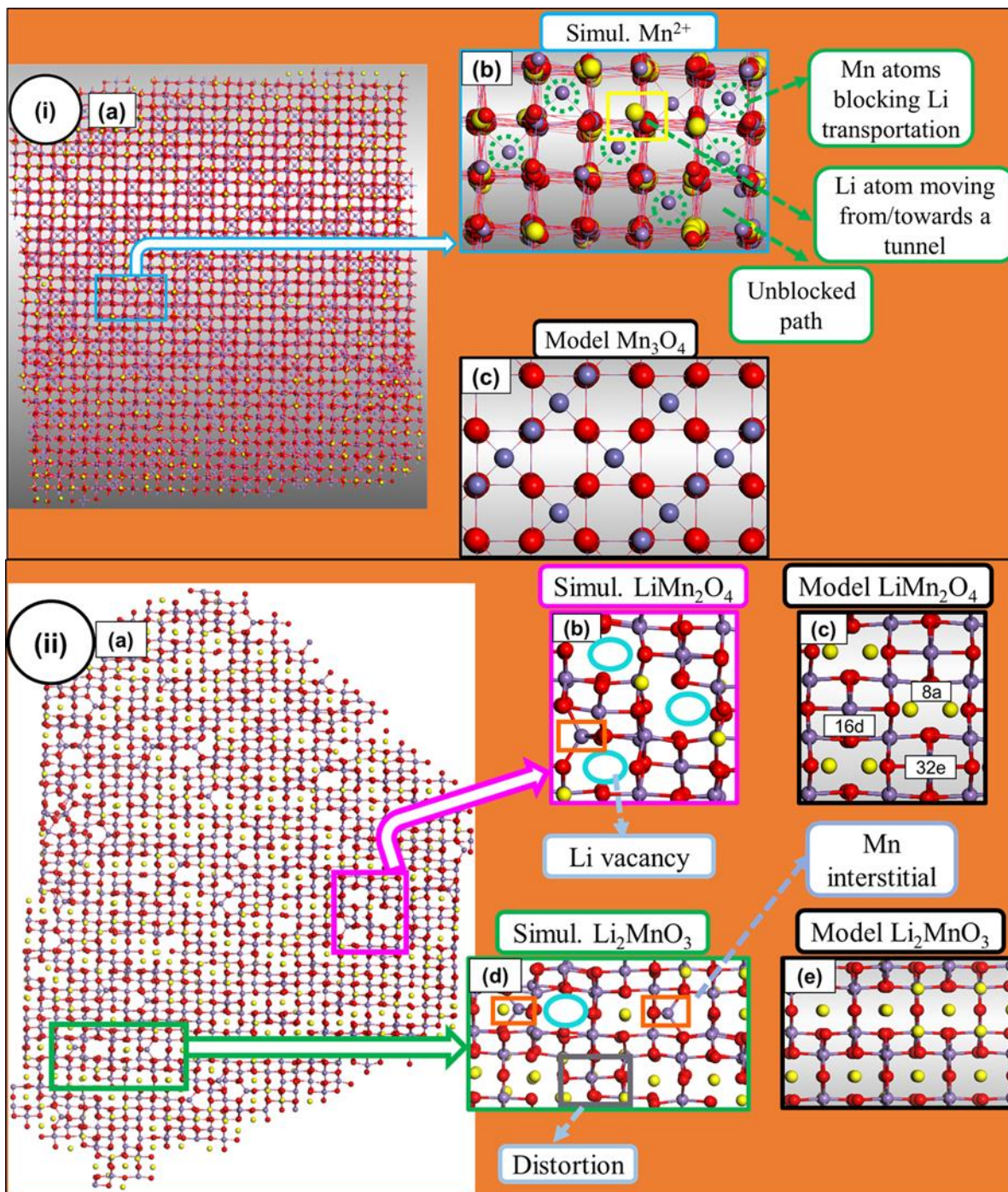


Figure 4. 25: The $\text{Li}_{1.25}\text{Mn}_2\text{O}_4$ bulk structure (i, a) illustrating the magnified section of (b) Mn^{2+} atoms retraining the tetrahedral tunnels compared to (c) the perfect Mn_3O_4 structural model. The microstructure (ii, a) of $\text{Li}_{1.25}\text{Mn}_2\text{O}_4$ bulk structure showing the (b) spinel LiMn_2O_4 and (d) the layered Li_2MnO_3 components, compared to (c, e) their perfect structural models

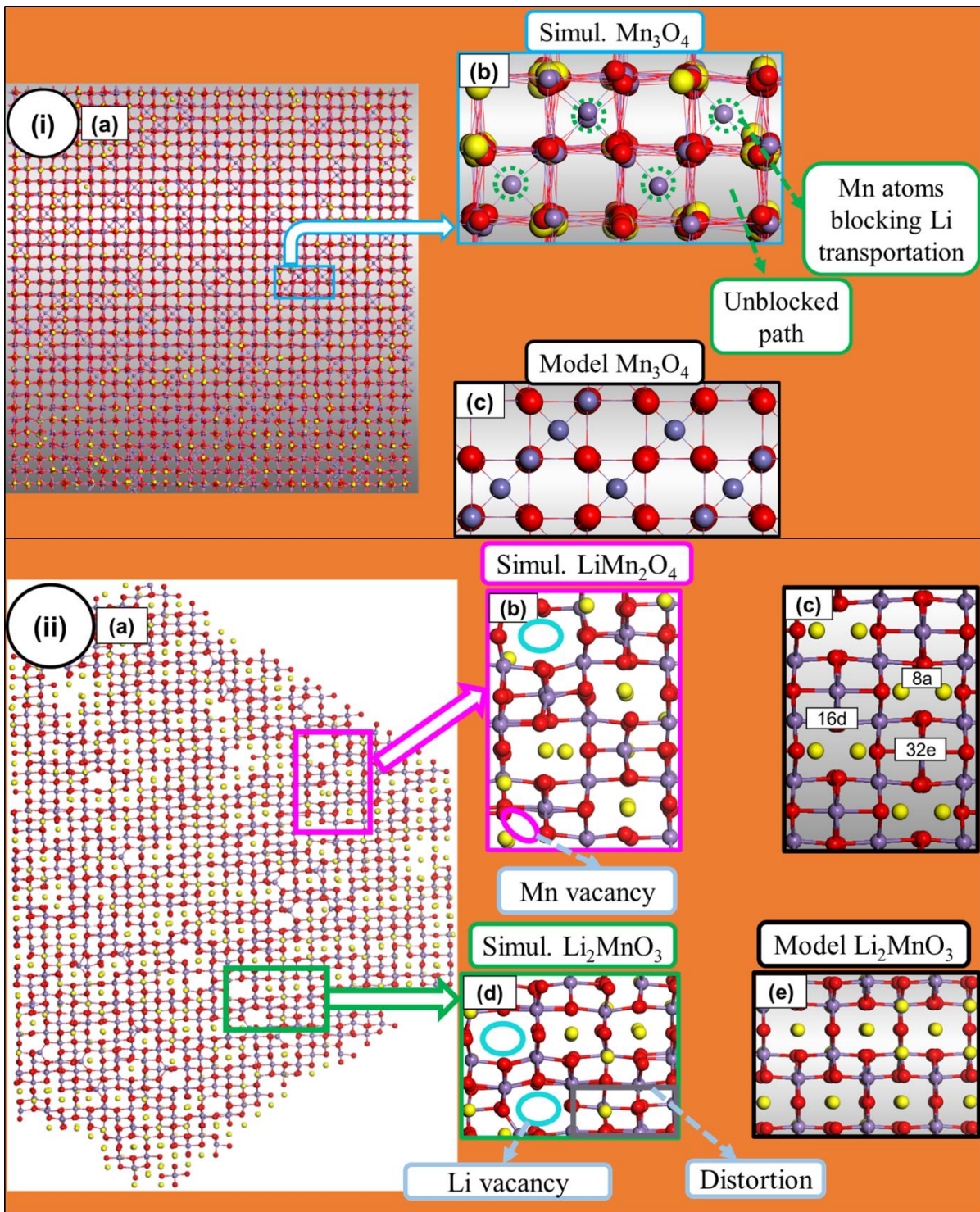


Figure 4. 26: The bulk structure (i, a) at $\text{Li}_{1.50}\text{Mn}_2\text{O}_4$ concentration demonstrating the (b) magnified section of Mn^{2+} atoms retraining the tetrahedral tunnels, compared to (c) the perfect Mn_3O_4 structural model. The microstructure (ii, a) of the $\text{Li}_{1.50}\text{Mn}_2\text{O}_4$ bulk structure illustrating the (b) spinel LiMn_2O_4 and (d) the layered Li_2MnO_3 components, which are comparable to (c, e) their perfect structural models, respectively.

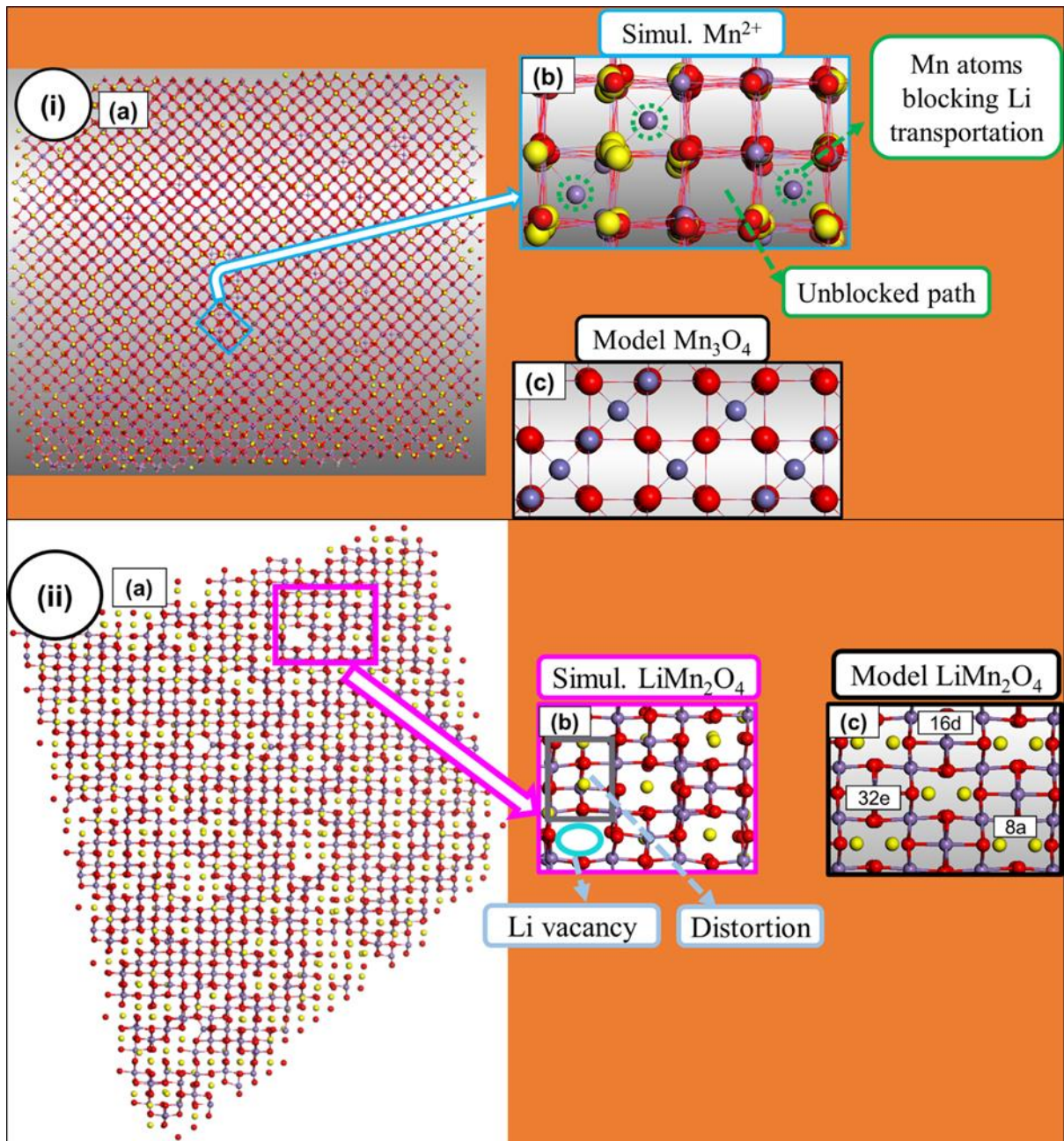


Figure 4. 27: The $\text{Li}_{1.75}\text{Mn}_2\text{O}_4$ bulk structure (i, a) depicting the magnification of (b) Mn^{2+} atoms retraining the tetrahedral tunnels, compared to (c) the perfect Mn_3O_4 structural model. The microstructure (ii, a) of $\text{Li}_{1.75}\text{Mn}_2\text{O}_4$ bulk structure capturing (b) the spinel LiMn_2O_4 component compared to (c) its perfect structural model.

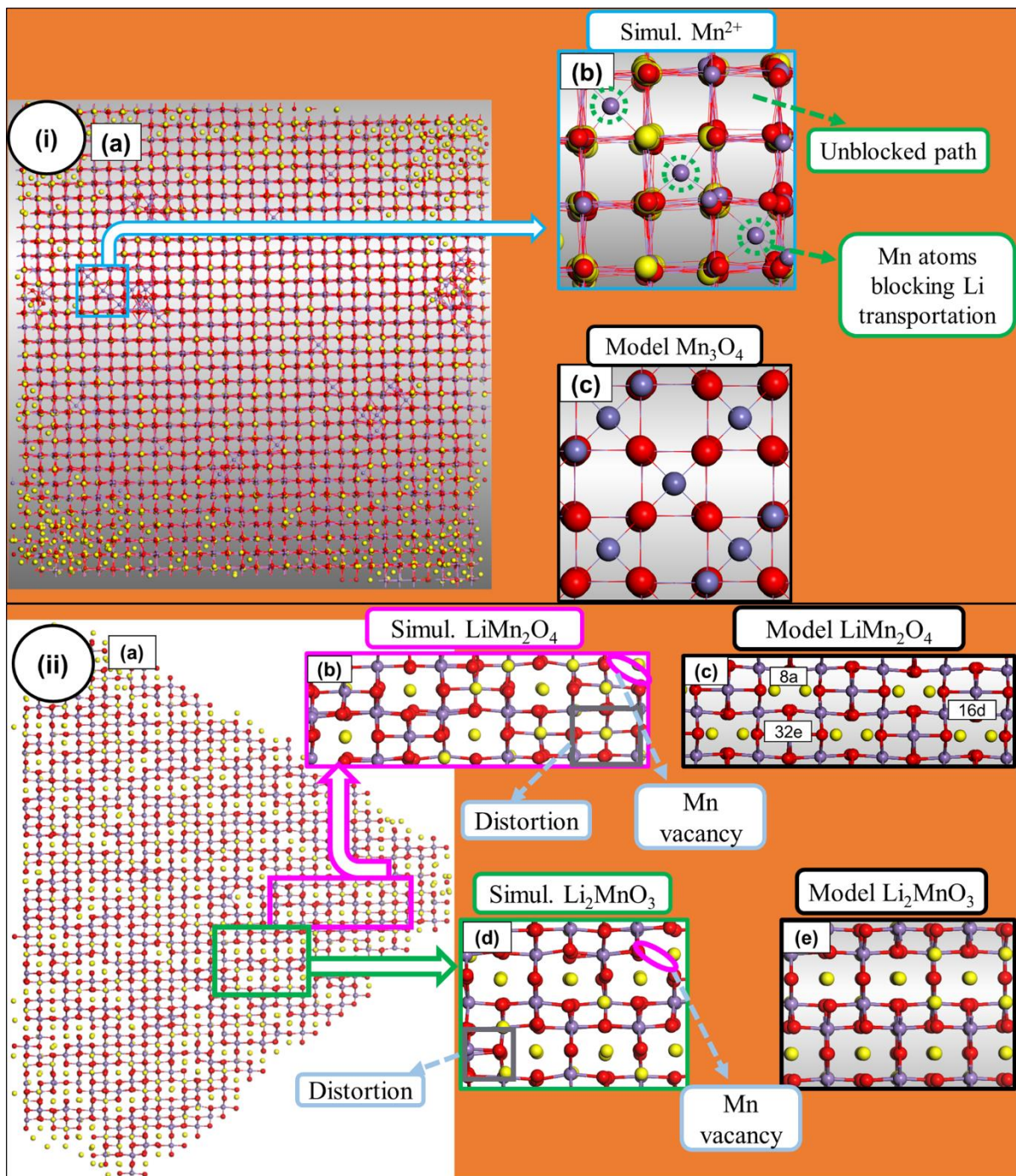


Figure 4. 28: The $\text{Li}_{2.00}\text{Mn}_2\text{O}_4$ bulk structure (i, a) illustrating (b) magnifications of Mn^{2+} atoms retraining the tetrahedral tunnels compared to (c) the perfect Mn_3O_4 structural model. The simulated microstructure of (ii, a) $\text{Li}_{2.00}\text{Mn}_2\text{O}_4$ bulk demonstrating the (b) layered Li_2MnO_3 and (d) spinel LiMn_2O_4 components, compared to their perfect structural models (c, e), respectively

4.5 Structural characterisation of the nanoporous and bulk structures by X-ray diffraction patterns

In this section, the X-ray diffractions patterns of nanoporous (75, 69 and 67 Å) and bulk structures are illustrated in figures 4.29 - 4.34, to characterise the structural components existing and formed within the materials during the discharge process under NST ensemble recrystallisation.

4.5.1 XRDs of nanoporous structures

The X-ray diffraction patterns for the simulated NST Li-Mn-O nanoporous structures in their pristine concentrations of $\text{Li}_{1.00}\text{Mn}_2\text{O}_4$ are illustrated in figure 4.29. These are compared with the experimental (d) spinel Mn_3O_4 [106], (e) spinel $\text{Li}_2\text{Mn}_2\text{O}_4$ [115], layered Li_2MnO_3 (f) [107] commonly found to co-exist with layered LiMnO_2 (g) [107] and spinel LiMn_2O_4 (h) [107]. The shoulder peak for $\sim 2\theta = 18 - 23^\circ$ related to spinel Mn_3O_4 , $\text{Li}_2\text{Mn}_2\text{O}_4$ and LiMn_2O_4 and layered Li_2MnO_3 show flattening peaks with a decrease in the lattice from nanoporous 75 Å to nanoporous 67 Å. The Peak at $\sim 2\theta = 32^\circ$ associated with spinel Mn_3O_4 decreases gradually in intensity with a decrease in lattice size for the nanoporous structures. The spinel $\text{Li}_2\text{Mn}_2\text{O}_4$ peak shifts towards the spinel Mn_3O_4 peak to the right at $\sim 2\theta = 36^\circ$ for all the nanoporous. Furthermore, peaks at $\sim 2\theta = 44^\circ$ associated with spinel LiMn_2O_4 , Mn_3O_4 and layered Li_2MnO_3 commonly coexisting with layered LiMnO_2 are observed in all the structures. The peak at $\sim 2\theta = 44^\circ$ is usually a common one for all the structures, however, the $\text{Li}_2\text{Mn}_2\text{O}_4$ polymorph is not yet observed and this is valid hence the structures are not yet full lithiated. Therefore, this peak is expected to be visible when the structures have been lithiated to $\text{Li}_{2.00}\text{Mn}_2\text{O}_4$ concentration. Finally, the peak at $\sim 2\theta = 67^\circ$ associated with LiMn_2O_4 , Mn_3O_4 and layered Li_2MnO_3 , has shifted towards the left where Li_2MnO_4 peaks are observed.

The XRD patterns for the simulated lithiated nanoporous 75 Å structures (a-e) with varying lithium concentrations; namely, $\text{Li}_{1.00}\text{Mn}_2\text{O}_4$, $\text{Li}_{1.25}\text{Mn}_2\text{O}_4$, $\text{Li}_{1.50}\text{Mn}_2\text{O}_4$, $\text{Li}_{1.75}\text{Mn}_2\text{O}_4$ and $\text{Li}_{2.00}\text{Mn}_2\text{O}_4$ are depicted in figure 4.30, showing significant peak splits and shifts during the discharge process. The shoulder peak for $\sim 2\theta = 18 - 23^\circ$ related to spinel-layered and their polymorphs for the simulated structures show peaks that are gradually decreasing with an increase in lithium concentration from $\text{Li}_{1.00}\text{Mn}_2\text{O}_4$ to $\text{Li}_{1.50}\text{Mn}_2\text{O}_4$. The peak re-emerges at $\text{Li}_{1.75}\text{Mn}_2\text{O}_4$ concentration and almost disappear again upon full lithiation ($\text{Li}_{2.00}\text{Mn}_2\text{O}_4$). Similar observations are made at $\sim 2\theta = 26 - 32^\circ$ for the peak associated with spinel Mn_3O_4 . Peaks at $\sim 2\theta = 36^\circ$ associated with spinel LiMn_2O_4 are observed for all the structures and tend to shift to the right favouring the Mn_3O_4 spinel component. Furthermore, the same peak for $\text{Li}_{1.25}\text{Mn}_2\text{O}_4$, $\text{Li}_{1.50}\text{Mn}_2\text{O}_4$ and $\text{Li}_{2.00}\text{Mn}_2\text{O}_4$ concentrations tend to split and spread over the range of $\sim 2\theta = 36 - 39^\circ$. Further splits and shifts are observed for the simulated structures at $\sim 2\theta = 44^\circ$ peak associated with spinel Mn_3O_4 , LiMn_2O_4 and layered Li_2MnO_3 . However, $\text{Li}_{1.00}\text{Mn}_2\text{O}_4$ and $\text{Li}_{1.75}\text{Mn}_2\text{O}_4$ do not split, rather shift to the left, favouring the LiMn_2O_4 spinel component. Moreover, splits and shifts are also observed at $\sim 2\theta = 64^\circ$ peak associated with spinel Mn_3O_4 , LiMn_2O_4 and layered Li_2MnO_3 , which shifts to the right still favouring both LiMn_2O_4 and layered Li_2MnO_3 components. The split and shift cover the range of $\sim 2\theta = 64 - 67^\circ$ and again, the splitting of the peak does not occur for $\text{Li}_{1.00}\text{Mn}_2\text{O}_4$ and $\text{Li}_{1.75}\text{Mn}_2\text{O}_4$. The $\text{Li}_{1.75}\text{Mn}_2\text{O}_4$ concentration depicts very broad peaks and this is the concentration where the structures showed grain boundaries; furthermore, going through a phase transition. The shifts, splits and broadening of peaks could be ascribed to the mixing of Li and Mn layers, phase transitions, defects generated in the Li-Mn-O systems during lithium intercalation [108, 109, 110].

Figure 4.31 illustrates (a-e) the XRDs for the simulated NST Li-Mn-O lithiated nanoporous 69 Å structures at different lithium concentrations ($\text{Li}_{1+x}\text{Mn}_2\text{O}_4$, $0 \leq x \leq 1$). The shoulder

peak at $\sim 2\theta = 18 - 23^\circ$ from the simulated structures associated with spinel Mn_3O_4 , $\text{Li}_2\text{Mn}_2\text{O}_4$ and LiMn_2O_4 and layered Li_2MnO_3 depict flatter peaks for all simulated concentrations. Furthermore, from the simulated structures, the peaks at $\sim 2\theta = 26 - 32^\circ$ associated with spinel Mn_3O_4 gradually decrease with an increase in lithium concentration from $\text{Li}_{1.00}\text{Mn}_2\text{O}_4$ to $\text{Li}_{1.50}\text{Mn}_2\text{O}_4$; then the peak re-emerges again at $\text{Li}_{1.75}\text{Mn}_2\text{O}_4$ concentration and disappears upon full lithiation ($\text{Li}_{2.00}\text{Mn}_2\text{O}_4$). The peak at $\sim 2\theta = 36^\circ$ for the simulated materials associated with spinel LiMn_2O_4 is observed and is shifting towards the right to the spinel Mn_3O_4 component. Splits are observed on the same peak for the $\text{Li}_{1.25}\text{Mn}_2\text{O}_4$, $\text{Li}_{1.50}\text{Mn}_2\text{O}_4$ and $\text{Li}_{2.00}\text{Mn}_2\text{O}_4$ concentrations. Further splits and shifts are observed at $\sim 2\theta = 44^\circ$; similar to peaks at $\sim 2\theta = 36^\circ$, only $\text{Li}_{1.25}\text{Mn}_2\text{O}_4$, $\text{Li}_{1.50}\text{Mn}_2\text{O}_4$ and $\text{Li}_{2.00}\text{Mn}_2\text{O}_4$ concentrations split. These shifts favour both the spinel and layered components. Moreover, for the peaks at $\sim 2\theta = 64^\circ$, splits and shifts are still observed for the concentrations of nanoporous 69 Å structures except for $\text{Li}_{1.00}\text{Mn}_2\text{O}_4$ and $\text{Li}_{1.75}\text{Mn}_2\text{O}_4$. The latter concentration shows narrower peaks compared to nanoporous 75 Å and its structure have only one grain boundary. This could imply that the structural changes happening to the structure are minimal. The splits and shifts observed on the nanoporous 69 Å structures are still believed to be attributed to the same factors mentioned in nanoporous 75 Å XRDs.

Simulated Li-Mn-O lithiated nanoporous 67 Å XRDs (a-e) structures with different lithium concentrations are illustrated in figure 4.32. The shoulder peaks from the simulated structures at $\sim 2\theta = 18 - 23^\circ$ associated with spinel Mn_3O_4 , $\text{Li}_2\text{Mn}_2\text{O}_4$ and LiMn_2O_4 and layered Li_2MnO_3 show flattening peaks, except for $\text{Li}_{1.75}\text{Mn}_2\text{O}_4$ concentration. Observations made at $\sim 2\theta = 26 - 32^\circ$, where the peak associated with spinel Mn_3O_4 is observed show a gradual decrease in intensity from $\text{Li}_{1.00}\text{Mn}_2\text{O}_4$ to $\text{Li}_{1.50}\text{Mn}_2\text{O}_4$ concentration. The peak then re-emerges at $\text{Li}_{1.75}\text{Mn}_2\text{O}_4$ concentration and almost disappear again when the

structure is fully lithiated at $\text{Li}_{2.00}\text{Mn}_2\text{O}_4$. The peak at $\sim 2\theta = 36^\circ$ for the simulated structures associated with spinel LiMn_2O_4 is observed with some shifts and splits and has shifted towards the right, to the spinel Mn_3O_4 component. Further splits are observed for $\text{Li}_{1.25}\text{Mn}_2\text{O}_4$ and $\text{Li}_{1.50}\text{Mn}_2\text{O}_4$ and $\text{Li}_{2.00}\text{Mn}_2\text{O}_4$ concentrations. Moreover, splits and shifts are observed at $\sim 2\theta = 44^\circ$ associated with spinel Mn_3O_4 , LiMn_2O_4 and $\text{Li}_2\text{Mn}_2\text{O}_4$ and layered Li_2MnO_3 . Lastly, at $\sim 2\theta = 64^\circ$ for the simulated structures, peak splits and shifts are also observed. The $\text{Li}_{1.00}\text{Mn}_2\text{O}_4$ and $\text{Li}_{1.75}\text{Mn}_2\text{O}_4$ concentrations do not split and the latter depict broad peaks. The $\text{Li}_{1.75}\text{Mn}_2\text{O}_4$ has shown grain boundaries and is transitioning from the cubic to the tetragonal phase.

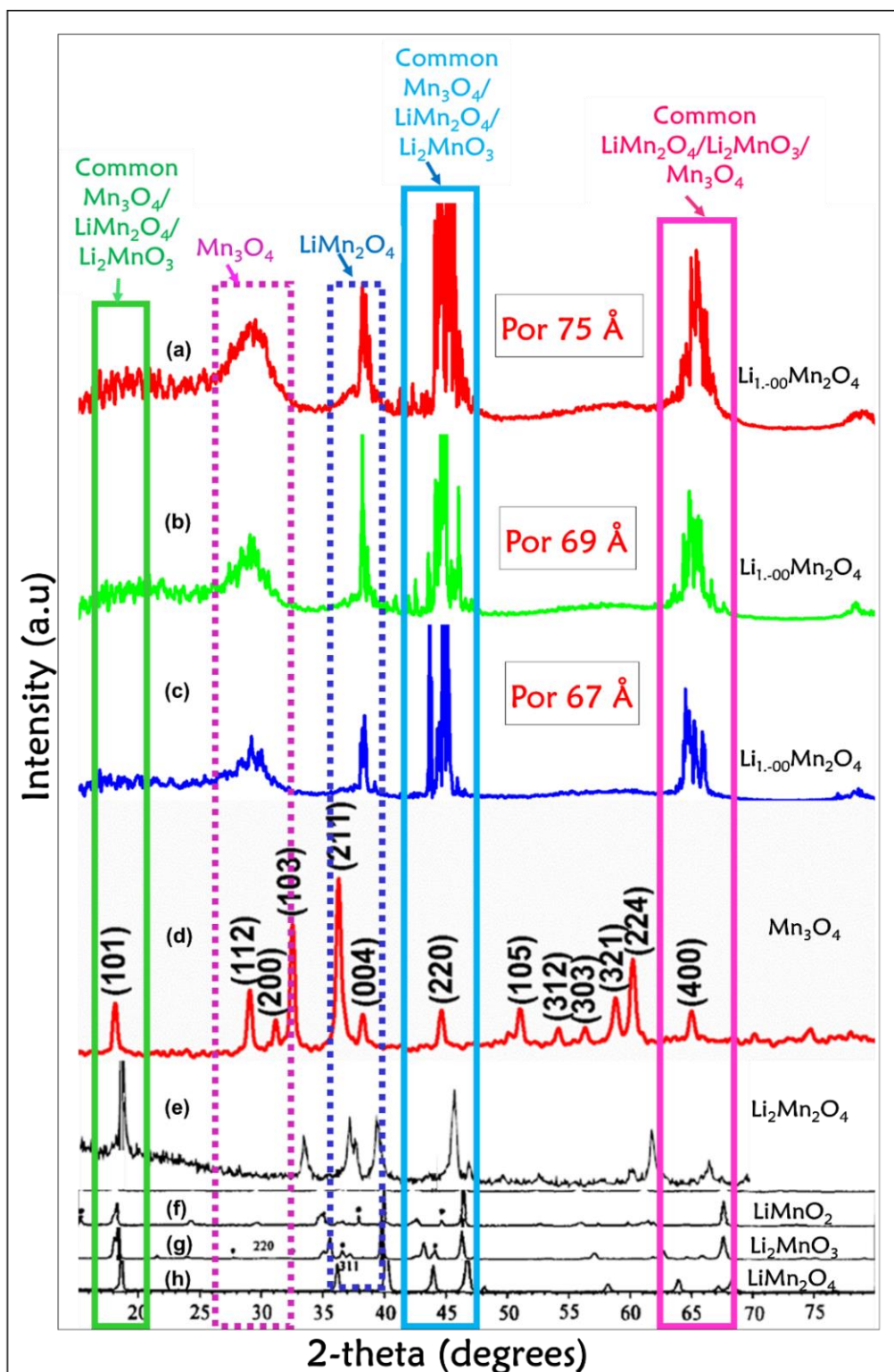


Figure 4. 29: The lithiated XRDs for structures recrystallised under NST ensemble in their pristine form of $\text{Li}_{1.00}\text{Mn}_2\text{O}_4$ concentration for (a) nanoporous 75 Å, (b) nanoporous 69 Å and (c) nanoporous 67 Å structures compared to experimental XRDs for (d) spinel Mn_3O_4 [106], (e) spinel $\text{Li}_2\text{Mn}_2\text{O}_4$ [115], (f) layered LiMnO_2 [107], (g) layered Li_2MnO_3 [107] and (h) spinel LiMn_2O_4 [107].

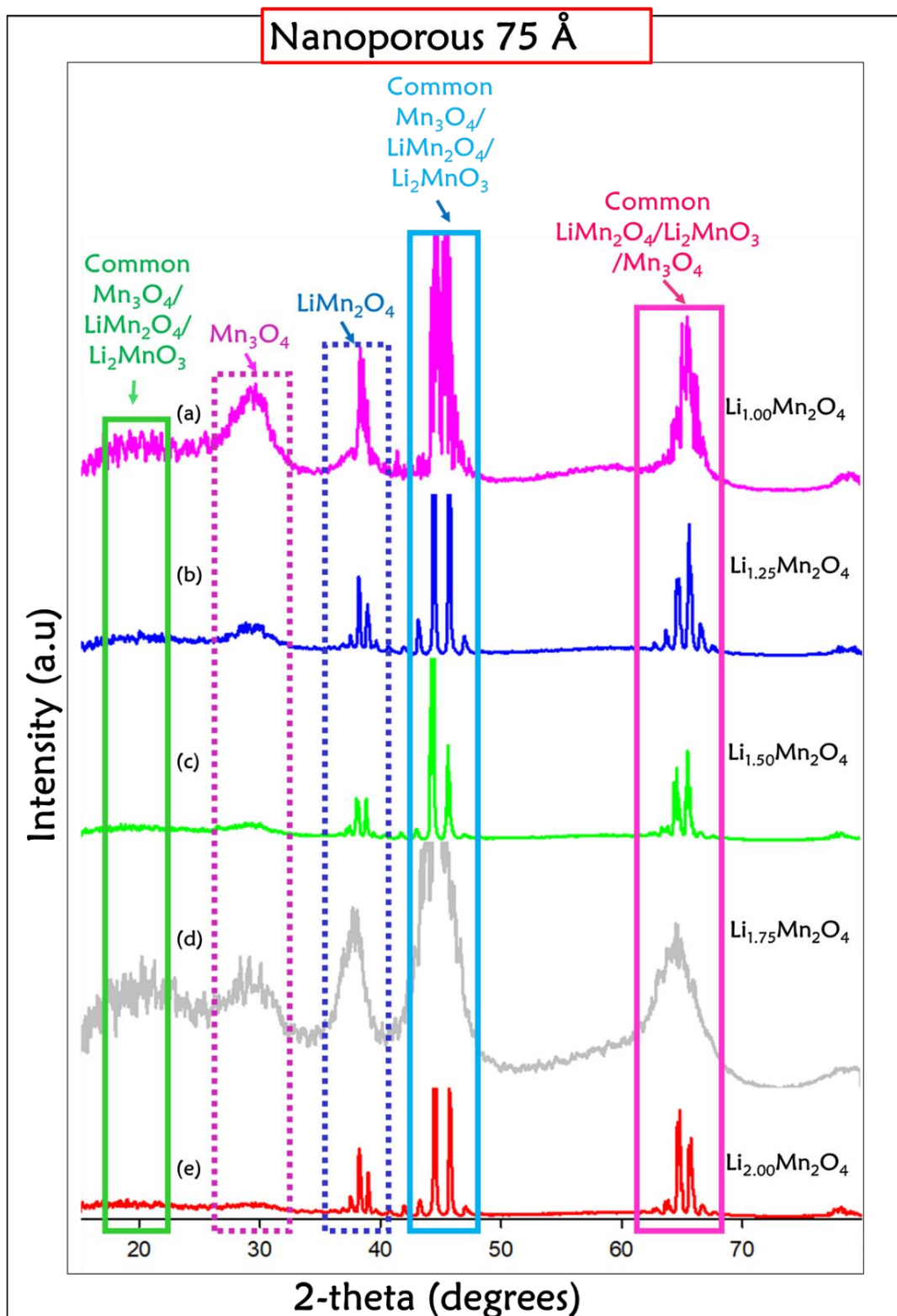


Figure 4. 30: The X-ray diffraction patterns (XRDs) for the $\text{Li}_{1+x}\text{Mn}_2\text{O}_4$, $0 \leq x \leq 1$ simulated nanoporous 75 Å structures where (a) is the $\text{Li}_{1.00}\text{Mn}_2\text{O}_4$, (b) $\text{Li}_{1.25}\text{Mn}_2\text{O}_4$, (c) $\text{Li}_{1.50}\text{Mn}_2\text{O}_4$, (d) $\text{Li}_{1.75}\text{Mn}_2\text{O}_4$ and (e) $\text{Li}_{2.00}\text{Mn}_2\text{O}_4$ concentration.

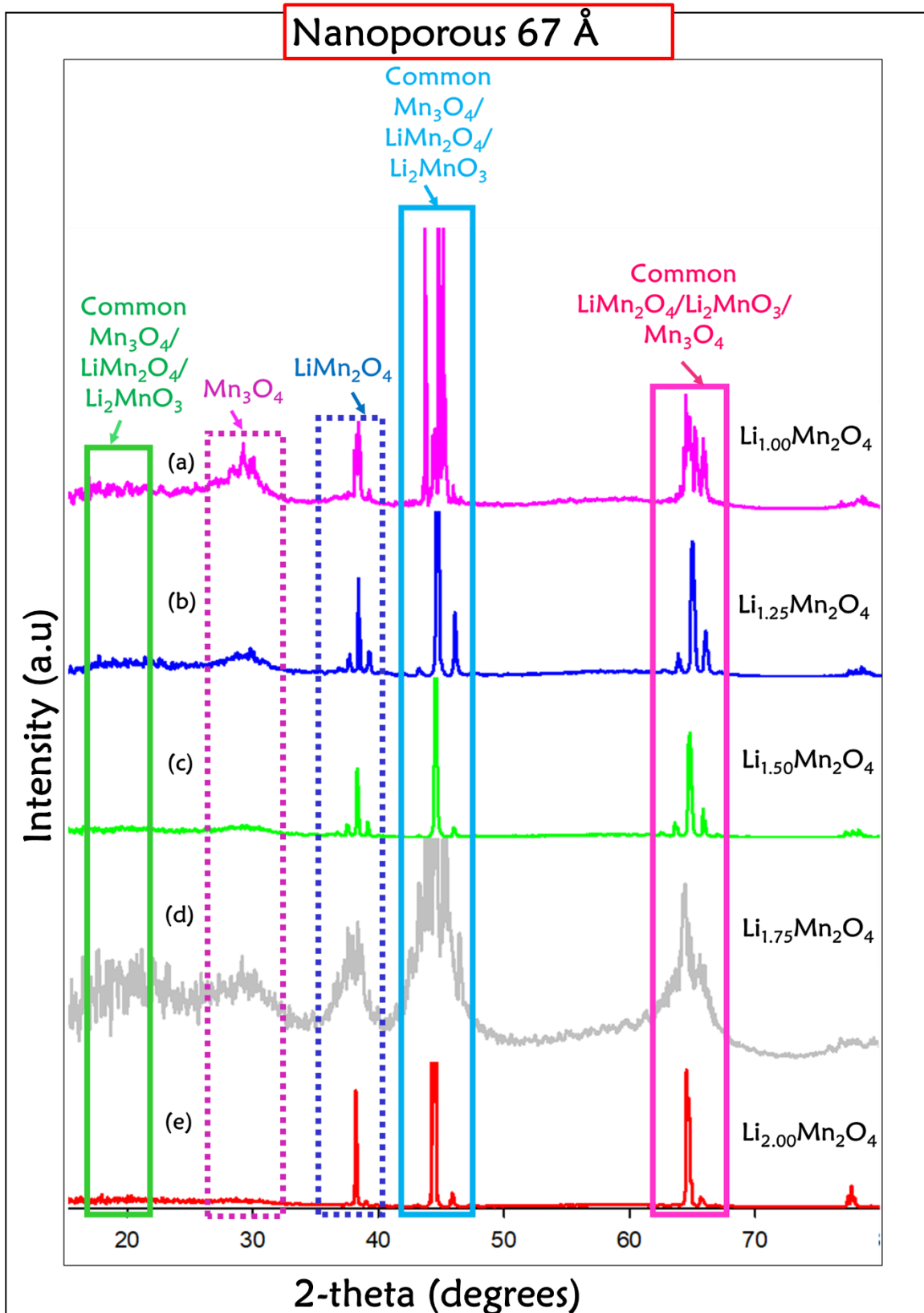


Figure 4. 32: The X-ray diffraction patterns for $\text{Li}_{1+x}\text{Mn}_2\text{O}_4$, $0 \leq x \leq 1$ nanoporous 67 Å structures for (a) $\text{Li}_{1.00}\text{Mn}_2\text{O}_4$, (b) $\text{Li}_{1.25}\text{Mn}_2\text{O}_4$, (c) $\text{Li}_{1.50}\text{Mn}_2\text{O}_4$, (d) $\text{Li}_{1.75}\text{Mn}_2\text{O}_4$ and (e) $\text{Li}_{2.00}\text{Mn}_2\text{O}_4$ concentrations.

4.5.2 XRDs for the bulk structure

The X-ray diffraction pattern for the simulated NST Li-Mn-O bulk (63 Å) structure in its pristine form of $\text{Li}_{1.00}\text{Mn}_2\text{O}_4$ concentration compared to the experimental results for (f) spinel Mn_3O_4 [106], (g) spinel $\text{Li}_2\text{Mn}_2\text{O}_4$ [115], layered Li_2MnO_3 (h) co-existing with layered LiMnO_2 (i) [107] and spinel LiMn_2O_4 (j) [107] is illustrated in figure 4.33. The pristine simulated XRD at $\sim 2\theta = 18 - 23^\circ$ depicts a peak shift to the right moving towards the Li_2MnO_3 component. The peak at $\sim 2\theta = 26 - 32^\circ$ associated with Mn_3O_4 is observed and has not shifted. Furthermore, at $\sim 2\theta = 36^\circ$, the peak associated with spinel LiMn_2O_4 is observed as well. Finally, the common peaks of layered and spinel at $\sim 2\theta = 44^\circ$ and $\sim 2\theta = 64^\circ$ are observed and appear to be broader compared to the experimental.

The XRDs for the simulated lithiated bulk structures with different concentrations, $\text{Li}_{1+x}\text{Mn}_2\text{O}_4$ ($0 \leq x \leq 1$) are illustrated in figure 4.34. Observations made on the simulated structures show that the shoulder peak at $\sim 2\theta = 18 - 23^\circ$ related to spinel Mn_3O_4 , $\text{Li}_2\text{Mn}_2\text{O}_4$ and LiMn_2O_4 and layered Li_2MnO_3 progressively decrease with increasing lithium from pristine spinel ($\text{Li}_{1.00}\text{Mn}_2\text{O}_4$) to full lithiation ($\text{Li}_{2.00}\text{Mn}_2\text{O}_4$). Furthermore, the peak observed at $\sim 2\theta = 26 - 32^\circ$ associated with spinel Mn_3O_4 gradually decrease with an increase in lithium concentration to $\text{Li}_{1.50}\text{Mn}_2\text{O}_4$ and re-emerge at $\text{Li}_{1.75}\text{Mn}_2\text{O}_4$ to completely disappear upon full lithiation. These peaks characterise the spinel Mn_3O_4 and are observed for all the structures. Moreover, for all the concentrations, there are no peak splits, this is contrary to what is observed on the NVT bulk structures. The $\sim 2\theta = 44^\circ$ peak associated with spinel Mn_3O_4 , LiMn_2O_4 and layered Li_2MnO_3 is also observed for all the structures and only splitting for the $\text{Li}_{1.75}\text{Mn}_2\text{O}_4$ but shift for the other concentrations. Lastly, at $\sim 2\theta = 64^\circ$, the peak associated with spinel Mn_3O_4 and LiMn_2O_4 and layered Li_2MnO_3 does not split for all the structures. The shifting and splitting of peaks could be

ascribed to the mixing of Li and Mn layers, phase transitions, defects generated in the Li-Mn-O systems during lithium intercalation [108, 109, 110].

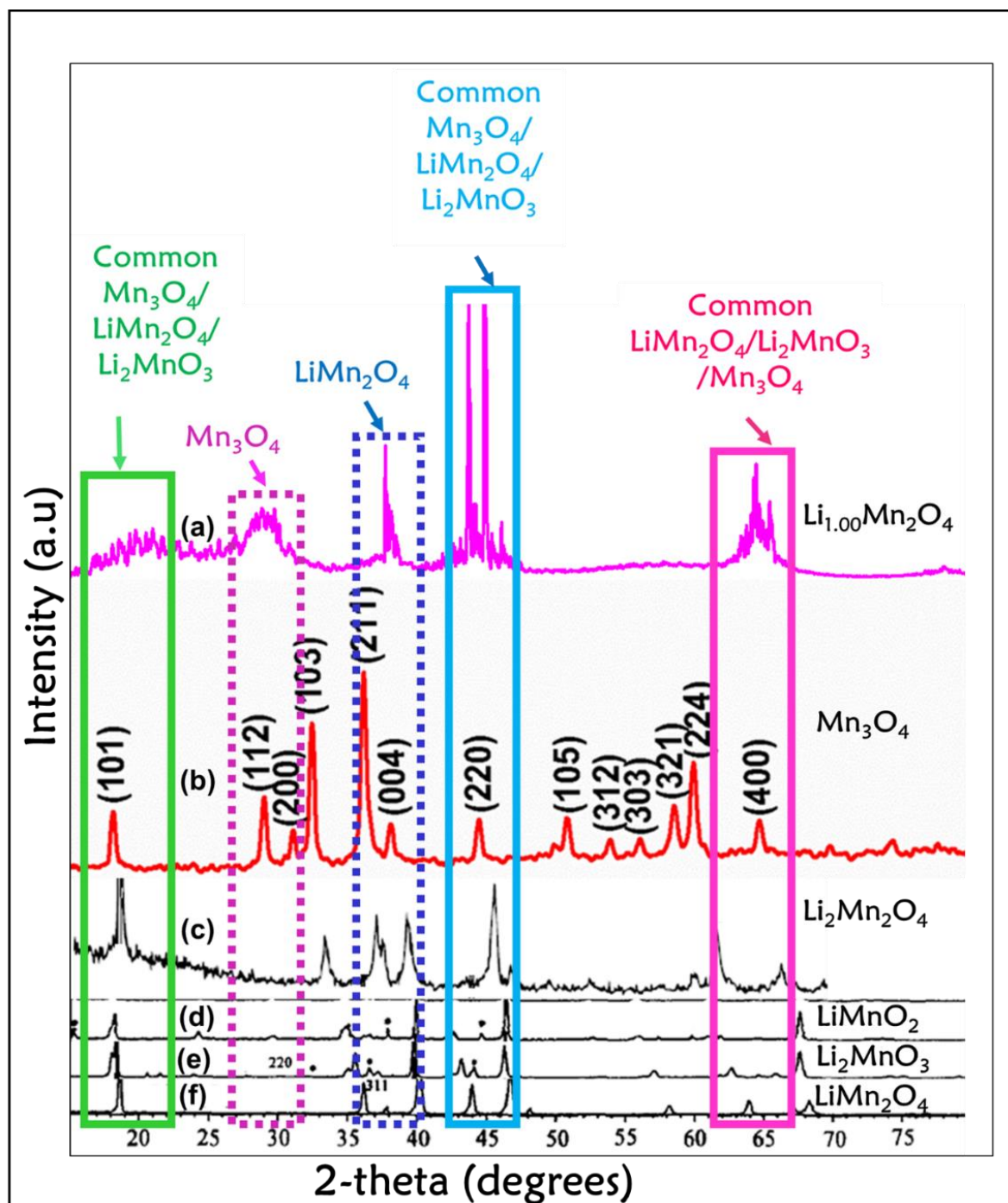


Figure 4. 33: The NST X-ray diffraction patterns (XRDs) for the simulated pristine bulk structure at (a) $\text{Li}_{1.00}\text{Mn}_2\text{O}_4$ concentration, compared with the experimental XRDs for (b) spinel Mn_3O_4 [106], (c) spinel $\text{Li}_2\text{Mn}_2\text{O}_4$ [115], (d) layered LiMnO_2 [107], (e) layered Li_2MnO_3 [107] and (f) spinel LiMn_2O_4 [107].

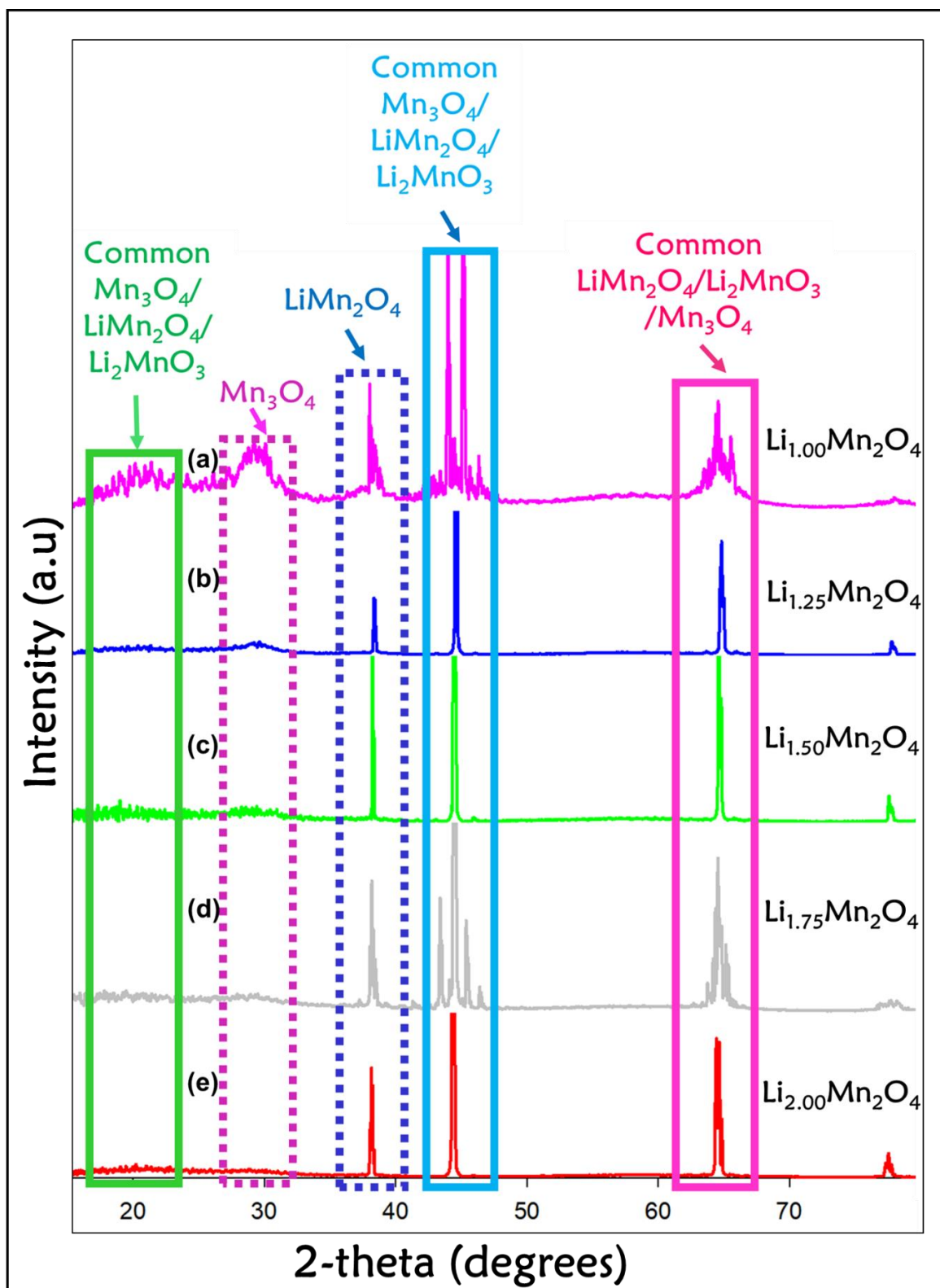


Figure 4. 34: The NST X-ray diffraction patterns (XRDs) for simulated bulk structures depicting the (a) $\text{Li}_{1.00}\text{Mn}_2\text{O}_4$, (b) $\text{Li}_{1.25}\text{Mn}_2\text{O}_4$, (c) $\text{Li}_{1.50}\text{Mn}_2\text{O}_4$, (d) $\text{Li}_{1.75}\text{Mn}_2\text{O}_4$ and (e) $\text{Li}_{2.00}\text{Mn}_2\text{O}_4$ concentrations.

4. 6 Discussion

The simulated three nanoporous and bulk structures with varying lithium concentrations $\text{Li}_{1+x}\text{Mn}_2\text{O}_4$, $0 \leq x \leq 1$ have been successfully recrystallised under the NST ensemble using molecular dynamics methods. The structures have evolved into single and multiple grains during recrystallisation and lithiation, especially at the $\text{Li}_{1.75}\text{Mn}_2\text{O}_4$ concentration. The pore sizes of the nanoporous structures reduce with increasing lithium content except for nanoporous 69 and 67 Å at $\text{Li}_{1.00}\text{Mn}_2\text{O}_4$ to $\text{Li}_{1.25}\text{Mn}_2\text{O}_4$; here, the pores increase in size. However, the pore reduces when the concentration is increased to $\text{Li}_{1.50}\text{Mn}_2\text{O}_4$ and eventually close up for nanoporous 69 and 67 Å at $\text{Li}_{1.75}\text{Mn}_2\text{O}_4$. Whilst for nanoporous 75 Å, the pore continuously reduce with increasing lithium concentration to $\text{Li}_{2.00}\text{Mn}_2\text{O}_4$. Similarly for all the structures, upon full lithiation at $\text{Li}_{2.00}\text{Mn}_2\text{O}_4$ concentration, the pores almost regain their original sizes.

The structural compositions and defects existing in both the nanoporous and bulk material are similar and decrease with increasing lithium content. The Mn_3O_4 component decreasing with increasing lithium content is also validated by the findings of Tang et al. [105] when investigating “surface structure evolution of LiMn_2O_4 cathode material upon charge and discharge”. Structures that evolve into multiple crystals denoted by grain boundaries are observed especially at $\text{Li}_{1.75}\text{Mn}_2\text{O}_4$ concentration; this is a critical concentration where the materials undergo a phase change from cubic to tetragonal phase. The phase transition from cubic spinel to tetragonal spinel was reported in literature that it occurs due to the non-equilibrium lithiation and loss of crystallinity during the cycling process [105]. Interestingly, the bulk does not have any grain boundaries at any concentration.

The X-ray diffraction patterns for the nanoporous and bulk structures show significant peak splits and shifts. Further observations on the NST XRDs shows that they are in accord with the NVT XRDs, with the shifts and splits of the same characteristic peaks only differing in intensity. The $\text{Li}_{1.75}\text{Mn}_2\text{O}_4$ concentration is more resistant to peak splits and displays very broad peaks for nanoporous 75 and 67 Å, whilst for nanoporous 69 Å and the bulk display narrow peaks. The peak associated with the Mn_3O_4 component at $\sim 2\theta = 36^\circ$ reduces with increasing lithium content; however, after almost disappearing at $\text{Li}_{1.50}\text{Mn}_2\text{O}_4$ the peak re-emerges at $\text{Li}_{1.75}\text{Mn}_2\text{O}_4$ and almost disappear again upon full lithiation at $\text{Li}_{2.00}\text{Mn}_2\text{O}_4$. This peak can be associated with the phase change occurring at this concentration.

It can clearly be deduced that the nanoporous 69 Å structure behaves differently from the other two nanoporous and bulk structures at the $\text{Li}_{1.75}\text{Mn}_2\text{O}_4$ concentration. The structure is resilient to expansion, showing a structure that recrystallises into only two crystals instead of multiple; narrower peaks instead of broad peaks are observed as well. Although the observations made on the bulk shows structures that have recrystallised to a single crystal throughout with lithiation, the structure fails to expand at $\text{Li}_{1.75}\text{Mn}_2\text{O}_4$ and reduce in size, however, the structural integrity is still maintained. It can be assumed that the spinel Mn_3O_4 walls have collapsed thus reducing the volume of the bulk. The observations made on NST recrystallised structures reveal that nanoporous 69 Å is more robust as it resistant to structural changes especially at the disruptive concentration of $\text{Li}_{1.75}\text{Mn}_2\text{O}_4$ its counterparts are mostly fragile. This shows that it is not easily prone to fracture since it can withstand cell expansion with increased lithium expansion, without damaging the structure.

CHAPTER 5

The effect of high temperature on $\text{Li}_{1+x}\text{Mn}_2\text{O}_4$ nanoporous and bulk materials

5.1 Introduction

One of the major limitations associated with lithium ion batteries despite their superior properties such as their high voltage [116], great cycling performance [117], being environmentally friendly and being cost-efficient is the impact of temperature which can also affect the diffusivity of lithium. This is of interest because the severe capacity fade or deterioration of spinel LiMn_2O_4 at elevated temperatures restrict the widespread application in lithium ion batteries [118]. The general acceptable operating temperature in literature for these batteries has been reported to range 253 - 333 K [119]. However, Pesaran and et al. [120] showed that the best and favourable operational temperature for lithium batteries is 228 ~ 308K. Once the temperature is out of these suitable ranges the battery may degrade fast during cycling and impose health hazards and explode [119].

The environment plays a role in implicating the functionality of the battery, which means that suitable operating temperature conditions need to be thoroughly investigated for its optimum functionality. In this chapter, the diffusion coefficients of the Li-Mn-O ions in the nanoporous structures 75, 69 and 67 Å together with the bulk (63 Å) while temperature (100 - 2500 K) is increased will be investigated using molecular dynamics simulations. The rationale behind the elevated temperatures up to 2500 K, and investigating the temperatures in between is to clearly understand the diffusion phenomena of lithium and how it may impact the cycling process. The diffusion coefficients of Li-Mn-O nanoporous structures have varying lithium concentrations of spinel $\text{Li}_{1+x}\text{Mn}_2\text{O}_4$, where $0 \leq x \leq 1$.

5.2 Method

Molecular dynamics simulations using the DL_POLY code was employed to perform all calculations yielding diffusion coefficients for the Li-Mn-O nanoporous (75, 69 and 67 Å) and bulk structures at different lithium concentrations, $\text{Li}_{1+x}\text{Mn}_2\text{O}_4$, where $0 \leq x \leq 1$. The structures were recrystallised at 1700 K for 150 ps using the NST ensemble where, N = constant number of particles, S = constant stress and T = constant temperature, equilibrated to 0 K using the NVT ensemble, where, N = constant number of particles, V = constant volume and T = constant temperature. The temperature was then systemically increased by intervals of 100 to 2500 K at 300 ps to investigate the diffusion coefficients of the Li-Mn-O ions in the nanoporous and bulk structures with varying lithium concentrations. Furthermore, the OUTPUT file was exported for each temperature to record the diffusion coefficients at each lithium concentration for all the structures.

5.3 The lithium diffusion coefficients for the nanoporous and bulk at different lithium concentrations

The lithium cation diffusion coefficients for nanoporous 75 Å with different concentrations of $\text{Li}_{1+x}\text{Mn}_2\text{O}_4$, where $0 \leq x \leq 1$ are depicted in figure 5.1. The lithium cations at $\text{Li}_{1.00}\text{Mn}_2\text{O}_4$, $\text{Li}_{1.25}\text{Mn}_2\text{O}_4$, $\text{Li}_{1.50}\text{Mn}_2\text{O}_4$ and $\text{Li}_{1.75}\text{Mn}_2\text{O}_4$ concentrations start to diffuse slightly above 600 K and the mobility increase exponentially until 1700K. The 1700 K has been reported as the melting temperature for the structures [72]. At temperatures 1800K and above, an increase in lithium mobility is observed, however, there are fluctuations in the increment. The lithium cations for the $\text{Li}_{2.00}\text{Mn}_2\text{O}_4$ concentration start to diffuse slightly above 100 K. There are fluctuations in the mobility of the lithium with an increment of temperature from 100 to 2500 K. For all the nanoporous 75 Å concentrations the diffusion coefficients increase with increasing temperature, with $\text{Li}_{2.00}\text{Mn}_2\text{O}_4$ concentration displaying the

highest diffusion. The high diffusion at $\text{Li}_{2.00}\text{Mn}_2\text{O}_4$ could be ascribed to the decrease of Mn_3O_4 content with increasing concentration allowing migration of lithium through the tetrahedral tunnels.

The diffusion coefficients for nanoporous 69 Å structures are illustrated in figure 5.2 with varying lithium concentrations of $\text{Li}_{1+x}\text{Mn}_2\text{O}_4$ ($0 \leq x \leq 1$). The lithium cations for all the structures start to show diffusion slightly above 700 K; which implies that there is very minimal diffusion, probably $< 1\text{nm}^2/\text{s}$ below 700 K and room temperature. From 1800 K the diffusivity of lithium in the materials continues to increase to 2500K. The $\text{Li}_{2.00}\text{Mn}_2\text{O}_4$ from 100 to 1700K shows the highest diffusion, followed by $\text{Li}_{1.00}\text{Mn}_2\text{O}_4$, then $\text{Li}_{1.25}\text{Mn}_2\text{O}_4$ and $\text{Li}_{1.50}\text{Mn}_2\text{O}_4$. Then finally, the $\text{Li}_{1.75}\text{Mn}_2\text{O}_4$ which is the structure that has been identified to have grain boundaries; and here it is observed that has lower diffusion compared to its counterpart's concentration nanoporous in this study.

Figure 5.3 illustrates the diffusion coefficients of nanoporous 67 Å with different lithium concentrations of $\text{Li}_{1+x}\text{Mn}_2\text{O}_4$, where $0 \leq x \leq 1$. The plots show that the lithium cations start to slowly diffuse at temperatures above 700 K and increase exponentially. Temperatures below 500 K illustrates diffusion coefficients rates at more or less $1\text{nm}^2/\text{s}$ for all the structures. Above the 1700 K temperature fluctuations in lithium diffusion coefficients are observed for all the concentrations. The $\text{Li}_{1.25}\text{Mn}_2\text{O}_4$ concentration shows the highest diffusivity, followed by the $\text{Li}_{1.00}\text{Mn}_2\text{O}_4$, $\text{Li}_{1.50}\text{Mn}_2\text{O}_4$ and $\text{Li}_{2.00}\text{Mn}_2\text{O}_4$ respectively, then finally, by the $\text{Li}_{1.75}\text{Mn}_2\text{O}_4$ concentration.

Figure 5.4 illustrates the lithium diffusion coefficients for bulk structures at varying concentrations of spinel $\text{Li}_{1+x}\text{Mn}_2\text{O}_4$, where $0 \leq x \leq 1$. The lithium cations start to diffuse slowly from a temperature above 900 K for all the concentrations except for $\text{Li}_{2.00}\text{Mn}_2\text{O}_4$ which start at 800 K. The lithium mobility increases with temperature for all the structures to 1800 K; such that above 1900 K $\text{Li}_{1.50}\text{Mn}_2\text{O}_4$ has the highest diffusivity, followed by

Li_{1.75}Mn₂O₄, then Li_{1.25}Mn₂O₄ and Li_{1.00}Mn₂O₄; with the Li_{2.00}Mn₂O₄ concentration having the least diffusion. Above 1800 K temperature lithium mobility fluctuations are observed within the structures up until 2500 K; with Li_{1.50}Mn₂O₄ having the highest diffusion, but now followed by Li_{1.00}Mn₂O₄, then Li_{1.25}Mn₂O₄ and Li_{1.75}Mn₂O₄, respectively. Li_{2.00}Mn₂O₄ have the lowest diffusion.

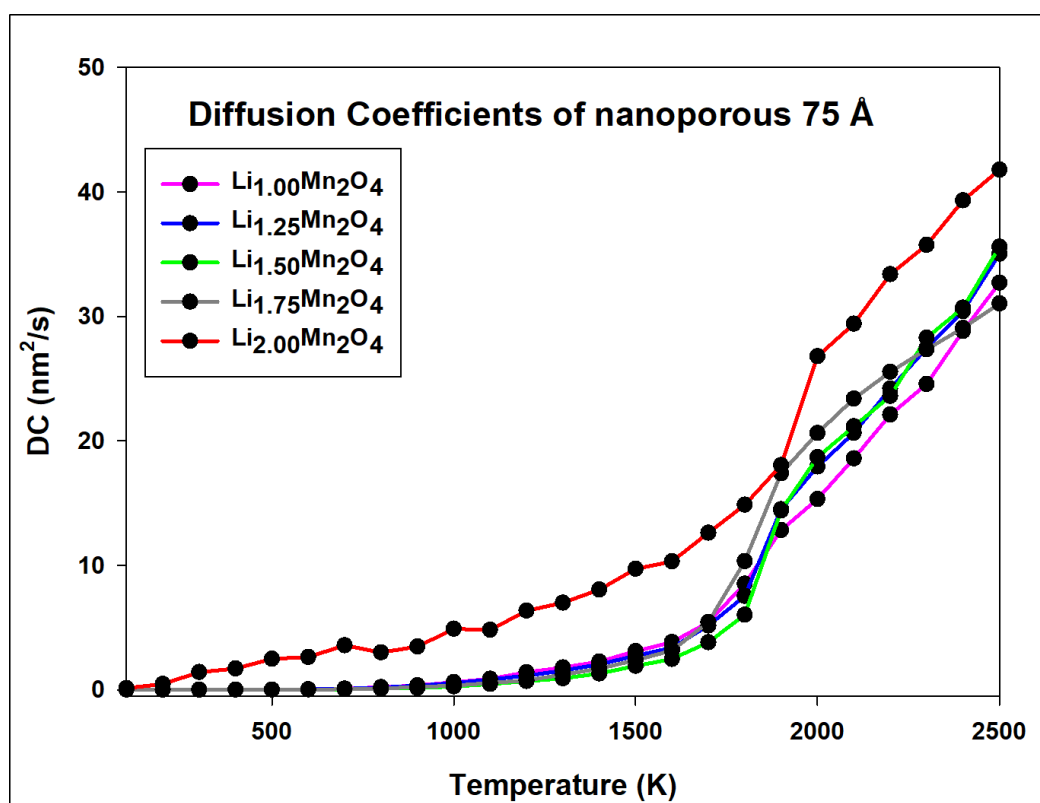


Figure 5.1: The diffusion coefficients plots for nanoporous 75 Å at different lithium concentrations of Li_{1+x}Mn₂O₄, where 0 ≤ x ≤ 1 with increasing temperature (K).

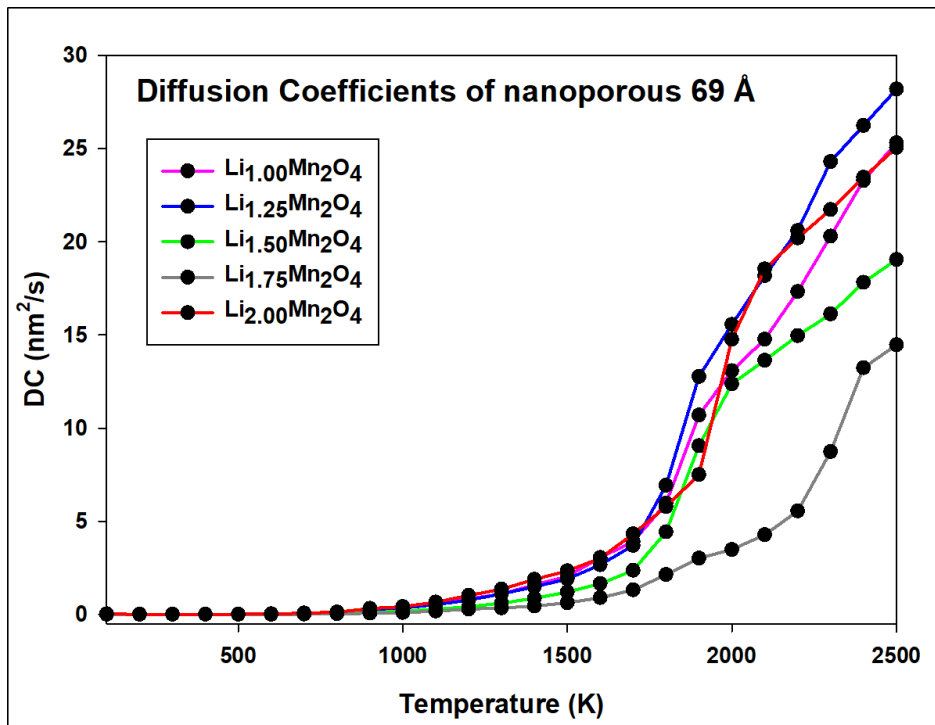


Figure 5.2: Plots for the diffusion coefficients of lithium for nanoporous 69 Å structure with different concentrations of $\text{Li}_{1.00}\text{Mn}_2\text{O}_4$, $\text{Li}_{1.25}\text{Mn}_2\text{O}_4$, $\text{Li}_{1.50}\text{Mn}_2\text{O}_4$, $\text{Li}_{1.75}\text{Mn}_2\text{O}_4$ and $\text{Li}_{2.00}\text{Mn}_2\text{O}_4$ with increasing temperature.

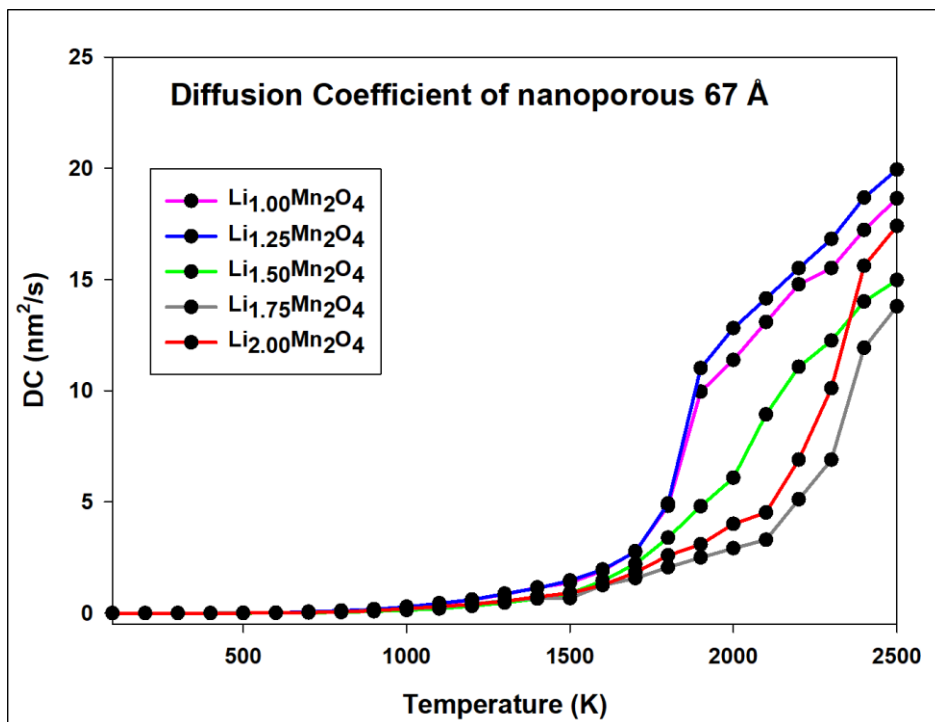


Figure 5.3: Different lithium concentrations, $\text{Li}_{1+x}\text{Mn}_2\text{O}_4$ ($0 \leq x \leq 1$) showing the diffusion coefficient plots for nanoporous 67 Å with increasing temperature (K).

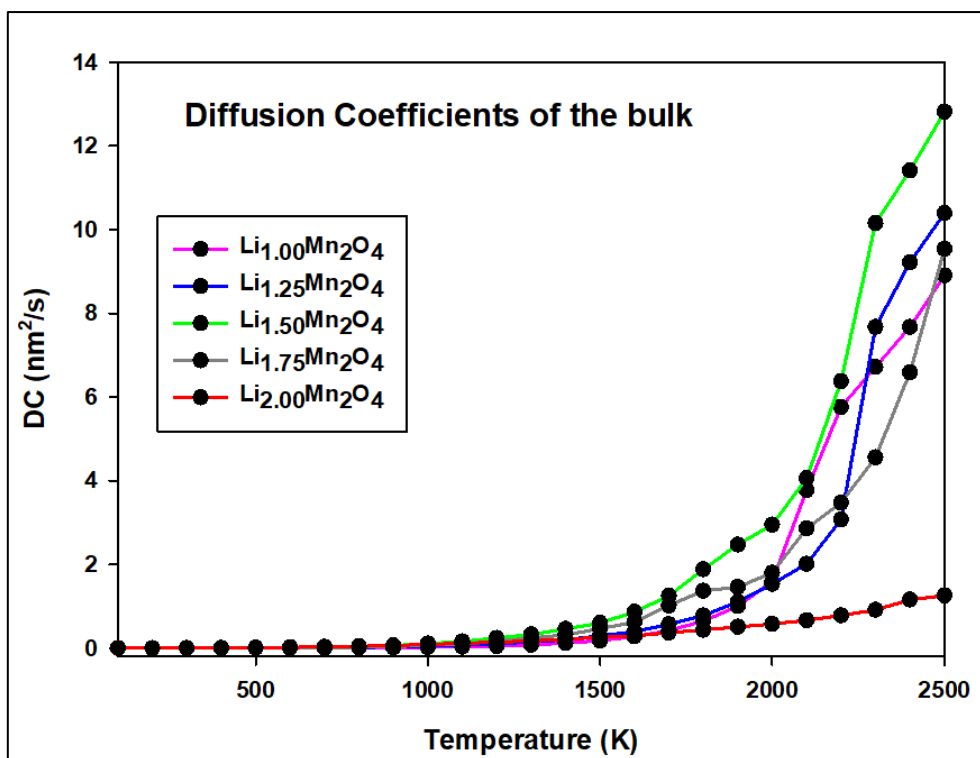


Figure 5.4: Diffusion coefficients for bulk structures at $Li_{1.00}Mn_2O_4$, $Li_{1.25}Mn_2O_4$, $Li_{1.50}Mn_2O_4$, $Li_{1.75}Mn_2O_4$ and $Li_{2.00}Mn_2O_4$ concentrations with increasing temperature (K).

5.4 The Li-Mn-O diffusion coefficients of the pristine nanoporous and bulk structures

The diffusion coefficients for the Li-Mn-O nanoporous 75 Å ions at $Li_{1.00}Mn_2O_4$ are illustrated in figure 5.5. Lithium cations start to diffuse at 500 K and show an exponential increase to 1900 K. However, it still increases to 2500 K. The manganese and oxygen cation and anion show a similar plot trend, where they slowly start to diffuse at 1600 K, then increase in mobility to 2500 K. The insert in the figure depicts conditions under a range of room temperature (293.15 – 295.15 K) where there is $< 1 \text{ nm}^2/\text{s}$ diffusion coefficients.

The individual element diffusion coefficients for the Li-Mn-O nanoporous 69 Å $Li_{1.00}Mn_2O_4$ is illustrated in figure 5.6. The lithium cations start to diffuse at 550 K and increase

exponentially to 1900 K. However, further increase in lithium diffusion is still observed until 2500 K. The manganese mobility is observed from 1700 K which is the melting point of the structure and increase slightly to 2500 K at a more or less the equivalent rate. The oxygen plot shows a similar diffusion pattern to that of manganese. The insert in the figure shows the diffusion of the Li-Mn-O components below room temperature where their mobility is $< 1 \text{ nm}^2/\text{s}$.

The Li-Mn-O nanoporous 67 Å structure at $\text{Li}_{1.00}\text{Mn}_2\text{O}_4$ concentration is depicted in figure 5.7 showing the diffusion coefficients of individual ions. The lithium cation starts to diffuse from 500 K and exponentially increase up to 1900 K. The lithium mobility continues to increase above 1900 to 2500 K, however, not exponentially. Manganese starts to diffuse slightly at 1700 K, where at 2100 K there is a turning point observed and consequently there is a decrease in diffusivity to 2200 K. Subsequently, a slight increase to 2500 K is observed. The diffusion of oxygen starts slightly at 1700K as well and increases to 2500 K. The insert in the figure shows the diffusion coefficients of structures below room temperature, where there is $< 1\text{nm}^2/\text{s}$ diffusivity.

The diffusion coefficient of Li-Mn-O ions for the bulk $\text{Li}_{1.00}\text{Mn}_2\text{O}_4$ is illustrated in figure 5.8. The lithium cations start to diffuse slowly above the temperature of 900 K and increase exponentially to 2000 K. A very sharp increase in lithium mobility is observed thereafter. The manganese plot starts to diffusion above 1200 K. At 1600 K there is a sharp increase in manganese mobility to 1700 K, followed by a significant decrease at 1800 K then a slight increase to 2000 K. The plot shows further mobility increase to 2500 K. The oxygen plot shows diffusion from 2000 K which increases to 2500 K. The insert in the figure depicts temperatures below 500 K; including those at room temperature showing the diffusivities of the ions where the values are negligible.

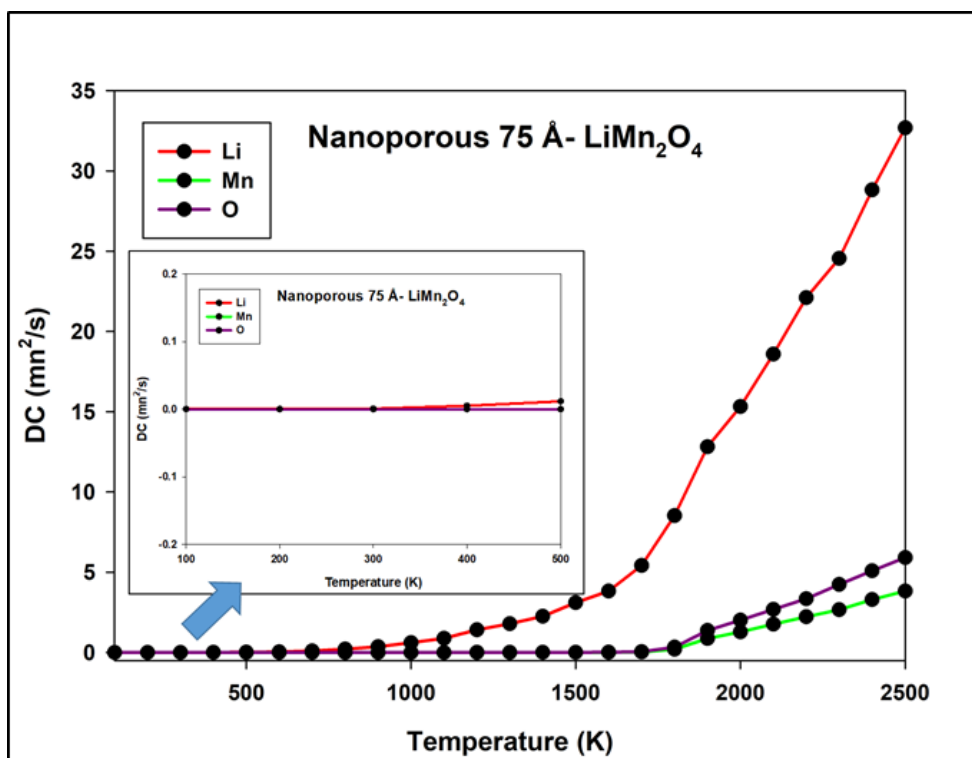


Figure 5.5: The diffusion coefficients of the Li-Mn-O nanoporous 75 Å structure at $\text{Li}_{1.00}\text{Mn}_2\text{O}_4$ concentration with different temperatures.

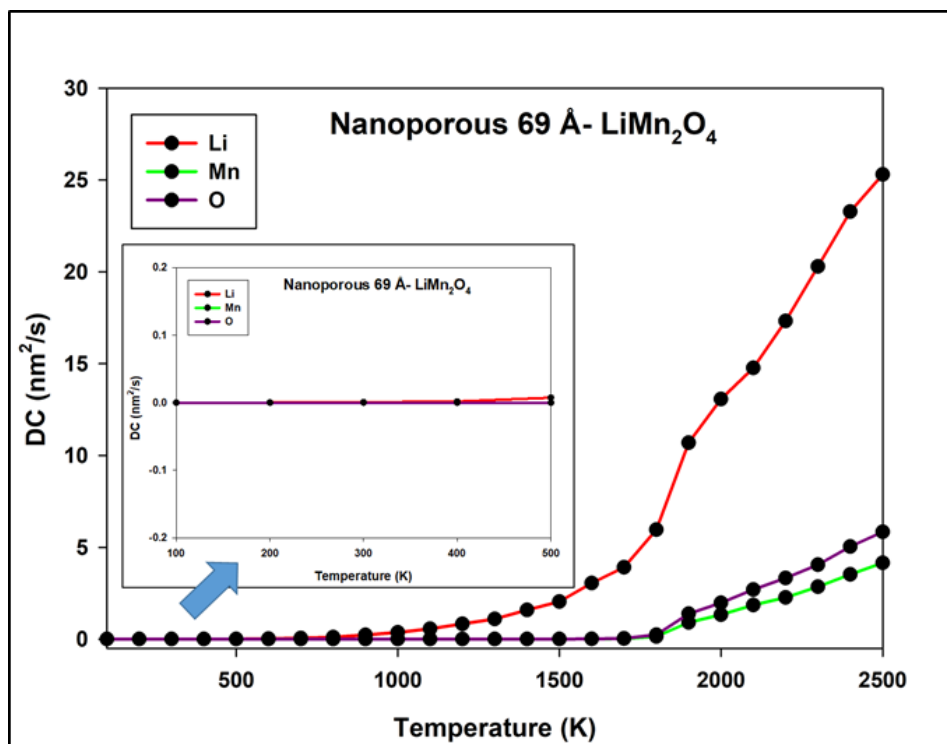


Figure 5.6: Nanoporous 69 Å structure at $\text{Li}_{1.00}\text{Mn}_2\text{O}_4$ concentration showing the diffusion coefficients of Li-Mn-O ions at different temperatures.

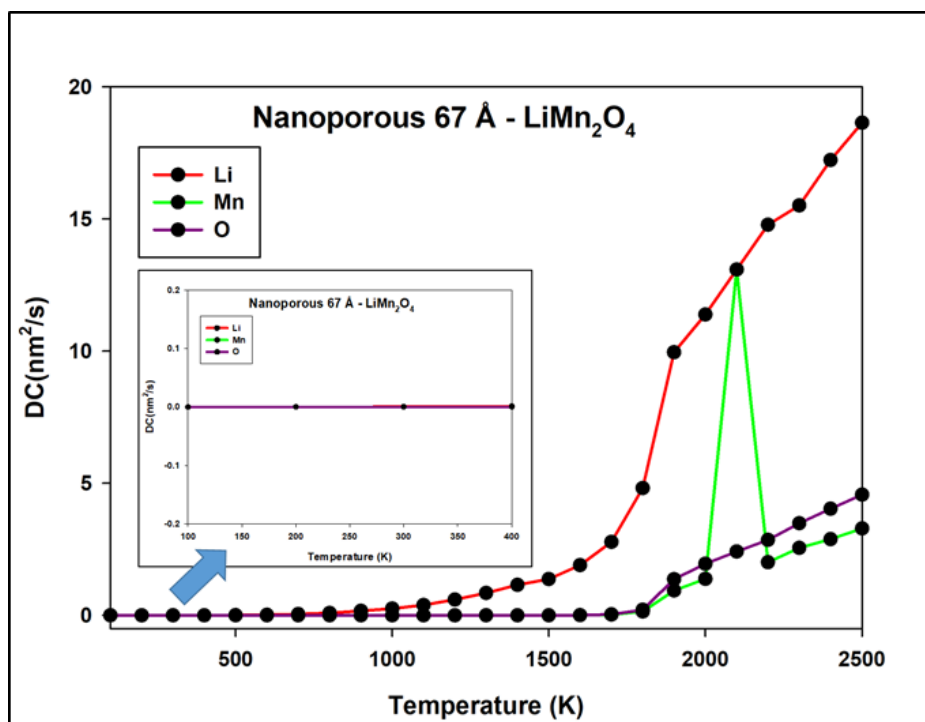


Figure 5.7: The diffusion coefficients of $Li_{1.00}Mn_2O_4$ nanoporous 67 Å structure illustrating the diffusivity of the Li-Mn-O ions at temperature increment.

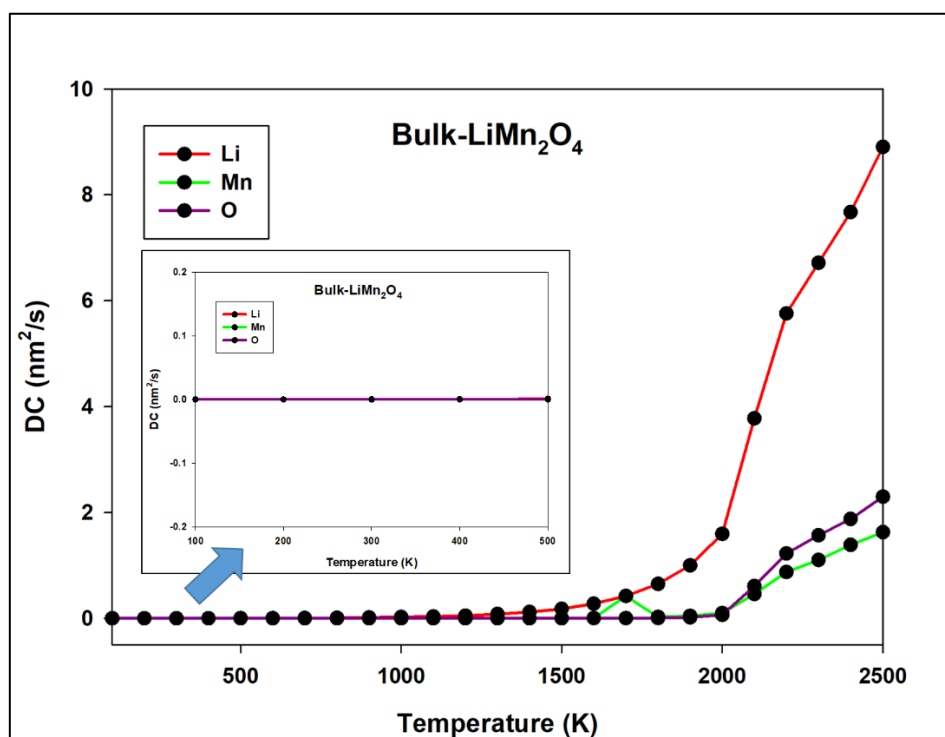


Figure 5.8: The diffusion coefficients for Li-Mn-O bulk structure at $Li_{1.00}Mn_2O_4$ concentration with increasing temperature (K).

5.5 Comparison of the lithium diffusion for nanoporous and bulk structures at similar concentrations

The lithium diffusion coefficients for nanoporous 75, 69 and 67 Å and the bulk structures at $\text{Li}_{1.00}\text{Mn}_2\text{O}_4$, $\text{Li}_{1.25}\text{Mn}_2\text{O}_4$, $\text{Li}_{1.50}\text{Mn}_2\text{O}_4$, $\text{Li}_{1.75}\text{Mn}_2\text{O}_4$ and $\text{Li}_{2.00}\text{Mn}_2\text{O}_4$ concentrations are illustrated in figures 5.9 to 5.13, respectively.

Figure 5.9 depicts the lithium diffusion coefficients plots for the nanoporous and bulk structures at $\text{Li}_{1.00}\text{Mn}_2\text{O}_4$ concentration. Nanoporous 75 Å shows the highest lithium diffusion up to $\sim 33 \times 10^{-9} \text{ m}^2 \cdot \text{s}^{-1}$, followed by nanoporous 69 Å with diffusion of up to $\sim 25 \times 10^{-9} \text{ m}^2 \cdot \text{s}^{-1}$, then nanoporous 67 Å with $\sim 19 \times 10^{-9} \text{ m}^2 \cdot \text{s}^{-1}$, and finally the bulk with the least at $\sim 9 \times 10^{-9} \text{ m}^2 \cdot \text{s}^{-1}$. This could imply that the lattice size and the porosity of a material play a pivotal role in its diffusion role.

The lithium diffusion coefficients plots of $\text{Li}_{1.25}\text{Mn}_2\text{O}_4$ concentration for the nanoporous and bulk structure is illustrated in figure 5.10. The lithium diffusion of nanoporous 75 Å is the highest with $\sim 36 \times 10^{-9} \text{ m}^2 \cdot \text{s}^{-1}$ at 2500 K. Then followed by nanoporous 69 Å with the lithium diffusion of up to $\sim 28 \times 10^{-9} \text{ m}^2 \cdot \text{s}^{-1}$, then nanoporous 67 Å with $\sim 20 \times 10^{-9} \text{ m}^2 \cdot \text{s}^{-1}$. The bulk has the lowest lithium diffusion of up to $\sim 10 \times 10^{-9} \text{ m}^2 \cdot \text{s}^{-1}$ at 2500 K. In this concentration again it is observed that lattice and pore size plays a role in lithium diffusion.

The diffusion coefficients of lithium when concentration is increased to $\text{Li}_{1.50}\text{Mn}_2\text{O}_4$ is demonstrated in figure 5.11. The trend of lithium diffusivity on the structures is similar to the $\text{Li}_{1.00}\text{Mn}_2\text{O}_4$ and $\text{Li}_{1.25}\text{Mn}_2\text{O}_4$ concentrations. Nanoporous 75 Å has the highest diffusion rate with $\sim 36 \times 10^{-9} \text{ m}^2 \cdot \text{s}^{-1}$ at 2500 K. The nanoporous (69 Å, 67 Å) and the bulk structures diffusion rates increases to a maximum of $\sim 19 \times 10^{-9} \text{ m}^2 \cdot \text{s}^{-1}$, $\sim 15 \times 10^{-9} \text{ m}^2 \cdot \text{s}^{-1}$ and $\sim 12 \times 10^{-9} \text{ m}^2 \cdot \text{s}^{-1}$ at 2500K, respectively.

Figure 5.12 illustrates the diffusion coefficients of the bulk and nanoporous structures at $\text{Li}_{1.75}\text{Mn}_2\text{O}_4$ concentration. A similar trend to that of the $\text{Li}_{1.50}\text{Mn}_2\text{O}_4$ concentration, where nanoporous 75 Å has the highest diffusion rate followed by the nanoporous (69 Å, 67 Å) and then the bulk structure. The diffusion rates at maximum for the nanoporous (75 Å, 69 Å and 67 Å) and the bulk structures are $\sim 32 \times 10^{-9} \text{ m}^2.\text{s}^{-1}$, $\sim 15 \times 10^{-9} \text{ m}^2.\text{s}^{-1}$, $\sim 14 \times 10^{-9} \text{ m}^2.\text{s}^{-1}$ and $\sim 10 \times 10^{-9} \text{ m}^2.\text{s}^{-1}$ respectively.

Fully lithiated structures at $\text{Li}_{2.00}\text{Mn}_2\text{O}_4$ concentration are illustrated in figure 5.13. Nanoporous 75 Å still maintains its high diffusion rate and now up to $\sim 42 \times 10^{-9} \text{ m}^2.\text{s}^{-1}$ at 2500 K, followed by nanoporous 69 Å with $\sim 25 \times 10^{-9} \text{ m}^2.\text{s}^{-1}$, then nanoporous 67 Å with $\sim 18 \times 10^{-9} \text{ m}^2.\text{s}^{-1}$, and finally the bulk with $\sim 2 \times 10^{-9} \text{ m}^2.\text{s}^{-1}$. The bulk shows a very minimal increase in diffusion rate from 1000 K to 2500 K. The minimal increase in the bulk at this concentration can be related to the drastic volume drop observed in Chapter 4, figures 4.7 and 4.8.

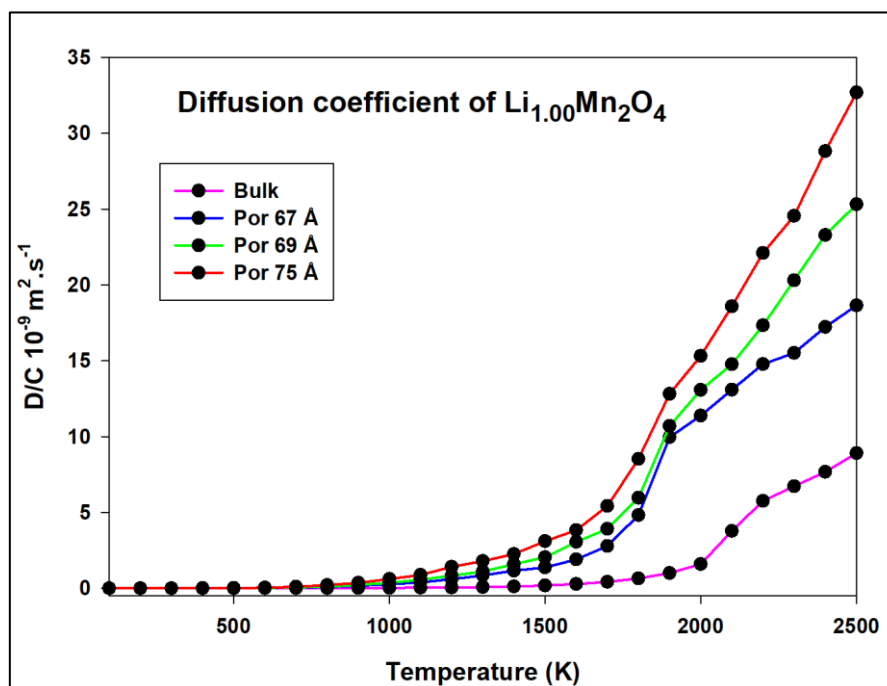


Figure 5.9: The lithium diffusion coefficients for the nanoporous (75, 69 and 67 Å) and bulk structures at $\text{Li}_{1.00}\text{Mn}_2\text{O}_4$ concentration with increasing temperature (K).

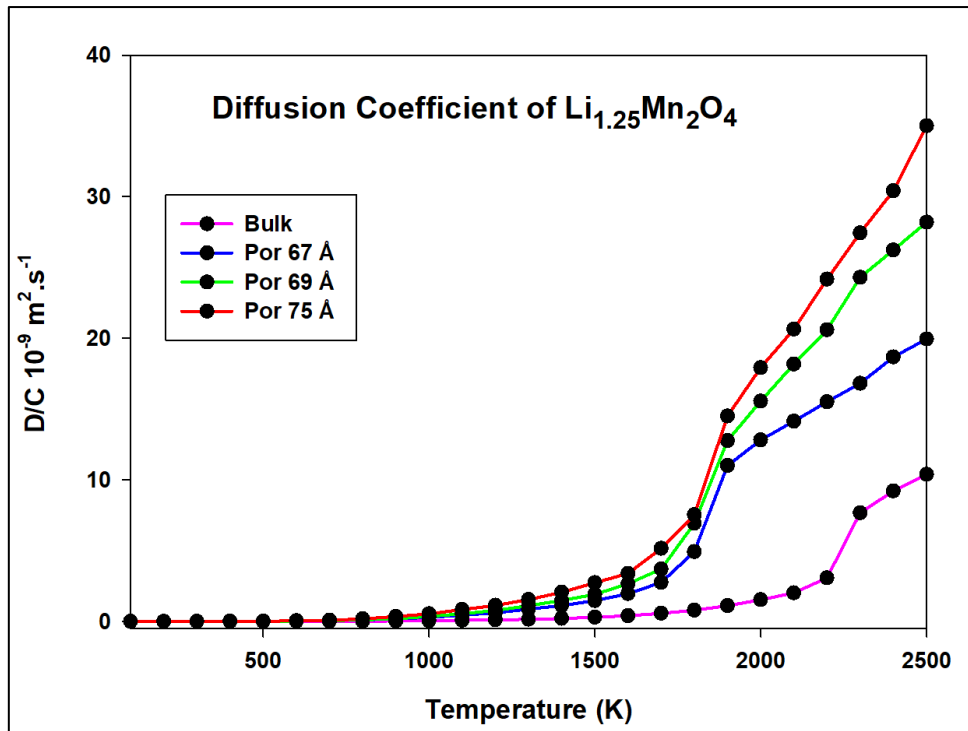


Figure 5.10: The diffusion coefficients of lithium for nanoporous and bulk structures at $\text{Li}_{1.25}\text{Mn}_2\text{O}_4$ concentration with increasing temperature (K).

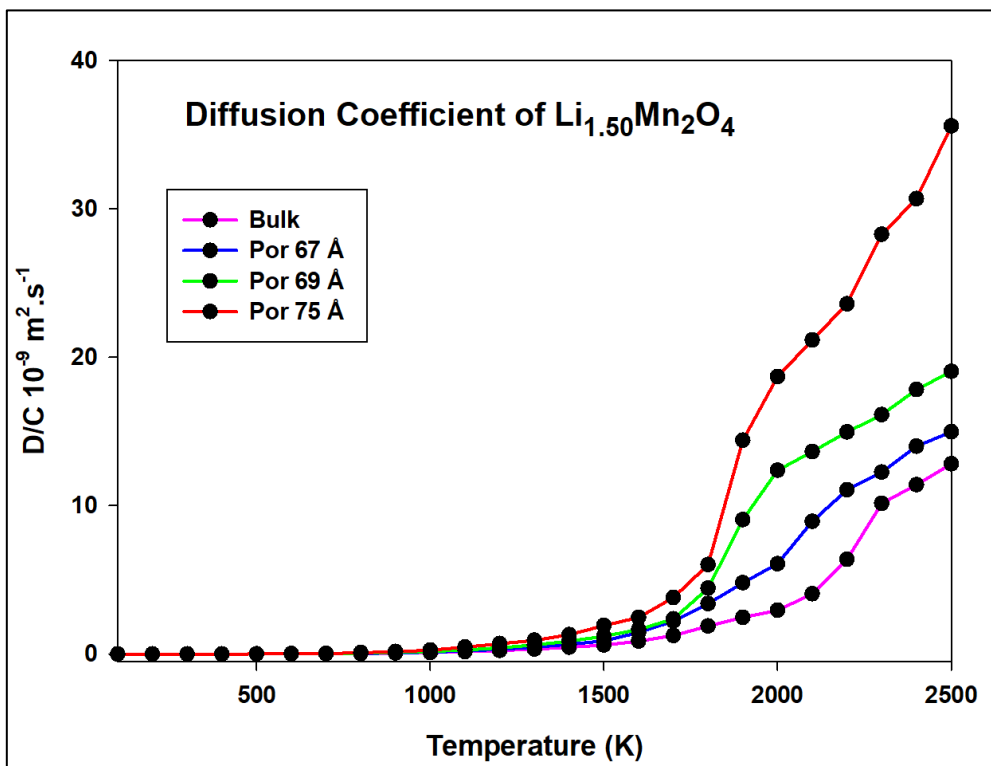


Figure 5.11: Nanoporous and bulk structures depicting the lithium diffusion coefficients at $\text{Li}_{1.50}\text{Mn}_2\text{O}_4$ concentration with increasing temperature (K).

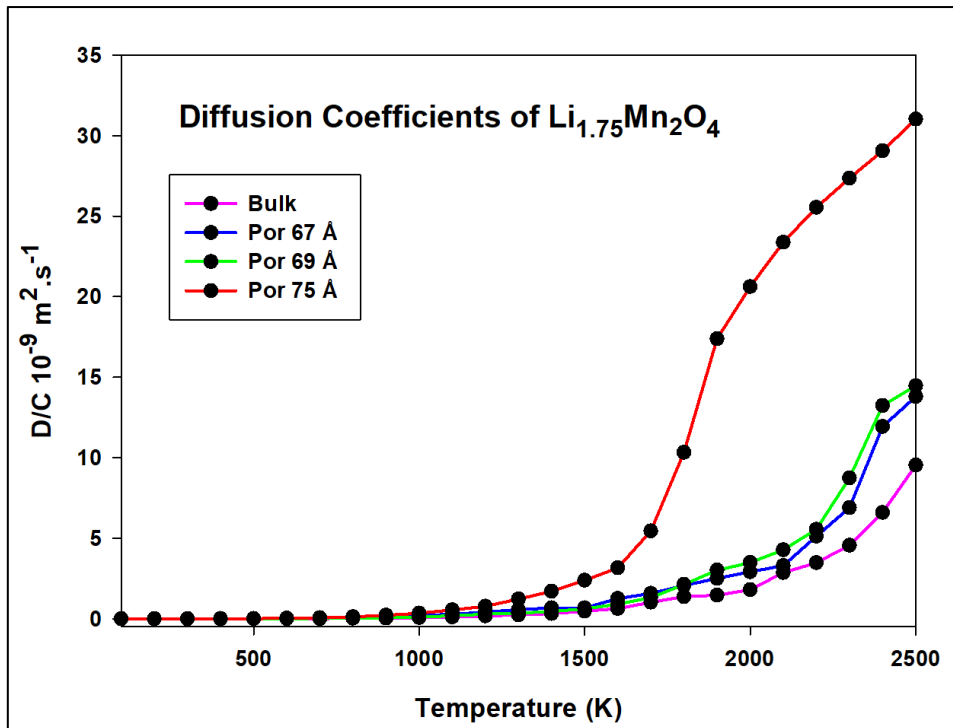


Figure 5.12: The diffusion coefficient plots for lithium of the nanoporous 75, 69, and 67 Å and bulk structures at $\text{Li}_{1.75}\text{Mn}_2\text{O}_4$ concentration with increasing temperature (K).

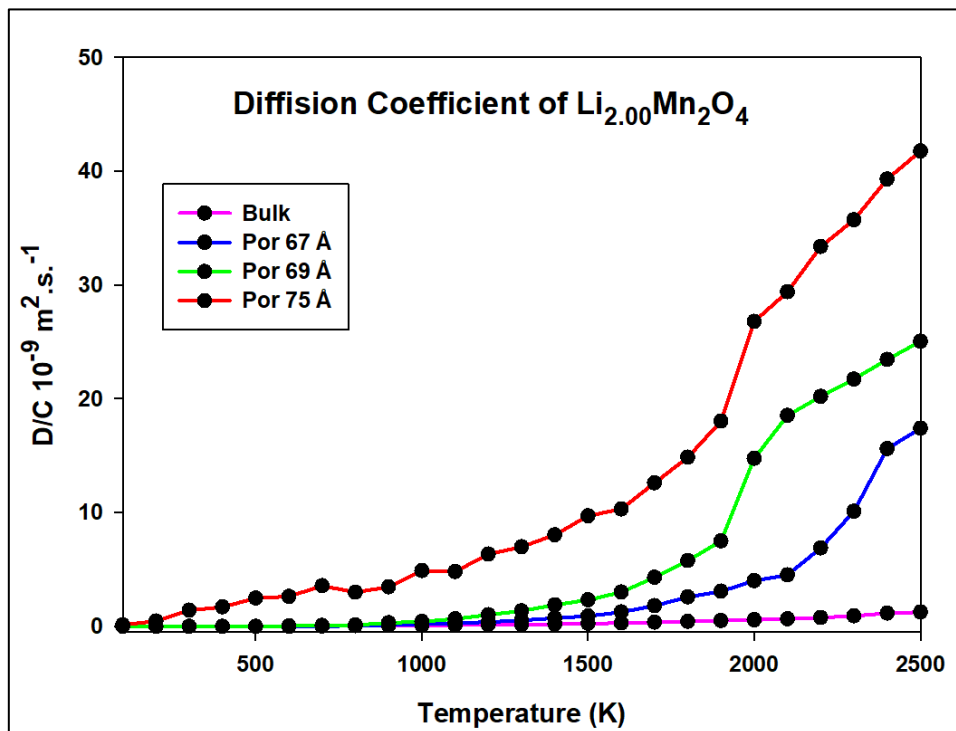


Figure 5.13: The plots of lithium diffusion coefficients for the nanoporous and bulk structures at $\text{Li}_{2.00}\text{Mn}_2\text{O}_4$ concentration with increasing temperature (K).

5.6 Discussion

The stability of cathode material in terms of diffusion rate for the nanoporous and bulk structures have been successfully investigated with increasing temperature. The diffusion coefficients for the nanoporous and bulk structures have been calculated successfully using molecular dynamics simulations methods. In most structures lithium diffusion is observed to start above 500 K and increase exponentially until the reported melting point temperature of 1700 K. However, some concentrations show fluctuations in their diffusion coefficients throughout, especially at $\text{Li}_{2.00}\text{Mn}_2\text{O}_4$ for nanoporous 75 Å. Moreover, the nanoporous 75 Å at $\text{Li}_{2.00}\text{Mn}_2\text{O}_4$ starts to diffuse above 100 K, in contrast to the other structures and concentrations. It is further observed that the $\text{Li}_{1.75}\text{Mn}_2\text{O}_4$ concentration shows the lowest diffusivity for nanoporous 69 and 67 Å. This is the concentration where grain boundaries are observed and can act as pathways, however, for nanoporous 69 and 67 Å structures the pathways do not accelerate the diffusion of lithium; rather, they slow them down. Nanoporous 75 Å have the highest diffusion rate, then followed by nanoporous 69 Å, then nanoporous 67 Å, and lastly, the bulk for all the concentrations. From these findings, it can be concluded that the morphology of materials does affect their diffusion rate and nanoporous materials allow for higher lithium transportation or diffusion compared to the bulk.

CHAPTER 6

The mechanical properties of nanoporous structures

6.1 Introduction

Durable, fast charge and high capacity are very crucial properties in battery development, especially their safety as energy storage materials. However, during cycling, strains and stresses which compromise the optimal performance of the battery occur. As the battery charges and discharges, lithium ions move from the anode to the cathode and vice versa, this process results in contraction and expansion of the battery and consequently, the battery may fracture due to the lithium induced stresses and strains endured [64]. Furthermore, volumetric changes result in large lithiation induced strains causing fracture and pulverization of the electrodes. Nanocrystalline materials have very high strength and demonstrate the ability to withstand high stresses which is up to ten times greater yield stress than their coarse-grained counterparts. However, they are limited by their strain failure, and efforts to enhance their deformability are usually found to compromise their strength [121].

Reducing electrode particle size into the nanoscale regime is also believed to substantially reduce the mechanical stresses caused by volumetric expansion and contraction during charge and discharge. A study has shown that a developed model should suggest that particles must have a size under a certain critical radius so that the strain produced by intercalation can be accommodated elastically, rather than by plastic deformation, allowing for the full recovery of the original, stable structure [122, 123]. Moreover, nanostructuring has been found to have resistance on intercalation induced stresses that are inflicted to electrodes; this enables for short diffusion path and facile strain relaxation

[79]. Several measures such as making a porous nanostructure to adapt to volume changes can be adopted [131].

The presence of extended defects in materials can reduce the mechanical strength of materials by 70% [124]. Herein, the mechanical properties of the three nanoporous (75, 69 and 67 Å) structures will be investigated with their defects to interrogate their robustness during the discharge process. In particular, the uniaxial stress of the materials will be analysed in the hope of understanding and finding a material that is resistant and responds better to strains and stresses during the discharge process. The mechanical properties of these materials at different lithium concentrations of $\text{Li}_{1+x}\text{Mn}_2\text{O}_4$ where, $0 \leq x \leq 1$ will be analysed for their elasticity, plasticity and deformation regions.

6.2 Method

6.2.1 Generating the atomistic model structures

The simulations carried out in this chapter are based on molecular dynamics simulations under the Born Model of the Ionic solids. The nanoporous structures were generated from a cubic unit cell of LiMn_2O_4 which was built up into a supercell, then amorphised to form a sphere. The spherical LiMn_2O_4 was then reduced in all three dimensions by applying a pressure of 100 GPa under the NPT ensemble to allow the nanoparticles to agglomerate in three dimensions produce the nanoporous structures of different lattice dimensions. The structures were then recrystallised under the NVT ensemble at temperatures of 1700 K for 150 ps until a crystalline model structure was obtained. The structures were later cooled to an equilibrium temperature of 0 K for 300 ps.

6.2.2 Simulating Uniaxial stress

The Li-Mn-O nanoporous structures used to calculate the uniaxial stress were equilibrated before carrying out molecular dynamics simulations under the NST ensemble where, $N =$

constant number of particles, S = constant stress and T = constant temperature. The DL_POLY code was used to execute all stress-strain calculations at the temperature of 300 K for 100 ps. The materials were compressed by imposing strain and sequentially increasing the stress in a uniaxial direction and allowing it to relax to zero stress under the NST ensemble. This implies that the stress was applied to one direction leaving the two components at zero. The uniaxial stress of 0.1 GPa along the y-direction was enforced on the materials, where the molecular dynamic simulation was carried out at the temperature of 300 K and timestep increment of 1000, enabling the simulation to record the statistics after every 50 steps. The equilibration period of 5 ps was used to assist in alleviating the effect of the high strain. The simulation methods used here have been successfully executed by R.S. Ledwaba on Li-Mn-O materials for a PhD study [72].

6.3 Uniaxial stress for the nanoporous structures

The stress-strain plots for nanoporous structures in the y-direction with varying lithium concentrations from $\text{Li}_{1.00}\text{Mn}_2\text{O}_4$ to $\text{Li}_{2.00}\text{Mn}_2\text{O}_4$ are illustrated in figures 6.1 to 6.4, showing the elastic regions (A-B), Plastic regions (B/B₁-C) and deformation regions (C-D).

The stress-strain plots for the nanoporous structures (75, 69 and 67 Å) at $\text{Li}_{1.00}\text{Mn}_2\text{O}_4$ compressed in the y-direction are demonstrated in figure 6.1. The $\text{Li}_{1.00}\text{Mn}_2\text{O}_4$ nanoporous 75 Å structure shows a material that has a proportional limit of 3.8 % strain at a stress of ~2.69 GPa and Young modulus of 67.25 GPa. The yield strength was observed at ~3.22 GPa and ~5.4 % strain. Furthermore, the plasticity of the material was observed from ~5.4 % to ~27.8 % strain. The structure eventually collapses at ~6 GPa where it fractured. The pristine structure ($\text{Li}_{1.00}\text{Mn}_2\text{O}_4$) of nanoporous 69 Å, has a proportional limit of ~4.70 % strain at ~5.64 GPa stress and elastic modulus of 112.8 GPa, greater than of nanoporous 75 Å. The yield strength of the material is observed at ~6.35 GPa stress and ~5.6 % strain. The plastic region is observed from the strain of ~5.6% to ~11.5 % and thereafter, the

structure ultimately collapses at a stress of ~ 7 GPa. The $\text{Li}_{1.00}\text{Mn}_2\text{O}_4$ nanoporous 67 Å structure responded elastically up to $\sim 4.1\%$ strain at a yield strength of ~ 6.15 GPa and elastic modulus of 153.75 GPa. The plasticity occurred between the strain of $\sim 4.1\%$ and $\sim 12.7\%$. Then, the material experienced maximum stress of ~ 8 GPa and eventually collapsed at a strain of $\sim 23.6\%$.

Figure 6.2 illustrates the stress-strain curves with lithium increment to $\text{Li}_{1.25}\text{Mn}_2\text{O}_4$ concentration for the three nanoporous structures, where nanoporous 75 Å structure has responded elastically up to a strain of $\sim 5.1\%$ at a yield strength of ~ 3.73 GPa and elastic modulus of 74.6 GPa. The structure further responded plastically from $\sim 5.1\%$ and reached a maximum strain of $\sim 24.4\%$ where it subsequently collapsed to the stress of ~ 6 GPa. Meanwhile, the nanoporous 69 Å structure has responded elastically up to a strain of $\sim 5.5\%$ at a yield strength of ~ 8.63 GPa and elastic modulus of 143.83 GPa. The structure responded plastically from the strain of $\sim 5.5\%$ to $\sim 6\%$, where it ultimately collapsed at ~ 9 GPa stress. On the other hand, nanoporous 67 Å shows the limit of proportionality at $\sim 3.6\%$ strain and ~ 6.54 GPa stress with the elastic modulus of 163.5 GPa. The yield strength is observed at 10.08 GPa stress, with a strain of $\sim 6.0\%$. The plastic region of the material is observed from $\sim 6.0\%$ strain to a maximum of $\sim 22.0\%$ where the structure permanently deformed and collapsed at a stress of ~ 10 GPa. In this concentration, the yield strength and elastic modulus increase with a reduction in cell lattice size.

Lithium increment to $\text{Li}_{1.50}\text{Mn}_2\text{O}_4$ is illustrated in figure 6.3 and shows the stress-strain curves of nanoporous 75, 69 and 67 Å structures. The analysis shows that nanoporous 75 Å responds elastically up to a strain of $\sim 4.8\%$ at a yield strength of ~ 5.22 GPa and Young's modulus of 104.4 GPa. The structure further responds plastically from the strain of $\sim 4.8\%$ to $\sim 6.1\%$ and collapses at ~ 6 GPa stress with $\sim 49.5\%$ strain. Nanoporous 69 Å has the elastic modulus of 146.3 GPa at the proportional limit of $\sim 2.7\%$ strain and ~ 4.39 GPa

stress. The elastic limit of the material is observed at ~5.3 % strain with a yield strength of ~8.82 GPa. Meanwhile, the plasticity of the material is observed from ~5.3 % to ~6.1 % strain, then the material collapses at a maximum strain of ~21.4 % and stress of ~10 GPa. On the other hand, nanoporous 67 Å $\text{Li}_{1.50}\text{Mn}_2\text{O}_4$ shows the proportional limit at ~3.3 % strain and the stress of ~5.48 GPa with the elastic modulus of 182.7 GPa. The yield strength of the material is observed at 13.40 GPa with a strain of ~6.0 %. The plasticity of the material is then observed from the strain of ~6.0 % to ~6.6 %. The structure then reaches a maximum strain of 20.8 % where it subsequently collapses at 13.72 GPa stress.

The stress-strain curves with lithium concentration increment to $\text{Li}_{1.75}\text{Mn}_2\text{O}_4$ for the three nanoporous structures are illustrated in figure 6.4. The nanoporous 75 Å structure is observed to have a proportional limit at ~4.5 % and stress of ~2.28 GPa with the elastic modulus 56.80 GPa. The yield strength of the material is observed at ~3.66 GPa stress and ~5.8 % strain. The material has further responded plastically from ~5.8 % to ~16.4 % strain, where it permanently deformed from the strain of ~16.4 % to a maximum of ~48.9 % and collapsed at ~5 GPa stress. Meanwhile, nanoporous 69 Å shows the proportional limit at ~3.4 % strain and ~5.19 GPa stress with the young modulus of 173 GPa. The yield strength of the material is observed at ~9.64 GPa stress and ~5.8 % strain. The material then responds plastically from the strain of ~5.8 % to 6.0 %, thereafter, it collapses at a maximum strain of ~35.6 % and ~10 GPa stress. Finally, the nanoporous 67 Å responds elastically up to ~4.8 % strain at a yield strength of ~8.91 GPa and Young's modulus of 136 GPa. Furthermore, it responds plastically from ~4.8 % strain up to ~10.8 % and collapse at a maximum of ~29.8 % strain and the of stress ~9 GPa.

The fully lithiated structures ($\text{Li}_{2.00}\text{Mn}_2\text{O}_4$) are illustrated in figure 6.5 showing the stress-strain curves for the nanoporous structures with 75, 69 and 67 Å lattice sizes. The nanoporous 75 Å structure has the proportional limit at ~2.7 % strain and ~2.48 stress

GPa with the elastic modulus of ~ 82.7 GPa. The yield strength of the material is observed at 5.61 GPa. The material has further responded plastically from ~ 5.50 % to ~ 6.10 % strain. The maximum strain of ~ 46.9 % was reached where the material fractured at the stress of ~ 6 GPa. The nanoporous 69 \AA structure then shows the proportional limit at 3.0 % strain and the stress of ~ 4.23 GPa with the elastic modulus of ~ 141 GPa. Furthermore, the yield strength of the material is observed at 7.19 GPa and a strain of ~ 4.5 %. The plasticity of material is observed from ~ 4.5 % strain to ~ 5.2 %. The maximum strain of ~ 39.9 % and the stress of ~ 9 GPa was reached where the material ultimately collapsed. Last but not least, the $\text{Li}_{2.00}\text{Mn}_2\text{O}_4$ nanoporous 67 \AA shows the proportional limit at the strain of ~ 2.7 % and stress of 5.08 GPa with the elastic modulus of 193.3 GPa. The yield strength of the material is observed at the stress of ~ 11.90 GPa and the strain of $\sim 5.2\%$. Lastly, the plastic region of the material is observed from ~ 5.2 % strain to ~ 6.7 %. The structure then collapses at the maximum strain of ~ 23.5 % and ~ 14.2 GPa stress.

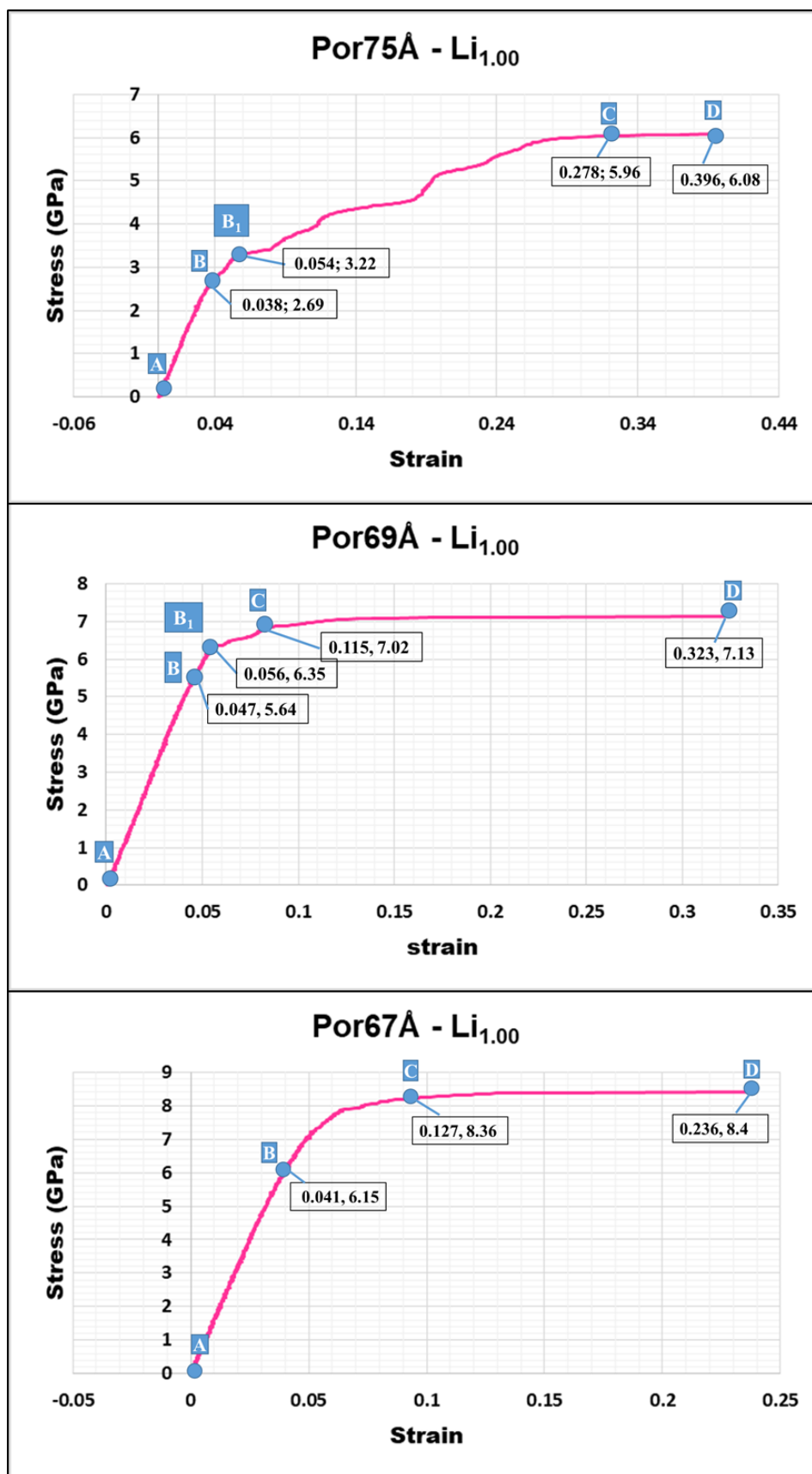


Figure 6.1: The stress-strain plots for nanoporous 75, 69 and 67 Å structures at $Li_{1.00}Mn_2O_4$ concentration.

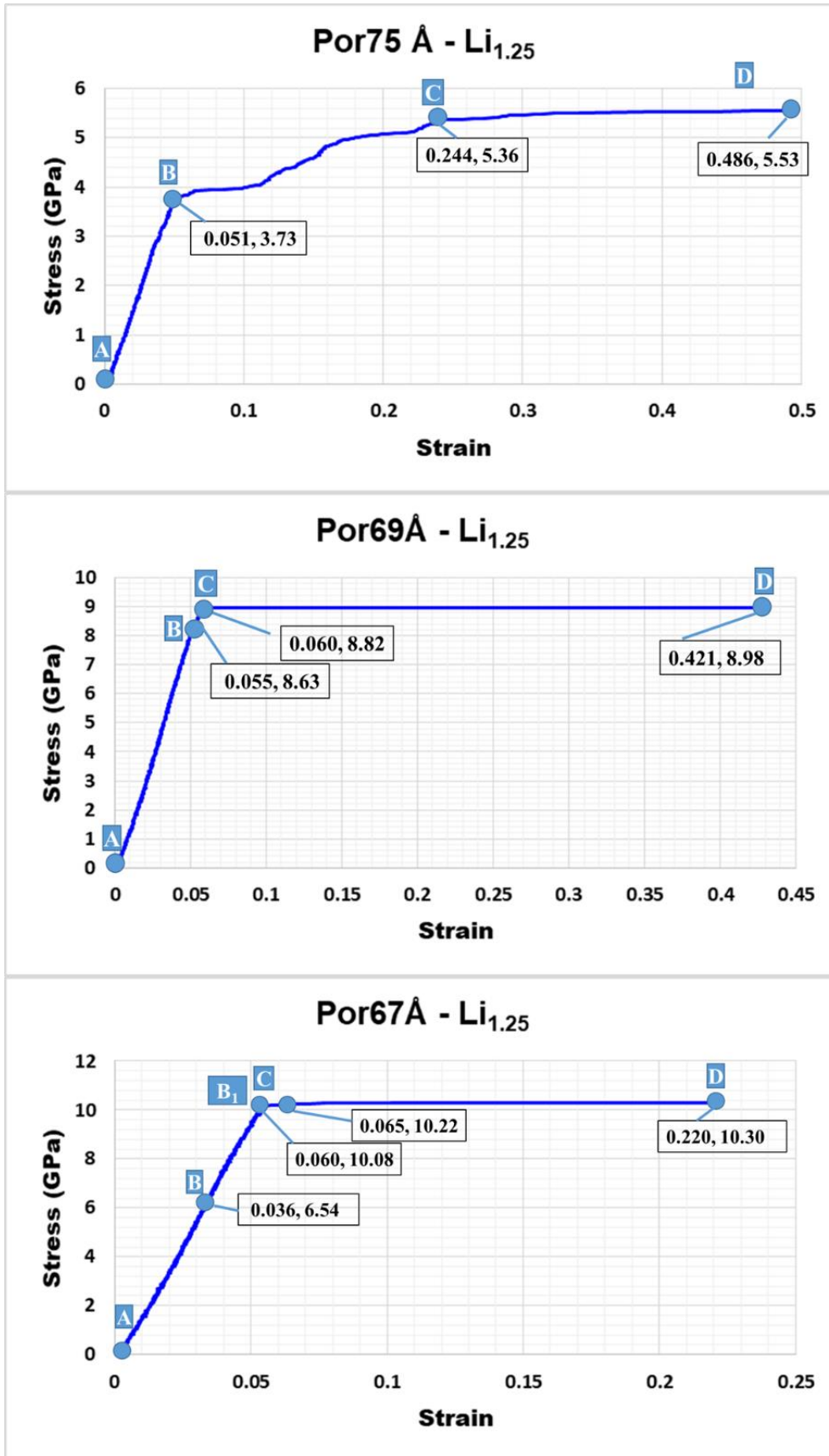


Figure 6.2: The stress-strain plots for nanoporous 75, 69 and 67 Å structures at $Li_{1.25}Mn_2O_4$ concentration.

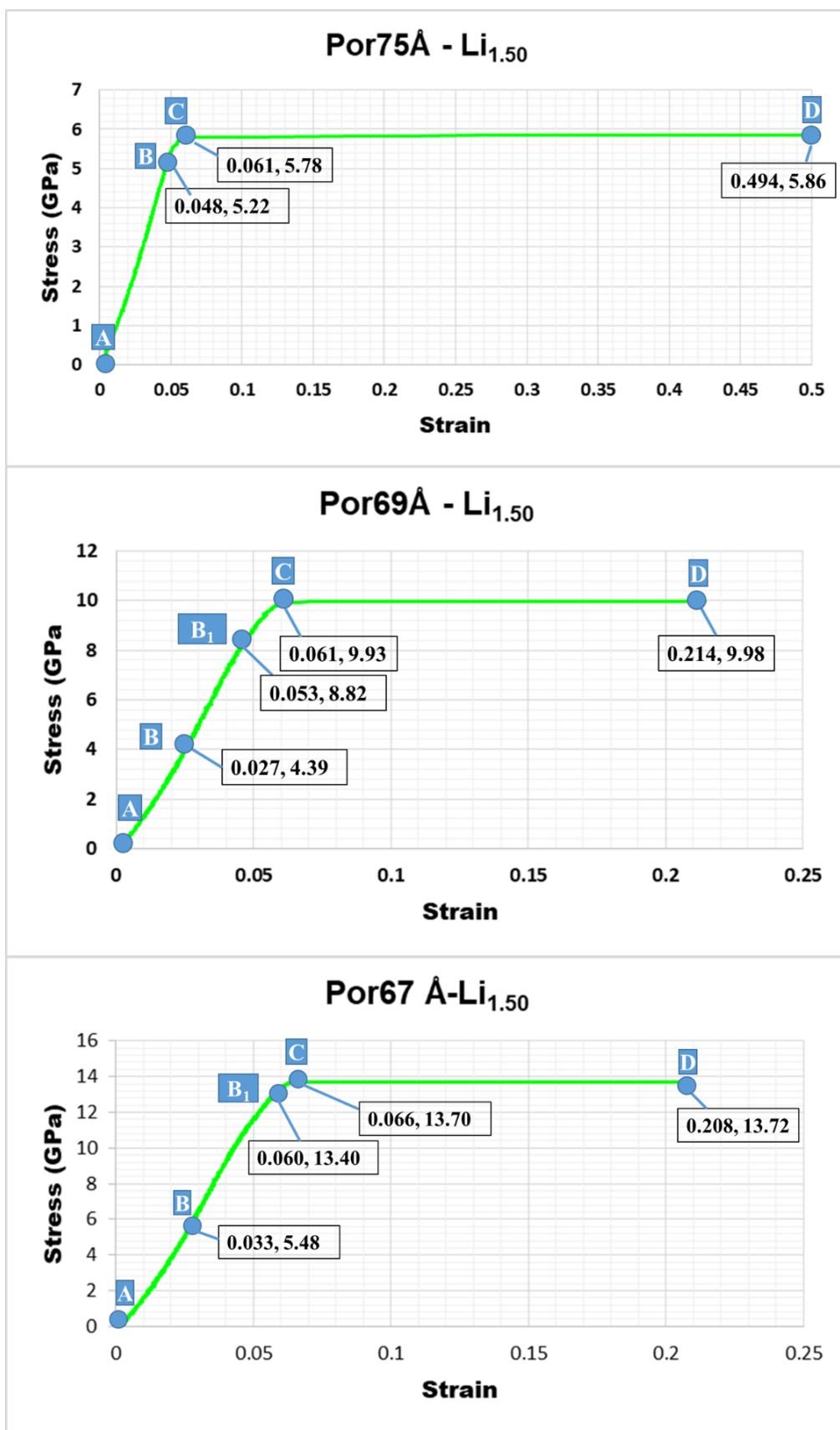


Figure 6.3: The stress-strain plots for nanoporous 75, 69 and 67 Å structures at $Li_{1.50}Mn_2O_4$ concentration.

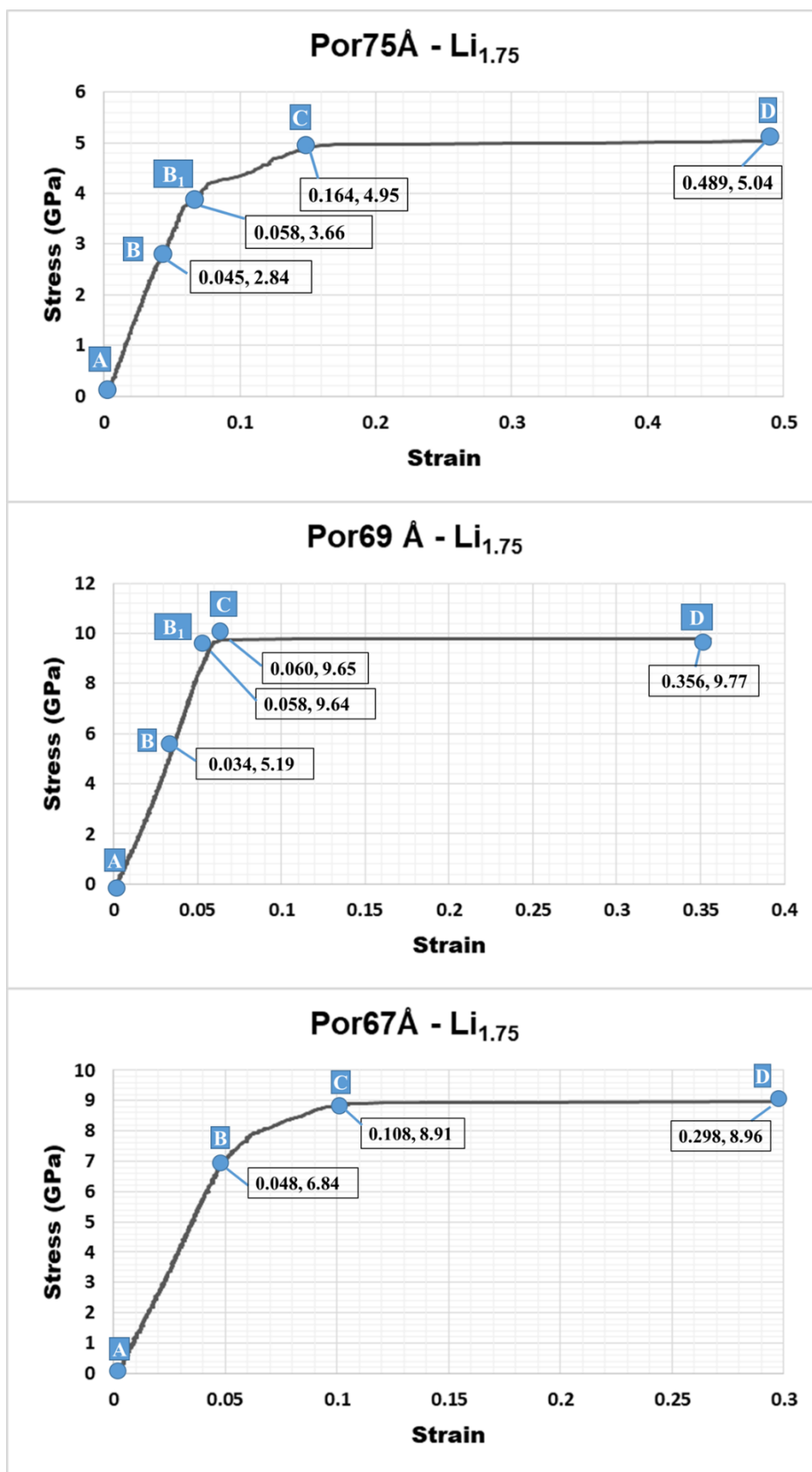


Figure 6.4: The stress-strain plots for nanoporous 75, 69 and 67 Å structures at $Li_{1.75}Mn_2O_4$ concentration.

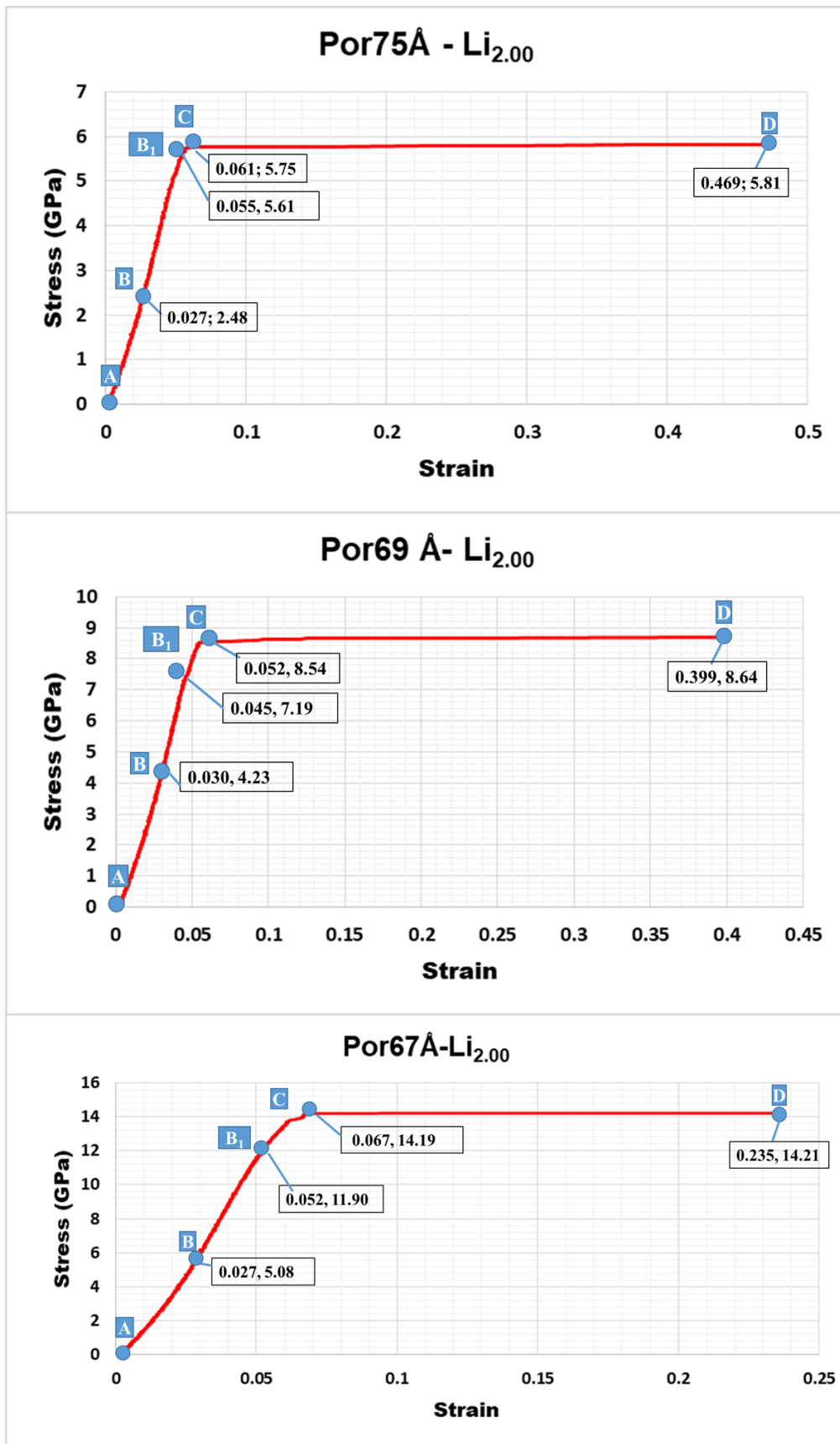


Figure 6.5: The stress-strain plots for nanoporous 75, 69 and 67 Å structures at $Li_{1.75}Mn_2O_4$ concentration.

6.4 Radial distribution functions and X-ray diffraction pattern analysis of the nanoporous structures under stress

6.4.1 Radial distribution functions response to stress

The snapshots of the total radial distribution functions (RDFs) for the lithiated Li-Mn-O nanoporous materials under the stress of 0.1 GPa are illustrated in figure 6.6. The snapshots for nanoporous 75 Å show graphs that have sharp peaks and those that have broad ones, with the first peak being observed at 2 Å. The plots show peaks that are broader becoming flat with increasing radial distance (r), especially after 8 Å. The defined peaks imply ordered structures; meanwhile, the broadening and flattening of peaks with increasing radial distance could signify that the structures are getting distorted with stress. For nanoporous 75 Å structure, the peaks become broad and less intense right after 8 Å radial distance. A similar trend is observed for the nanoporous 69 Å structure, however, the peaks for $\text{Li}_{1.50}\text{Mn}_2\text{O}_4$ and $\text{Li}_{2.00}\text{Mn}_2\text{O}_4$ concentrations are more defined when compared to the other concentrations after 8 Å. Similarly, nanoporous 67 Å depicts a similar peak trend to nanoporous 69 Å, however, in this structure, the peaks for $\text{Li}_{1.50}\text{Mn}_2\text{O}_4$ and $\text{Li}_{1.75}\text{Mn}_2\text{O}_4$ concentrations are more defined compared to the other concentrations after 8 Å. This could imply that the concentrations with peaks that are still defined after the 8 Å are less distorted when stress is imposed on them. However, under recrystallisation of NVT and NST the peaks are defined, but, less intense.

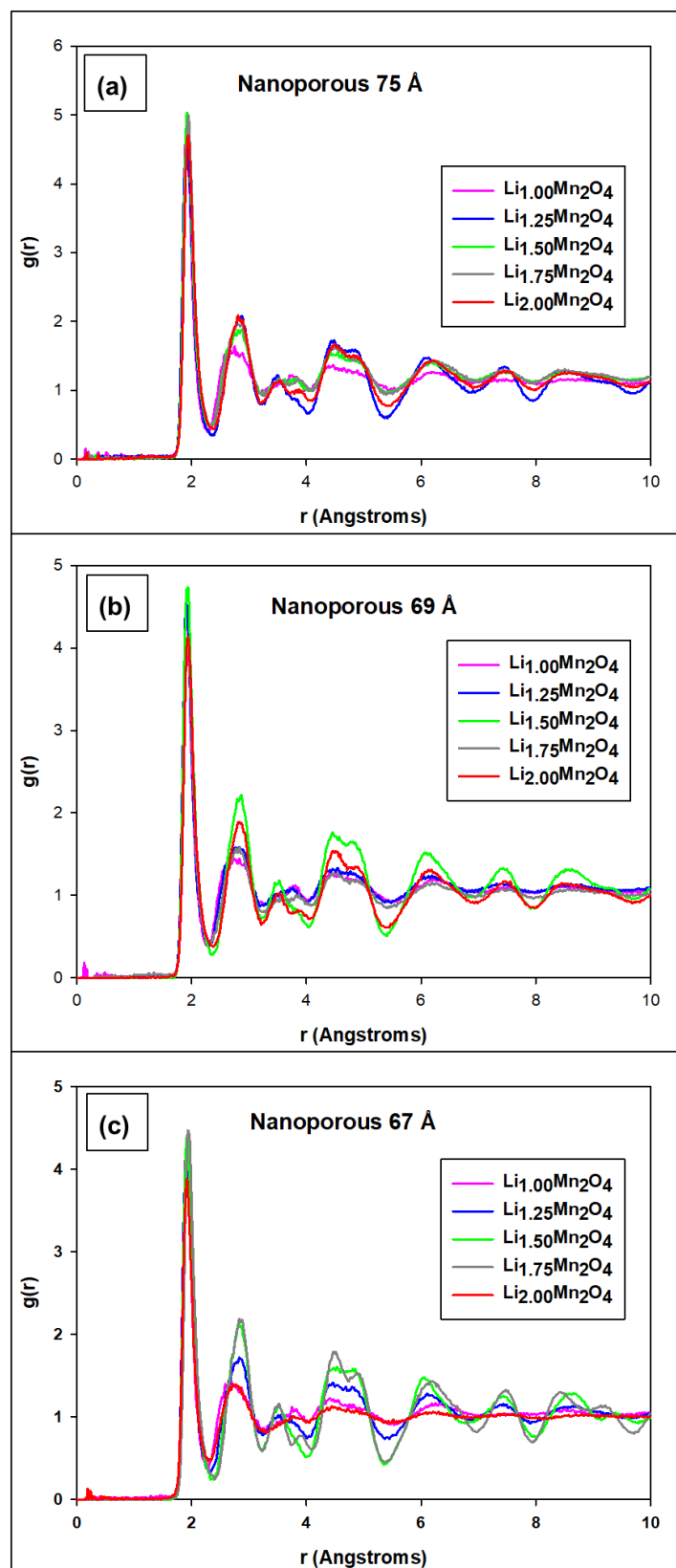


Figure 6.6: The total RDFs of the lithiated Li-Mn-O nanoporous structures under the stress of 0.1 GPa with different lithium concentrations for (a) nanoporous 75 Å, (b) nanoporous 69 Å and (c) nanoporous 67 Å.

6.4.2 The X-ray diffraction pattern's response to stress

The X-ray diffraction patterns under the uniaxial stress of 0.1 GPa for the simulated nanoporous structures in their pristine form ($\text{Li}_{1.00}\text{Mn}_2\text{O}_4$) are illustrated in figure 6. 7. The XRDs from the simulated structures are compared with the experimental (d) spinel Mn_3O_4 [106], (e) spinel $\text{Li}_2\text{Mn}_2\text{O}_4$ [115], layered Li_2MnO_3 (f) [107] which commonly co-exist with layered LiMnO_2 (g) [107] and spinel LiMn_2O_4 (h) [107]. The peak at $\sim 2\theta = 18 - 23^\circ$ associated with spinel Mn_3O_4 , LiMn_2O_4 and $\text{Li}_2\text{Mn}_2\text{O}_4$ and layered $\text{Li}_2\text{Mn}_2\text{O}_3$, appear to be flat for nanoporous 75 Å, whereas for nanoporous 69 Å and 67 Å it appears to have shifted towards the right and merge to form a wide peak at $\sim 2\theta = 32^\circ$ associated with spinel Mn_3O_4 and LiMn_2O_4 . The merged peak is broad and spans to $\sim 2\theta = 39$. The peaks at $\sim 2\theta = 45^\circ$ associated with spinel LiMn_2O_4 , Mn_3O_4 and layered Li_2MnO_3 which commonly co-exists with layered LiMnO_2 are observed for all the structures and are broad. Moreover, the peak appears to have the lowest intensity for nanoporous 75 Å. Finally, the peaks at $\sim 2\theta = 64^\circ$ associated with LiMn_2O_4 , Mn_3O_4 and layered Li_2MnO_3 is observed for all the structures and have shifted towards the left favouring the spinel Li_2MnO_4 content.

The X-ray diffraction patterns for the simulated nanoporous 75 Å structure under the stress of 0.1 GPa are illustrated in figure 6.8 with varying lithium concentrations, $\text{Li}_{1+x}\text{Mn}_2\text{O}_4$, where $0 \leq x \leq 1$. The peaks at $\sim 2\theta = 18 - 23^\circ$ related to spinel Mn_3O_4 , LiMn_2O_4 and $\text{Li}_2\text{Mn}_2\text{O}_4$ and layered $\text{Li}_2\text{Mn}_2\text{O}_3$ have almost disappeared for all the structures from $\text{Li}_{1.00}\text{Mn}_2\text{O}_4$ to $\text{Li}_{2.00}\text{Mn}_2\text{O}_4$. The peak at $\sim 2\theta = 26 - 32^\circ$ associated with spinel Mn_3O_4 seems to disappear with increasing lithium concentration where it is visible for $\text{Li}_{1.00}\text{Mn}_2\text{O}_4$, $\text{Li}_{1.25}\text{Mn}_2\text{O}_4$, $\text{Li}_{1.50}\text{Mn}_2\text{O}_4$ and flat for $\text{Li}_{1.75}\text{Mn}_2\text{O}_4$ and $\text{Li}_{2.00}\text{Mn}_2\text{O}_4$. Meanwhile, the peak at $\sim 2\theta = 36^\circ$ associated with spinel LiMn_2O_4 is observed for all concentrations with splits for the $\text{Li}_{1.25}\text{Mn}_2\text{O}_4$ and $\text{Li}_{2.00}\text{Mn}_2\text{O}_4$ concentrations. Further observations on the peaks, at $\sim 2\theta = 45^\circ$ associated with spinel Mn_3O_4 , LiMn_2O_4 and layered Li_2MnO_3 , peaks split for

$\text{Li}_{1.25}\text{Mn}_2\text{O}_4$, $\text{Li}_{1.50}\text{Mn}_2\text{O}_4$ and $\text{Li}_{2.00}\text{Mn}_2\text{O}_4$ concentrations are observed. Whereas for $\text{Li}_{1.00}\text{Mn}_2\text{O}_4$ and $\text{Li}_{1.75}\text{Mn}_2\text{O}_4$ concentrations, the peaks are observed to be broad. The splits and broadening of the peaks span over $\sim 2\theta = 41 - 52^\circ$ at most. The peaks at $\sim 2\theta = 64^\circ$ almost disappear for $\text{Li}_{1.00}\text{Mn}_2\text{O}_4$, split for $\text{Li}_{1.25}\text{Mn}_2\text{O}_4$ and $\text{Li}_{1.50}\text{Mn}_2\text{O}_4$, then broaden up for $\text{Li}_{1.75}\text{Mn}_2\text{O}_4$ and $\text{Li}_{2.00}\text{Mn}_2\text{O}_4$ concentrations.

The X-ray diffraction patterns for nanoporous 69 Å structure under the stress of 0.1 GPa are illustrated in figure 6.9. The peak at $\sim 2\theta = 18 - 23^\circ$ related to spinel Mn_3O_4 , LiMn_2O_4 , $\text{Li}_2\text{Mn}_2\text{O}_4$ and layered $\text{Li}_2\text{Mn}_2\text{O}_3$ is merging with the peak at $\sim 2\theta = 26 - 32^\circ$ associated with spinel Mn_3O_4 for the $\text{Li}_{1.00}\text{Mn}_2\text{O}_4$ and $\text{Li}_{1.25}\text{Mn}_2\text{O}_4$ concentrations. The peaks almost disappear for $\text{Li}_{1.50}\text{Mn}_2\text{O}_4$, $\text{Li}_{1.75}\text{Mn}_2\text{O}_4$ and $\text{Li}_{2.00}\text{Mn}_2\text{O}_4$ concentrations. The peak at $\sim 2\theta = 36^\circ$ associated with spinel LiMn_2O_4 is observed for all structures and $\text{Li}_{1.00}\text{Mn}_2\text{O}_4$ merges peaks at $\sim 2\theta = 18 - 23^\circ$ and $\sim 2\theta = 26 - 32^\circ$, where the spinel Mn_3O_4 and LiMn_2O_4 components are favoured. The peak at $2\theta \sim 45^\circ$ has split with shifts and spans over the range of $\sim 2\theta = 42 - 53^\circ$ at most for all the concentrations, except for the $\text{Li}_{1.00}\text{Mn}_2\text{O}_4$ and $\text{Li}_{1.75}\text{Mn}_2\text{O}_4$ concentrations which their peaks are broad. The splits and shifts favour both the spinel and layered components. Further observation on the XRDs, for peaks at $\sim 2\theta = 64^\circ$ associated with spinel LiMn_2O_4 , Mn_3O_4 and layered $\text{Li}_2\text{Mn}_2\text{O}_3$ shifts to the right are observed while the $\text{Li}_{1.25}\text{Mn}_2\text{O}_4$ and $\text{Li}_{1.50}\text{Mn}_2\text{O}_4$ split. Meanwhile, for $\text{Li}_{1.00}\text{Mn}_2\text{O}_4$, $\text{Li}_{1.75}\text{Mn}_2\text{O}_4$ and $\text{Li}_{2.00}\text{Mn}_2\text{O}_4$ the peaks are broad. The $\text{Li}_{1.75}\text{Mn}_2\text{O}_4$ concentration is still resilient to peak split even when stress is imposed on it. However, the peaks have become broad in contrast to observations made under NVT and NST recrystallisation in which the peaks were narrow.

Figure 6.10 shows the X-ray diffraction patterns for nanoporous 67 Å concentrations under the applied stress of 0.1 GPa. The shoulder peak for $\sim 2\theta = 18 - 23^\circ$ associated with layered and spinel composites have almost disappeared for all the concentrations, except

for $\text{Li}_{1.75}\text{Mn}_2\text{O}_4$ which shows its emergence. The peak at $\sim 2\theta = 26 - 32^\circ$ related to spinel Mn_3O_4 , is observed for all concentrations however its intensity for $\text{Li}_{1.50}\text{Mn}_2\text{O}_4$ and $\text{Li}_{2.00}\text{Mn}_2\text{O}_4$ is low. Furthermore, the peak is shifting towards the right favouring the spinel LiMn_2O_4 content. The peak at $\sim 2\theta = 36^\circ$ associated with spinel LiMn_2O_4 is observed for all concentrations, however, for $\text{Li}_{1.00}\text{Mn}_2\text{O}_4$ the peak merged with that of $\sim 2\theta = 26 - 32^\circ$ forming a very broad peak. Peaks at $\sim 2\theta = 45^\circ$ related to the coexistence of layered and spinel composites are broad for $\text{Li}_{1.00}\text{Mn}_2\text{O}_4$ and the $\text{Li}_{1.75}\text{Mn}_2\text{O}_4$ concentrations; whereas for the $\text{Li}_{1.25}\text{Mn}_2\text{O}_4$, $\text{Li}_{1.50}\text{Mn}_2\text{O}_4$ and $\text{Li}_{2.00}\text{Mn}_2\text{O}_4$ concentrations they split and span over $\sim 2\theta = 42 - 52^\circ$ favouring both the layered and spinel compositions. For peaks at $\sim 2\theta = 64^\circ$ associated with spinel LiMn_2O_4 , Mn_3O_4 and layered Li_2MnO_3 , they appear to be very broad for the pristine ($\text{Li}_{1.00}\text{Mn}_2\text{O}_4$) and the full lithiated ($\text{Li}_{2.00}\text{Mn}_2\text{O}_4$) concentrations. Meanwhile, for the $\text{Li}_{1.25}\text{Mn}_2\text{O}_4$ and $\text{Li}_{1.50}\text{Mn}_2\text{O}_4$, they split. The peaks span over $\sim 2\theta = 60 - 69^\circ$ at most.

The peak trends for the structures when they are subjected to the stress of 0.1 GPa is similar for some structures and different for some to those recrystallised under the under NVT and NST ensemble. For nanoporous 75 Å concentrations under 0.1 GPa stress, the peaks differ significantly from those recrystallised under NVT and NST ensemble. Recrystallisation of structures under the two ensembles rendered narrow peaks, however, when they endure stress they become broad. Furthermore, characteristics peaks at $\sim 2\theta = 18 - 23^\circ$ and $\sim 2\theta = 26 - 32^\circ$ when stress is applied almost disappear, while at $2\theta \sim 64^\circ$ they become less intense. Meanwhile, the nanoporous 69 Å structure with different concentrations under stress, have peaks that merge to form one broad peak especially for $2\theta \sim 18 - 23^\circ$ and $2\theta \sim 26 - 32^\circ$. Furthermore, the peaks at $\sim 2\theta = 64^\circ$ are less intense under stress. The concentration of $\text{Li}_{1.75}\text{Mn}_2\text{O}_4$ which had narrow peaks under NVT and NST for nanoporous 69 Å under stress become broad with some almost disappearing.

Nanoporous 67 Å structure shows broad peaks as well, different from NVT and NST. However, the $\text{Li}_{1.75}\text{Mn}_2\text{O}_4$ peak trend is similar under stress where a broadening of peaks is observed. The peaks under $\text{Li}_{1.50}\text{Mn}_2\text{O}_4$ concentration is similar for NVT, NST and under 0.1 GPa.

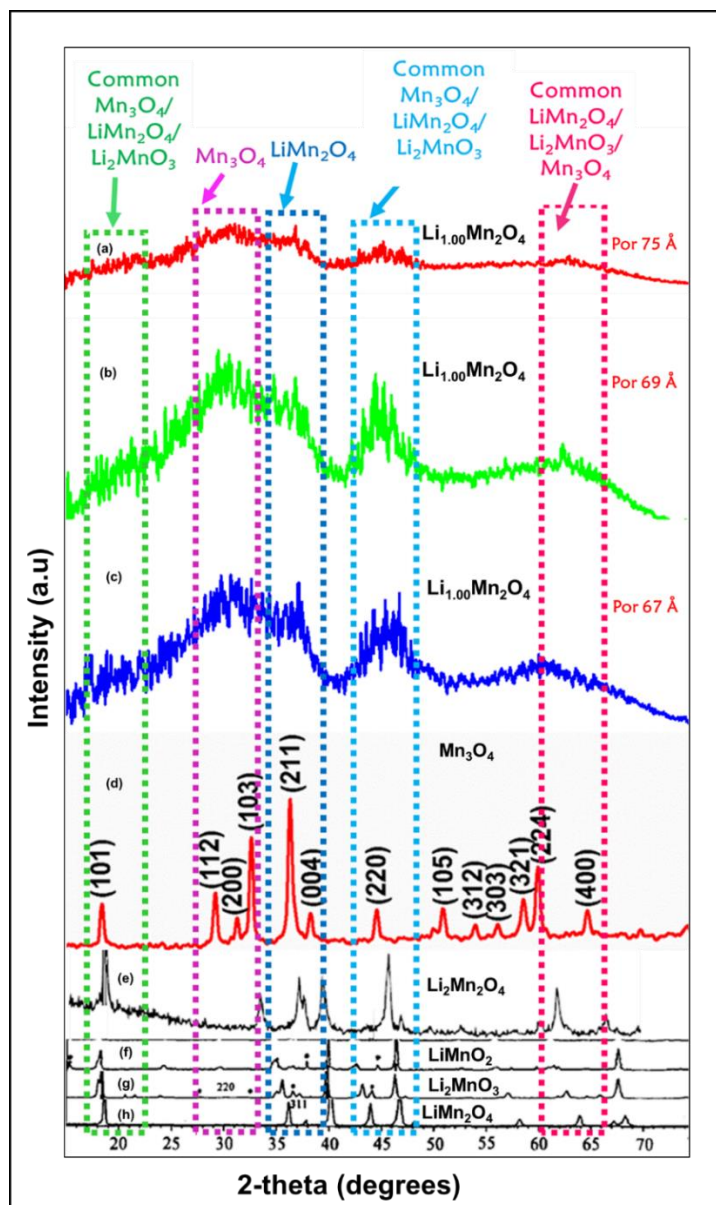


Figure 6.7: The X-ray diffraction patterns (XRDs) for structures in their pristine form at $\text{Li}_{1.00}\text{Mn}_2\text{O}_4$ concentration under the stress of 0.1 GPa for (a) nanoporous 75 Å, (b) nanoporous 69 Å and (c) nanoporous 67 Å structures; compared to the experimental XRDs for (d) spinel Mn_3O_4 [106], (e) spinel $\text{Li}_2\text{Mn}_2\text{O}_4$ [115], (f) layered LiMnO_2 [107], (g) layered Li_2MnO_3 [107] and (h) spinel LiMn_2O_4 [107].

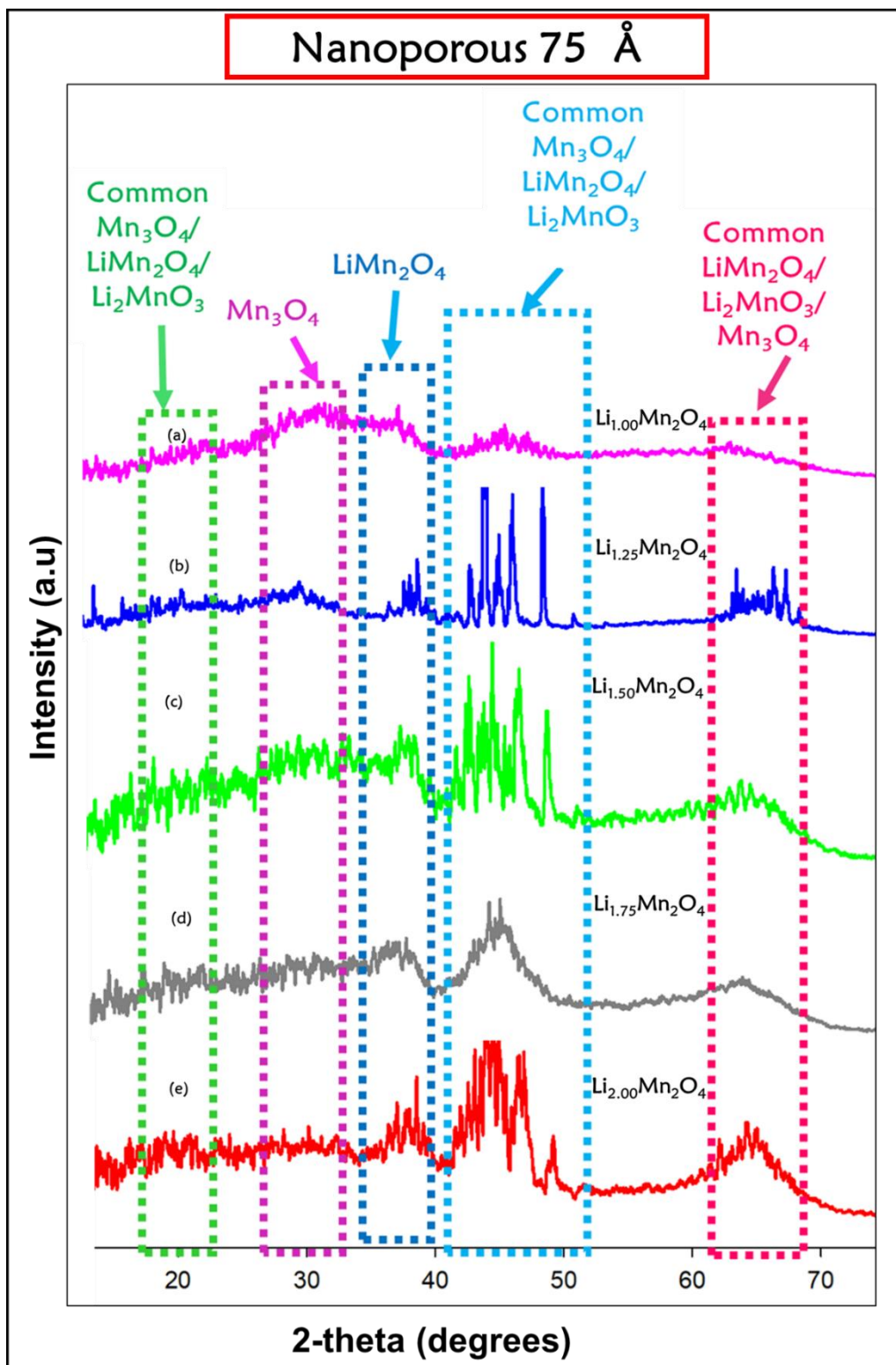


Figure 6.8: The X-ray diffraction patterns (XRDs) for nanoporous 75 Å structure under the stress of 0.1 GPa, at $\text{Li}_{1+x}\text{Mn}_2\text{O}_4$ where $0 \leq x \leq 1$, for the simulated (a) $\text{Li}_{1.00}\text{Mn}_2\text{O}_4$, (b) $\text{Li}_{1.25}\text{Mn}_2\text{O}_4$, (c) $\text{Li}_{1.50}\text{Mn}_2\text{O}_4$, (d) $\text{Li}_{1.75}\text{Mn}_2\text{O}_4$ and (e) $\text{Li}_{2.00}\text{Mn}_2\text{O}_4$ concentrations.

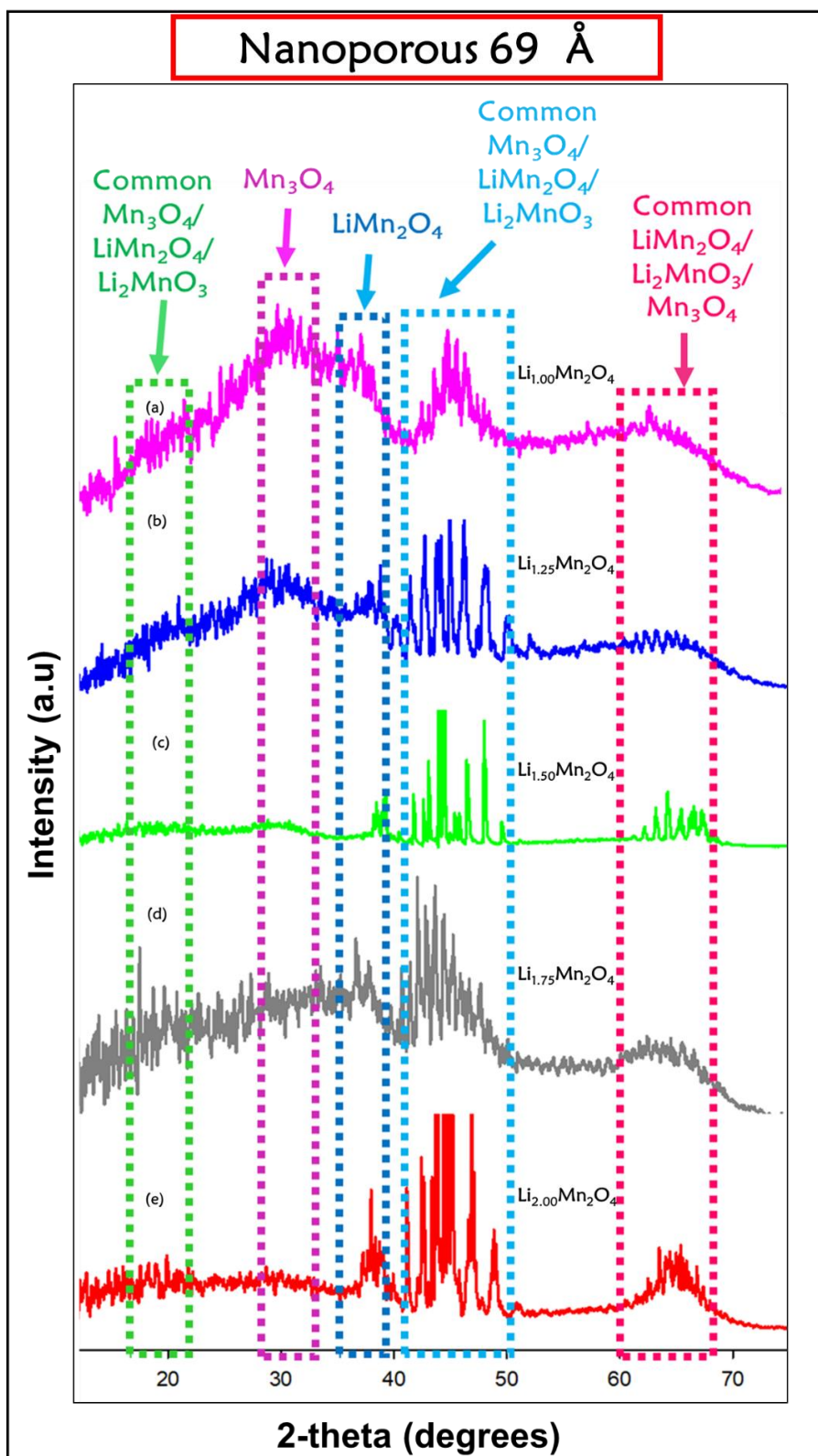


Figure 6.9: The X-ray diffraction patterns (XRDs) under the stress of 0.1 GPa for nanoporous 69 Å structure at $\text{Li}_{1+x}\text{Mn}_2\text{O}_4$ where $0 \leq x \leq 1$, for the simulated (a) $\text{Li}_{1.00}\text{Mn}_2\text{O}_4$, (b) $\text{Li}_{1.25}\text{Mn}_2\text{O}_4$, (c) $\text{Li}_{1.50}\text{Mn}_2\text{O}_4$, (d) $\text{Li}_{1.75}\text{Mn}_2\text{O}_4$ and (e) $\text{Li}_{2.00}\text{Mn}_2\text{O}_4$ concentrations.

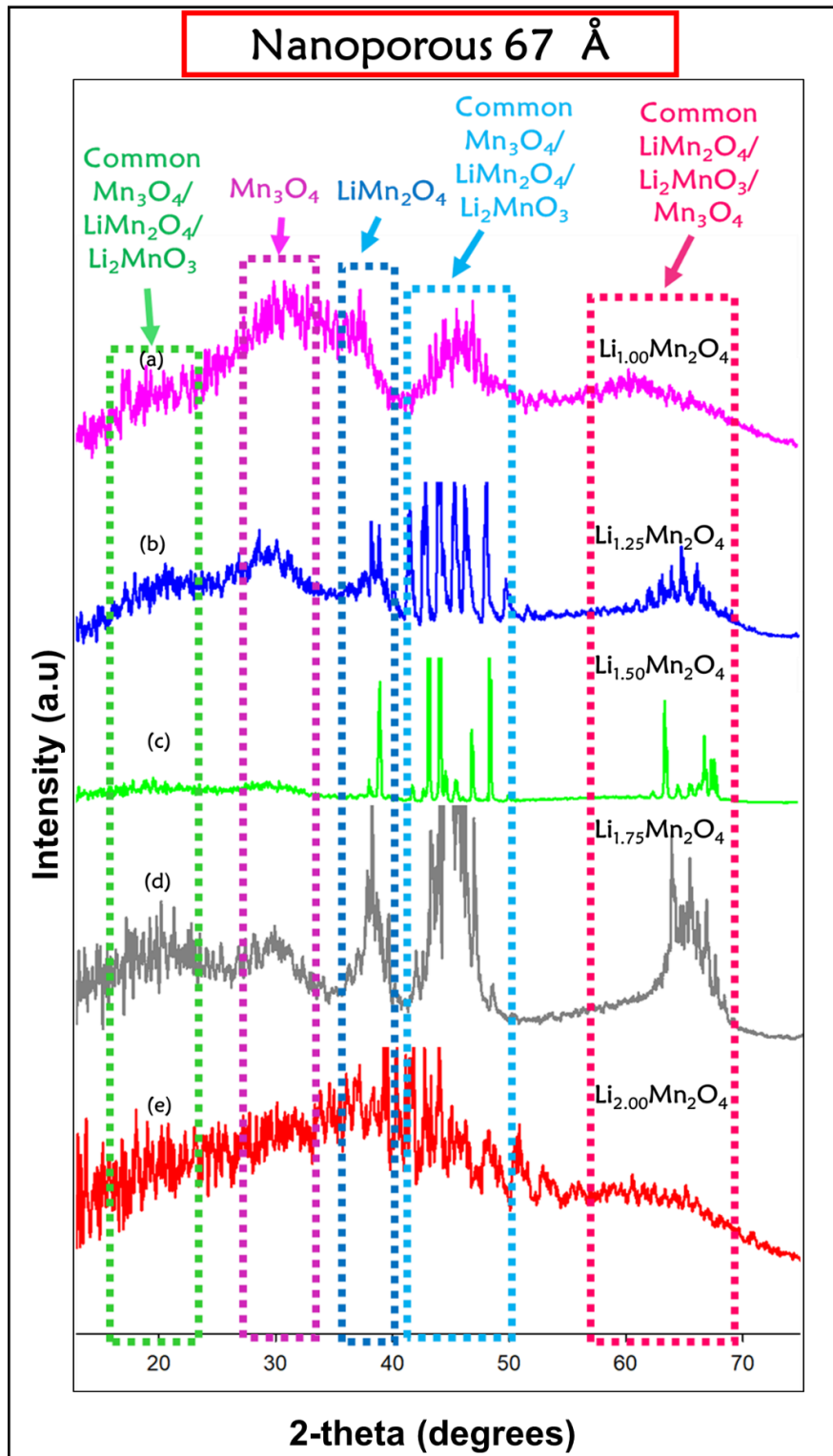


Figure 6.10: The simulated nanoporous 67 Å structure at $\text{Li}_{1+x}\text{Mn}_2\text{O}_4$, where $0 \leq x \leq 1$ concentrations illustrating the X-ray diffraction patterns (XRDs) under the stress of 0.1 GPa for (a) $\text{Li}_{1.00}\text{Mn}_2\text{O}_4$, (b) $\text{Li}_{1.25}\text{Mn}_2\text{O}_4$, (c) $\text{Li}_{1.50}\text{Mn}_2\text{O}_4$, (d) $\text{Li}_{1.75}\text{Mn}_2\text{O}_4$ and (e) $\text{Li}_{2.00}\text{Mn}_2\text{O}_4$.

6.4 Discussion

The mechanical properties calculations have been successfully executed by employing molecular dynamics methods to investigate the mechanical response of nanoporous structures at various lithium concentrations and lattice sizes when the uniaxial stress of 0.01 GPa is applied to the materials along the y-direction. The analysis made from the stress-strain plots of the structures shows that the yield strength of the materials and elastic modulus increases with lattice size reduction for the $\text{Li}_{1.50}\text{Mn}_2\text{O}_4$ and $\text{Li}_{2.00}\text{Mn}_2\text{O}_4$ concentrations. Meanwhile, at $\text{Li}_{1.00}\text{Mn}_2\text{O}_4$ and $\text{Li}_{1.25}\text{Mn}_2\text{O}_4$ concentration for nanoporous 69 Å structure, high yield strengths were observed; on the other hand, for nanoporous 67 Å, a high elastic modulus was observed. Moreover, at the $\text{Li}_{1.75}\text{Mn}_2\text{O}_4$ concentration for nanoporous 69 Å structure the highest yield strength and elastic modulus was observed followed by nanoporous 67 Å. While the yield strengths and elastic modulus for the materials fluctuate with lattice size and lithium concentrations, nanoporous 69 Å has shown great strength compared to its counterparts, especially at $\text{Li}_{1.75}\text{Mn}_2\text{O}_4$ concentration where the materials became distorted and gained grain boundaries.

The radial distribution functions under stress demonstrated the broadening and flattening of peaks with increasing radial distance r , especially after 8 Å. This could imply that the structures are becoming distorted/ disordered with the continuous 0.01 GPa stress imposed on them. The X-ray diffraction patterns showed the disappearance of some peaks after stress was applied to the structures. On the other hand, other peaks merged to form one broad peak, while others become less intense. The XRDs for nanoporous 69 Å, under stress, behaves similar to those of nanoporous 75 and 67 Å when recrystallised under NVT and NST ensembles showing broad peaks, especially at $\text{Li}_{1.75}\text{Mn}_2\text{O}_4$. Similar to NVT and NST, shifts and splits are still observed. The shifts, splits and broadening of peaks could be attributed to the mixing of Li and Mn layers, phase transitions, defects generated in the

Li-Mn-O systems during lithium intercalation [108, 109, 110]. Furthermore, they could also be attributed to the 0.1 GPa stress in the y-direction imposed on the structures. Although under stress nanoporous 69 Å shows broad peaks on its XRDs at $\text{Li}_{1.75}\text{Mn}_2\text{O}_4$ concentration, its yield strength is relatively high compared to its counterparts. This is the critical concentration where the structures have changed in symmetry from cubic to tetragonal phase. This further validates that nanoporous 69 Å is special and can probably be a better material to withstand the harsh conditions that come with stress during the discharge process which causes fractures within the battery material.

CHAPTER 7

Conclusion and Recommendations

7.1 Conclusion

Cost-effective energy storage batteries could transform the energy landscape for the better, especially in mitigation measures against climate change. Hence, harnessing cheap and abundant materials like manganese can be of great advantage; especially in South Africa where manganese constitutes over 80% of the world's reserves [125, 126, 127]. A discharge process for the spinel lithium manganese oxide (LMO) nanoparticles, epitomised by inserting surplus lithium atoms, results in disruptive structural changes, with $\text{Li}_{1.75}\text{Mn}_2\text{O}_4$ clearly identified as transitional multi-grained structure, between the cubic ($\text{Li}_1\text{Mn}_2\text{O}_4$) and tetragonal ($\text{Li}_2\text{Mn}_2\text{O}_4$) phases [128]. Such drastic transition is associated with a problem of cracking and pulverisation of the cathode material which needs to be solved in order to attain higher capacity.

Consequently, an attempt of changing the disruptive transition into a smooth structural transition in the spinel $\text{Li}_{1+x}\text{Mn}_2\text{O}_4$, where $0 \leq x \leq 1$, particularly at $\text{Li}_{1.75}\text{Mn}_2\text{O}_4$, was explored by investigating Li-Mn-O bulk and nanoporous architectures, the latter with different pore sizes. Simulated amorphisation and recrystallisation technique, based on molecular dynamics method, and using the Born model of ionic solids parameters was employed to amorphise and recrystallise the $\text{Li}_{1+x}\text{Mn}_2\text{O}_4$ ($0 \leq x \leq 1$) bulk and nanoporous structures. The technique is capable of producing microstructural features like those observed experimentally [68]. Related structural, mechanical properties, volume changes and diffusion coefficients with varying lithium concentrations were calculated in order to

establish structural integrity of the spinel Li-Mn-O, which could likely yield full potential capacity that has not been achieved thus far.

Structural aspects of nanoporous $\text{Li}_{1+x}\text{Mn}_2\text{O}_4$ ($0 \leq x \leq 1$), as deduced from simulated XRDs, are now scrutinized; commencing with the smallest 67 and highest 75 Å lattice sizes. The XRDs showed the existence of hetero-structural components of layered and spinel structures [107]. On increasing lithium content in $\text{Li}_{1+x}\text{Mn}_2\text{O}_4$ ($0 \leq x \leq 1$), XRDs reflect narrow peaks at $x = 0$ and $x = 1$ and significant broad peaks at $\text{Li}_{1.75}\text{Mn}_2\text{O}_4$ concentration; this is the concentration where the structures have evolved into multiple crystals for the nanoporous structures. This transformation signifies a change from spinel cubic to tetragonal symmetries. However, for the nanoporous 69 Å lattice size, the narrow peaks were maintained in the whole range ($0 \leq x \leq 1$), including the transition concentration $\text{Li}_{1.75}\text{Mn}_2\text{O}_4$. The bulk depicted broad peaks at such concentration [129] consistent with the current smallest and largest nanoporous lattice sizes; implying that the 69 Å one is unique.

Microstructural features of the $\text{Li}_{1+x}\text{Mn}_2\text{O}_4$ ($0 \leq x \leq 1$) nanoporous architecture that were generated spontaneously by the A+R method are now considered. Generally, recrystallised structures evolved into hetero-structural layered and spinel phases as shown in nanospheres [72] and experiments [7, 130, 26]. In concurrence with XRD analysis, for 67 and 75 Å lattice size structures, single grains are noted at low and high lithium concentrations. However, multigrains are dominant at the transition from cubic to tetragonal spinel, i.e. $\text{Li}_{1.75}\text{Mn}_2\text{O}_4$, consistent with observations in the nanosphere [128] and expanded freely upon lithiation due to their ability to flex within their pores. The microstructures and XRDs showed the existence of hetero-structural components. In contrast, for the 69 Å lattice size structure, the microstructure, whilst intrinsically hetero-structural, appears uniform without obvious grain boundaries, throughout all

concentrations, including the critical transition concentration of $\text{Li}_{1.75}\text{Mn}_2\text{O}_4$. This is in concurrence with observed narrow XRD peaks for the 69 Å lattice sized nanoporous architecture.

Mechanical properties calculations of the nanoporous $\text{Li}_{1+x}\text{Mn}_2\text{O}_4$ ($0 \leq x \leq 1$) were executed to help investigate the mechanical response at various lithium concentrations and pore sizes and by monitoring response to strain when uniaxial stress is imposed. The analysis shows that the yield strength and elastic modulus increases with lattice size reduction for the $\text{Li}_{1.50}\text{Mn}_2\text{O}_4$ and $\text{Li}_{2.00}\text{Mn}_2\text{O}_4$ concentrations. Meanwhile, for $\text{Li}_{1.00}\text{Mn}_2\text{O}_4$ and $\text{Li}_{1.25}\text{Mn}_2\text{O}_4$ concentrations, the 69 Å lattice size nanoporous architecture has the highest yield strength with nanoporous 67 Å featuring the highest elastic modulus. On the other hand, the nanoporous 69 Å reflects both the highest yield strength and elastic modulus at the $\text{Li}_{1.75}\text{Mn}_2\text{O}_4$ concentration, followed by the nanoporous 67 Å. While the yield strengths and elastic moduli for structures fluctuate with lattice sizes and lithium concentrations, nanoporous 69 Å lattice size has depicted pronounced strength compared to its counterparts, especially at $\text{Li}_{1.75}\text{Mn}_2\text{O}_4$ concentration, where multiple grain boundaries are prevalent. The total RDFs for the Li-Mn-O nanoporous and bulk structures exposed to the uniaxial stress of 0.01 GPa depict broad and flat peaks with increasing radial distance r ; implying atomic arrangement disorder or scattering of atoms. Furthermore, the Li-Mn-O XRDs under stress capture significant shifts, splits and broadening of peaks [108, 110]; which some merge to form one broad peak. This could imply the deformation or distortion of some regions within the structures. Although nanoporous 69 Å shows broad peaks at the critical concentration of $\text{Li}_{1.75}\text{Mn}_2\text{O}_4$ when subjected to the uniaxial stress, it is evident that it is robust since it had narrow and sharp peaks during volume changes, withstanding expansion which causes battery cracks [60].

It is of significance to explore reasons pertaining to the structural stability of the 69 Å lattice sized nanoporous architecture at $\text{Li}_{1.75}\text{Mn}_2\text{O}_4$ concentration. A closer look at volume changes, under the NST ensemble, across such concentration provides valuable insights. The nanostructure with the 69 Å lattice size exhibits limited volume expansion with increasing lithium concentration, whilst those of its counterparts are significant and distinct. Since the nanoporous 69 Å is more robust and resilient to the volume change at $\text{Li}_{1.75}\text{Mn}_2\text{O}_4$, this could imply that the cavity to wall ratio of nanoporous 69 Å might possibly result in an electrode structure that can provide appropriate electrochemical and mechanical properties for Li-ion batteries as it is not easily susceptible to fracture.

In order to verify the robustness of the stable 69 Å lattice size nanostructure, it was subjected to high temperatures through molecular dynamics method. No obvious structural changes were noted and lithium ions diffused well within the temperature range studied. The low diffusion rate of lithium ions in cathodes may result in the loss of specific capacity [52, 65]. Therefore, the diffusion rates of the Li-Mn-O materials were investigated to evaluate their stability with increasing temperatures. It was observed that pore size influences the diffusion rate where nanoporous 75 Å showed the highest diffusivity, followed by nanoporous 69 Å, then nanoporous 67 Å and finally the bulk. This indicates that porosity or pore size plays a huge role in lithium diffusion with increasing temperatures. In nanoporous 75 Å, especially at $\text{Li}_{1.75}\text{Mn}_2\text{O}_4$, the high mobility could be ascribed to the presence of grain boundaries which act as pathways or transport medium for lithium migration [131]. Furthermore, the microstructures have shown the reduction of Mn_3O_4 with increasing lithium content which allows for high Li migration due to fewer Mn^{2+} residing in the tunnels during lithiation. The diffusion coefficients for lithium showed an increased diffusion rate with increasing structural lattice size.

The study, for the first time, has shared information on the electrochemical and mechanical properties, at intermediate lithium concentrations to full lithiation at $\text{Li}_{2.00}\text{Mn}_2\text{O}_4$ for nanoporous structures with distinct lattice parameters and the bulk. The major findings of the study revealed structural changes at the $\text{Li}_{1.75}\text{Mn}_2\text{O}_4$ concentration. This abrupt concentration showed a wealth of grain boundaries where the structures transitioned from cubic to tetragonal phase [128]. Interestingly, nanoporous 69 Å at this abrupt concentration showed minimal to no grain boundaries under NST and NVT recrystallisation, respectively. Furthermore, the structure showed resilience to expansion at $\text{Li}_{1.75}\text{Mn}_2\text{O}_4$. Finally, it had the highest yield strength compared to nanoporous 75 and 67 Å. This clearly indicates that nanoporous 69 Å is setting itself apart from its counterparts and shows desirable properties, which have the potential to restrain battery degradation. Therefore, the insights shared in this study will help pave the way in the understanding and improvement of future Li-ion battery cathode materials.

7.2 Recommendations

The current study has proved that lithiation of the Li-Mn-O nanoarchitectures is rarely affected by increasing the lithium content in materials, as it was observed that the structural integrity is easily not compromised; except at the harsh concentration of $\text{Li}_{1.75}\text{Mn}_2\text{O}_4$ where the structures transitioned from cubic to tetragonal phase. This can be supported by observations made on the bulk and porous nanoarchitectures where the spinel and layered components were captured co-existing within the structures at mono, intermediate and full lithiated concentrations. The nanoporous structures showed fluctuations in pore size with increasing lithium content. The spinel Mn_3O_4 component and the crystallographic defects within the materials were reduced with an increase in lithium concentration. The volume changes analysis showed that nanoporous structures can

withstand lithium increment to full capacity ($\text{Li}_{2.00}\text{Mn}_2\text{O}_4$). Nanoporous 69 Å, in particular, showed desirable properties even when stress was imposed on it. The material has a high yield strength at an abrupt concentration where a phase transition from cubic to tetragonal occur, which is most likely to compromise the structural integrity.

However, the need to investigate the nanoporous material at intermediate lattice sizes between 75 and 67Å, still require full attention, as they could provide better electrochemical and mechanical properties compared to the nanoporous 69 Å. Furthermore, the wall thickness of the current studied materials still needs to be investigated, as it plays a vital role in the diffusion of lithium [132]. This will contribute towards the understanding of the capabilities of the Li-Mn-O structures while designing future Li-ion battery cathode materials; taking into consideration what type of cathode material to use, their texture, pore size, particle size, wall thickness, etc. for optimal battery use and performance.

REFERENCES

- [1] G. Zubi, R. Dufo-Lopez, M. Carvalho, G. Pasaoglu, "The lithium-ion battery: State of the art and future perspectives," *Renewable and Sustainable Energy Reviews*, vol. 89, pp. 292-308, 2018.
- [2] P. Mohtat, S. Lee, V. Sulzer, J.B. Siegel and A.G. Stefanopoulou, "Differential expansion and voltage model for Li-ion batteries at practical charging rates," *Journal of the Electrochemical Society*, vol. 167, pp. 1-13, 2020.
- [3] S. Wang, H. Liu, M. Xiang, J. Guo, W. Bai, H. Bai, X. Liu and C. Su, "Improved electrochemical properties and kinetics of LiMn_2O_4 -based co-modified via Cu doping with truncated octahedron morphology," *New Journal Chemistry*, vol. 44, pp. 10569-10577, 2020.
- [4] F. Saidani, F.X. Hutter, R.G. Scurtu, W. Braunwarth and J.N. Burgharz, "Lithium-ion battery models: a comparative study and a model-based powerline communication," *Advances in Radio Science*, vol. 15, pp. 83-91, 2017.
- [5] X.D. Lou, Y.Z. Yin, M. Yuang, W. Zeng, G. Lin, B. Huang, Y.W. Li and S.H. Xiao, "High performance composites of spinel LiMn_2O_4 /3DG for lithium ion batteries," *Royal Society of Chemistry Advances*, vol. 8, pp. 877-884, 2018.
- [6] F. Fu, G.L. Xu, Q. Wang, Y.P. Deng, X. Li, J.T. Li, L. Huang and S. G. Sun, "Synthesis of single crystalline hexagonal nanobricks of $\text{LiNi}_{1/3}\text{Co}_{1/3}\text{Mn}_{1/3}\text{O}_2$ with high percentage of exposed {010} active facets as high rate performance cathode

- material for lithium-ion battery," *Journal of Materials Chemistry A*, vol. 1, pp. 3860-3864, 2013.
- [7] B.R. Long, J.R. Croy, J.S. Park, J. Wen, D.J. Miller and M.M. Thackeray, "Advances in stabilizing layered-layered $x\text{Li}_2\text{MnO}_3\cdot(1-x)\text{LiMO}_2$ (M=Mn, Ni, Co) electrodes with a spinel component," *The Electrochemical Science*, vol. 161, pp. 2160-2167, 2014.
- [8] S. Yao, J. Zhang, X. Gou and X. Qui, "Preparation and electrochemical properties of $x\text{Li}_2\text{MnO}_3\cdot(1-x)\text{LiMn}_2\text{O}_4$ composites," *Chemical Research*, vol. 29, pp. 307-310, 2013.
- [9] F. Lai, X. Zhang, Q. Wu, J. Zhang, Q. Li, Y. Huang and Z. Liao, "Effect of surface modification with spinel NiFe_2O_4 on enhanced cyclic stability of LiMn_2O_4 cathode materials in lithium ion batteries," *Sustainable Chemistry and Engineering*, vol. 6, pp. 570-578, 2018.
- [10] Y.S. Meng and M.E. Dompablo, "First principles computational materials design for energy storage materials in lithium ion batteries," *Energy and Environmental Science*, vol. 2, pp. 589-609, 2009.
- [11] Y. Haung, Y. Dong, S. Li, J. Lee, C. Wang, Z. Zhu, W. Xue, Y. Li and J. Li, "Lithium manganese spinel cathodes for lithium-ion batteries," *Advanced Energy Materials*, vol. 11, pp. 1-21, 2020.
- [12] T. Kozawa, T. Harata and M. Naito, "Fabrication of an $\text{LiMn}_2\text{O}_4@ \text{LiMnPO}_4$ composite cathode for improved cycling performance at high temperatures," *Journal of Asian Ceramic Societies*, vol. 8, pp. 309-317, 2020.

- [13] H. Xia, Z. Lou and J. Xie, "Nanostructured LiMn_2O_4 and their composites as high-performance cathodes for lithium-ion batteries.," *Progress in Natural Science: Materials International*, vol. 22, pp. 572-584, 2012.
- [14] M.J. Lee, S. Lee, P. Oh, Y. Kim and J. Cho, "High performance LiMn_2O_4 cathode materials grown with epitaxial layered nanostructure for Li-Ion batteries," *Nano Letters*, vol. 14, pp. 993-999, 2014.
- [15] J.C. Hunter, "Preparation of a new crystal form of manganese dioxide: $\lambda\text{-MnO}_2$," *Journal of Solid State Chemistry*, vol. 39, pp. 142-147, 1981.
- [16] M.M. Thackeray, W.I.F. David, P.G. Bruce and J.B. Goodenough, "Lithium insertion into manganese spinels," *Materials Research Bulletin*, vol. 18, pp. 461-472, 1983.
- [17] M.M. Thackeray, P.J. Johnson, L.A. Depicciotto, P.G. Bruce and J.B. Goodenough, "Electrochemical extraction of lithium from LiMn_2O_4 ," *Materials Research Bulletin*, vol. 19, pp. 179-187, 1984.
- [18] R.J. Gummow, A. Dekock, M.M. Thackeray, "Improved capacity retention in rechargeable 4 V lithium/ lithium-manganese oxide (spinel) cells," *Solid State Ionics*, vol. 69, pp. 59-67, 1994.
- [19] A. Manthiram, K. Chemelewski and E.S. Lee, "A perspective on the high-voltage $\text{LiMn}_{1.5}\text{Ni}_{0.5}\text{O}_4$ spinel cathode for lithium-ion batteries," *Energy & Environmental Science*, vol. 7, pp. 1339-1350, 2014.
- [20] R. Schmuch, R. Wagner, G. Horpel, T. Placke and M. Winter, "Performance and cost of materials for lithium-based rechargeable automotive batteries," *Nature Energy*, vol. 3, pp. 267-278, 2018.

- [21] J. Zhao, S. Ellis, Z. Xie and Y. Wang, "Facile synthesis of integrated layered-spinel composite cathode materials for high-voltage lithium-ion batteries up to 5.0 V," *ChemElectroChem*, vol. 2, pp. 1821-1829, 2015.
- [22] D. Kim, G. Sandi, J.R. Croy, K.G. Gallagher, S.H. Kang, E. Lee, M.D. Slater, C.S. Johnson and M.M. Thackeray, "Composite layered-layered-spinel cathode structures for lithium ion batteries," *Journal of Electrochemical Society*, vol. 160, pp. A31-A38, 2013.
- [23] J.R. Croy, J.S. Park, Y. Shin, B.T. Yonemoto, M. Balasubramanian, B.R. Long, Y. Ren and M.M. Thackeray, "Prospects for spinel-stabilized, high-capacity lithium-ion battery cathodes," *Journal of Power Sources*, vol. 334, pp. 213-220, 2016.
- [24] X. Li and X. Sun, "Nanostructured materials for Li-ion batteries and beyond," *Nanomaterials*, vol. 6, pp. 1-3, 2016.
- [25] G. Venugopal, A. Hunt and F. Alamgir, "Nanomaterials for energy storage in lithium-ion battery application," *Material matters*, vol. 5.2, pp. 1-2, 2010.
- [26] Y.P. Deng, Z.W. Yin, S.J. Zhang, F. Fu, T. Zhang, J.T. Li, L. Huang and S.G. Sun, "Layered/spinel heterostructured and hierarchical micro/nanostructured Li-rich cathode materials with enhanced electrochemical properties for Li-ion batteries," *Applied Materials & Interfaces*, vol. 9, pp. 21065-21070, 2017.
- [27] Y.P. Deng, F. Fu, Z.G. Wu, Z.W. Yin, T. Zhang, J.T. Li, L. Huang and S.G. Sun, "Layered/spinel heterostructured Li-rich materials synthesized by a one-step solvothermal strategy with enhanced electrochemical performance for Li-ion batteries," *Journal of Materials Chemistry A*, vol. 4, pp. 257-263, 2016.

- [28] J. An, L. Shi, G. Chen, M. Li, H. Liu, S. Yuan, S. Chen and D. Zhang, "Insights into the stable layered structure of a Li-rich cathode material for lithium-ion batteries," *Journal of Materials Chemistry A*, vol. 5, p. 19738–19744, 2017.
- [29] R. Van Roy, "Designing applications with lithium ion batteries," Richteck Technology Corporation, Chupei city, Taiwan, 2014.
- [30] N. Ross, S. Willenberg and E. Iwuoha, "Analysis of electrochemical and structurally enhanced LiMn_2O_4 nanowire cathode system," in *Nanowires-synthesis, properties and applications*, Western Cape, South Africa, IntechOpen, 2019, pp. 39-51.
- [31] X. Sun, X. Hu, J. Tan, X. Tan, Q. Yu, Z. Li and Y. Zhai, "The synthesis and electrochemical property of spinel cathode material $\text{Li}_{1.05}[(\text{Mn}_{1.99}\text{Gd}_{0.01})_{0.91}(\text{Mn}_{1.8}\text{Co}_{0.2})_{0.09}]\text{O}_4$ for lithium ion batteries," *International Journal of Electrochemical Science*, vol. 13, pp. 2355-2365, 2018.
- [32] S. Martinez, I. Sobrados, D. Tonti, J.M. Amarilla and J. Sanz, "Chemical vs. electrochemical extraction of lithium from the Li-excess $\text{Li}_{1.10}\text{Mn}_{1.90}\text{O}_4$ spinel followed by NMR and DRX techniques," *Physical Chemistry Chemical Physics*, vol. 16, pp. 3282-3291, 2014.
- [33] M.G. Matshaba, D.C. Sayle, T. X.T. Sayle and P.E. Ngoepe, "Amorphisation and recrystallisation study of lithium intercalation into TiO_2 nano-architecture.," *Materials Science and Engineering*, vol. 169, pp. 1-6, 2017.
- [34] T.X.T. Sayle, R.R. Maphanga, P.E. Ngoepe and D.C. Sayle, "Predicting the electrochemical properties of MnO_2 nanomaterials used in rechargeable Li

- batteries: simulating nanostructure at the atomistic level,” *Journal of the American Chemical Society*, vol. 131, pp. 6162-6163, 2009.
- [35] Y. Zhang, H. Xie, H. Jin, Q. Zhang, Y. Li, X. Li, K. Li and C. Bao, “Research status of spinel LiMn_2O_4 cathode materials for lithium ion batteries,” *Earth and Environment Science*, vol. 603 (012051), pp. 1-6, 2020.
- [36] N. Nitta, F. Wu, J.T. Lee and G. Yushin, “Li-ion battery materials: present and future,” *Materials Today*, vol. 15, pp. 252-264, 2015.
- [37] S.K. Jeong, J.S. Shin, K.S. Nahm, T.P. Kumar and A.M. Stephan, “Electrochemical studies on cathode blends of LiMn_2O_4 and $\text{Li}[\text{Li}_{1/15}\text{Ni}_{1/15}\text{Co}_{2/5}\text{Mn}_{1/3}\text{O}_2]$,” *Material Chemistry and Physics*, vol. 111, pp. 213-214, 2008.
- [38] N. Bensalah and H. Dawood, “Review on synthesis, characterization, and electrochemical properties of cathode materials for lithium ion batteries,” *Material Science and Engineering*, vol. 5, pp. 10-13, 2016.
- [39] B.L. Ellis, K. Town and L.F. Nazar, “New composite materials for lithium ion batteries,” *Electrochimica Acta*, vol. 84, pp. 145-154, 2012.
- [40] E. Zhao, L. Fang, M. Chen, D. Chen, Q. Huang, Z. Hu, Q. Yan, M. Wu and X. Xiao, “New insight into Li/Ni disorder in layered cathode materials for lithium ion batteries: a joint study of neutron diffraction, electrochemical kinetic analysis and first-principles calculations,” *Journal of Materials Chemistry A*, vol. 5, pp. 1679–1686, 2017.
- [41] L. Ben, H. Yu, B. Chen, Y. Chen, Y. Gong, X. Yang, L. Gu and X. Huang, “Unusual spinel to layered transformation in LiMn_2O_4 cathode explained by electrochemical

- and thermal stability investigation,” *ACS Applied Materials and Interfaces*, vol. 9, pp. 35463-35475, 2017.
- [42] R.S. Ledwaba, J.C. Womack, C.K. Skylaris and P.E. Ngoepe, “Intercalation voltages for spinel $\text{Li}_x\text{Mn}_2\text{O}_4$ ($0 \leq x \leq 2$) cathode materials: Calibration of calculations with the ONETEP linear-scaling DFT code,” *Materials Today Communications*, vol. 27(102380), pp. 1-5, 2021.
- [43] K. Ragavendran, H. Xia, P. Mandal and A.K. Arof, “Jahn-Teller effect in LiMn_2O_4 : influence on charge ordering, magnetoresistance and battery performance,” *Physical Chemistry Chemical Physics*, vol. 19, pp. 6481-6486, 2017.
- [44] R.E. Warburton, F.C. Castro, S. Deshpande, K.E. Madsen, K.L. Bassett, R. Dos Reis, A.A. Gewirth, V.P. Dravid and J. Greeley, “Oriented LiMn_2O_4 particle fracture from delithiation-driven surface stress,” *ACS Applied Materials and Interfaces*, vol. 12, pp. 49182-49191, 2020.
- [45] B. Xu, D. Qian, Z. Wang and Y.S. Meng, “Recent progress in cathode materials research for advanced lithium ion batteries,” *Material Science and Engineering*, vol. 73, pp. 51-65, 2012.
- [46] J.W. Fergus, “Recent developments in cathode materials for lithium ion batteries,” *Journal of Power Sources*, vol. 195, pp. 939-954, 2010.
- [47] C.S. Johnson, J.T. Li, S.A. Vaughey and M.M. Thackeray, “Lithium manganese oxide electrodes with layered-spinel composite structures $x\text{Li}_2\text{MnO}_3 \cdot (1-x)\text{Li}_{1+y}\text{Mn}_{2-y}\text{O}_4$ ($0 < x < 1$, $0 \leq y \leq 0.33$) for lithium batteries,” *Electrochemical Communications*, vol. 7, pp. 528-536, 2005.

- [48] E.S. Lee, A. Huq, H.Y. Chang, A. Manthiram, "High-voltage, high-energy layered-spinel composite cathodes with superior cycle life for lithium-ion batteries," *Chemistry of Materials*, vol. 24, pp. 600-612, 2012.
- [49] Y. Liu, Y. Gao and A. Dou, "Influence of Li content on structure and electrochemical performance of $\text{Li}_{1+x}\text{Ni}_{0.25}\text{Mn}_{0.75}\text{O}_{2.25+x/2}$ cathode for Li-ion battery," *Journal of Power Sources*, vol. 248, pp. 679-684, 2014.
- [50] Y. Su-mei, Z. Jing-wen, G. Xun and Q. Xin-ping, "Preparation and electrochemical properties of $x\text{Li}_2\text{MnO}_3\cdot(1-x)\text{LiMn}_2\text{O}_4$ composites," *Chemical Research*, vol. 29, pp. 307-310, 2013.
- [51] Y. Ding and Z. Zhang, "Nanoporous metal for advanced energy technologies," in *Nanoporous material for Li battery applications*, Cham, Springer, 2016, pp. 175-209.
- [52] J. Song, J. Kim, T. Kang and D. Kim, "Design of a porous cathode for ultrahigh performance of a Li-ion battery: An overlooked pore distribution," *Scientific Reports*, vol. 7, pp. 1-8, 2017.
- [53] B. Qiu, C. Yin, Y. Xia and Z. Liu, "Synthesis of three-dimensional nanoporous Li-rich layered cathode oxides for high volumetric and power energy density lithium battery," *ACS Applied Materials and Interfaces*, vol. 9, pp. 3661-3666, 2017.
- [54] C.M. Julien, A. Mauger, K. Zaghib and H. Groult, "Comparative issue of cathode materials for Li-ion batteries," *Inorganics*, vol. 2, pp. 132-154, 2014.

- [55] W. Xiao, C. Xin, S. Li, J. Jie, Y. Gu, J. Zheng and F. Pan, "Insight into fast Li diffusion in Li-excess spinel lithium manganese oxide," *Journal of Materials Chemistry A*, vol. 6, pp. 9893-9898, 2018.
- [56] M.C. Rao, "LiMn₂O₄ cathodes for solid state lithium ion batteries - Energy storage and conversion," *Journal of Optoelectronics and Biomedical Materials*, vol. 5, pp. 9-16, 2013.
- [57] M.O. Guler, A. Akbulut, T. Cetinkaya, M. Usaya, and H. Akbulut, "Improvements of electrochemical and structural properties of LiMn₂O₄ spinel based electrode materials for Li-ion batteries," *International Journal of Hydrogen Energy*, vol. 39, pp. 21447-21460, 2014.
- [58] C. Liu, Z.G. Neale and G. Cao, "Understanding electrochemical potentials of cathode materials in rechargeable batteries," *Materials Today*, vol. 19, pp. 109-122, 2016.
- [59] K. Zhao, M. Pharr, J.J. Vlassak and Z. Sou, "Fracture of electrodes in lithium-ion batteries caused by fast charging.," *Journal of Applied Physics*, vol. 108, pp. 073517-1, 2010.
- [60] Z. Haizhou, "Modeling of lithium-ion battery for charging/discharging characteristics based on circuit model," *International Journal of Online Engineering*, vol. 13, pp. 86-95, 2017.
- [61] A. Mukhopadhyay and B.W. Sheldon, "Deformation and stress in electrode materials for Li-ion batteries," *Progress in Material Science*, vol. 63, pp. 58-116, 2014.

- [62] L.S. Willenberg, P. Dechent, G. Fuchs, D.U. Sauer and E. Figgemeier, "High-precision monitoring of volume change of commercial lithium-ion batteries by using a strain gauge," *Sustainability*, Vol. 12, pp. 1-15, 2020.
- [63] A. Pfrang, A. Kersys, A. Kriston, D.U. Sauer, C. Rahe, S. Kabitz and E. Figgemeier, "Long-term cycling induced jelly roll deformation in commercial 18650 cells," *Journal of Power Sources*, vol. 392, pp. 168-175, 2018.
- [64] A.J. Louli, J. Li, S. Trussler, C.R. Fell, J.R. Dahn, "Volume, pressure and thickness evolution of Li-ion pouch cells with silicon-composite negative electrodes," *Journal of The Electrochemical Society*, vol. 164, pp. 2689-2696, 2017.
- [65] L. Wang, X. He, W. Sun, J. Wang, Y. Li and S. Fan, "Crystal orientation tuning of LiFePO₄ nanoplates for high rate lithium ion battery cathode materials," *Nano Letters*, vol. 12, pp. 5632-5636, 2012.
- [66] G. Li, Y. Qiu, Y. Hou, H. Li, L. Zhou, H. Deng and Y. Zhang, "Synthesis of V₂O₅ hierarchical structures for long cycle-life lithium-ion storage," *Journal of Material Chemistry A*, vol. 3, pp. 1103-1109, 2015.
- [67] M.G. Matshaba, D.C. Sayle, T.X.T. Sayle and P.E. Ngoepe, "Structure of surface entrance sites for Li intercalation into TiO₂ nanoparticles, nanosheets, and mesoporous architectures with application for Li-ion batteries," *Journal of Physical Chemistry*, vol. 120, pp. 14001-14008, 2016.
- [68] R.R. Maphanga, D.C. Sayle, T.X.T. Sayle and P.E. Ngoepe, "Amorphization and recrystallization study of lithium insertion into manganese dioxide," *Journal of Physical Chemistry*, vol. 13, pp. 1308-1309, 2011.

- [69] K. Alberi, M.B. Nardelli, A. Zakutayev, L. Mitas, S. Curtarolo, A. Jain, M. Fornari, N. Marzari, I. Takeuchi, M.L. Green, M. Kanatzidis, M.F. Toney, S. Butenko, B. Meredig, S. Lany, U. Kattner, A. Davydov, A. Walsh, N.G. Park and J. Perkins, "The 2019 materials by design roadmap," *Journal of Physics D: Applied Physics*, vol. 52, pp. 1-48, 2019.
- [70] E. Wimmer, "The growing importance of computations in material science: Current capabilities and perspectives," *Material Science-Poland*, vol. 23, pp. 325-344, 2005.
- [71] M.O. Steinhauser and S. Heirmaier, "A review of computational methods in material science: Examples from shock-wave and polymer physics," *International Journal of Molecular Sciences*, vol. 10, pp. 5136-5209, 2009.
- [72] R.S. Ledwaba, "Atomistic simulation studies of composite layered-spinel Li-Mn-O nanoarchitectures," University of Limpopo, PhD Thesis, South Africa, Polokwane, 2017.
- [73] P.E. Ngoepe, R.R. Maphanga and D.C. Sayle, "Towards the nanoscale," in *Computational approaches to energy materials, First Edition*, John Wiley and Sons, Ltd., 2013, pp. 264-266.
- [74] D.C. Sayle, J.A. Doige, M.S. Andrata and G.W. Watson, "Atomistic structure of oxide nanoparticles supported on an oxide substrate," *Physical Review B*, vol. 65, pp. 2-3, 2002.
- [75] "Azo materials," *Protechips*, 2 April 2014. [Online]. Available: <http://www.azom.com/article.aspx?ArticleID=10826>. [Accessed 5 May 2017].

- [76] J. Hafner, "Atomistic-scale computational materials science," *Acta materialia*, vol. 48, pp. 71-77, 2000.
- [77] T.X.T. Sayle, F. Caddeo, X. Zhang, T. Sakthivel, S. Das, S. Seal, S. Ptasinska and D.C. Sayle, "Structure-activity map of ceria nanoparticle, nanocubes, and mesoporous architectures," *Chemistry of Materials*, vol. 28, pp. 7287-7295, 2016.
- [78] H. Zhang and J.F. Banfield, "Aggregation, coarsening, and phase transformation in ZnS nanoparticles studied by molecular simulations," *Nano Letters*, vol. 4, pp. 713-718, 2004.
- [79] L. Verlet, "Computer experiments on classical fluids. I. thermodynamical properties of Lennard-Jones molecules," *Physical Review*, vol. 159, pp. 98-103, 1967.
- [80] J. Li, "Basic molecular dynamics," in *Handbook of materials modelling*, Springer, 2005, pp. 565-588.
- [81] C. Kittel and K. Herbet, *Thermal Physics*, 2nd Edition, San Fransisco: W.H Freeman and company, 1980.
- [82] L.D. Landau and E.M. Lifshits, *Statistical Physics*, Britain: Pergamon Press, 1980.
- [83] B. Wisdom, *Statistical mechanics: A concise introduction for chemists*, England: Cambridge University Press, 2002.
- [84] B.L. Dutrow and C.M. Clark, "Research education," *Geochemical instrumentation and analysis*, [Online]. Available: <http://serc.carleton.edu>. [Accessed 28 February 2018].

- [85] D.P. Moecher, "Characterization and identification of mineral unknowns," *Journal of Geoscience Education*, vol. 52, pp. 5-9, 2004.
- [86] M.P. Groover, *Fundamentals of Modern Manufacturing 2/e*, John Wiley & Sons, 2002.
- [87] D. Collins, "Mechanical properties of materials: Stress and strain," Linear motion tips, 8 March 2019. [Online]. Available: <http://www.linearmotiontips.com>. [Accessed 31 January 2021].
- [88] D.C. Sayle, J.A. Doig, S.A. Maicaneanu and G.W. Watson, "Atomistic structure of oxide nanoparticles supported on an oxide substrate," *Physical Review B*, vol. 65, pp. 2-3, 2002.
- [89] D.C. Sayle, B.C. Mangili, D.W. Price and T.X. Sayle, "Nanopolycrystalline materials; a general atomistic model for simulation," *Physical Chemistry Chemical Physics*, vol. 12, pp. 8584-8596, 2010.
- [90] D.C. Sayle, "The predicted 3-D atomistic structure of an interfacial screw-edge dislocation," *Journal of Materials Chemistry*, vol. 9, pp. 2961-2962, 1999.
- [91] T.X.T. Sayle, C.R.A. Catlow, R.R. Maphanga, P.E. Ngoepe and D.C. Sayle, "Generating MnO₂ nanoparticles using simulated amorphisation and recrystallization," *Journal of American Chemistry Society*, vol. 127, pp. 12828-12837, 2006.
- [92] D.C. Sayle and S.C. Parker, "Encapsulated oxide nanoparticles: the influence of the microstructure on associated impurities within a material," *Journal of the American Chemical Society*, vol. 125, pp. 8581-8588, 2003.

- [93] W. Smith and T.R. Forester, "DL_POLY_2.0: A general-purpose parallel molecular dynamics simulation package," *Journal of Molecular Graphics*, vol. 14, pp. 136-141, 1996.
- [94] I.T. Todorov and W. Smith, "The DL_POLY_4 user manual," England, United Kingdom, 2016.
- [95] C.R.A Catlow, L. Ackermann, R.G. Bell, F. Cora, C.D.H. Gay, "Introductory lecture computer modelling as a technique in solid state chemistry," *Faraday Discussions*, vol. 106, pp. 1-40, 1997.
- [96] M. Born and K. Haug, "Dynamical theory of crystal lattices," *Oxford University Press*, pp. 1-19, 1954.
- [97] R.A. Buckingham, "The classical equations of state of gaseous helium, neon and argon," *Proceedings of Royal Society A*, vol. 168, pp. 264-283, 1938.
- [98] A. Abadi, "Materials Properties," [Online]. Available: uotechnology.edu.iq/appsciences/filesPDF/material/Materials_prproperties3.pdf. [Accessed 6 November 2018].
- [99] J.W. Morris, "Defects in crystals," California, Materials Science, 2013, pp. 76-79.
- [100] C. Kittel, "Introduction to solid state physics, 8th Edition," in *Point defects*, John Wiley & Sons, 2005, pp. 584-586.
- [101] P. Porlaz and B. Smarsly, "Nanoporous materials," *Journal of Nanoscience and Nanotechnology*, vol. 6, pp. 581-612, 2002.

- [102] N.P. Lyakishev, M.I. Alymov, and S.V. Dobatkin, "Structural bulk nanomaterials," *Russian Metallurgy (Metally)*, vol. 3, pp. 191-202, 2003.
- [103] P. Ehrhart, "Properties and interactions of atomic defects in metals and alloys," in *Landolt-Börnstein, New series III, Chapter 2*, Berlin, Springer, 1991.
- [104] K. M. Kgatwane, "Atomistic simulation studies of lithiated MnO₂ nanostructures," M.Sc Dissertation, University of Limpopo, 2011.
- [105] D. Tang, Y. Sun, Z. Yang, L. Ben, L. Gu and X. Huang, "Surface structural evolution of LiMn₂O₄ cathode material upon charge/discharge," *Chemistry of Materials*, vol. 26, pp. 3535-3543, 2014.
- [106] T. Ramachandran, N. Naveen, K. Vishista and F. Hamed, "Investigation on electrochemical performance of Hausmannite Mn₃O₄ nanoparticles by ultrasonic irradiation assisted co-precipitation method for supercapacitor electrodes," *Journal of Taibah University for Science*, vol. 1, pp. 1-24, 2017.
- [107] M.M. Thackeray, M.F. Mansuetto, D.W. Dees and D.R. Vissers, "The thermal stability of lithium-manganese-oxide spinel phases," *Materials Research Bulletin*, vol. 31, pp. 133-140, 1996.
- [108] W. Hua, B. Schwarz, M. Knapp, A. Senyshyn, A. Missiul, X. Mu, S. Wang, C. Kubel, J.R. Binder, S. Indris and H. Ehrenberg, "(De)Lithiation mechanism of hierarchically layered LiNi_{1/3}Co_{1/3}Mn_{1/3}O₂ cathodes during high-voltage cycling," *Journal of Electrochemical Society*, vol. 166, pp. A5025-A5032, 2019.

- [109] T.X.T. Sayle, F. Caddeo, N.O. Monama, K.M. Kgatewane, P.E. Ngoepe and D.C. Sayle, "Origin of electrochemical activity in nano-Li₂MnO₃; stabilizing via a point defect scaffold," *Nanoscale*, vol. 7, pp. 1167-1180, 2015.
- [110] T.X.T. Sayle, K. Kgatewane, P.E. Phuti and D.C. Sayle, "'Breathing-crystals' the origin of electrochemical activity of mesoporous Li-MnO₂," *Journal of Materials Chemistry A*, vol. 1, pp. 1-8, 2016.
- [111] D. Qu, "Fundamental principals of battery design: Porous electrodes," *Review on Electrochemical Storage Materials and Technology*, vol. 1597, pp. 14-25, 2014.
- [112] M. Anilkumar, V. Rajanesh, K. Prabhu, C.S. Sunandana, "A Basic study on nano-Li₂NiO₂ highly porous spheres for lithium ion battery applications," *International Journal of Scientific and Engineering Research*, vol. 7, pp. 448-450, 2016.
- [113] W. Łojkowski, A. Proykova and R. Turan, "European nanotechnology gateway; Nanometrology," July 2006. [Online]. Available: www.nanoforum.org. [Accessed 24 February 2021].
- [114] W. Tian, C. Tang, Q. Wang, S. Zhang and Y. Yang, "The effect and associate mechanism of Nano SiO₂ particles on the diffusion behaviour of water in insulating oil," *Materials*, Vol. 11, 2373, pp. 2-10, 2018.
- [115] J. Choa and M.M. Thackeray, "Structural changes of LiMn₂O₄ spinel electrodes during electrochemical cycling," *Journal of The Electrochemical Society*, vol. 140, pp. 3577-3581, 1999.
- [116] M. Hu, X. Pang and Z. Zhou, "Recent progress in high-voltage lithium ion batteries," *Journal of Power Sources*, vol. 237, pp. 229-242, 2013.

- [117] R. Santhanam and B. Rambabu, "Research progress in high voltage spinel $\text{LiNi}_{0.5}\text{Mn}_{1.5}\text{O}_4$ material," *Journal of Power Sources*, vol. 195, pp. 5442–5451. , 2010.
- [118] C. Zhang, X. Liu, Q. Su, J. Wu, T. Huang and A. Yu, "Enhancing the electrochemical performance of LiMn_2O_4 cathode material at elevated temperature by uniform nanosized TiO_2 coating," *Sustainable Chemistry and Engineering*, vol. 5, pp. 640–647, 2017.
- [119] S. Ma, M. Jiang, P. Tao, C. Song, J. Wu, J. Wang, T. Deng and W. Shang, "Temperature effect and thermal impact in lithium-ion batteries: A review," *Progress in Natural Science: Materials International*, vol. 28, pp. 653-666, 2018.
- [120] A. Pesaran. S. Santhanagopalan and G.H. Kim, "Addressing the impact of temperature extremes on large format Li-ion batteries for vehicle applications," in *Proceedings of the 30th international battery seminar*, Ft Lauderdale, Florida, 2013.
- [121] Z.W. Shan, G. Adesso, A. Cabot, M.P. Sherburne, S.A. Syed Asif, O.L. Warren, D.C. Chrzan, A.M. Minor and A.P. Alivisatos, "Ultrahigh stress and strain in hierarchically structured hollow nanoparticles," *Nature Materials*, vol. 7, pp. 947-952, 2008.
- [122] R.A. Huggins, W.D. Nix, "Decrepitation model for capacity loss during cycling of alloys in rechargeable electrochemical systems," *Ionics*, vol. 6, pp. 57-63, 2000.
- [123] G. Venugopal, A. Hunt and F. Alamgir, "Nanomaterials for energy storage in lithium-ion battery applications," *Material Matters*, vol. 5, pp. 42-49, 2010.

- [124] T.X.T. Sayle, B.J. Inkson, A. Karakoti, A. Kumar, M. Molinari, G. Mobus, S.C. Parker, S. Seal and D.C. Sayle., "Mechanical properties of ceria nanorods and nanochains; the effect of dislocations, grain-boundaries and oriented attachment," *Nanoscale*, vol. 3, pp. 1823-1837, 2011.
- [125] "South 32," South 32 Limited, 18 May 2015. [Online]. Available: www.south32.net. [Accessed 07 September 2021].
- [126] M. Creamer, "Mining Weekly," Creamer Media's Mining Weekly, 2020 September 28. [Online]. Available: <https://m.miningweekly.com>. [Accessed 2021 September 10].
- [127] "Pocket Guide to South Africa," 2012/13. [Online]. Available: <http://www.gcis.gov.za>. [Accessed 27 September 2021].
- [128] R.S. Ledwaba, D.C. Sayle and P.E. Ngoepe, "Atomistic simulation and characterization of spinel $\text{Li}_{1+x}\text{Mn}_2\text{O}_4$ ($0 \leq x \leq 1$) nanoparticles," *ACS Applied Energy Materials*, vol. 3, pp. 1429-1438, 2020.
- [129] B. Shibiri, R.S. Ledwaba and P.E. Ngoepe, "Discharge induced structural variation of simulated bulk $\text{Li}_{1+x}\text{Mn}_2\text{O}_4$ ($0 \leq x \leq 1$)," *Optical Materials*, vol. 92, pp. 67-70, 2019.
- [130] S.H. Park, S.T. Myung, S.W. Oh, C.S. Yoon and Y.K. Sun, "Ultrasonic spray pyrolysis of nanocrystalline spinel LiMn_2O_4 showing good cycling performance in the 3 V range," *Electrochimica Acta*, vol. 51, pp. 4089-4095, 2006.
- [131] C. Liu, H. Xia, Y. Wei, J. Ma, L. Gan, F. Kang and Y.B. He, "Grain boundaries contribute to highly efficient lithium-ion transport in advanced $\text{LiNi}_{0.8}\text{Co}_{0.15}\text{Al}_{0.05}\text{O}_2$

secondary sphere with compact structure,” *SusMat Wiley*, vol. 1, pp. 255-265, 2021.

[132] B. Lesel, Development of pseudocapacitive properties in nanostructured LiMn_2O_4 as fast charging cathode for lithium ion batteries, Los Angeles: University of California, 2017.

SCIENTIFIC CONTRIBUTIONS

Papers at local conferences

1. The mechanical properties study of $\text{Li}_{1+x}\text{Mn}_2\text{O}_4$, ($0 \leq x \leq 1$) cathode materials, 65th South African Institute of Physics (SAIP) Virtual Conference, North-West University, Potchefstroom Campus, (July 2021)
2. Structural evolution of LiMn_2O_4 nanoporous cathode material upon lithiation, 13th Centre for High Performance Computing Conference (CHPC) National Meeting, Johannesburg, Birchwood Hotel (December 2019)
3. Investigating the mechanical properties of lithiated $\text{Li}_{1+x}\text{Mn}_2\text{O}_4$, ($0 \leq x \leq 1$) nanoporous composites, 13th Centre for High Performance Computing Conference (CHPC) National Meeting, Johannesburg, Birchwood Hotel (December 2019)
4. Electrochemical and mechanical properties of lithiated Li-Mn-O layered-spinel nanoporous materials, 10th Postgraduate Research Day, University of Limpopo Polokwane, Protea Hotel Ranch Resort (September 2019)
5. Stress-induced structural changes of lithiated $\text{Li}_{1+x}\text{Mn}_2\text{O}_4$ ($0 \leq x \leq 1$) nanoporous electrode materials, 64th South African Institute of Physics (SAIP) Conference, University of Venda, Polokwane, Protea Hotel Ranch Resort, (July 2019)
6. Investigating the structural and volume changes of composite layered-spinel nanoporous Li-Mn-O electrode materials, 12th Centre for High Performance Computing Conference (CHPC) National Meeting, Cape Town, Century City Hotel, (December 2018)
7. The effect of lithiation on layered-spinel Li-Mn-O nanoarchitectures, 9th Postgraduate Research Day, University of Limpopo, Polokwane, Fusion Boutique Hotel (September 2018)

8. Effects of pore size on the electrochemical properties of Li-Mn-O nanoporous cathode materials, 63th South African Institute of Physics (SAIP) Conference, University of Free State, Bloemfontein, (June 2018)
9. Simulating the discharge process of Li-Mn-O nanospheres, 11th Centre for High Performance Computing Conference (CHPC) National Meeting, Pretoria, Velmoreé Hotel Estate, (December 2017)

Papers at international conferences

1. Scrutinizing the structural and mechanical behaviour of Li-Mn-O nanoporous structures for Li-ion battery cathode materials, Women in STEM, East London, East London ICC, (February 2020)
2. Atomistic Perspectives on Mechanical Properties of Nanoporous Li-Mn-O Cathode upon Li-Intercalation, International Battery Association (IBA), USA, San Diego, (March 2019)
3. Lithiation induced structural changes in layered-spinel bulk and nanoporous Li-Mn-O electrode materials, 13th Europhysical Conference for Defects in Insulating Materials (EURODIM), Poland, University of Bydgoszcz, Holiday Inn Hotel, (July 2018)

Awards

1. 13th Centre for High Performance Computing Conference – 1st prize Best PhD student poster presentation, Johannesburg, Birchwood Hotel (December 2019)
2. 10th Postgraduate Research Day – 3rd prize oral presentation, Polokwane, Protea Hotel Ranch Resort, (September 2019)
3. 64th South African Institute of Physics Conference – Best Oral MSc Presentation, Polokwane, Protea Hotel Ranch Resort (July 2019)

4. 12th Centre for High Performance Computing Conference – 1st Prize MSc student poster presentation, Cape Town, Century City Hotel, (December 2018)
5. Europhysical Conference for Defects in Insulating Materials – Best MSc poster presentation, Poland, Holiday Inn Hotel, (July 2018)

Publications

Discharge induced structural variation of simulated bulk $\text{Li}_{1+x}\text{Mn}_2\text{O}_4$ ($0 \leq x \leq 1$), *Optical Materials*, (2019), **92**, 67-70,